Université de Toulouse

THÈSE

En vue de l'obtention du

DOCTORAT DE L'UNIVERSITÉ DE TOULOUSE

Délivré par *l`INSTITUT NATIONAL DES SCIENCES APPLIQUEES DE TOULOUSE*
Discipline ou spécialité : *Nanophysique*

Présentée et soutenue par
Sergej KUNZ
Le *7 février 2013*

Titre : *Magneto-optical properties of individual GaAs/AlGaAs Quantum Dots grown by Droplet Epitaxy*

JURY

Daniel PAGET	*Rapporteur*
Christophe TESTELIN	*Rapporteur*
Guillaume CASSABOIS	*Examinateur*
Michel GOIRAN	*Examinateur*
Thierry AMAND	*Directeur de Thèse*
Bernhard URBASZEK	*Directeur de Thèse*

Ecole doctorale : *Sciences de la Matiére*
Unité de recherche : *Laboratoire de Physique et Chimie de Nano-Objets UMR 5215*
Directeur(s) de Thèse : *Thierry AMAND*
Bernhard URBASZEK
Rapporteurs : *Daniel PAGET*
Christophe TESTELIN

N° ordre 1187

THESE

présentée à

L'INSTITUT NATIONAL DES SCIENCES APPLIQUEES DE TOULOUSE

vue de l'obtention du

DOCTORAT DE L'UNIVERSITE DE TOULOUSE

Spécialité : Nanophysique

par

Sergej KUNZ

Magneto-optical properties of individual GaAs/AlGaAs Quantum Dots grown by Droplet Epitaxy

Soutenue le 7 février 2013, à Toulouse

devant la commission d'examen :

Rapporteur	D. PAGET	Directeur de Recherche, LPMC-CNRS Palaiseau
Rapporteur	C. TESTELIN	Directeur de Recherche, UPMC Paris
Examinateur	G. CASSABOIS	Professeur des Universités, Montpellier II
Examinateur	M. GOIRAN	Professeur UPS, LNCMI Toulouse
Directeur de thèse	T. AMAND	Directeur de Recherche, LPCNO-CNRS Toulouse
Directeur de thèse	B. URBASZEK	Chargé de Recherche, LPCNO-CNRS Toulouse

Cette thèse a été préparée au sein du Laboratoire de Physique et Chimie des Nano-Objets, UMR 5215 INSA-CNRS-UPS.

Contents

Summary

In this thesis the magneto-optical properties of single GaAs semiconductor quantum dots in AlGaAs barriers are presented. The strain free dots are grown by original Volmer-Weber ("droplet") epitaxy techniques in a molecular beam epitaxy system at the National Institute for Material Science NIMS, Tsukuba, Japan. Contrary to conventional strain-driven quantum dot growth, droplet epitaxy allows a wide choice of the lattice constants and crystallographic orientations of the barrier materials. The samples investigated during this thesis are original in several aspects: GaAs droplet dots allow the investigation of carrier and nuclear spin physics in the absence of strain i.e. strong nuclear quadrupole effects. Also, symmetric dots with a very small exciton fine structure grown along the [111] axis have allowed us to uncover novel spin physics in samples without a wetting layer.

The single dot spectroscopy measurements were performed under non-resonant optical excitation in the $Al_{0.3}Ga_{0.7}As$ barrier at low temperature (4 K) in a confocal microscope. A top-loading magneto-cryostat was used to apply a magnetic field parallel to the growth sample growth axis, which is also the light propagation axis (Faraday configuration). To carry out single dot measurements in Voigt geometry i.e. with a magnetic field applied perpendicular to the growth axis, a home built adapter associated to a phase compensation device was conceived and achieved during this thesis.

In Chapter 3 of this thesis we show the first optical investigation of symmetric GaAs quantum dots grown on (111)A substrates. The inherently small neutral exciton fine structure splitting makes this a promising system for the generation of polarisation entangled photons via the exciton-biexciton radiative cascade. In photoluminescence spectra in longitudinal magnetic fields applied along the growth axis, we observe in addition to the expected bright states also nominally dark transitions for both charged and neutral excitons. We uncover a strongly non monotonic, sign-changing field dependence of the bright neutral exciton splitting resulting from the interplay between exchange and Zeeman effects. We present a microscopic theory developed in close collaboration with the A. F. Ioffe Institute (St. Petersburg, Russia) of the magnetic field induced mixing of heavy-hole states with angular momentum projections $\pm 3/2$ in GaAs droplet dots grown on (111)A substrates. The proposed theoretical model takes into account the striking dot shape with trigonal C_{3v} symmetry revealed in atomic force microscopy. Our calculations of the hole states are carried out within the Luttinger Hamiltonian formalism, supplemented with allowance for the triangularity of the confining potential. The model is in good quantitative agreement with the experimentally observed polarization selection rules, emission line intensities and energy splittings in both longitudinal and transverse

magnetic fields for neutral and charged excitons in all measured single dots. The hole gyro-magnetic tensor and electron Landé g-factor and this novel system are extracted.

Chapter 4 of this thesis is focused on the charge tuneable structures grown on n^+-(100) GaAs substrate. In non-intentionally doped samples, due to charge fluctuations, the neutral X^0 exciton and the positively (negatively) charged exciton $X^+(X^-)$ are observed simultaneously in time integrated spectra. We present here deterministic charging of droplet dots with single electrons. Detailed studies in transverse magnetic fields allowed unambiguously identifying the charge states and determining the exciton fine structure. The neutral exciton fine structure was tuned to zero in finite transverse fields, a crucial property for achieving efficient polarization entangled two photon sources.

In chapter 5, we focus on the nuclear spin effects in [111] grown quantum dots under optical pumping conditions. An optically oriented electron spin can transfer its polarization to a nucleus (Overhauser effect). In the well-studied strained InGaAs dots in GaAs, dynamic nuclear polarization (DNP) at zero applied magnetic field is possible due to screening of the nuclear dipole-dipole interaction by strong nuclear quadrupole effects. Here we present the first observation of DNP in strain free dots, i.e. in the absence of nuclear quadrupole effects. We investigated in detail the role of the strong effective magnetic field acting on the nuclei due to the presence of a well-oriented electron spin (Knight field). This Knight field in the order of 15 mT for most dots is an important ingredient for the observed DNP at zero field. The intricate interplay between the Knight field and the Overhauser field is studied in a transverse magnetic field. These Hanle measurements performed on single dots allow us to determine the sign of the confined electron g-factor and spin relaxation time.

New research directions and future plans are discussed in the closing chapter of this thesis.

Glossary

QD	quantum dot
MBE	molecular beam epitaxy
MOCVD	metalorganic chemical vapor deposition
In	Indium
Al	Aluminum
Ga	Galium
As	Arsenic
P	Phosphor
HeNe	helium neon
STM	scanning tunneling microscopy
AFM	atomic force microscopy
AEI	anisotropic exchange interaction
X-SST	cross-sectional scanning tunneling
ML	mono layer
PL	photoluminescence
RHEED	reflection high-energy electron diffraction
HH	heavy hole
LH	light hole
SO	split-off states
CCD	charge coupled device
ODNMR	optically detected nuclear magnetic resonance
S_c&P_c	s- and p-energy levels of conduction states
V_c&V_c	s- and p-energy levels of valence states
m_s	electron angular momentum
$\hbar$	Planck‘s constant
J_z	hole angular momentum projection
S_z	electron angular momentum projection
J	total angular momentum
J_z^{total}	total angular momentum projection

$\chi_{\pm}$	spinors
ϕ_{l,m_l}	Bloch basic functions
l	orbital angular momentum
m_l	orbital angular momentum quantum number
m_0	electron mass in vacuum
m_{HH}	effective heavy-hole mass
m_{LH}	effective light-hole mass
m_{SO}	effective split-off band mass
e	electron charge
$\hat{\boldsymbol{p}}$	vector of the kinetic momentum
$\mathbf{A}$	potential vector
δ_0	bright dark splitting of an exciton
δ_1	bright fine structure splitting
δ_2	dark fine structure splitting
m_{HH}	effective heavy-hole mass
m_{LH}	effective light-hole mass
m_{SO}	effective split-off band mass
e	electron charge
$\hat{\boldsymbol{p}}$	vector of the kinetic momentum
$\mathbf{A}$	potential vector
$\hat{p}_i, i = x,y,z$	potential vector components
$\lvert S\rangle$	s-like conduction state
$\lvert X\rangle$, $\lvert Y\rangle$ und $\lvert Z\rangle$	p-like valence states
Δ_{HL}	heavy-hole light-hole splitting
$\mathbf{B}$	magnetic field vector
B_z	z-component of applied magnetic field
$B_{z'}$	z-component of applied magnetic field in new frame system
D_{2d}, C_{3v}, C_{2v}	symmetry groups
λ	wave length
$E(\sigma^{\pm})$	energy of $\sigma^{\pm}$ polarised transitions
$\Gamma_{5,6}$	irreducible representations of the group C_{3v}
μ_{B}	the Bohr magneton
$g^{\perp}_{h1,2}$	transverse effective hole g-factors
$g^{\perp}_{e}$	transverse effective electron g-factors

$g_{h1,2}^{\parallel}$	longitudinal effective hole g-factors
$g_{e}^{\parallel}$	longitudinal effective electron g-factors
$C_{1,2}$	heavy-hole coupling coefficients
$\lvert h,+\rangle$ and $\lvert h,-\rangle$	modified heavy-hole states
$\mathbf{r}$	vector
$\mathscr{V}(\boldsymbol{r})$	the operator of the hole potential energy
k_j, $(j = x,y,z)$	the Cartesian components
F, G, H, and I	matrix elements of the Luttinger Hamiltonian
I^j	nuclear spin of j specious
g_{N}	nuclear g-factor
μ_{N}	nuclear magneton
ν_0	the two atom cell volume
$\boldsymbol{r}_j$	position of the nuclei j
A^j	constant of the hyperfine interaction
B_K	Knight field
f_e	filling factor
$\tilde{A}$	the average of the hyperfine constants
$\hat{H}_{hf}$	Hamiltonian of Hyperfine interaction
B_{L}	local magnetic field
γ_α	gyromagnetic factor of α nuclei
k_{B}	Boltzmann constant
Θ	the nuclear temperature
$\left\langle \vec{S} \right\rangle$	electron spin polarisation
$\langle S_0 \rangle$	initial electron spin polarisation
$\vec{B}_n'$	effective nuclear field
f	leakage factor
ρ	polarisation of emitted PL
ρ_0	initial polarisation of PL
$\rho_0(0)$	initial polarisation of PL at 0 T
κ	effective Knight field
$\alpha_{x,y}^2$	bright relative oscillator strengths
$\beta_{x,y}^2$	dark relative oscillator strengths

Introduction

Electronic spins in most semiconductors are relatively well decoupled from orbital or charge degrees of freedom. As a consequence, electronic spin coherence is not hindered by the prevalent charge decoherence, rendering spins good candidates for the realization of novel devices whose functionalities rely on quantum coherence. The isolation of spins from adverse effects of fluctuating charge environments is particularly effective in quantum dots (QDs) where electronic motion is quantum confined in all directions to length scales on the order of 10 nanometers. In such atom-like structures, hyperfine coupling is the dominant interaction for both the spin of the electron confined to the QD and the nuclear spins, making this system a nearly ideal realization of the central spin model.

The basic principle of optical manipulation and measurement of QD spins we describe has its roots in the use of strong spin-orbit interaction of valence band states which allow for correlating the optically excited electron spin with the polarisation of the excitation laser. This is in fact the same physics used in optical pumping experiments carried out in atomic vapors: in 1952 Kastler, Brossel and Winter investigated Mercury atoms in a weak magnetic field which splits the electron states into Zeeman sublevels. By irradiation of the atoms with circularly polarised light the authors could selectively populate one of the electron Zeeman levels [1]. Subsequent optical pumping experiments on atoms with nonzero nuclear spin resulted in direct preparation of correlated electron-nuclear spin states in atoms.

In pioneering work in the solid-state, Knight observed that polarised electrons lead to a shift in nuclear magnetic resonance frequency [2]. In 1953 Overhauser proposed to polarise nuclear spins by transferring spin polarization from electrons to the nuclear spin system. In this original proposal, a net electron spin polarisation was created simply by allowing thermalisation in an applied longitudinal field [3]. Soon afterwards the ideas of Overhauser and Brossel *et al* were combined in the first work on optical preparation of electron spins and the resulting interaction of these spin polarised electrons with the nuclear spin system in a semiconductor [4]. In this experiment performed with silicon the initial pumping of spin oriented conduction electrons induced by polarised light leads to a polarisation of the nuclear spins of the atoms of the silicon lattice via the hyperfine interaction (Overhauser effect). This is based on the angular momentum transfer between photons and electrons and subsequently between electrons and nuclei. The nuclear polarisation was detected by Lampel through the enhancement of the nuclear magnetic resonance signal. A detailed review of the nuclear spin effects in bulk semiconductor optics can be found in [5], where the key ingredients for strong hyperfine effects in solids were clearly identified: localization

of the carrier wave function around a finite number of nuclei and temporal fluctuations in the electron spin system i.e. a short correlation time of the hyperfine interaction. As a result strong nuclear effects imprinted on the polarisation of the emitted photons were observed in n-doped bulk semiconductors which show strong localization of carriers around donors [6, 7, 8].

Due to the strong localization of the carrier wave function in a QD, the role of hyperfine interactions in spin dynamics is drastically enhanced; this is a direct consequence of enhanced fluctuations in the effective magnetic field seen by the electron spin (Overhauser field) due to its interactions with randomly oriented QD nuclei. Similarly, the effective magnetic field seen by each nucleus (Knight field) is more susceptible to fluctuations in the electron spin. Soon after the first observation of emission from single QDs [9] it became clear that studies of the electron spin system cannot be done without taking nuclear effects into account. Conversely, ultra-narrow QD optical transition line widths allow for a direct measurement of the nuclear field, greatly enhancing the possibilities for investigating nuclear spin dynamics using optical spectroscopy. This is shown in pioneering work on optically detected nuclear magnetic resonance ODNMR in GaAs dots in AlGaAs [10, 11].

Initialization of an individual electron or hole spin with a laser pulse is possible due to angular momentum transfer between photons and electrons, enabled by spin-orbit interaction and ensuing optical selection rules. Once initialized, the prospects for controlled, coherent manipulations of spins in QDs are very good as the main spin relaxation mechanisms known from experiments in bulk or 2D semiconductors do not apply to localized carriers in dots [12, 13, 14]. However, it had been pointed out early [15, 16, 17, 18] that interactions with fluctuating, arbitrarily aligned nuclear spins of the atoms that form the QD might severely limit the electron spin coherence time. This prediction has indeed been confirmed independently for electrons in transport measurements and in optical spectroscopy [19, 20]. Extending the carrier spin coherence time for controlled quantum state (qubit) manipulation was one of the strong motivations that led to increased interest in nuclear spin physics in QDs [21]. Many fascinating experiments have been reported confirming the strong, reciprocal interaction between the two spin systems. For example, the magnitude and direction of the Overhauser field created via optical pumping can be tuned by adjusting laser power and polarisation [22, 23, 24, 25]. The nuclear spin system can be stable up to several hours under certain conditions, which is interesting for information storage schemes [26]. The hyperfine interaction allows for tuning the exact energy of the electronic states and for controlling the polarisation of the emitted light. This is particularly true for experiments in the absence of magnetic fields [27, 28, 29] and could become important for applications in photonics. For example, knowing the exact polarisation basis is crucial when evaluating the degree of entanglement of a source of photon pairs based on optical transitions from the conduction to valence state in a single quantum dot [30, 31, 32].

Hyperfine effects in QDs can have other spectacular consequences, such as locking of a QD transition to a resonant pump laser [33, 34, 35], bistability of the nuclear spin system [24, 36, 37, 38] depending not only on the experimental parameters at the time the measurement was performed but also on the history of the experiment (non-Markovian behavior). The mesoscopic nuclear spin system may enable observation of physical phenomena such as Levy flights [39], spin-squeezed states [40] and dissipative quantum phase transitions [41, 42]. Studies of hyperfine effects in dots are also relevant for other

systems with localized carriers, such as nitrogen vacancy centers in diamond [43, 44].

Scope of this thesis

In this thesis we report experimental results performed at single Droplet Dots under non-resonant optical excitation.

In Chapter 1 basics of single dot physics are introduced. We start with growth techniques including the Modified Molecular Beam Epitaxy so-called Droplet Epitaxy. The different growth directions used in investigated QDs are introduced and also their advantages. Since we studied the spin properties of QDs by optical excitation it is essential to know how the angular momentum of a photon is transfered to a carrier resulting in a polarised carrier. Hence the optoelectronic properties including the optical selection rules are introduced. Finally, the main optical spectroscopy techniques successfully used in last decades to study spin properties of electron and nuclear system are described including the non-resonant PL single dot spectroscopy, by means of which the QDs were investigated in framework of this thesis.

Chapter 2 describes the experimental setup used to study our droplet dots. The principle of a confocal microscopy is shortly introduced following by in detail described experimental issues relevant for measurements.

In Chapter 3 we report on the dark bright mixing induced by applied longitudinal magnetic field in (111)A QDs. While in common grown QDs heavy hole states are pure $\left|\pm\frac{3}{2}\right\rangle$ in (111)A QDs they are not pure any more, but mixtures of both $\left|+\frac{3}{2}\right\rangle'$ and $\left|-\frac{3}{2}\right\rangle'$ namely $|h,+\rangle = C_1\left|+\frac{3}{2}\right\rangle' + C_2\left|-\frac{3}{2}\right\rangle'$ and $|h,-\rangle = -C_2\left|+\frac{3}{2}\right\rangle' + C_1\left|-\frac{3}{2}\right\rangle'$ resulting in 2 additionally opened recombination channels-dark states. The in-depth theoretical approach revealed that these phenomenological results have their origins in the geometrical shape of the investigated dots. All the experimental results could be explained very precisely by using our theoretical approach.

Chapter 4 is dealing with the first report on (100) charge tunable Droplet Dot structure where the charge of a single droplet dot was successfully controlled opening new perspectives in implementing droplet dots. Furthermore, interesting results were observed in charge tunable structure. Depending on the QD orientation with respect to applied transverse magnetic field the hole g-factor changes its sign. In addition, the very big electron g-factor up to 1 was observed opening new investigation perspectives to explain how the electron g-factor can exceed the g-factor of AlGaAs barrier.

In Chapter 5 the observation of Knight field in longitudinal and transverse magnetic field is reported These results were observed in (111)A droplet dots. The Knight field in longitudinal field could be tuned by varying the excitation polarisation according to the theoretical prediction. In Voigt configuration by means of Hanle effect the Knight field affected at the spin depolarisation Hanle curve resulting in a W-shape of Hanle curve in low field. A theoretical approach containing the Knight field value observed in Faraday geometry could qualitatively describe the observed Hanle curve.

CHAPTER 1

Basics of semiconductor quantum dots

Semiconductor QDs are nanometer sized objects that contain typically several thousand atoms of a semi-conducting compound resulting in a quantum confinement of the carriers in the three spatial directions. As a consequence, the energy levels in semiconductor QDs are discrete.

A semiconductor QD is an island on nanometer scale embedded in a barrier material with a higher bandgap. Well characterized QD/barrier combinations are strained InAs/GaAs and strain-free GaAs/$Al_xGa_{1-x}As$.

Since the carriers in a QD are confined in all three directions the carrier energies are discrete and QDs are often referred to as " Artificial Atoms ". Indeed, micro-photoluminescence experiments [9], photon correlation measurements [45] and resonant laser scattering [46] have established the atom like character of the interband transitions. This motivated many research groups to probe and manipulate charge and spin states of individual carriers. These experiments test the possibility of using these QD states as qubits for quantum information processing [47].

1.1 Growth and sample structures

1.1.1 General growth techniques

Semiconductor QDs can be synthesized by a large variety of methods based on colloidal chemistry, molecular beam epitaxy (MBE) or metalorganic chemical vapor deposition (MOCVD). QDs can be formed at interface steps of thin quantum wells [48, 10, 49, 50] or by self assembly in the Stransky-Krastanov growth mode during molecular beam epitaxy [51, 52]. The latter process is driven by the strain resulting from the smaller lattice parameter of the matrix (barrier) compared to that of the dots, for example 7% for InAs dots in GaAs. The QDs obtained in this well studied system are typically 20 nm in diameter and 5 nm in height (see Figure 1.1) and are formed on a thin InAs quantum well called *wetting layer*, as can be seen in STM measurements [53].
Samples used for optical spectroscopy are then covered again by the barrier material. In realistic samples InAs dots contain a significant fraction x of Ga, leading to the formation of $In_{1-x}Ga_xAs$ dots. The Stransky-Krastanov growth mode is applied to a large variety of III-V and II-VI compounds.

In this thesis we focus on the *optical* manipulation of spin states. A very high degree of control over carrier spin states and the mesoscopic nuclear spin system is also achieved in QDs defined by electrostatic potentials as summarized in the detailed review by [54].

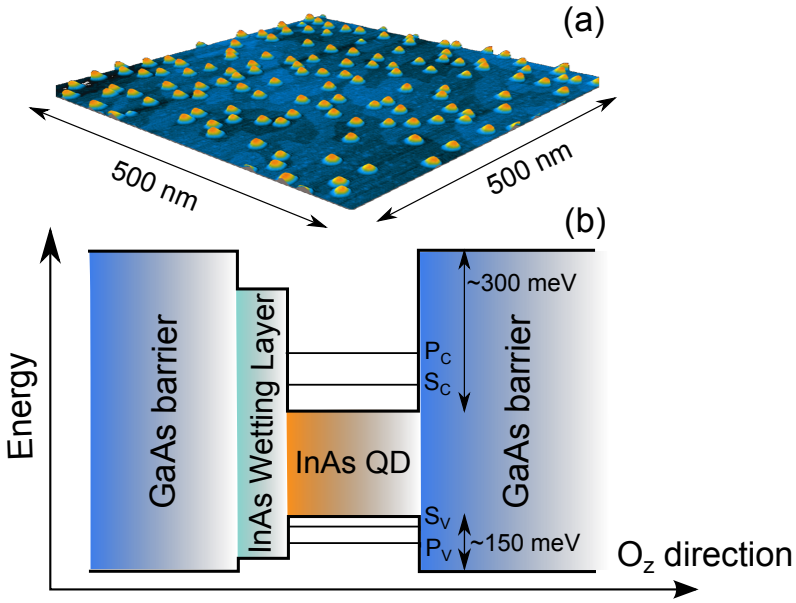

Figure 1.1: (a) 0.5 μm × 0.5 μm Atomic Force Microscopy image of InAs dots on GaAs. The AFM picture was taken from scanning probe microscopy library of the University of Technology of Eindhoven, Holland. (b) Schematic energy level diagram for an InAs QD in GaAs, where the growth axis is along the O_z direction. Indeed, the carrier confinement is well approximated by a 2D harmonic parabolic potential, but from here on the square potential form will be taken for simplicity.

The electron (not hole) spin physics probed in these transport measurements at very

low temperature (100mK) provide a powerful, complementary approach [21, 19, 55] to optical spectroscopy.

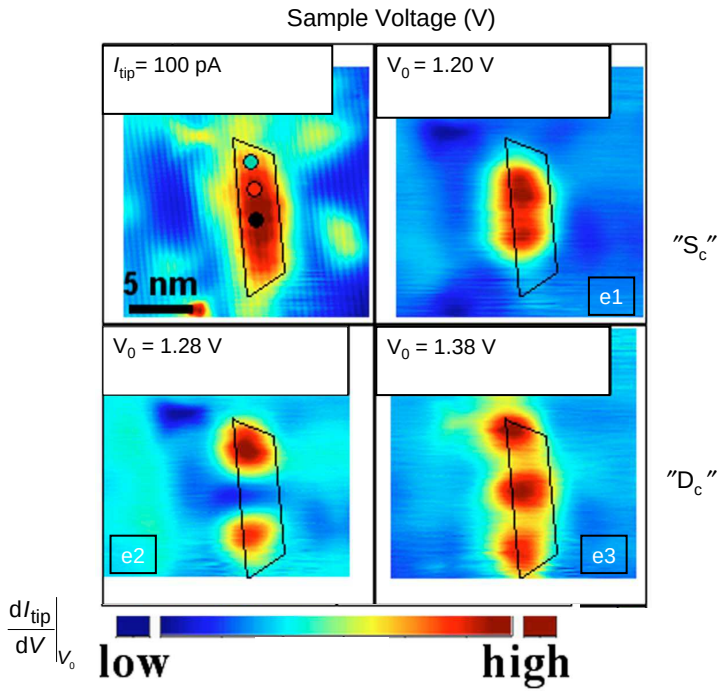

Figure 1.2: Stranski-Krastanov grown In(Ga)As/GaAs quantum dots [56]. Cross-sectional scanning tunneling microscopy and subsequent electronic wave-function imaging at a low temperature (T = 77 K) on cleaved In(Ga)As/GaAs QDs. The dI/dV spectra exhibit a set of discrete and well-defined peaks in the QD conduction band. Differential conductance dI/dV maps, obtained on a series of individual dots, display clearly the real space spatial variation at the nanometer scale of the envelope (amplitude) of the electron wave functions for the successive ground state and excited states. Wave-function symmetry of the first two excited states are identified in the measurements. S_C and D_C stand for s- and d - orbitals.

1.1.2 Droplet Dot Epitaxy

An interesting alternative for fabricating GaAs or InAs QDs is provided by a technique which is not strain driven, called molecular droplet epitaxy [57], see Figure 1.3(b) for a cross-sectional scanning tunneling microscopy image of a GaAs dot in AlGaAs [58]. This new technique was developed in Japan at the National Institute for Material Science (NIMS) and is based on the Volmer-Weber growth process. All samples studied in this thesis were grown at the NIMS in the group of K. Sukoda, T. Mano and T. Kuroda. The control of the growth conditions: As- and Ga-flux, pressure, growth and annealing temperature leads to a QD formation with different shapes and with a relatively low QD density. Figure 1.3 shows the Atomic Force Microscopy (AFM) images of droplet dots exhibiting different shapes: droplet shape, ring shape and double ring. A low QD density

allows the single dot spectroscopy carried out in this thesis. The typical dimensions of the droplet dots are: diameter ≈20-30 nm and height ≈5-15 nm. While the interface fluctuation GaAs/AlGaAs QDs are very weakly confined [49], ≈5 meV, the lateral confinement in GaAs/AlGaAs droplet dots is very large, ≈100-150 meV resulting in a much stronger confinement.

The Figure 1.3 at the bottom shows Cross-Sectional Scanning Tunneling (X-SST) images of (100) grown droplet dots obtained in the group of Paul Koenraad from University of Technology, Eindhoven [58]. The height/basis ratio of the dot showed here is very high ≈ 1. This study confirmed experimentally that the droplet dots are indeed strain-free[1]. Furthermore the observations revealed that aluminum fraction diffused into a GaAs QD does not exceed 6 %. So the droplet dots are nearly pure GaAs.

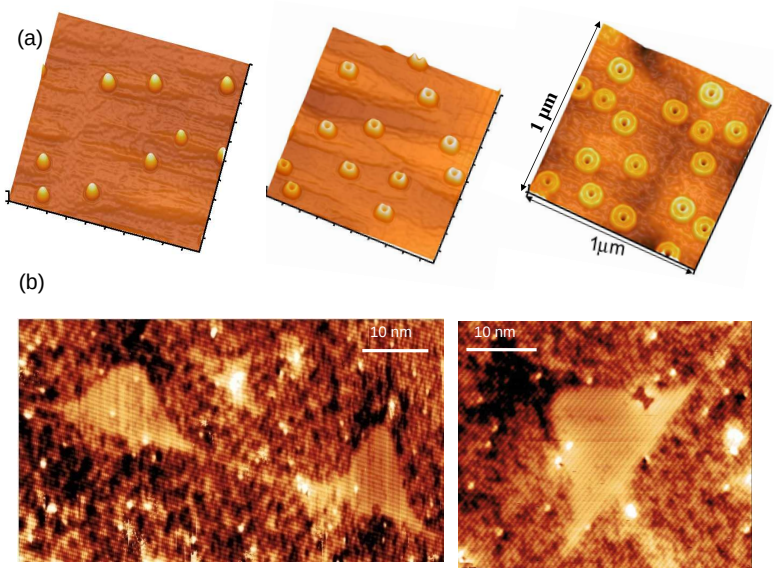

Figure 1.3: Droplet quantum dots grown by modified MBE Droplet Epitaxy. At the top the AFM images show different shapes of the droplet dots according to the growth conditions. All the squares are of the same size: 1x1 μm. At the bottom X-SST microscopic images of typical (100) droplet dots [58] allowing estimation of the height and plane diameter.

The recently achieved high optical quality of GaAs droplet dots has allowed first investigations of carrier and nuclear spin dynamics [59] and in framework of this thesis we report other successful optical measurements on droplet dots.

Due to carrier confinement potentials between tens and hundreds of meV, the samples elaborated with the above techniques are suitable for optical spin manipulation often carried out at a temperature of 4K, with the possibility for detailed spectroscopy up to few tens of Kelvin.

Another important feature of the Droplet Epitaxy growth is the possibility to grow

1 The measured lattice constants of barrier and dot material are identical [58].

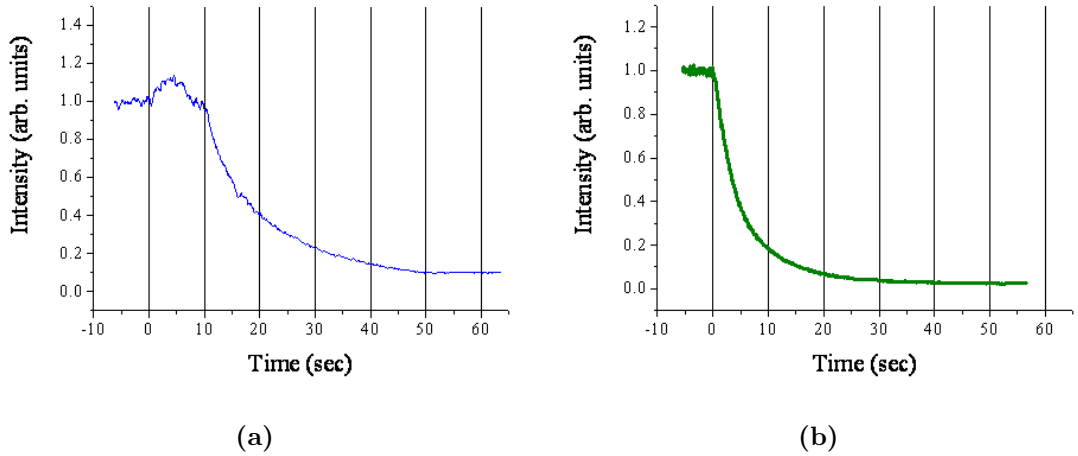

Figure 1.4: Wetting layer free formation of GaAs droplet dots revealed by using Reflection High-Energy Electron Diffraction (RHEED). (a) The formation of wetting layer in common (100)-grown GaAs dots.(b) The wetting layer free formation in (111)A -grown droplet dots. The vertical lines indicate the Ga-monolayers [60].

quantum dots with and without wetting layer according to growth conditions. When Ga is deposited to GaAs surfaces, Ga droplet nucleation occurs after the surface becomes most Ga-rich (growing surface) reconstruction. On the GaAs (100)-reconstructed surface, there are 1.2 - ≈1.75 ML of excess As atoms. Therefore, the first deposited 1.2 - ≈1.75 ML of Ga change into two- dimensional GaAs (wetting layer), Figure 1.4(a). And the rest of Ga form Ga droplets. In contrast, GaAs (111)A-reconstructed surface is already most Ga-rich surface. Therefore, Ga droplets nucleate immediately after the supply of Ga without wetting layer formation, Figure 1.4(b).

The Figure 1.4 shows the changes of RHEED-specular beam spot intensities during the supply of Ga to (100)- and (111)A-surfaces. The specular beam intensity is affected according to the surface roughness. So, the drastic decrease of the intensity indicates the droplet nucleation. On (100)-substrate, it is clear that the droplet nucleation starts after 1ML Ga supply. In contrast, droplet nucleation occurs immediately after the Ga supply in the case of (111)A-substrate, confirming the no-wetting layer formation.

1.2 Optoelectronic properties

1.2.1 Optical selection rules

The electric-dipole interaction of an electromagnetic wave with carriers in a semiconductor is governed by strict optical selection rules [5]. Energy and angular momentum are conserved for transitions between the valence and conduction band of typical zincblende semiconductors like GaAs, InGaAs, InP, etc. The periodic part of the Bloch function of the conduction states is s-like, so the electron angular momentum is simply $m_s = \pm 1/2$ in units of $\hbar$ ($\uparrow$ or $\downarrow$). The p-like valence states are determined by spin-orbit coupling and we consider here only the states with total angular momentum of $J = 3/2$ as the split-off

states $J = 1/2$ are very far in energy (hundreds of meV in GaAs based samples) and can usually be neglected.

In the Table 1.1 the Bloch wave function for conduction and valence states are given, where $\chi_\pm \equiv |\uparrow\downarrow\rangle$ are the spinors and the basic orbital functions $\phi_{l,m_l} = |l,m_l\rangle$ are given by:

$$\phi_{0,0} = |S\rangle\,;\;\; \phi_{1,1} = -\frac{1}{\sqrt{2}}\left(|X\rangle + i\,|Y\rangle\right);\;\; \phi_{1,-1} = \frac{1}{\sqrt{2}}\left(|X\rangle - i\,|Y\rangle\right);\;\; \phi_{1,0} = |Z\rangle\,. \quad (1.2.1)$$

The quantization axis z is chosen perpendicular to the QD plane and in most experiments z is also parallel to the excitation light propagation direction. Following absorption of a photon of suitable energy, an electron is promoted from a valence state to a conduction state. The absorption of a photon can increase the electron angular momentum by 1 for a σ^+ polarised photon or lower it by 1 for a σ^- polarised photon, see Figure 1.5 for all possible transitions between valence and conduction states in a simple picture. The selection rules for photon absorption and emission are identical. The unoccupied valence state left behind due to the promotion of the electron to the conduction state is called hole. It is the collective valence state obtained after removing an electron. In the QD, within a phase factor, it corresponds to the remaining electron on the level. The states with a projection of $J_z = \pm 3/2$ ($\Uparrow$ or $\Downarrow$) are called heavy holes, $J_z = \pm 1/2$ are called light holes.

The transition of an electron from valence state to conduction state is described by the electro-magnetic field interaction with crystal by optical Hamiltonian:

$$\hat{H}_{opt} = \frac{e}{m_0}\mathbf{A}\cdot\hat{\boldsymbol{p}}, \quad (1.2.2)$$

where $\mathbf{A} = A_0\mathbf{e}$ is the potential vector of electromagnetic field and $\mathbf{e}$ its polarisation. This Hamiltonian is proportional to a scalar product: $\mathbf{e}\cdot\hat{\boldsymbol{p}} = e_x\hat{p}_x + e_y\hat{p}_y + e_z\hat{p}_z$. Since we are interested in study of circular polarised light it is convenient to rewrite this scalar product as : $\mathbf{e}\cdot\hat{\boldsymbol{p}} = e_+\hat{p}_+ + e_-\hat{p}_- + e_z\hat{p}_z$ with $e_\pm = 1/\sqrt{2}(e_x \mp ie_y)$ and $\hat{p}_\pm = 1/\sqrt{2}(\hat{p}_x \pm i\hat{p}_y)$. The circularly polarised light $\sigma^\pm$ propagates in z-direction so that the electric field polarisation is characterized by: $e_\pm = 1$ and $e_z = 0$. The optical Hamiltonian is simplifies under circular polarisation and is proportional to $\mathbf{e}\cdot\hat{\boldsymbol{p}} = \hat{p}_\pm$.

Table 1.1: The Bloch wave functions as linear combination of basic functions ϕ_{l,m_l} determined by spin-orbit interaction and the spinors for conduction states Γ_6 and valence states Γ_8.

	$\lvert J, J_z\rangle$	wave function
Γ_6	$\lvert 1/2,1/2\rangle$	$\phi_{0,0}\chi_+$
	$\lvert 1/2,-1/2\rangle$	$\phi_{0,0}\chi_-$
Γ_7	$\lvert 1/2,1/2\rangle$	$-\sqrt{1/3}\phi_{1,0}\chi_+ + \sqrt{2/3}\phi_{1,1}\chi_-$
	$\lvert 1/2,-1/2\rangle$	$-\sqrt{2/3}\phi_{1,-1}\chi_+ + \sqrt{1/3}\phi_{1,0}\chi_-$
Γ_8	$\lvert 3/2,3/2\rangle$	$\phi_{1,1}\chi_+$
	$\lvert 3/2,1/2\rangle$	$\sqrt{2/3}\phi_{1,0}\chi_+ + \sqrt{1/3}\phi_{1,1}\chi_-$
	$\lvert 3/2,-1/2\rangle$	$\sqrt{1/3}\phi_{1,-1}\chi_+ + \sqrt{2/3}\phi_{1,0}\chi_-$
	$\lvert 3/2,-3/2\rangle$	$\phi_{1,-1}\chi_-$

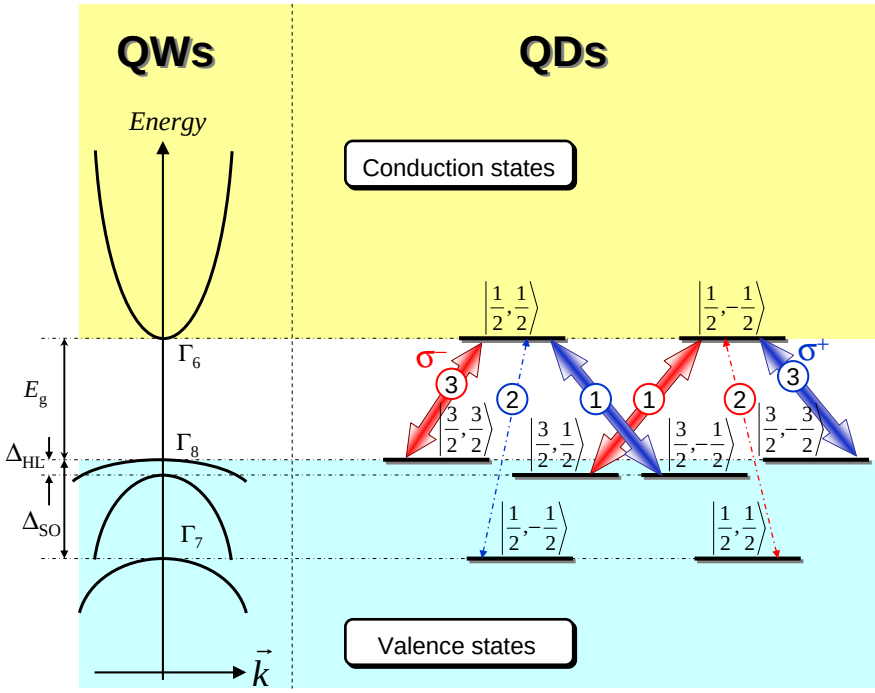

Figure 1.5: Schematical band structure of GaAs quantum wells and optical selection rules for inter-band transitions of GaAs QDs. The effective masses of holes are: $m_{\mathrm{HH}} = 0.51m_0, m_{\mathrm{LH}} = 0.082m_0$ and $m_{\mathrm{SO}} = 0.15m_0$[61] hence the different curvatures in valence states. The normalized probabilities to promote one electron from valence state to conduction state are given in the circles. The dashed lines represent transitions between split-off valence states and conduction states. Since the split-off gap is in GaAs QDs ≈ 0.4 eV [61] the split-off states can be neglected.

The oscillator strength for optical transitions between valence and electron states is now calculated by: $\left|\langle c|\left(\hat{p}_x \pm i\hat{p}_y\right)|v\rangle\right|^2$. In the group theory for the zincblende semiconductors only the following matrix elements do not vanish: $\langle S|\,\hat{p}_x\,|X\rangle = \langle S|\,\hat{p}_y\,|Y\rangle = \langle S|\,\hat{p}_z\,|Z\rangle$. The equalities result from cubic symmetry. Using these non-vanishing matrix elements one can calculate all optically allowed transitions shown in Figure 1.5.

Non-resonant excitation in the GaAs barrier for InAs dots or the AlGaAs barrier for GaAs dots involves both light and heavy hole transitions. As a result, a circularly polarised excitation creates both up and down electron spins (see Figure 1.5 for selection rules). The heavy-hole transition has a 3 times larger oscillator strength than the light hole transition. As a result, under σ^- excitation for 3 spin $\uparrow$ electrons only 1 spin $\downarrow$ electron is created in a conduction state. This corresponds to an optical spin initialization of $P_e = \frac{n_\uparrow - n_\downarrow}{n_\uparrow + n_\downarrow} = \frac{3-1}{3+1} = 50\%$. The polarised electrons recombine after a spin life time with holes and emmit $\sigma^\pm$-polarized light. The photoluminescence circular polarisation is given by: $P_C = \frac{I_{\sigma^+} - I_{\sigma^-}}{I_{\sigma^+} + I_{\sigma^-}}$, where $I_{\sigma^\pm}$ are $\sigma^\pm$-polarised intensities. These intensities are proportional to the electron populations: $I_{\sigma^\pm} \propto n_{\uparrow\downarrow} + 3n_{\downarrow\uparrow}$. So consequently the maximal

circular polarisation of the photoluminescence in bulk is : $P_C = 25\%$.

To increase the optically generated average spin, excitation into the bi-dimensional wetting layer (if present in the sample) allows in principle injection of 100% spin polarised electrons (resulting in maximal circular polarisation $P_C = 50\%$) when driving heavy hole transitions, which are separated in energy from the light hole transitions in the wetting layer due to confinement and/or strain.

The heavy and light hole valence states are separated by an energy Δ_{HL} of typically several tens of meV due to quantum confinement and/or strain. For most of the experiments the light hole states can safely be ignored and optical exciton spin state preparation is straightforward. In practice however, strain, interface rotational symmetry breaking [62, 63, 64] and shape anisotropy introduce heavy to light hole coupling which make all the transitions between the states indicated in Figure 1.5 possible, yet with very different probabilities [65, 66, 67, 68].

1.2.2 Addressing individual charge states and Carrier Coulomb exchange interactions

Controlling the charge state of QDs relies on the remarkable possibility of doping semiconductor materials with n-type or p-type impurities. In some cases the non-intentional residual doping is sufficient to obtain singly-charged QDs [28, 69], see Figure 1.6(a), but usually a delta-doped layer is grown a few nanometers below the QD layer with a density adjusted to reach the desired average QD charge [70, 71, 72]. This modulation doping technique can be significantly improved by controlling the chemical potential of the QD electrons with an electric voltage applied between the doped layer and a semitransparent top contact [73]. In these charge-tunable structures a given QD is coupled to a reservoir of free carriers (a heavily doped layer) through a tunnel barrier as in Figure 4.1(b) and (c).

The energy levels of the QD can be adjusted with respect to the Fermi level in the highly doped barrier, to vary deterministically the charge state with the precision of a single elementary charge due to Coulomb blockade. This effect is clearly observed in micro-photoluminescence (PL) spectra by abrupt jumps of the (charged) exciton emission energy when the gate voltage is varied (see Figure 1.6(b)) as a result of changes of the strong few particle direct Coulomb terms [74].

QDs can be populated by valence holes and conduction electrons through optical excitation and/or through controlled tunneling in charge tunable structures [75]. For a simplified calculation of optical transition energies between conduction band electron states and valence band hole states the single particle energies are determined by treating the electron-hole confinement potential within the harmonic approximation. For self-assembled as well as interface fluctuation dots the vertical confinement energies (along the growth axis z) are almost an order of magnitude larger than the lateral confinement energies in the x,y plane. The quantization energies of both electrons and holes are larger than the Coulomb energies. The Coulomb effects can therefore be treated as perturbations to the single particle structure [74]. At zero magnetic field the lowest lying conduction (valence) level $S_c(S_v)$ is twofold degenerate and the adjacent $P_c(P_v)$ level is fourfold degenerate in the case of axial symmetry, as in an ideal two-dimensional harmonic potential [75], see Figure 1.1 for the energy level diagram. Here S and P refer to the symmetry of the envelope part of the Bloch function of the carrier state (s-like and p-like, respectively). For

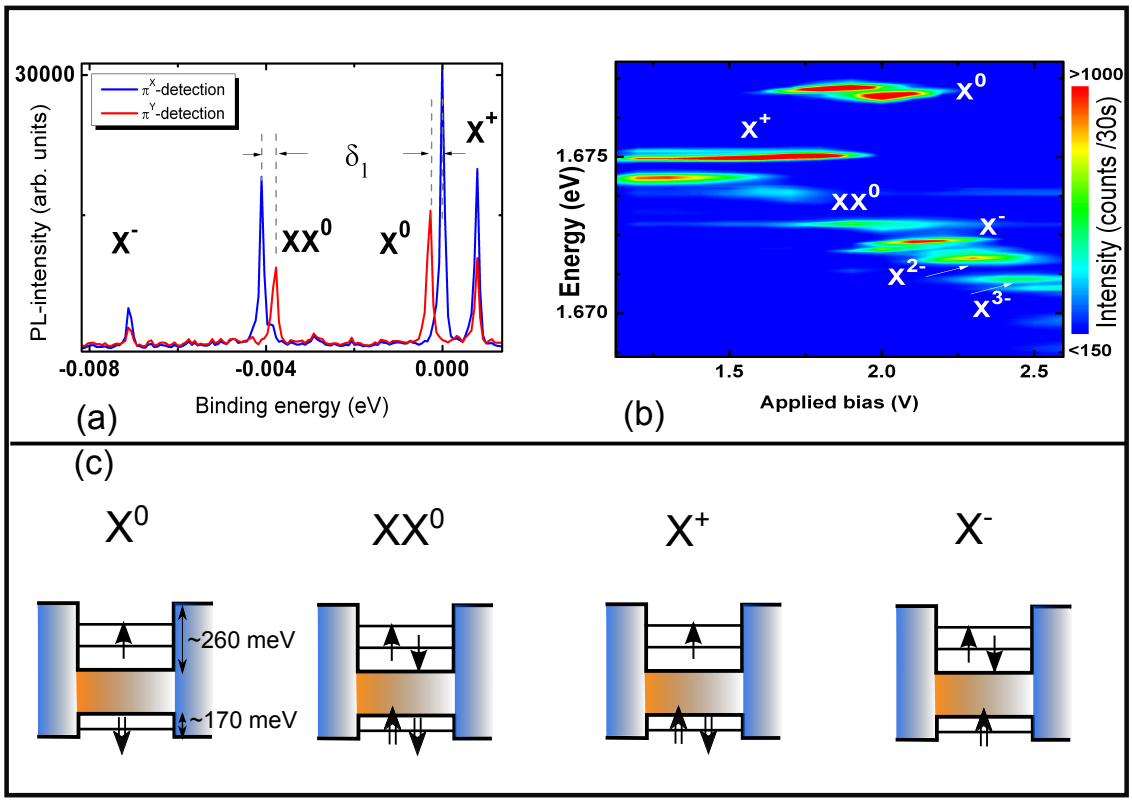

Figure 1.6: (a) A typical PL-spectrum of non-intentionally doped (100) GaAs droplet dots integrated over times much longer than the carrier tunneling-in- and out-time[28]. In addition to the power dependence of the PL-intensity of each transition the fine structure splitting (δ_1, here $\delta_1 \approx$300 μeV) is used to identify all excitonic states. The neutral exciton energy is 1.7283 eV. (b) The charging of a single GaAs droplet QD with electrons is accompanied by discrete jumps in the emission energy when going from the positively charged exciton X^+ to the neutral exciton X^0 (1 electron, 1 hole) then to the charged exciton X^- (2 electrons, 1 hole) etc. (c) The most relevant excitonic states studied in the framework of this thesis X^0, XX^0, X^+ and X^- are schematically shown.

brevity, a Coulomb correlated electron-hole pair trapped inside a dot by the confinement potential will be called *exciton* in the following.

Optical excitation of a dot in its ground state with a suitable energy results in a transition from a valence to a conduction state and in the formation of excitonic states. After a life time in the order of 1 ns the conduction electron recombines with a hole and emits according the the excitonic state. Here we focus on the most relevant configurations: a conduction electron-valence hole pair X^0, XX^0 formed by two electron-hole pairs, the negatively charged exciton (trion) X^- ($\Uparrow\uparrow\downarrow$ or $\Downarrow\uparrow\downarrow$) and the positively charged exciton X^+ ($\Uparrow\Downarrow\uparrow$ or $\Uparrow\Downarrow\downarrow$). Here $\uparrow$ ($\downarrow$) and $\Uparrow$ ($\Downarrow$) represent the conduction electron spin and hole pseudo-spins, and for example $\Downarrow\uparrow\downarrow$ stands for $\frac{1}{\sqrt{2}}(\uparrow\downarrow - \downarrow\uparrow)\otimes\Downarrow$, where the antisymmetrization of the conduction states is more explicit, Figure 1.6 (c). Due to strong localization of the carrier wave function, direct and exchange Coulomb, as well as correlation effects are very strong in dots.

The Figure 1.6 (a) shows all four excitonic states. The emission line corresponding to the neutral exciton X^0 exhibits a fine structure splitting $\delta_1 \approx 300$ μeV due to the anisotropic part of the electron-hole exchange interaction. For neutral excitons (in zero magnetic field and in the absence of strong nuclear polarisation) selection rules are affected by the electron hole Coulomb exchange interaction. This interaction includes an anisotropic exchange interaction (AEI) contribution [65, 76] due to deviation of the real QD shape from a perfectly circular shape and/or due to the dot-semiconductor matrix interface anisotropy. Due to anisotropic exchange, X^0 recombination results in a doublet of *linearly polarised* transitions, separated by δ_1 that varies from a few (in high symmetrical QDs) to a few hundreds of μeV (in elongated QDs) from dot to dot in GaAs samples, see table A.3.2. The biexciton emission energy is red shifted ($\approx$4 meV) due to the competition between attractive and repulsive Coulomb energies and can be considered like a mirrored spectrum of the neutral exciton X^0.

We remind here that the angular momentum projections for the electrons are $S_z = \pm 1/2(\uparrow\downarrow)$ and for heavy-holes $J_z = \pm 3/2$ ($\Uparrow\Downarrow$). The total angular momentum projection is given by: $J_z^{total} = S_z + J_z$. Hence all four possible neutral exciton states are: $J_z^{total} = \pm 1$, optically allowed states ($\downarrow\Uparrow$ or $\uparrow\Downarrow$) called *bright* states, and $J_z^{total} = \pm 2$, two optically forbidden states ($\uparrow\Uparrow$ or $\downarrow\Downarrow$) called *dark* states.

Without any AEI all four states are degenerated, see Figure 1.7. Indeed due to the isotropic electron-hole exchange interaction the degeneracy is lifted resulting in splitting the bright and dark states by δ_0. The values for δ_0 depend on the confinement and the QD shape and typically are of the order of magnitude few hundreds μeV (for GaAs droplet dots: 200-550 μeV varying from dot to dot) compared to 100 μeV in GaAs bulk.

In general the QDs have low symmetry, typically C_{3v}, C_{2v} or C_2. Due to the low symmetry the degeneracy of the bright and dark states is lifted as well and splitted by δ_1, δ_0, and δ_2 are modified. In general for QDs with C_{2v} geometry the emission of the non-degenerated dark and bright states is linearly polarised parallel the principal crystallographic axes [110] and [1$\bar{1}$0], Figure 1.7. The bright sates are $|X\rangle = \frac{1}{\sqrt{2}}(|-1\rangle - |+1\rangle)$ and $|Y\rangle = -\frac{1}{i\sqrt{2}}(|-1\rangle + |+1\rangle)$. They splitting δ_1 is defined as $\delta_1 = E(|Y\rangle) - E(|X\rangle)$. The dark states are $\left|X^2 - Y^2\right\rangle = \frac{|2,2\rangle + |2,-2\rangle}{\sqrt{2}}$ and $|2XY\rangle = \frac{|2,2\rangle - |2,-2\rangle}{i\sqrt{2}}$ with corresponding splitting $\delta_2 = E(\left|X^2 - Y^2\right\rangle) - E(|2XY\rangle)$.

If a QD possesses a residual carrier, an electron or an hole, before it has been excited the negatively or positively charged excitons can be generated. Due to their content of three carriers they are also called *trions*. The positively charged exciton X^+ can be red or blue shifted [77, 78] with respect to the neutral exciton X^0. In the Figure 1.6 (a) X^+ is blue shifted by $\approx$1 meV. The negatively charged exciton is always red shifted with respect to X X^0 (in Figure 1.6 (a) $\approx$7 meV). For the trions the direct and exchange Coulomb interaction lead to a renormalization of the transitions energies in the meV range but no fine structure splitting due to Kramers degeneracy [46, 65, 59].

The electronic structure of QDs can be analyzed by techniques such as capacitance-voltage measurements, scanning-tunneling microscopy [56], electron-spin resonance, photocurrent spectroscopy and a large variety of optical spectroscopy experiments. The latter allow a detailed study of the optically active electronic states and their symmetry by analyzing the energy and polarisation of absorbed or emitted photons. These experiments

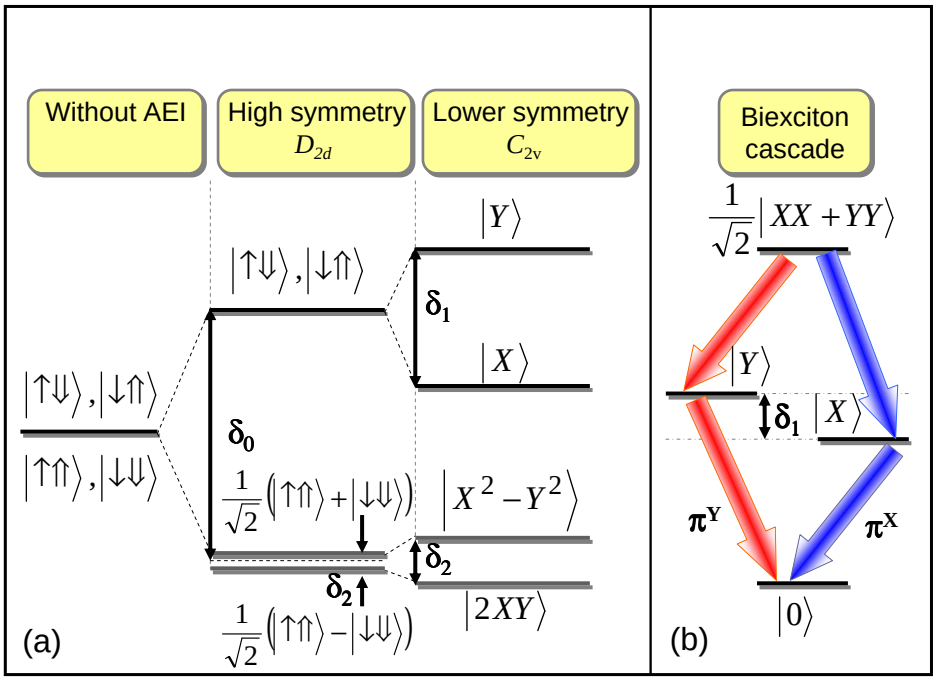

Figure 1.7: (a) Energy fine structure system in a QD. The two linearly polarised bright states $|X\rangle$ and $|Y\rangle$ are separated by δ_1. The optically forbidden dark states are drawn in gray and become optically active only under certain circumstances, when mixed with bright states. The energy separations in the figure are not drawn in the right scale. (b) The radiative cascade of a biexciton (2 electrons, 2 holes) according to selections rules consisting of a recombination from the XX^0 into the X^0 and a recombination into the ground state $|0\rangle$. The transitions π^X and π^Y are polarised parallel the principal crystallographic axes [110] and [1$\bar{1}$0] respectively.

probe the interplay between carrier confinement, direct and exchange Coulomb terms and the hyperfine interaction.

1.2.3 Magnetic coupling of electrons to nuclei: Hyperfine interaction

In this subsection we focus on the basics of the magnetic coupling between electrons and nuclei which are essential by understanding the fascinating nuclear spin effects observed in optical spectroscopy experiments in quantum dots for a wide range of experimental conditions.

The strength of the hyperfine interaction in QDs is enhanced compared to semiconductor bulk or quantum well structures due to the strong localization of the electron wave function over typically only 10^5 lattice sites. This number is too small for efficient cancellation of the total nuclear spin by averaging [15, 16], yet too large to address each nuclear spin

state individually. In III-V QDs like GaAs, InP and InAs, 100% of the lattice sites have a non-zero nuclear spin and these materials are taken here as model systems. Even for solids with very few isotopes carrying a nuclear spin like diamond [43], ZnO [79] or CdSe [80] hyperfine effects still play a key role in the carrier spin state evolution.

There are two main contributions to the hyperfine interaction [81]: (i) The Fermi contact interaction is efficient when there is a physical overlap of the carrier wave function with the lattice site. This type of interaction is dominant for s-type wave functions (periodic part of the Bloch function) of conduction electrons. (ii) The dipole-dipole interaction is effective for p-type (non-zero orbital angular momentum) wave functions. This term is therefore dominant for valence-band states (holes). It is about one order of magnitude weaker than the Fermi contact interaction for conduction electrons [82, 83, 84, 85, 86]. In this thesis we concentrate on the interaction of a conduction electron with nuclear spins.

To introduce the orders of magnitude of the energy shifts due to the hyperfine interaction between electron and nuclear spins, a comparison with the Zeeman splitting of the spin levels in an external magnetic field $\boldsymbol{B} = (0,0,B_z)$ is helpful [81, 88]: The Zeeman energy of an electron spin with $\hat{S}^e_z = \frac{1}{2}\hat{\sigma}^e$ is

$$\hat{H}^e_{Zee} = \mu_B g_e B_z \hat{S}^e_z = \hbar\omega^e_Z \hat{S}^e_z \tag{1.2.3}$$

where g_e is the longitudinal electron g-factor and $\mu_B = 9.27 \times 10^{-24}$ J/T= 58 μeV/T. The Zeeman energy of a system of nuclear spins I^j is given by:

$$\hat{H}^N_{Zee} = -\mu_\mathrm{N} \sum_j g_{Nj} B_z \hat{I}^j_z \tag{1.2.4}$$

summing over all nuclei j in the system. Here g_N is the nuclear g-factor and $\mu_\mathrm{N} \simeq \frac{\mu_\mathrm{B}}{2000}$ is the nuclear magneton. For an order of magnitude calculation, we take the example of Indium and an electron g-factor of 0.6, and find $(g_e\mu_\mathrm{B})/(g_\mathrm{N}\mu_\mathrm{N}) \simeq 1000$. The energy separation between the nuclear spin states is therefore negligible compared to that of the electron spins.

The Fermi contact (fc) hyperfine interaction in a QD between an electron spin and the

Table 1.2: Hyperfine constants in GaAs, InAs, InP and CdTe for a cell containing two atoms, see [87] and references therein. Please note that an average is quoted for Ga and In for which two stable isotopes exist.

isotope	nuclear spin I	abundance (%)	hyperfine constant A in μeV
In	9/2	100	56
Ga	3/2	100	42
As	3/2	100	46
P	1/2	100	44
Cd	1/2	25	-30
Te	1/2	8	-45

N nuclei of the atoms forming the dot is [81, 89]:

$$\hat{H}_{hf}^{fc} = \frac{\nu_0}{2} \sum_j A^j |\psi(\boldsymbol{r}_j)|^2 \left(2\hat{I}_z^j \hat{S}_z^e + [\hat{I}_+^j \hat{S}_-^e + \hat{I}_-^j \hat{S}_+^e]\right) \tag{1.2.5}$$

where ν_0 is the two atom cell volume, $\boldsymbol{r}_j$ is the position of the nuclei j with spin $\hat{I}^j$ and $\psi(\boldsymbol{r}_j)$ is the normalized electron envelope function. The nuclear spin is 3/2 for Ga and As, 5/2 for Al, 9/2 for In in units of $\hbar$. A^j is the constant of the hyperfine interaction with the electron in the order or 50 μeV for In, Ga and As, see table 1.2.

As an electron interacts simultaneously with about 10^5 lattice sites, one can consider in the mean field approach that the electron spin is affected by a mean nuclear spin polarization $\langle \hat{\boldsymbol{I}}^j \rangle$ acting like an effective magnetic field B_n (**Overhauser field**) :

$$\boldsymbol{B}_n = \frac{\nu_0 \sum_j A^j |\psi(\boldsymbol{r}_j)|^2 \langle \hat{\boldsymbol{I}}^j \rangle}{g_e \mu_{\mathrm{B}}} \tag{1.2.6}$$

For uniform nuclear polarization, the field B_n is independent of the electron localization volume and is in the order of $B_n^{\max} \simeq 5$ T for fully polarized nuclei in GaAs [6], as the maximum Overhauser shift is simply $g_e \mu_{\mathrm{B}} B_n^{\max} = I^{Ga} A^{Ga} + I^{As} A^{As} = 135 \mu$eV.

The hyperfine interaction is reciprocal, see scheme in Figure1.8, so also the nuclei are effected by the average electron spin polarisation acting like an effective magnetic field B_K (**Knight field**). The time averaged Knight field acting on one specific nucleus j is given by:

$$\boldsymbol{B}_{Kj} = f_e \frac{\nu_0 A^j}{g_N \mu_N} |\psi(\boldsymbol{r}_j)|^2 \langle \hat{\boldsymbol{S}}^e \rangle \tag{1.2.7}$$

where f_e is the filling factor $\in$ [0,1] characterizing the occupation of the dot by electrons, underlining that the Knight field is zero in the absence of electrons.

The maximum Knight field can be estimated as $B_{\mathrm{K}}^{\max} \simeq \frac{B_n^{\max}}{N} \frac{g_e \mu_{\mathrm{B}}}{g_{\mathrm{N}} \mu_{\mathrm{N}}}$, so for $N \simeq 10^5$ results in $B_{\mathrm{K}}^{\max}$ in the tens of mT range. The amplitude of the Knight field for a nucleus situated in the center of the dot (where electron occupation probability is strongest) will be higher than for a nucleus in the dot periphery. The Knight field experienced by the nuclei leads to frequency shifts in ODNMR spectra of individual QDs [11].

Introducing $\tilde{A}$ as the average of the hyperfine constants A^j and assuming a strongly simplified, uniform electron wave function $\psi(\boldsymbol{r}) = \sqrt{2/(N\nu_0)}$ over the involved nuclei,

Table 1.3: Electron Overhauser splitting in μeV for 100 % nuclear polarization $\hbar\omega_{\mathrm{OHS}}^e = I^{\mathrm{Ga}} A^{\mathrm{Ga}} + I^{\mathrm{As}} A^{\mathrm{As}}$ for GaAs and InAs quantum dots, using the nuclear spin and hyperfine constant values from table 1.2

Semiconductor	OHS (μeV)
InAs	315
$In_{0.5}Ga_{0.5}As$	230
GaAs	135

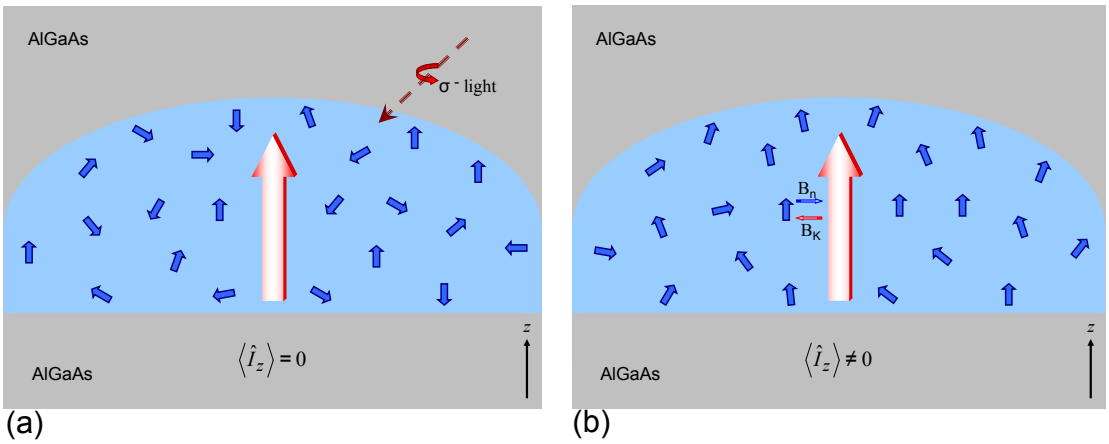

Figure 1.8: Schematical drawing of reciprocal coupling electrons to nuclei and nuclei to electrons. (a) A typical GaAs QD embedded between AlGaAs barriers contains 10^5 nuclei, which are randomly oriented when an electron is optically polarised. The averaged nuclear polarisation at the excitation time is therefore $\left\langle \hat{I}_z \right\rangle$=0. (b) After an electron is polarised the spin-flips via hyperfine interaction take place and the nuclei become polarised, so that the averaged nuclear polarisation is $\left\langle \hat{I}_z \right\rangle \neq 0$. The created nuclear polarisation acts as an effective field Overhauser field B_n affecting the electron polarisation. The electron polarisation, in turn, acts as a weaker effective field, Knight field B_{K}, which affect the nuclear polarisation.

Equation 1.2.5 simplifies to:

$$\hat{H}_{hf}^{fc} = \frac{2\tilde{A}}{N}\left(\hat{I}_z\hat{S}_z^e + \frac{\hat{I}_+\hat{S}_-^e + \hat{I}_-\hat{S}_+^e}{2}\right) \tag{1.2.8}$$

where $\hat{I} = \sum_{j=1}^{N} \hat{I}^j$.

The energy level splittings between the different nuclear and electron spin states are determined by the hyperfine interaction in combination with the applied magnetic field B_z. $\hbar\omega_{\mathrm{OHS}} = 2\tilde{A}\langle\hat{I}_z\rangle/N = \mu_{\mathrm{B}} g_e B_n$ relates the Overhauser shift $\hbar\omega_{OS}$ to the average nuclear polarisation. We can therefore access the average nuclear polarisation by measuring $\hbar\omega_{\mathrm{OHS}}$ in single dot spectroscopy. For example, when the nuclear spins are polarised (i.e. the RF source is off) the *total* electron Zeeman splitting $\hbar\omega_e$ is given by $\hbar\omega_e = \hbar(\omega_Z^e + \omega_{\mathrm{OHS}}^e)$. When the RF source is on, the nuclei are depolarised, the Overhauser field B_n is vanishingly small and $\hbar\omega_e = \hbar\omega_Z^e$. The difference between the two cases allows to measure the Overhauser shift $\hbar\omega_{\mathrm{OHS}}^e$.

The hyperfine interaction is time dependent since the electron lifetime is finite and its spin may also relax during its lifetime. The time dependence of the second term in Equation 1.2.8 can be explicitly written as: $\hat{H}_1(t) = \frac{\tilde{A}}{N}(\hat{I}_+\hat{S}_-^e + \hat{I}_-\hat{S}_+^e)h_1(t)$. This term allows for spin transfer via simultaneous spin flips (flip-flop) of a carrier and nuclear spin. As the nuclear Zeeman splitting is negligible, the electron Zeeman splitting plays a crucial role in determining the probability of these spin flip-flops, as already pointed out in the original paper by [3]. It should be emphasized that while the term $\propto \hat{I}_z\hat{S}_z^e h_1(t)$

also fluctuates in time, it does not directly induce any spin flips. Depending on the exact experimental conditions, the electron-nuclear spin flip-flop term can lead to electron spin dephasing [20], dynamic nuclear polarisation [10] or nuclear spin dephasing [81, 16].

$\hat{H}_1(t)$ can be visualized as a random perturbation between states split in energy by $\hbar\omega_e$. The function $h_1(t)$ is characterized by its mean value $\overline{h_1(t)} = f_e$ and a simple, auto-correlation function $\overline{h_1(t)h_1^*(t+\tau)} = \exp(-\frac{|\tau|}{\tau_c^e})$ with a correlation time τ_c^e. The fraction of time the quantum dot contains an electron f_e takes values between 0 and 1. The rate of nuclear polarisation will depend on the splitting $\hbar\omega_e$ and the level broadening $\hbar/\tau_c^e$, [23, 90].

For commonly achieved nuclear spin polarisation values well below 100%, the nuclear field fluctuates around a mean value $\langle B_n \rangle$. The fluctuations (root mean square deviation) can be written as an effective field $\delta B_n = \sqrt{\langle B_n^2 \rangle - \langle B_n \rangle^2}$. Several theoretical studies have predicted that the dominant mechanism of electron spin relaxation in QDs at low temperature and zero external magnetic field is due to the hyperfine interaction with these nuclear field fluctuations δB_n [15, 91, 16, 92]. The reason for the non-negligible δB_n lies in the finite number of nuclei within the dot: The mesoscopic nuclear spin system of a QD is described by the nuclear spin operators $\hat{I}_x$,$\hat{I}_y$,$\hat{I}_z$. These operators do not commute, it is therefore impossible to determine the x,y and z components of the nuclear spin system with equal precision i.e. they can not all be exactly zero. In the absence of DNP *repeated* measurements of the expectation value of B_n at time intervals longer than the nuclear spin correlation time of the order of 10^{-4} s give an average of $\langle B_n \rangle = 0$. But, employing a useful qualitative physical picture [1], an electron spin will interact during its lifetime (about 1ns in InAs QDs) with a field of typical magnitude δB_n and random orientation during about 10^{-4} s; this is referred to as the *frozen fluctuation model* [16].

An important interaction between nuclear spins is the dipole-dipole interaction that allows for example nuclear spin diffusion in bulk GaAs samples [93] with spatially inhomogeneous nuclear polarisation. The dipole-dipole interaction of a nucleus n with the other nuclei n' separated by the translation vector $\boldsymbol{r}_{nn'}$ can be written as [81]:

$$\hat{H}_{dd} = \frac{\mu_N^2}{2} \sum_{n \neq n'} \frac{g_n g_{n'}}{r_{nn'}^3} \left(\hat{\boldsymbol{I}}^n \hat{\boldsymbol{I}}^{n'} - 3 \frac{(\hat{\boldsymbol{I}}^n \boldsymbol{r}_{nn'})(\hat{\boldsymbol{I}}^{n'} \boldsymbol{r}_{nn'})}{r_{nn'}^2} \right) \tag{1.2.9}$$

As a result of the dipole-dipole interaction each nucleus experiences a fluctuating local effective magnetic field δB_L, where $\delta B_L \simeq 0.15$ mT in GaAs, created by the other nuclei. Via the non-secular (non spin conserving) part of the dipole-dipole interaction nuclear spin is transferred to the crystal as a whole and is not conserved, see Chapter VIII.E of [81] were secular and non-secular parts of the dipole-dipole interaction are detailed. The precession of the nuclear spins around B_L is one of the reasons why dynamic nuclear polarisation in GaAs bulk in the absence of any applied magnetic field is not possible [5]. In QDs two interactions, namely the Knight field B_{K} and the nuclear quadrupole interaction can in principle dominate B_L already at zero field.

1 The electron really interacts with a quantum field of indeterminate magnitude and direction at any time scale for $B = 0$.

1.2.4 Optical spectroscopy techniques

To investigate the spin dynamics of carriers and nuclei a large variety of optical spectroscopy techniques have been developed, each adapted to the time scales relevant for the experiment. The typical radiative lifetime of a neutral or charged exciton is hundreds of picoseconds [13, 94], electron spin coherence times can be prolonged up to 200 μs [21, 72]. Efficient collection of single dot photoluminescence following non-resonant excitation [37] and resonant fluorescence [95] result in signal integration times well below the millisecond range, which provides the time resolution necessary to measure for example the nuclear polarisation build-up time.

The discreteness of the QD energy states was demonstrated in optical spectroscopy experiments as early as 1994 [9]. Reducing the detection spot size in optical experiments to an area that contains only one nano-object permits studying directly the optical properties of an individual dot. A simple and powerful tool is non-resonant photoluminescence (PL), where carriers are optically excited in the surrounding semiconductor matrix by a laser tuned above the QD resonance energy i.e. either into wetting layer or barrier states. The carriers are subsequently trapped by the QD confinement potential and, following energy relaxation, recombine radiatively at the ground state energy, see S_c to S_v transition in Figure 1.1 (b). More recently resonant fluorescence experiments where the excitation laser is resonant with the energy necessary for absorption from the highest lying valence level to the lowest lying conduction level [96] have shown beautiful analogies to atomic physics [97]. Two closely related, powerful techniques developed in charge tunable structures are differential transmission and reflectivity, which also allow resonant probing of QD states [46, 98]. These experiments are carried out with pulsed or cw excitation. The challenge is to detect a very weak optical signal stemming from only one photon per recombination process. In practice efficient cw detection with Si-based CCD cameras and avalanche photo diodes are adapted to single dot measurements. For time resolved measurements and also to observe the spin physics in several thousand dots simultaneously experiments on QD ensembles are useful, that allowed important discoveries in the field, in resonant PL [13], Kerr and Faraday rotation probing the real part of the refractive index [72] and photo induced circular dichroism [83] probing the imaginary part of the refractive index. An interesting alternative to conventional pump-probe techniques is to passively detect the spectrum of intrinsic random spin fluctuations of carriers in thermal equilibrium (i.e., without optical pumping or initialization). This technique labeled *spin noise spectroscopy* has been successfully applied to electron [99] and hole spins [100, 101], respectively, interacting with nuclear spins.

All the results presented in this thesis were obtained by using the non-resonant cw excitation PL single dot spectroscopy based on the confocal microscopy. The significantly improved growth quality in last decades enables low QD density up to 1 dot per μm. Thanks to the high spatial and spectral resolution of a confocal microscope emission lines can be addressed to a single dot and even weak nuclear effects in a QD can be studied in detail.

CHAPTER 2

Experimental setup

This chapter describes the experimental set-ups used during this thesis. The quantum dots studied here were investigated with use of a fiber-based confocal microscopy in a magneto-cryostat.

In the first section the principle of the confocal microscopy is introduced. The second section explains the experimental methods of characterization and calibration for used optical elements, also including the magneto-cryostat and the different magnetic field configurations: Faraday and Voigt geometries.

2.1 Confocal microscopy

In framework of this thesis the optical properties of single quantum dots were investigated. Different sophisticated experimental methods were introduced in the previous chapter. In the study presented in this thesis the confocal microscope was used.
In order to be able to perform single dot spectroscopy measurements two crucial conditions need to be fulfilled: an excitation and a detection of only one single quantum dot. Etching of a mask on the sample or so-called mesas can reduce the illuminating sample area and consequently the low excited quantum dot number. The investigated droplet dot samples do not have any mask. The special growth of the droplet quantum dots allows to have a very low quantum dot density $\simeq$1-2/μm^2. The confocal microscope combined with small laser spot size ($\simeq$1 μm, see spatial resolution section) allows to study luminescence stemming from a single quantum dot.

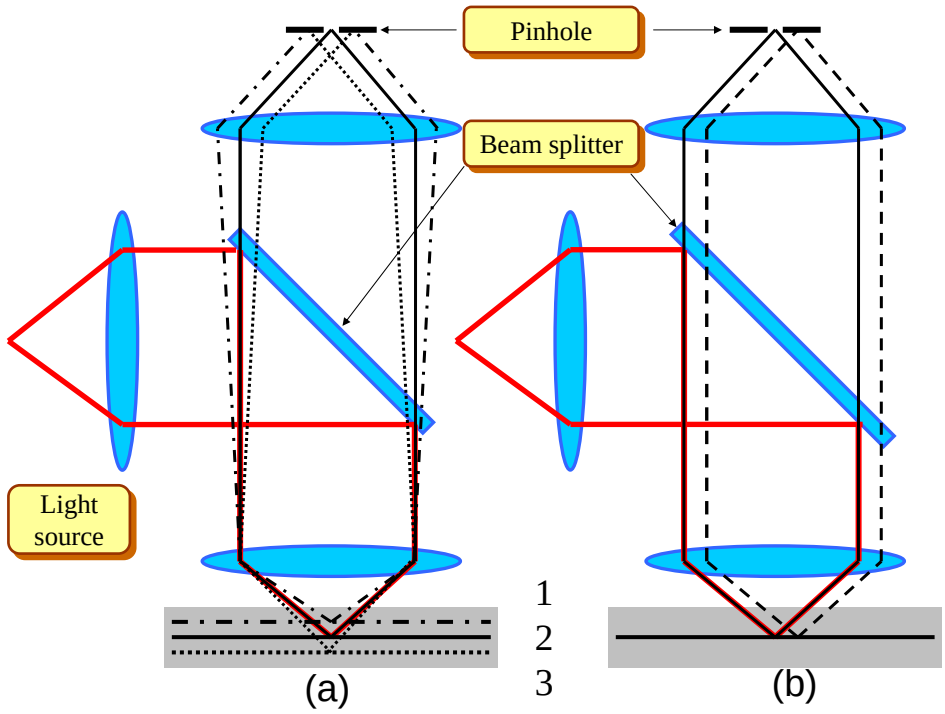

Figure 2.1: The principle of confocal microscopy adapted to single dot spectroscopy. (a) The laser is collimated by a lens reflected by a beam splitter and focused by another lens. The QD-luminescence is collimated by the same lens. The plane 2 is a focal plane. (b) the overlap principle of two shifted spots.

The idea of a confocal microscopy was invented by Marvin Minsky 1953 and patented 1957 [102, 103]. Brakenhoff with his colleagues [104] and Wilson with Shepphard [105] developed the principle further adapted to applications. Confocal microscopy is an optical imaging technique used to increase optical resolution and contrast of a micrograph by using point illumination and a spatial pinhole to reject light coming from an out-of-focus

plane in specimens, the name "confocal" stems from this configuration. In single dot spectroscopy the aim of confocal microscope is to only collect in-focus luminescence from a single quantum dot.

The confocal microscope used in spectroscopy aims to select only a luminescence from the quantum dots under investigation, plane 2 in Figure 2.1 (a). As light source in spectroscopy applications a laser with desired frequency can be focused onto the focal plane to excite a quantum dot layer. A pinhole[1] placed in an optically conjugate plane in front of the detector or a camera eliminates out-of-focus signal. That means that only luminescence emitted by quantum dots very close to the focal plane can be detected. The luminescences from plane 1 and 3 are not focused onto the pinhole plane and are not detected.

Another very important issue is the overlap of excitation and detection beam. If the excitation and detection beams do not overlap the signal can not be detected, Figure 2.1 (b).

2.2 Experimental methods

2.2.1 The microscope head

The main optical elements of the microscope head developed during my thesis are shown in Figure 2.2. All studied structures are excited non resonantly in the AlGaAs barrier with a cw HeNe laser at the wavelength λ=633 nm. The maximal excitation power arriving at the sample does not exceed 3 μW. The laser beam is collimated by a lens (Thorlabs C260TMB-B) and passes a linear polariser (Glan-Taylor prism GT) and Liquid Crystal Retarder LCR (LRC100-VIS-MOD, MeadowLark). Depending on the bias applied to the LCR, the laser beam can be linearly or circularly polarised. The beam is then reflected twice by a 96:4 beam splitter (BS) to the sample. These beam splitters were chosen in order to allow the maximal collection of the luminescence passing the beam splitters before it is coupled into the fiber. Even when we lose twice 96 % of excitation power the remaining power still allow us to perform all our measurements.

The sample is placed in the magneto-cryostat AttoDry 1000 and is described in detail later. The experiments can be performed in two configuration: in Faraday geometry, i.e. the excitation axis is parallel to applied magnetic field, and in Voigt geometry, where the applied magnetic field is orthogonal to the excitation axis. In order to perform the experiments in Voigt geometry a home-built Voigt module is adapted into the setup.

The laser beam arriving at the sample is focused by a lens (Thorlabs C390TMB-B) acting as the objective and excites the quantum dots. The quantum dot luminescence is collimated by the same lens and passing a BS and a LCR (LRC100-IR1-MOD) with GT as analyzer is focused by another lens (Thorlabs C280 TMB-B) and collected by a monomode optical fiber (Fibercore SM600) into the spectrometer (Acton SpectraPro 500i). The core diameter of the used fiber is $\approx$5 μm. Between the LCR and GT a $\lambda/2$-plate is placed allowing studying PL-polarisation in linear basis.

1 The optical fiber core 5 μm plays the role of the pinhole. Only in-focus light can be collected by this fiber.

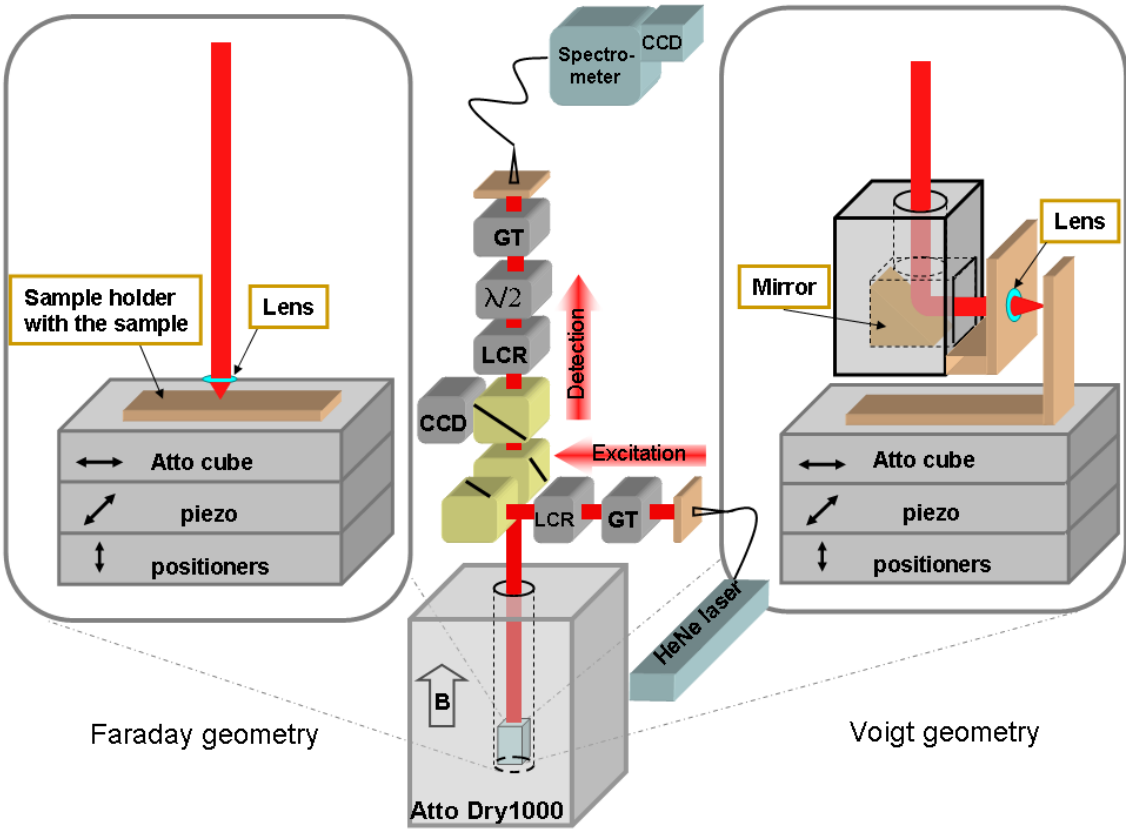

Figure 2.2: The experimental setup microscope head with home-built Voigt module. In Faraday configuration the beam is focused by the lens as used in Voigt module.

2.2.2 Spatial resolution

As mentioned before to perform single dot spectroscopy measurements the laser beam spot needs to be diffraction limited and the spot size cannot exceed $1/\sqrt{QD-density}$. The resolution of the confocal microscope depends on the objective lens and the operating wavelength of the setup. In general the spatial resolution of a confocal microscope is better than that of a conventional far-field [106].

The focused laser beam is a Gaussian beam and can be described by means of Gaussian beam optics [107, 108, 109, 110, 111]. In Figure 2.3(a) the radius w of a focused Gaussian beam is plotted as a function of the distance z from the focal plane. In the plane, the electric field amplitude of a Gaussian beam has its maximum value in the center following a Gaussian distribution. The radius of a Gaussian beam is defined as the distance where the electric field has dropped to 1/e of its maximum value. The beam waist is ω_0 and the divergence angle is θ. The radius of the Gaussian beam as a function of z is then given by [110, 111]:

$$w(z) = w_0\sqrt{1+(\frac{z}{z_R})^2}. \tag{2.2.1}$$

The distance from the focal plane at which the radius of the Gaussian beam is $\sqrt{2}\omega_0$ is

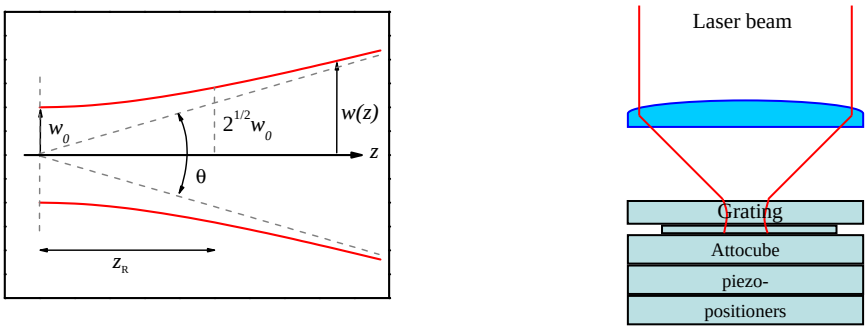

(a) **(b)**

Figure 2.3: (a) The propagation of the Gaussian beam. The vertical dashed line represents the focal plane. (b) A schematical draw of spatial resolution measurement. The photo diode is mounted behind the grating and onto the piezo positioners.

the Rayleigh range z_R. The Rayleigh range gives an approximative dividing line between the near-field and the far-field for a focused Gaussian beam. By illuminating the lens whose radius is equal to the $1/e^2$ beam waist of the Gaussian beam, the intensity distribution in the focal plane is Gaussian. The diffraction-limited spot size Δx of a lens can be calculated as follows [107, 108, 109]:

$$\Delta x = K_{FWHM}\frac{\lambda}{2tan\theta} \approx K_{FWHM}\frac{\lambda}{2NA}, \tag{2.2.2}$$

with the geometry factor K_{FWHM} defined as:

$$K_{FWHM} = 1.029 + \frac{0.7125}{(R-0.2161)^{2.179}} - \frac{0.6445}{(R-0.2161)^{2.221}}, \tag{2.2.3}$$

where $R = \frac{r_{beam}}{r_{lens}}$ the beam/lens ratio. As told before the spatial resolution of the confocal microscope is optimized [105] and is given by:

$$\Delta x \approx 0.44\frac{\lambda}{NA}, \tag{2.2.4}$$

where NA is the numerical aperture of the objective.

In order to characterize the spatial resolution of the confocal microscope developed during this thesis at cryogenic temperature 4 K the following method was used. Both a transmission and a reflection grating can be used for this characterization. In Faraday configuration the transmission grating was used whereas in Voigt geometry the reflection grating was used. The transmission grating consists of a glass substrate with 5 μm wide aluminum stripes with 5 μm distance between them. The grating is placed onto the nano-positioners in order to scan the grating with focused laser beam. The z-piezo-positioner serves to focus the laser beam onto the grating and the in-plane positioners, x- and y-positioners, serve to scan the grating.

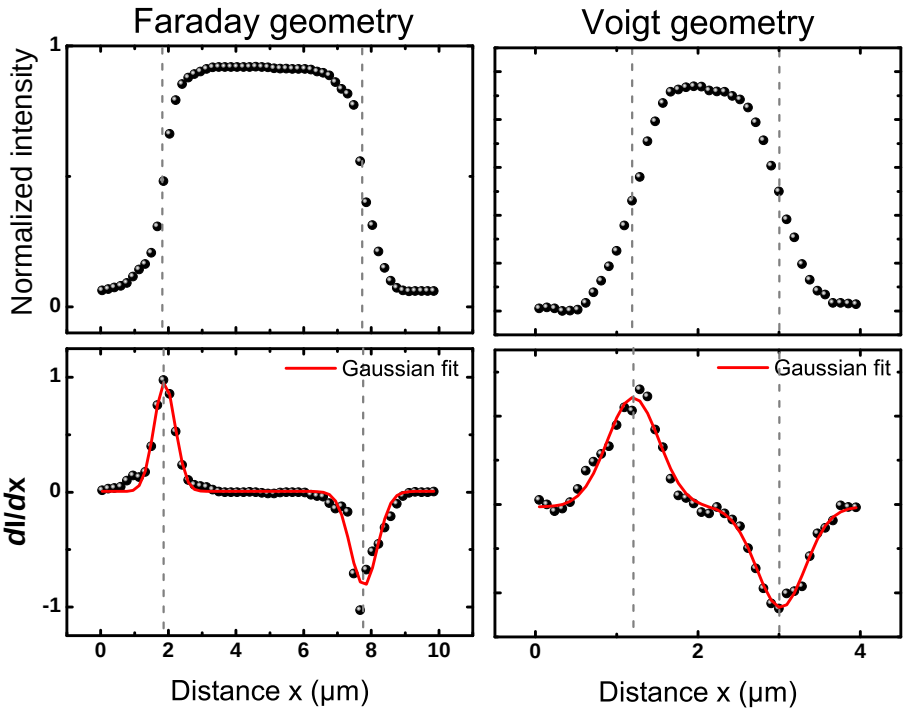

Figure 2.4: Measurement of the spatial resolution of the confocal microscope. The measurement of resolution in Voigt geometry was performed by using of reflection grating.

For both excitation and detection part of the microscope head the spatial resolution must be characterized. The diameter of the excitation laser spot is determined at 633 nm. The diameter of the detected beam on the sample is measured with a laser diode emitting at the QD emission wave length of 690 nm.

Behind the grating a small Si-photo-detector was mounted in order to measure the transmitted signal, Figure 2.3. While scanning the piezo positioner the transmitted intensity was measured as function of distance. Figure 2.4 shows a typical transmitted signal curve in Faraday geometry. Two plateau are pronounced: the maximum plateau is measured when the laser beam is positioned right between the aluminum stripes whereas the minimum corresponds to an aluminum stripe. The measured transmission signal as a function of the scan position is given by the integral over a Gaussian curve. Hence, the derivation of the measured intensity is directly proportional to the intensity profile in the focus, Figure 2.4. The distance between two extrema corresponds to the distance between two stripes, 5 μm. This allows the renormalization of the x-scale. The Gaussian fit of the derivative yields a Full Width at Half Maximum (FWHM) corresponding to a spatial resolution of the confocal microscope. The measured values in both configurations are given in Table 2.1.

The larger spot size in Voigt geometry can be explained by the less precise positioning of the objective in this configuration, which was unavoidable due to the limited space in

Table 2.1: The spatial resolution of the confocal microscope in Faraday and Voigt geometries.

	Spatial resolution (nm)	
λ(nm)	Faraday	Voigt
633	700	850
690	760	930

the sample chamber.

2.2.3 Polarisation resolution

In this thesis we were interested in the study of polarisation properties of the photoluminescence of QDs. To be able to perform polarisation based experiments the control of polarisation of the excitation as well as of the detection is required. The fiber based confocal microscopy has two disadvantages. Firstly, the monomode fiber does not maintain any polarisation. So it is not possible to transfer the polarised light coupled into the fiber to a spectrometer without any lost of polarisation. Secondly, the spatial coupling into the fiber can be lost by microscopically rotating the optical elements. A combination of a GT and a LCR in excitation and detection arms of the μ-head can resolve this problem. Since there are several optical elements in microscope head one needs to calibrate any influence on the polarisation of every optical element.

In the experimental setup we use two identical BSs in reflection and two others in transmission. The first BS placed in excitation path builds an angle 45° between the BS-plane and the incident beam. Reflection and transmission on the BS depends on the in-plane polarisation of the incident light, i.e. it depends on whether the light is polarised parallel to the s or p-axis of the BS. Hence there is a systematic error in the polarisation in reflection and transmission. Another identical BS can compensate this error by placing the second BS rotated by 90° with respect to first one.

A LCR acts as a tunable waveplate with retardation $\Delta\lambda = 0 - 5/4\lambda$. A standard LCR consists of a cavity filled with liquid crystals. The electric field generated by applied bias align the LC molecules and acts on the wave propagation through the LCR medium as a wave retarder. The molecules modify the retardation light propagation with polarisations along the principal axis of component. Figure 2.5(a) shows schematically the principle of a LCR. The bias is applied to the transparent electrodes. According to the generated electric field the LC molecules align. For no electric field, the bias V_1=0, the molecules are aligned parallel to the propagation direction of the incident light so that the optical axis of the LCR coincides with the propagation axis. If any electric field is created, bias $V_2 \neq 0$, the molecules are aligned according the applied electric field and change their optical axis. In this case the optical axis of the LCR builds an angle as function of the applied bias. This distortion of the molecules acts on the wave propagation as a phase retarder.

Placing the LCR between two cross- or co-polarised GT prisms with an angle 45° with respect to the optical axes of the GT prisms creates a variable attenuator Figure 2.5(b). Only this configuration enables using the LCR as a variable attenuator and controlling the polarisation of the light.

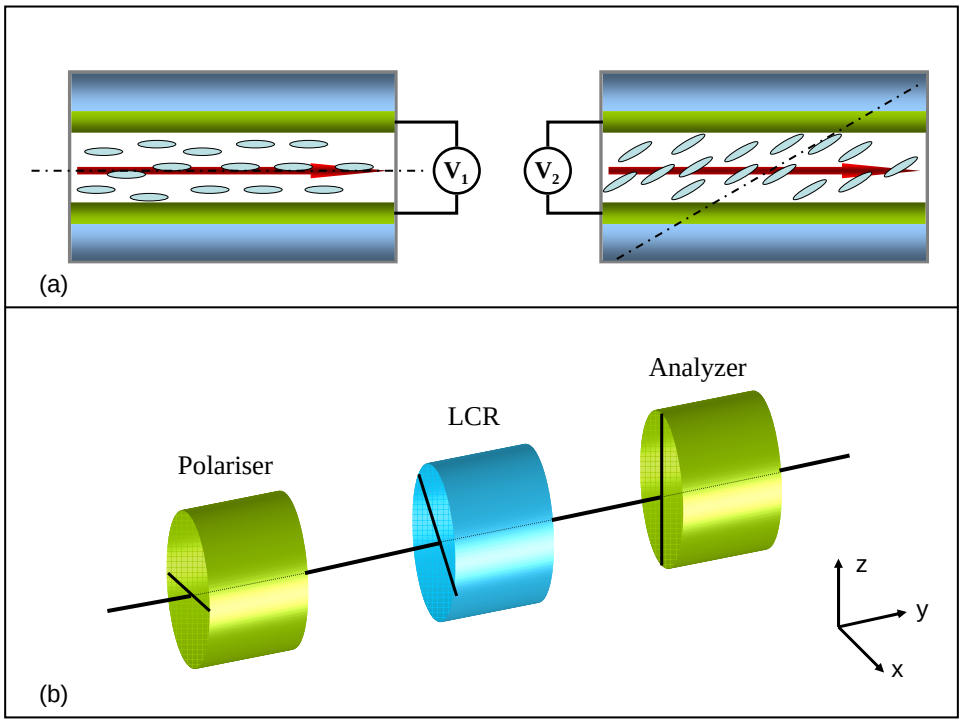

Figure 2.5: The principle of Liquid Crystal Retarder. (a) the alignment of the LC molecules as function of applied bias. The red arrow represents the light propagation and the dashed line is the optical axis of the LCR. (b) the calibration configuration consisting of two GT prisms and one LCR. The LCR optical axis is rotated by 45° with respect to the polariser optical axis. This configuration acts as a variable attenuator.

Faraday configuration

In order to calibrate the LCRs of the excitation and detection arms an additional GT and a photo diode are necessary. The calibration for the detection is identical to the excitation. The GT mounted between the fiber and the LCR acts as a linear polariser. The *s*- or *p*-axes are chosen as the polarisation axis of the polariser. The second GT together with the photo diode is placed after the second BS. By rotating the analyzer the minimum (maximum) of the photo diode intensity can be found corresponding to cross-polarisation (co-polarisation) of the analyzer respectively. Once the axes of the analyzer have been found the LCR is put into the setup and the LCR neutral axis can be found by looking for the minimum or maximum depending on the polarisation axis of the analyzer.

When the LCR neutral axis has been found it needs to be turned by ±45° and the calibration of the LCR can be performed by applying bias to the LCR and measuring the photo diode signal. In the orthogonal configuration, i.e. the analyzer is cross-polarised with respect to the polariser, the applied bias at which the minimum (maximum) is measured corresponds to the phase retardation $\Delta\lambda$=0 ($\lambda/2$), Figure 2.7. So the light excitation for these bias values is linear and is parallel to *s*- and *p*-axis of polariser. The

same characteristics we obtain for the co-polarisation of the analyzer where the maximum (minimum) corresponds to the phase retardation 0 ($\lambda/2$). The crossing points in the calibration curves Figure 2.7 correspond to the phase retardation of $\lambda/4$ and $3\lambda/4$. The corresponding light polarisation is $\sigma^{\pm}$.

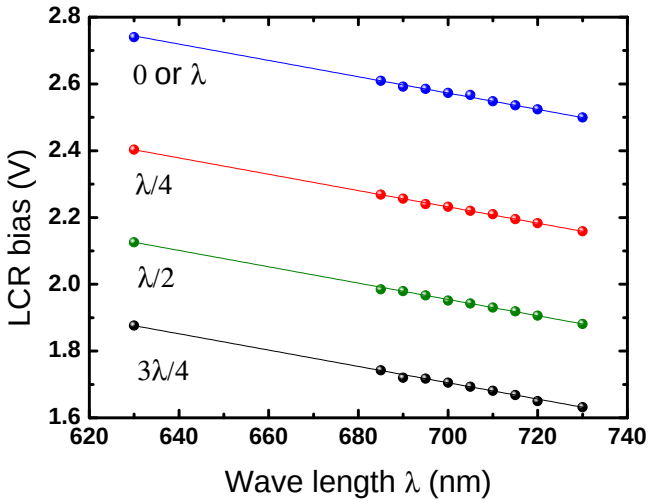

Figure 2.6: LCR-calibration for different wave lengths for the detection path of the microscope. The calibrations were performed by means of a tunable cw TiSa-laser.

The same calibration was done for the detection but with the wave length λ=690 nm near to QD emission range $\approx$ 690-740, Figure 2.7 (b). Since the phase retardation of the LCR depends on the wave length the calibration for different wave lengths was performed by means of a tunable cw TiSa-laser. The extracted applied bias for all four polarisations are linear functions of the wave length, Figure 2.6. Hence the bias values can be adapted to the studied dots according to this linear dependence.

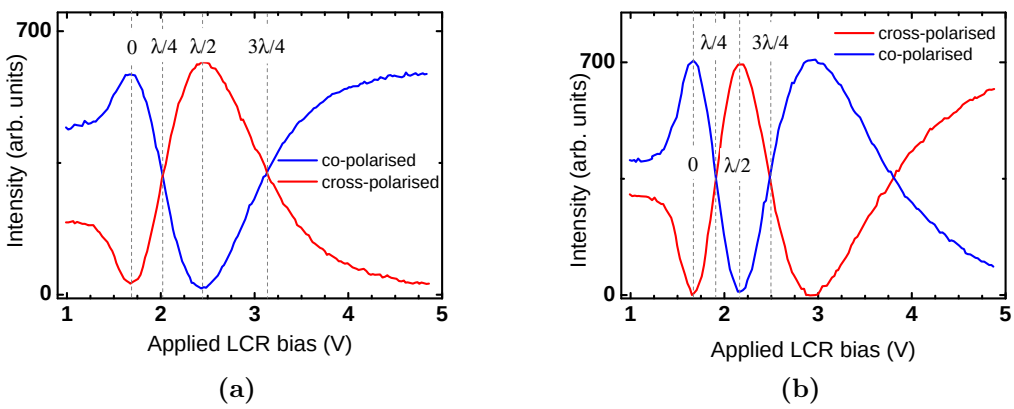

Figure 2.7: Phase retardation of LCR as function of applied bias in Faraday geometry: (a) performed for excitation at wave length λ=633 nm and (b) performed for detection at wave length λ=690 nm.

Voigt configuration

In Voigt geometry the beam is reflected by 90° by a gold mirror. Although the amplitudes of the reflection coefficients for s- and p-waves are (nearly) identical, the reflection introduces a phase shift between s- and p-waves. Our approach is to pre-compensate this phase shift with a LCR, so that the light has the desired polarisation after being reflected by the mirror.

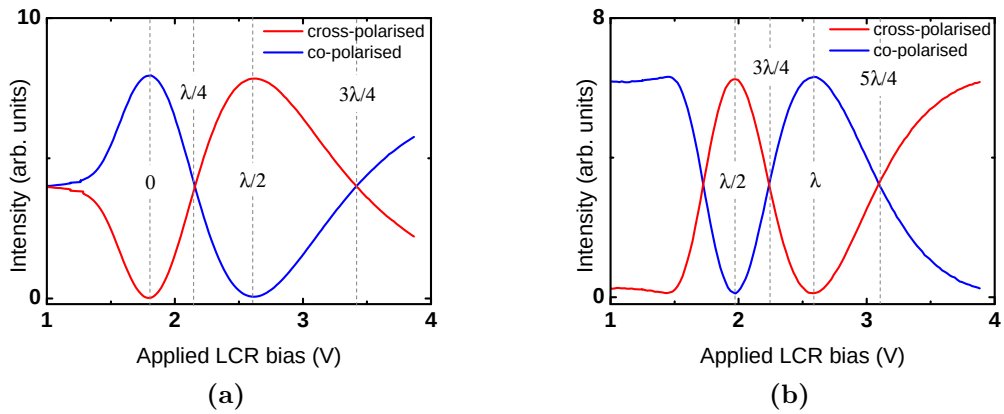

Figure 2.8: Phase retardation of LCR as function of applied bias in Voigt geometry: (a) performed for excitation at wave length λ=633 nm and (b) performed for detection at wave length λ=690 nm.

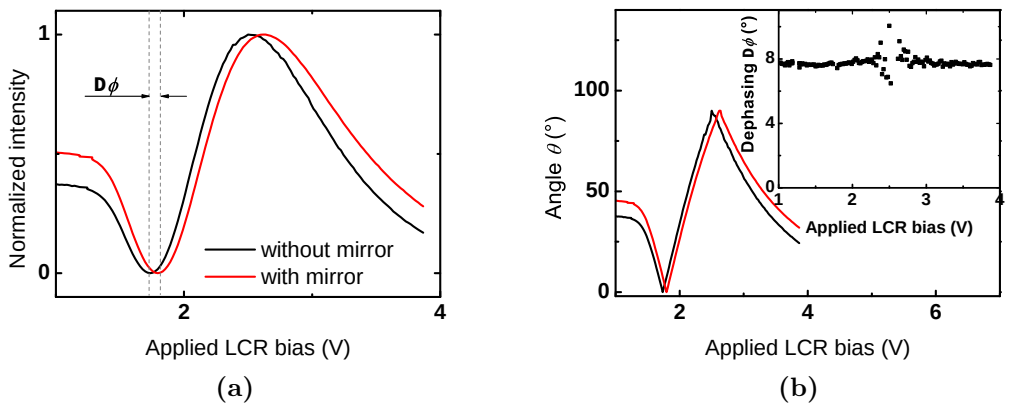

Figure 2.9: Dephasing of golden mirror as function of applied bias. (a) two calibration curves measured with and without the mirror showing the dephasing. (b) The angle obtained from the calibration curves with a dephasing in the inset graph. The dephasing here was measured at the wavelength λ=633 nm.

For the example shown in Figure 2.9 the dephasing is 8°. It is worth to mention that the dephasing varies from one mirror to another even if they are made of the same material. The coating thickness plays a crucial role for the dephasing. So the LCR calibration needs

to be performed for every mirror used.

2.2.4 Spectral resolution

The used spectrometer consists of a 0.5 m focal length monochromator Acton SpectraPro 500i with a turret of 3 gratings with different dispersion and a liquid nitrogen cooled Charge-Coupled Device (CCD) camera (RoperScientific)[112]. The characteristics of the monochromator are given in the Table 2.3. The monochromator includes a direct digital grating scan mechanism with full wavelength scanning capabilities. The gratings are blazed at $\lambda = 0.5$ μm.

The observed transitions can be fitted by Lorentzian curves. It is important to note that the central energy of the transition can be determined extremely precisely due to the high signal to noise ratio. In what follows the error of the fit is referred to as the spectral resolution. Figure2.10 (a) shows the spectral resolution in first order of monochromator of $\approx$2 μeV, and in second order $\approx$0.8 μeV. Thus, all measurements need to be carry out in second order of the monochromator. The disadvantage of the second order measurements is that the PL-intensity in second order is lower than the intensity in first order. So the studied QDs needed to have high enough intensities in order to allow the measurements in second order of the monochromator.

The used CCD-camera consists of a rectangular photoactive region (an epitaxial layer of silicon) with 100 x 1024 pixels with size: 20 x 20 μm. The capacitors are based on the photoelectric effect where an incident photon is converted to an electron-hole pair. The generated electrons are transfered to a neighbor capacitor causing each capacitor to accumulate an electric charge. The whole accumulated electron packet is then transfered to read-out zone where it is converted into a digital value.

In order to improve the signal-to-noise ratio the CCD-camera is cooled with liquid nitrogen. Furthermore the camera operates in back illuminated geometry, i.e. in contrary to the common front illuminated systems the light arrives at the back surface of the

Table 2.2: The extracted polarisation degrees for the excitation at λ =633 nm and λ =690 nm.

Excitation at λ=633 nm									
Retardance		λ		$3\lambda/4$		$\lambda/2$		$\lambda/4$	
PD voltage (μV)		Max	Min	Max	Min	Max	Min	Max	Min
		899	2	470	450	906	2	487	463
Polarisation degree	linear	99.33 %		2.18 %		99.56 %		2.53 %	
	circular	11.56 %		99.98 %		9.37 %		99.97 %	
Detection at λ=690 nm									
Retardance		λ		$3\lambda/4$		$\lambda/2$		$\lambda/4$	
PD voltage (μV)		Max	Min	Max	Min	Max	Min	Max	Min
		1390	4	701	661	1381	8	712	683
Polarisation degree	linear	99.43 %		2.94 %		98.84 %		2.08 %	
	circular	10.66 %		99.96 %		15.19 %		99.98 %	

Table 2.3: The characteristics of the monochromator Acton SpectraPro 500i for different gratings.

Grating (stripes/mm)	Spectral range (nm)	Dispersion nm/mm	Pixel resolution (μeV)
300	170	6.5	162
600	80	3.2	79.4
1200	31	1.5	37.2

capacitor because the capacitor back side is more sensitive then the front side. In this geometry the quantum efficiency of 95 % at the wavelength λ = 500 - 950 nm can be achieved.

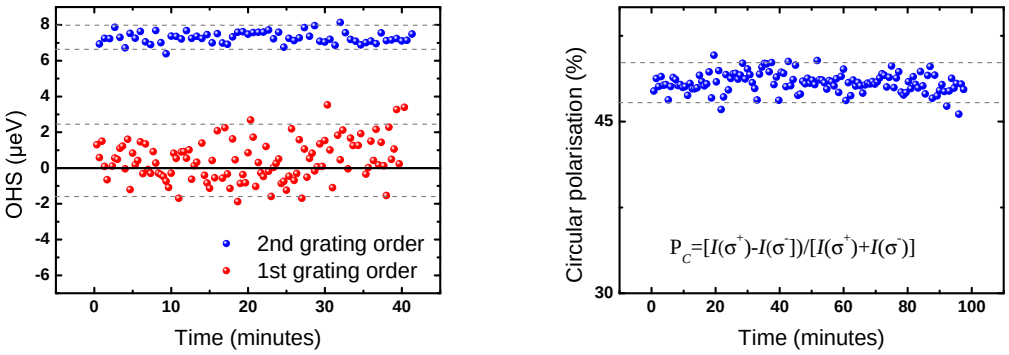

(a) (b)

Figure 2.10: Experimental resolution limited by the fit functions. (a) The spectral resolution determined by measuring the Overhauser splitting. The blue data is a measurement at a QD in second order of monochromator and the red one is a measurement in first order of the spectral position of the laser detected with $\sigma^{\pm}$. (b) The polarisation resolution determined by measuring the circular polarisation of X^{+} at B=2T.

2.2.5 "Helium-Free" magneto-cryostat

The used magneto-cryostat is a "Helium-Free" cryostat (attoDRY1000) built by Attocube. This cryostat is a cryogenic system capable of achieving low temperatures of 4 K and magnetic fields up to ±9 T without the transfer of cryogenic liquids. It is designed to combine the advantages of a bath cryostat system with the easy of use of a cryogenic free system. Special care has been taken to minimize the vibrations due to the pulse tube cold head. So that the single dot spectroscopy measurements can be performed longer times without loosing the QD of interest.

The cooling effect of the pulse tube is based on the compression and displacement of the working gas, Helium gas, and it is achieved by a compressor. The pulse tube cooler consists of a regenerator with a porous magnetic material inside. The regenerator is connected to the cold end of the hollow pulse. At the warm end the tube is connected to a reservoir

volume by an oriffice. The gas flow through the oriffice separates the heating and the cooling effects.

During the first step the piston moves towards the regenerator and compresses the gas, the generated heat is removed by a heat exchanger to the cooling water circuit. The gas flows to the reservoir and the regenerator takes heat out of the gas while flowing through the porous magnetic material. At the warm end of the pulse tube the gas flows through the oriffice and gives heat to the surroundings.

During the expansion process, while the piston increases the volume, the gas reduces its temperatue, flows out of the reservoir through the oriffice and takes heat from the regenerator. The function of the pulse tube is to separate the warm from the cold end. Therefore the tube has to be large enough that the gas travels only a part of the tube length. The gas in the middle of the pulse tube forms an insulating barrier between the cold end and the warm end because it never leaves the pulse tube. The gas at the cold end will never reach the warm end.

CHAPTER 3

Dark-bright mixing of interband transitions in symmetric semiconductor QDs grown along [111]

The search of methods to generate and manipulate entangled quantum states is one of the driving forces behind experimental physics on the nano-scale. The initial proposal to use the exciton-biexciton cascade in quantum dots to generate entangled photon pairs [113] relies on symmetric dots where the neutral exciton X^0 states are degenerate, i.e. have zero fine structure splitting δ_1 induced by anisotropic electron-hole Coulomb exchange. As in practice $\delta_1 \neq 0$ in the majority of quantum dot systems [48, 50, 114], very inventive research has been developed trying to tune the fine structure splitting to zero with original techniques [30, 115, 116, 117]. An alternative, recent approach is to use samples grown along the $z' \parallel [111]$ crystallographic axis, which is also the orientation of most nano-wires [118]. This growth axis has the advantage of providing microscopically identical interfaces for quantum well or dot structures, resulting in C_{3v} point symmetry. Hence, small fine structure splittings in *as grown* [111] quantum dot structures have been recently predicted [119, 120] and observed [121, 122, 123].

In this chapter the study of the effect of a longitudinal magnetic field $\boldsymbol{B} \parallel z' \parallel [111]$ in strain free [111] grown GaAs quantum dots is described in details. In longitudinal magnetic field the optically forbidden dark transitions in addition to optically active bright transitions for both charged and neutral excitons were observed. The strongly non-monotonous, sign changing field dependence of the bright neutral exciton splitting resulting from the interplay between exchange and Zeeman effects is also described. The theory[1] describes how these surprising experimental results due to magnetic-field-induced $\pm 3/2$ heavy-hole mixing can be explained by an inherent property of systems with C_{3v} point-group symmetry. The theoretical approach can be extended also to the observations

1 The theory was developed in collaboration with E. L. Ivchenko, M. M. Glazov and M. V. Durnev from the Ioffe-Institut, St. Petersburg, Russia.

in Voigt geometry where the magnetic field is applied orthogonal to the growth and excitation axis.

3.1 Investigated structure:(111)A GaAs/AlGaAs droplet quantum dots: F09-102-111A

The structure studied in this chapter is a sample with (111)A GaAs/AlGaAs droplet dots. The letter following the growth direction determines the substrate surface, on which the nanostructure is grown. A does mean the Ga-rich substrate surface and B stands for As-rich surface, Figure 3.1. Since (111)B-QDs have As-rich substrate the formation of the wetting layer would favoured. The sample does not contain any wetting layer as explained in the previous subsecton.

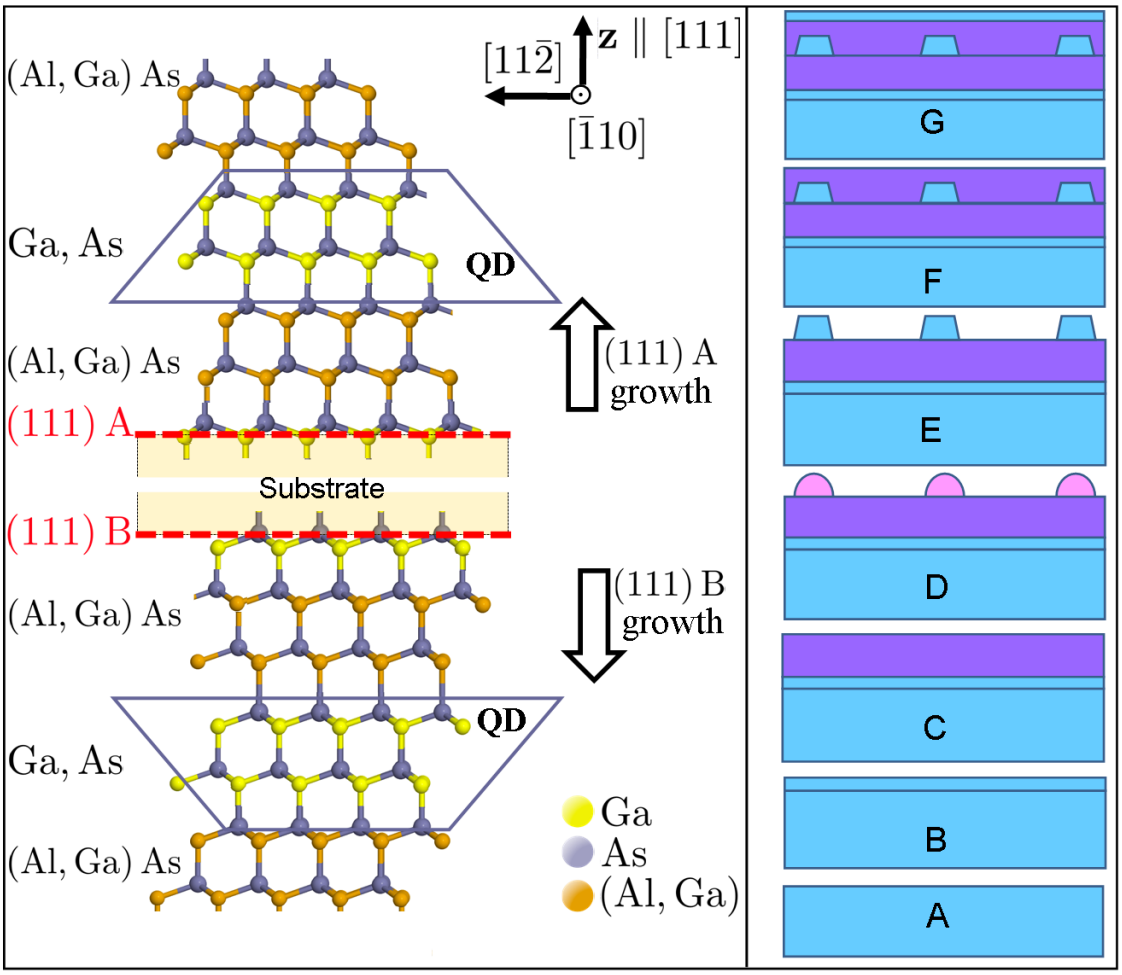

Figure 3.1: (111)A GaAs/AlGaAs droplet quantum dots: F09-102-111A. On the left atomic schematic reconstruction of (111)A and (111)B growth. On the right the sample growth is shown in details.

The sample was grown using a conventional molecular beam epitaxy system. After the growth of a GaAs buffer (B) and 100 nm $Al_{0.3}Ga_{0.7}As$ barrier layer (C) on the GaAs(111)A substrate (A) at 500 °C, followed by annealing at 600 °C, Ga droplets were formed by supplying a 0.05 monolayer (ML) of Ga (0.01 ML/s) at 400 °C (D). Then, the substrate was cooled down to 200 °C, and crystallized into GaAs by supplying an As_4 flux of $2{\cdot}10^{-6}$

Torr beam equivalent pressure (E). The sample was then annealed at 500 °C for 10 min, followed by capping with an 50 nm $Al_{0.3}Ga_{0.7}As$ (F) and 10 nm GaAs layers (G). Finally, the annealing was performed at 600 °C for 5 min to improve the optical properties.

The team from Japan at NIMS observed shape transition from hexagonal to triangular QD shape with increasing crystallizing temperature. The statistics of QD size show the self-limiting growth of GaAs QDs whose characteristic size is determined by that of Ga droplets[124].

The AFM images revealed that the studied (111)A dots have in-plane triangular shape, Figure 3.2. The (111)-growth direction stimulates the enhanced atom migration in all three in-plane principal crystallographic axes: $[\bar{1}10]$, $[1\bar{1}0]$ and $[\bar{1}\bar{1}2]$. So the triangular dot formation is favoured under certain conditions. As the AFM images show in Figure 3.2 the more pronounced triangular shape of the dots highly depends on the annealing temperature. While at temperature 200 °C the dots are rather round at the temperature 500 °C the dots exhibit very pronounced triangular shape.

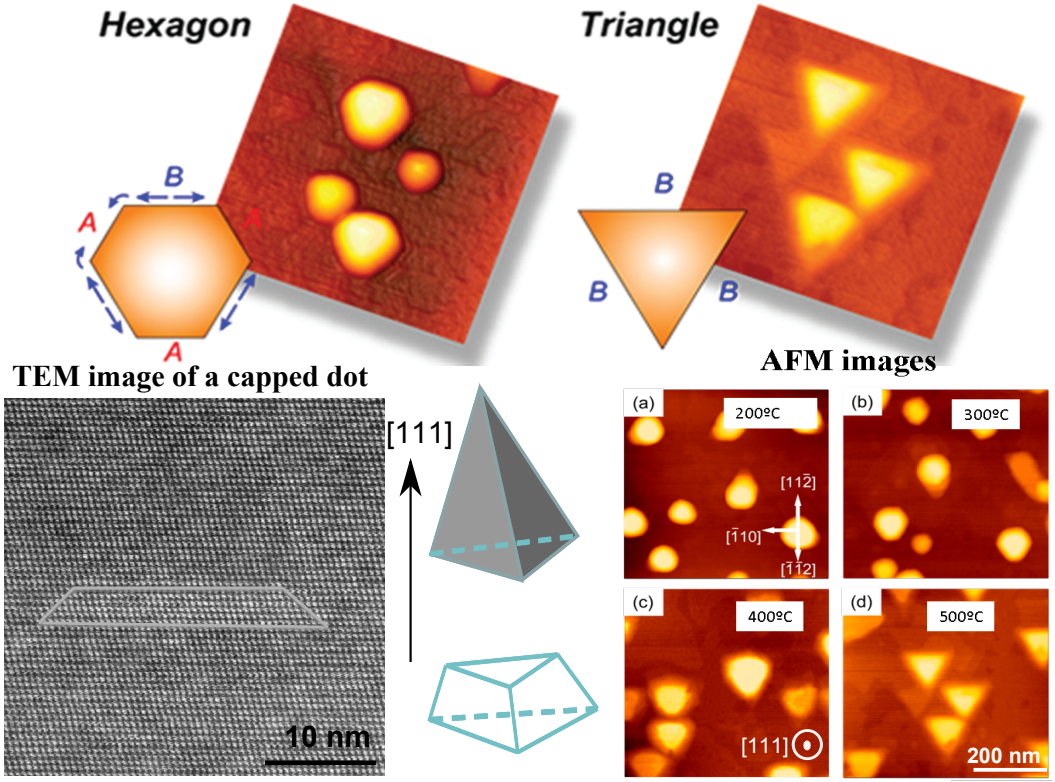

Figure 3.2: At the top the magnified AFM images of (111)A droplet dots are shown for hexagonal and triangular shapes. On the left the TEM images of the droplet dots. On the right are the AFM images for the dots crystallized at different temperatures resulting in transition from hexagonal to triangular dot shape. Height scale is different for each image: (a) 30, (b) 22, (c) 14, and (d) 10 nm [124].

3.2 Surprising appearance of the optically forbidden dark states

The investigated sample was grown by droplet epitaxy using a conventional molecular beam epitaxy system [59, 78, 121] on a GaAs(111)A substrate at the Quantum Dot Research Center at the NIMS, Tsukuba. The dots are grown on 100nm thick $Al_{0.3}Ga_{0.7}As$ barriers and are covered by 50nm of the same material. There is no continuous wetting layer in the sample connecting the dots (typical height ≃3nm, radius ≃15nm), see details in [121]. Optical excitation is achieved by pumping the AlGaAs barrier with a HeNe laser at 1.96 eV that is linearly polarised to exclude the effects of optical carrier orientation and dynamic nuclear polarisation [28].

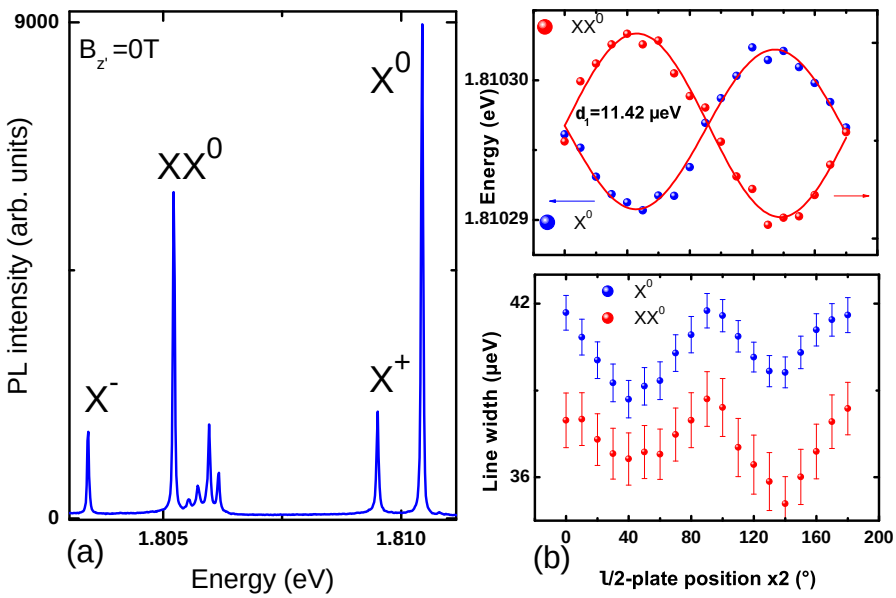

Figure 3.3: (a) Typical single dot PL spectra at $B_{z'} = 0$ in σ^- polarisation with identified excitonic states and (b) the fine structure splitting δ_1 measurement method including the line width measurement for the same QD with $\delta_1 = 11\mu$eV. Data are shown for **QD I**.

Figure 3.3(a) shows the different emission lines originating from a typical quantum dot QD I at zero magnetic field. The neutral exciton X^0, the biexciton XX^0, the negatively charged exciton X^- (2 electrons, 1 hole) and the positively charged exciton X^+ (1 electron, 2 holes) are identified using fine structure analysis and optical orientation experiments [28]. The high symmetry of the dots is reflected in typical values for the splitting of the X^0 emission due to anisotropic electron-hole exchange δ_1 of a few μeV [121], extracted from angle dependent PL polarisation analysis in the linear basis. In order to measure the fine structure splitting δ_1 which is lower than the spectral resolution the following method can be used: the spectral position of an emission line is recorded as function of Half Wave retarder ($\lambda/2$) position. When one of the linearly polarised eigenstates of the exciton is detected the line width exhibits its minimum whereas in the middle position, where the both line merge together, it shows its maximum. From the evolution of the spectral

position δ_1 can be extracted see Figure 3.3(b). The amplitude between the maximum and the minimum is δ_1.

In an applied longitudinal magnetic field $B_{z'} \neq 0$ *four* emission lines are observed, as two nominally dark transitions emerge in addition to the usual bright Zeeman doublet for charged excitons and X^0 of all quantum dots investigated. The experimental observations show that the heavy hole states with spin projections $+3/2$ or $-3/2$ onto the growth axis z' are coupled in a longitudinal magnetic field. The resulting appearance of forbidden charged exciton and dark X^0 transitions due to hole mixing is an inherent feature of [111] grown dots and is not related to a symmetry lowering, of the confinement potential or due to strain, as in [100] grown dots [50, 114].

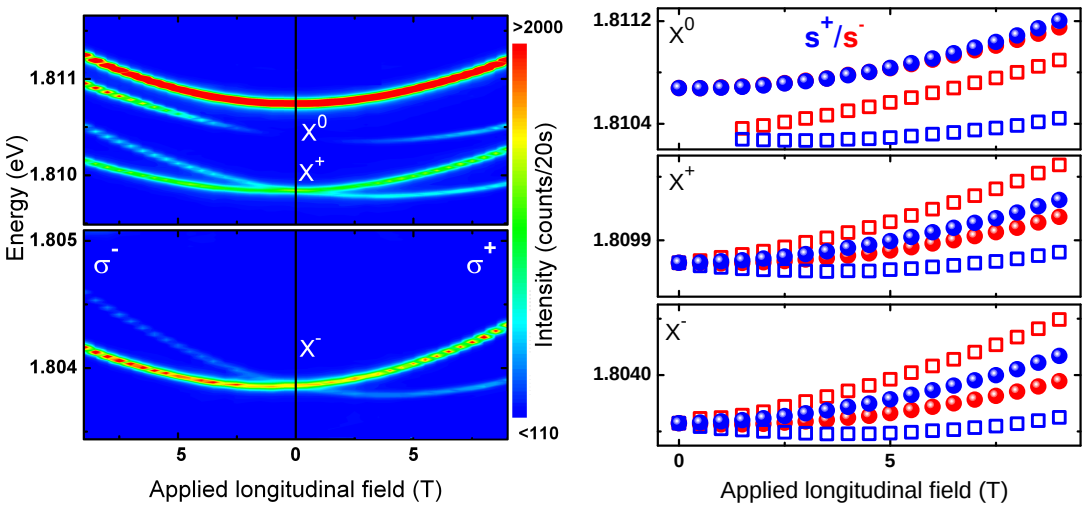

(a) **(b)**

Figure 3.4: (a) Contour plot of QD emission in applied longitudinal magnetic field for σ^- and σ^+ detections; (b) transition energies as a function of $B_{z'}$, for σ^- polarisation: dark (red hollow squares) and bright (red circles) and σ^+ polarisation: (blue hollow squares) and bright (blue circles).

We are able to measure the dark-brightX^0 separation δ_0 and observe a strongly non-monotonous bright X^0 splitting that changes sign as a function of $B_{z'}$ due to the competition between isotropic electron-hole exchange and the Zeeman interactions.

In Figure 3.4a and 3.4b the σ^+ and σ^- polarised emission from the same exciton states are presented in the presence of a longitudinal magnetic field. For the positively and negatively charged excitons X^+ and X^-, in contrast to the widely studied [100] grown samples, where a Zeeman doublet is observed, with one σ^+ and one σ^- polarised branch [59, 68, 78, 114] the emission patterns are strikingly different: in total four transitions are observed, two of them are σ^+ polarized, and two others are σ^- polarised. For each polarisation, the more intense emission line will be called "bright", the less intense "dark" in the following. The emission of two doublets is observed for the X^+ and the X^- exciton of all the dots studied as soon as $|B_{z'}| > 0$ in this sample, see Figure 3.4. But also the

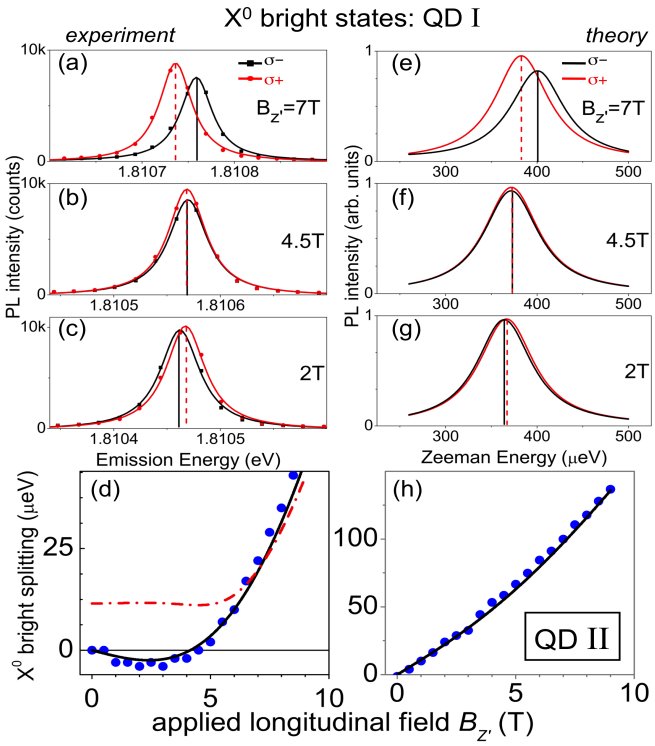

Figure 3.5: : (a)-(c) PL spectra in $\sigma^{+/-}$ polarisations of bright X^0 for different $B_{z'}$. (d) bright X^0 Zeeman splitting $E(\sigma^-) - E(\sigma^+)$ vs $B_{z'}$: experiment (circles), theory (black line), theoretical value of total splitting including $\delta_1 = 11\mu eV$ (dotted red line); (e)-(g) calculated spectra. Panels (a)-(g) correspond to **QD I**. (h) as (d) but for **QD II**.

appearance of dark states for the X^0 emission, shown in Figure 3.4, is observed. For typically $|B_{z'}| > 2T$ we are able to detect that the bright X^0 emission is accompanied by less intense lines at $\delta_0 \simeq 350\mu$eV lower in energy, as confirmed in all other investigated dots. This energy separation δ_0 is due to isotropic electron-hole exchange which splits bright and dark states. Previously, dark X^0 states have been observed generally for dots grown along the [100] axis either in high *transverse* magnetic fields (Voigt geometry) [125] or exceptionally in high *longitudinal* magnetic fields for dots with lowered symmetry [68, 114]. In the dots grown along [111] investigated here the dark X^0 is clearly visible for *all* dots in this sample in the Faraday configuration, even for highly symmetric dots with vanishing δ_1. The measured ratio of the emission intensity bright/dark transitions remains constant as $|B_{z'}|$ changes. The measured ratio shown in Figure 3.6 is 0.39. Another surprising feature of the X^0 emission is shown in Figure 3.4b and analyzed in detail in Figure 3.5(a)-(c). At 2T, the σ^+ polarised branch is at *higher* energy, at 4.5T both σ^+ and σ^- emission coincide in energy and at $B_{z'} > 4.5T$ the σ^+ is finally at *lower* energy. So the Zeeman splitting versus $B_{z'}$ is first tending towards negative values, before decreasing in amplitude to pass through zero at $B^0_{z'} \simeq 4.5T$ to finally become positive. For dots showing this reversal in sign for the Zeeman splitting, the exact value of $B^0_{z'}$ varies from dot to dot. The magnetic field induced (Zeeman) splitting can be extracted from the X^0 spectra even

in the presence of anisotropic electron-hole exchange following the procedure outlined in the supplementary material to [28]. The results are plotted in Figure 3.5(d) and clearly demonstrate the change in sign of the Zeeman splitting.

The evolution of the bright X^0 splitting varies dramatically from dot to dot: For QD II which has at $B_{z'} = 0$ very similar emission characteristics to QD I (transition energy, exciton states, values of g-factors and exchange energies) we record a splitting that is always positive and does not change sign, see Figure 3.5(h). The absolute value of the Zeeman splitting at $B_{z'} = 9$ Tesla is a factor of three higher in QD II than in QD I. Both dots QD I and QD II show prominent dark state emission and for both dots the dark state Zeeman splitting is a monotonous function of $B_{z'}$.

3.3 Theoretical approach

3.3.1 Phenomenological analysis

At the origin of all these surprising effects lies the magnetic field induced mixing between the heavy hole states with the angular momentum projection $\pm 3/2$ onto the growth axis z'. Let us introduce the coordinate system $x' \parallel [11\bar{2}]$, $y' \parallel [\bar{1}10]$ and $z' \parallel [111]$ relevant for the structure under study and the heavy-hole basis functions $|3/2\rangle', |-3/2\rangle'$ which transform according to the representation $\Gamma_5 + \Gamma_6$, where $\Gamma_{5,6}$ are irreducible representations of the group C_{3v}. It is crucial to note that the symmetry properties of the field $B_{z'}$ are described by the representation Γ_2 and the direct product $(\Gamma_5 + \Gamma_6) \times (\Gamma_5^* + \Gamma_6^*) = 2\Gamma_1 + 2\Gamma_2$ contains not one, but two representations Γ_2. As a result the heavy-hole Zeeman splitting in the basis $|3/2\rangle', |-3/2\rangle'$ is described by the 2×2 matrix with two linearly independent coefficients:

$$\mathscr{H}_{\boldsymbol{B}} = \frac{1}{2}\mu_{\mathrm{B}} B_{z'} \begin{bmatrix} g_{h1} & g_{h2} \\ g_{h2} & -g_{h1} \end{bmatrix}. \tag{3.3.1}$$

Here μ_{B} is the Bohr magneton, g_{h1} and g_{h2} are the effective hole g-factors. The derivation of the heavy-hole Hamiltonian is shown in Appendix A.1. We emphasize that the above arguments hold for heavy holes in a system of any dimensionality nD ($n = 0...3$) provided its symmetry is trigonal, including an exciton formed in bulk Germanium by an electron in the L-valley and a Γ_8^+ hole [126]. In contrast, in conventional [100] grown structures, the longitudinal-field induced mixing of heavy holes is symmetry-forbidden, $g_{h2} \equiv 0$ [1].

In a longitudinal magnetic field, the hole eigen energies are $E_\pm = \pm g_h \mu_{\mathrm{B}} B_{z'}/2$ with $g_h = \sqrt{g_{h1}^2 + g_{h2}^2}$ and the hole eigenstates $|h,\pm\rangle$ are admixtures of $|3/2\rangle'$ and $|-3/2\rangle'$, as indicated in Figure 3.7, with the coefficients $C_{1,2}$ determined solely by the ratio g_{h2}/g_{h1}.

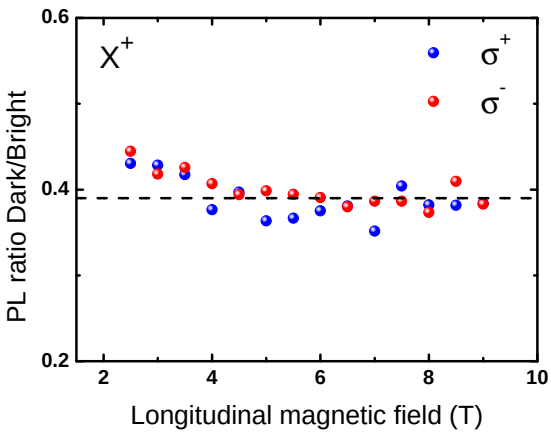

Figure 3.6: The PL ratio of dark/bright intensities for X^+ as function of applied longitudinal magnetic field.

For non-zero g_{h2}, all the four radiative transitions are allowed, each transition being

1 A symmetry analysis for a transverse magnetic field in the plane of (111) grown dots predicts in first order no mixing of the $|3/2\rangle'$ and $|-3/2\rangle'$ states.

circularly polarised, either σ^+ or σ^- [1]. For illustration, the four channels of radiative recombination of a positively charged trion are shown in Figure 3.7, together with the corresponding sign of circular polarisation. Each X^+ state forms a Λ system with the two hole states $|h,+\rangle$ and $|h,-\rangle$ which opens up the possibility of coherent optical hole spin control [127].

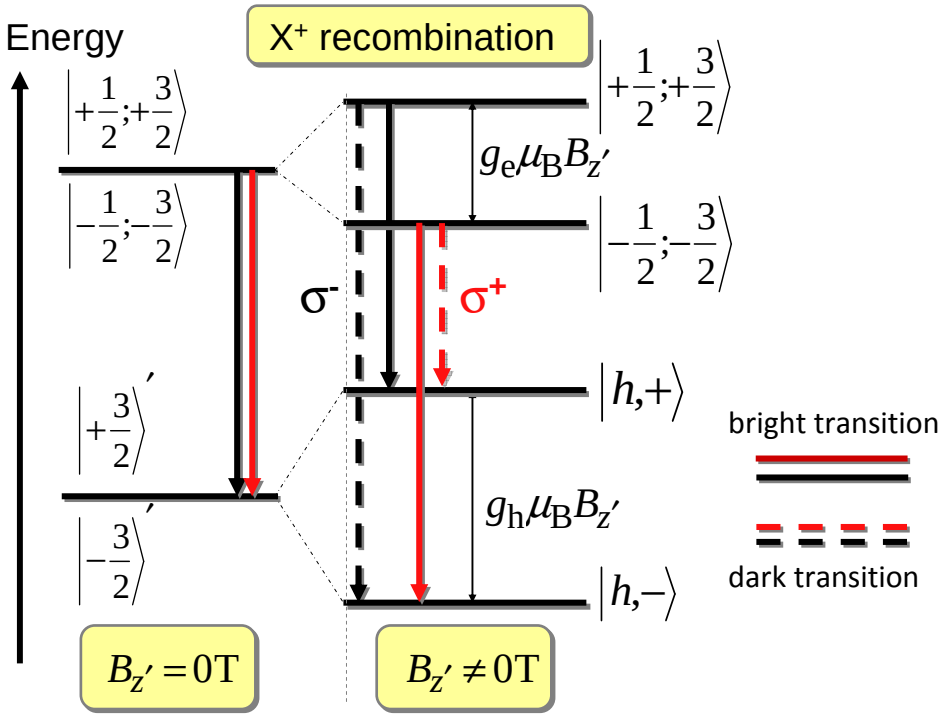

Figure 3.7: Modified optical selection rules in the X^+ recombination as an example. The upper state is the initial X^+ state consisting of an electron and two holes and the lower one is the final state with only an hole. While in conventional [100] grown structures, for pure heavy-hole states, only two optically allowed transitions are observed, solid lines, in the [111] QDs the dark states become optically active, dashed lines, due to the $\pm 3/2$ heavy-hole mixing induced by longitudinal magnetic field.

The transition energies are determined by combinations of the electron and hole effective g-factors which allows to find a pair of parameters, g_e and $g_h = \sqrt{g_{h1}^2 + g_{h2}^2}$. The intensities of circularly polarised lines are proportional to $|C_1|^2$ and $|C_2|^2$ and independent of the magnetic field, in full agreement with our experiments, see Figure 3.6. From the ratio of intensities of identically polarised lines we can find the ratio g_{h1}/g_h and, therefore, determine values of g_e, g_{h1} and modulus of g_{h2}.

The values of the g-factors vary from dot to dot and even for different complexes X^0, X^+, X^- in the same dot revealing the importance of confinement and Coulomb interaction

1 If in addition to the discussed effects heavy-hole to light-hole coupling were important, four lines would be observed for both σ^+ and σ^- polarised emission.

for the g-factor renormalization. Values for five typical dots are listed in Table 3.1 [1]. The experimental observation of dark states for all dots investigated leads logically to $g_{h2} \neq 0$ for all dots.

Dark transition related to X^+ and X^- complexes are always present in the spectra for all non-zero values of the field. By contrast, emission intensities of dark X^0 states increase gradually with $B_{z'}$. This is a result of the interplay between the electron-hole Coulomb exchange interaction and magnitude field effects. Taking into account isotropic short-range and long-range exchange interaction and assuming that the confining potential possesses a 3-fold rotation axis we obtain for the X^0 sublevel energies

$$E_{s,m} = s g_e \mu_\mathrm{B} B_{z'} + \frac{1}{2}(\delta_0 + m\delta_s)\,, \tag{3.3.2}$$
$$\delta_s = \sqrt{\delta_0^2 + (g_h \mu_\mathrm{B} B_{z'})^2 - 4 s g_{h1} \mu_B B_{z'} \delta_0}\,.$$

Hereafter we assume the exchange splitting between bright and dark states, $\delta_0 > 0$. The exciton state is labeled by two subscripts: $s = \pm 1/2$ denotes electron spin, and the index $m = \pm 1$ distinguishes between eigen-energies with the same s. At zero magnetic field the bright states are at higher energy $E_{\pm 1/2,+} = \delta_0$, where we refer to the zero-field dark exciton energy as $E_{\pm 1/2,-} = 0$. The optical activity of the dark states is induced by the magnetic field in our experiments [2]. It follows from Equation 3.3.2 that the splitting of bright X^0 states, $E_{+1/2,+}(B_{z'}) - E_{-1/2,+}(B_{z'})$, can be a non-monotonous and sign-changing function of $B_{z'}$. This is confirmed by our measurements shown in Figure 3.5 (d), where the calculation (solid line) follows closely the experiment (dots). The most

Table 3.1: g-factors (typ. error $\leq 10\%$) for charged and neutral excitons obtained from fitting the data. For the X^0 the g_e and g_h values obtained for X^+ for the same dot are taken and only $|g_{h2}|$ is varied to fit the bright and dark X^0 splitting *simultaneously*. The full table of all extracted coefficients for all investigated dots is attached in Appendix A.3.1.

	QD I	QD II	QD III	QD IV	QD V	QD VI
X^- : g_e	0.49	0.46	0.51	0.48	0.50	0.47
g_h	0.83	0.71	1.21	0.79	0.74	0.81
$\lvert g_{h2}\rvert$	0.53	0.60	0.33	0.57	0.57	0.53
X^+ : g_e	0.47	0.44	–	0.47	0.50	0.44
g_h	0.71	0.72	–	0.72	0.73	0.72
$\lvert g_{h2}\rvert$	0.62	0.72	–	0.70	0.72	0.68
X^0 : g_e	0.47	0.44	0.49	0.47	0.50	0.44
g_h	0.71	0.72	1.16	0.72	0.73	0.72
$\lvert g_{h2}\rvert$	0.50	0.68	0.42	0.59	0.65	0.56

1 In bulk GaAs $g_e = -0.44$ and for AlGaAs $g_e = 0.5$. g_e evolves monotonously towards the barrier material for GaAs/AlGaAs quantum wells of decreasing thickness [128]. These results, together with the fact that $|g_e| > 0.44$ in most cases confirm that g_e is positive.

2 The short-range anisotropic cubic exchange interaction $\propto \sigma_x J_x^3 + \sigma_y J_y^3 + \sigma_z J_z^3$ can mix bright and dark X^0 states. Our measurements show that its effect is negligible since no dark X^0 state emission is detected at $B_{z'} = 0$. So the cubic exchange term can be neglected in our [111] grown dots, which helps clarifying differences between previous predictions of the nature of the X^0 emission [119, 120, 122].

surprising feature, the vanishing X^0 Zeeman splitting at $B_{z'} = B^0_{z'}$ is well reproduced by the model. This result is another striking difference when comparing with the work on [100] grown dots, where the observed splitting increases monotonously as a function of the applied longitudinal field [50, 68, 114]. The fit of the data in Figure 3.5 (d) and 3.8 (c) is very sensitive to the exact value of $|g_{h2}|$ which explains the strong variations of the X^0 bright splittings as a function of $B_{z'}$ from dot to dot. To go from the strongly non-monotonous behavior for QD I to the more monotonous graph for QD II in Figure 3.5 (h), a change of $|g_{h2}|$ of only about 20% is sufficient, all other parameters remaining constant [1]. Here the development of a microscopic theory for g_{h1} and g_{h2} for realistic quantum dot samples will deepen our understanding.

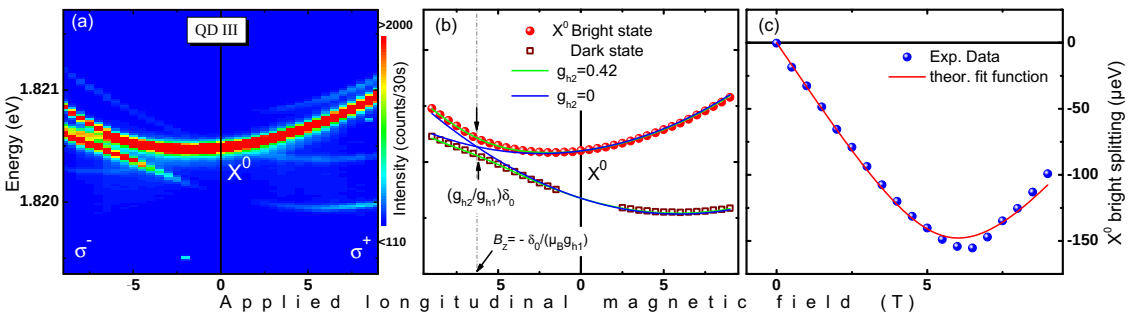

Figure 3.8: (a) and (b) X^0 bright and dark transitions showing anticrossing behavior in applied longitudinal magnetic field for QD III. The transitions are fitted with theoretical fit function Equation 3.3.2 including $g_{h2} = 0$ (blue line) and $g_{h2} \neq 0$ (green line) (for more information see the next section). (c) X^0 bright splitting exhibiting stronger non-monotonous behavior with respect to QD I in Figure 3.5.

In contrary to the QD I the QD III, with very high $g_h = 1.16$ see Table 3.1, exhibits even more pronounced non-monotonous behavior of the unusual bright splitting, see Figure 3.8 (c). The QD III shows also an other interesting phenomenon, which can be described as well in terms of our theoretical approach. In Figure 3.8 (a) and (b) the bright and dark transitions do not cross each other at certain magnetic field but exhibit relatively well pronounced anticrossing. The non-vanishing g_{h2} (see the next section for explanation) causes the anticrossing. The theoretical fit of the analyzed data including and excluding g_{h2} confirms this hypotheses. In Figure 3.8 (b) we see that if the fit function does not include g_{h2}, i.e. $g_{h2} = 0$, the bright and dark transitions cross each other. Whereas the fit function including g_{h2} does fit excellently the anticrossing transitions. In order to obtain the magnetic field value where the transitions cross both the bright and dark energies need to bee set equal. The obtained magnetic field is given by: $B_{z'} = -\frac{\delta_0}{\mu g_{h1}}$.
The advantage of the QDs with anticrossing behavior is that one can extract g_{h1} and also g_{h2} with high certainty and independently of other methods.

Taking into account (i) the energy dependence of the bright X^0 on $B_{z'}$, (ii) the polarisation of the X^0 eigenstates and our spectral resolution we calculate the emission spectra in

1 We find in the tested samples a wide spread of g_{h2} values $0 < |g_{h2}| \leq g_h$. There are no 'classes' of dots but we find rather a smooth transition in the character of the Zeeman splitting (non-monotonous to linear) when analysing a large number of dots.

the σ^+/σ^- basis using the fitted g-factor values. Our theory shown in Figure 3.5 (e)-(g) reproduces the measurements very accurately in terms of sign and value of the splitting and emission polarisation. Interestingly, the X^0 eigenstates 'exchange' polarisation at the field value $B^0_{z'}$. For $B_{z'} < B^0_{z'}$ the calculations and measurements show that the higher lying state is σ^+ polarised and the lower σ^-; at $B_{z'} > B^0_{z'}$ it is the opposite. Inclusion of small but non-zero anisotropic splitting of bright doublet, δ_1, results in the non-vanishing splitting of the eigenstates for all values of $B_{z'}$, as shown in Figure 3.5 (d) by the dash-dotted curve. However, at $B_{z'} \approx 0$ and $B^0_{z'}$ σ^+ and σ^- polarised lines exchange their places. Our measurement scheme allows us to separate the pure Zeeman splitting from Coulomb effects [28]. The influence of δ_1 and the determination of exact polarisation eigenstates of the system sets the challenge for future experiments, aiming to eventually tune the X^0 splitting to zero to erase the 'which path' information, a necessary condition for the generation of entangled photon pairs from the biexction-exciton cascade [115, 116]. Also additional energy shifts due to nuclear spin effects will be explored in this context.

3.3.2 Microscopical theory

Quantization of the hole motion in the pyramidal quantum dot

The hole states in a QD are described in the framework of the Luttinger Hamiltonian $\mathscr{H}_{\Gamma_8} + \mathscr{V}(\boldsymbol{r})$, where $\mathscr{V}(\boldsymbol{r})$ is the operator of potential energy of the hole and $\mathscr{H}_{\Gamma_8}$ is written in the standard matrix form [129]

$$\mathscr{H}_{\Gamma_8} = \begin{pmatrix} F & H & I & 0 \\ H^* & G & 0 & I \\ I^* & 0 & G & -H \\ 0 & I^* & -H^* & F \end{pmatrix}. \tag{3.3.3}$$

In the spherical approximation used hereinafter, the functions F, G, H, and I read

$$F = (A-B)k_z^2 + \left(A + \frac{B}{2}\right)\left(k_x^2 + k_y^2\right),$$

$$G = (A+B)k_z^2 + \left(A - \frac{B}{2}\right)\left(k_x^2 + k_y^2\right),$$

$$H = -\sqrt{3}Bk_z\left(k_x - \mathrm{i}k_y\right), \quad I = -\frac{\sqrt{3}}{2}B\left(k_x - \mathrm{i}k_y\right)^2.$$

Here k_j ($j = x,y,z$) are the Cartesian components of the wavevector in the axes frame $x \parallel [11\bar{2}]$, $y \parallel [\bar{1}10]$ and $z \parallel [111]$, constants A and B are related with the Luttinger parameters γ_1 and $\gamma_2 \equiv \gamma_3$ as $A = -\hbar^2\gamma_1/2m_0$, $B = -\hbar^2\gamma_2/m_0$, m_0 is the free electron mass. In the effective Hamiltonian (3.3.3) the wavevector $\boldsymbol{k}$ is replaced by the operator $-\mathrm{i}\nabla$.

We take the potential in the following matrix form

$$\mathscr{V}(\boldsymbol{r}) = \begin{pmatrix} V_{hh}(\boldsymbol{r}) & 0 & 0 & 0 \\ 0 & V_{lh}(\boldsymbol{r}) & 0 & 0 \\ 0 & 0 & V_{lh}(\boldsymbol{r}) & 0 \\ 0 & 0 & 0 & V_{hh}(\boldsymbol{r}) \end{pmatrix},$$

allowing for different potential energies of the heavy (V_{hh}) and light (V_{lh}) holes. Potentials acting on each hole type $n = hh$ or $n = lh$ are modeled here by the separable function,

$$V_n(\boldsymbol{r}) = V_z^n(z) + V_{\parallel}^n(\rho, \varphi), \tag{3.3.4}$$

where for convenience we use the cylindrical coordinate system with the principal axis z and in-plane polar coordinates $\rho = \sqrt{x^2 + y^2}$ and φ. In self-organized QDs the size quantization along the growth axis z is stronger than that in the dot plane allowing one to separate the hole motion along z and in the (x,y) plane.

In the effective Hamiltonian method the eigenstates and eigenenergies are found from the time-independent Schrödinger equation

$$[\mathscr{H}_{\Gamma_8} + \mathscr{V}(\boldsymbol{r})]\hat{\Psi}(\boldsymbol{r}) = E\hat{\Psi}(\boldsymbol{r}),$$

where $\hat{\Psi}(\boldsymbol{r})$ is a column formed by four envelopes $\Psi_m(\boldsymbol{r})$, $m = -3/2, -1/2, 1/2, 3/2$. The heavy-light hole mixing is described by the off-diagonal components of the Luttinger Hamiltonian (3.3.3). In this work, while calculating the hole g-factor, we take into account this mixing in the first-order approximation. Let us start from the zeroth-order approximation and, at first stage, completely separate heavy- and light-hole states so that the four-component hole wavefunction $\hat{\Psi}$ has only one non-zero component Ψ_m^n with $m = -3/2$ or $3/2$ for $n = hh$ and $m = -1/2$ or $1/2$ for $n = lh$ [130]. Due to the assumed separable potential (3.3.4) the envelopes $\Psi_m^n(\boldsymbol{r})$ are sought as separable wavefunctions [131]:

$$\Psi_{m;lp}^n(\boldsymbol{r}) = F_l^n(z)\psi_p^n(\rho,\varphi)\,. \tag{3.3.5}$$

Here $F_l^n(z)$ describes the hole size-quantization along the growth axis, with $l = 1,2\ldots$ is an integer enumerating the size-quantized states along this axis, and $\psi_p^n(\rho,\varphi)$ is the in-plane envelope with $p = 1,2\ldots$ labeling the in-plane confined states states.

In the further specification of the potential (3.3.4) we bear in mind that the QDs under consideration have the shape of triangular pyramids asymmetric with respect to the $z \to -z$ reflection and possess the three-fold rotation symmetry in the (x,y) plane. The asymmetry along the growth axis can be modeled by the triangular potential well

$$V_z^n(z) = \begin{cases} e\mathscr{F}z, & z > 0 \\ +\infty, & z < 0 \end{cases}, \tag{3.3.6}$$

where $z = 0$ corresponds to the quantum dot base, $\mathscr{F}$ is the effective electric field breaking the $z \to -z$ symmetry and confining hole along the z-axis, $-e$ is the electron charge. The

corresponding z-dependent envelopes can be expressed via the Airy functions

$$F_l^n(z) = C_l^n \mathrm{Ai}(Z_l^n)\,, \tag{3.3.7}$$

where C_l^n is the normalization factor,

$$Z_l^n = \frac{z}{L_n} - \mu_l \quad , \quad L_n = \left(\frac{\hbar^2}{2m_{n,z}e\mathscr{F}}\right)^{1/3} ,$$

μ_l is the l-th root of the equation $\mathrm{Ai}(-Z) = 0$, and the effective mass $m_{n,z}$ equals to $m_0/(\gamma_1 \pm 2\gamma_2)$ with the $\pm$ sign corresponding to the light and heavy holes.

The in-plane potential acting on holes is taken to be an analytical function of ρ and comprise the main parabolic term [132, 133, 134] and a cubic correction describing the trigonal warping, as follows,

$$V_{\parallel}^n(\rho,\varphi) = \frac{\hbar^2\rho^2}{2m_{n,\parallel}a_n^4}\left(1 + \frac{\beta\rho}{a_n}\cos 3\varphi\right) . \tag{3.3.8}$$

Here $m_{n,\parallel} = m_0/(\gamma_1 \pm \gamma_2)$ are the effective masses for heavy (top sign) and light (bottom sign) holes in the QD plane, a_n are the effective localization radii and the dimensionless parameter β characterizes the quantum dot triangularity.

Figure 3.9 represents equipotential surfaces of the dot confining potential defined by Eqs. (3.3.4), (3.3.6), and (3.3.8) for $\beta = 0$ (a) and $\beta = -0.2$ (b) and illustrates the transfer from the axial to trigonal symmetry.

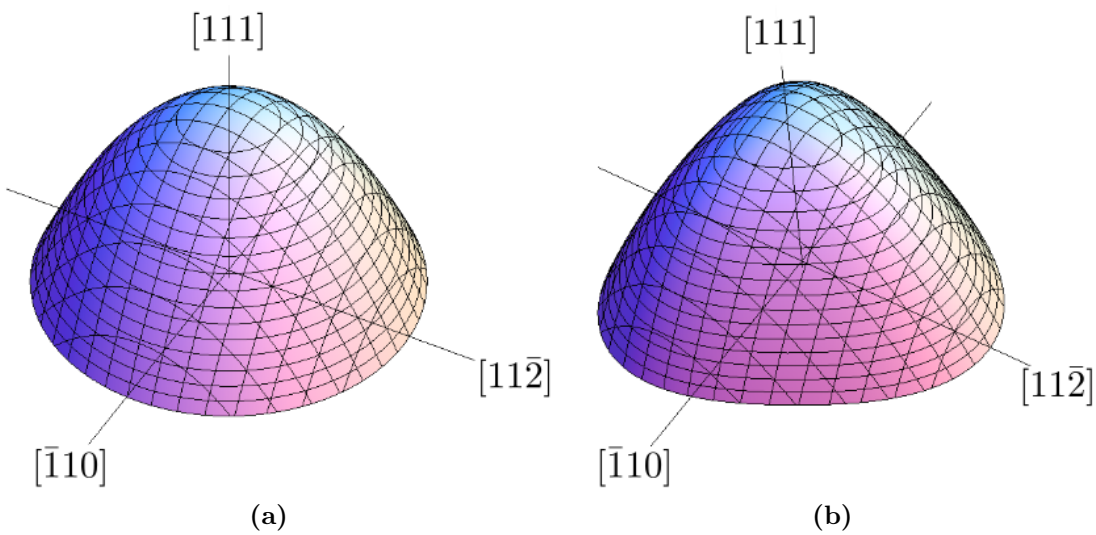

Figure 3.9: Equipotential surface of the dot confining potential Eqs. (3.3.6), (3.3.8) for the values of $\beta = 0$ (a) and $\beta = -0.2$ (b)

For the GaAs parameters $\gamma_1 = 6.98$ and $\gamma = 2.58$, one has $m_{hh,z} = 0.55m_0$, $m_{lh,z} = 0.08m_0$ $m_{hh,\parallel} = 0.1m_0$, and $m_{lh,\parallel} = 0.22m_0$. The size-quantization energies for the motion

along z-axis are given by

$$E^n_{z,l} = \frac{\hbar^2 \mu_l}{2m_{n,z}L_n^2}. \tag{3.3.9}$$

It is convenient to introduce the effective size of the dot in z-direction as $L = \sqrt{L_{hh}L_{lh}}$. For $L = 30$ Å the values of energies of the ground heavy and light-hole states are, respectively, $E^{hh}_{z,1} \approx 33$ meV and $E^{lh}_{z,1} \approx 63$ meV. The energies of size quantization in the quantum dot plane are labeled as $E^{hh}_{\parallel,p}$ and $E^{lh}_{\parallel,p}$ for heavy and light holes, respectively. If $\beta = 0$ the energies of in-plane size-quantization form an equidistant set with the spacing

$$\hbar\omega_n = \frac{\hbar^2}{2m_{n,\parallel}a_n^2}, \tag{3.3.10}$$

and the eigenfunctions are those of two-dimensional axially-symmetric harmonic oscillator. In what follows we assume that the confining in-plane potential in the case of $\beta = 0$ is identical for the heavy and light holes. This implies that $m_{hh,\parallel}a^4_{hh} = m_{lh,\parallel}a^4_{lh}$ and the ratio of two localization radii for GaAs is $a_{hh}/a_{lh} \approx 1.21$. Taking 75 Å as a reasonable estimation for a_{hh} we obtain $\hbar\omega_{hh} \approx 6.5$ meV and $\hbar\omega_{lh} \approx 4.4$ meV. These values are small as compared to the energy $E^{lh}_{z,1} - E^{hh}_{z,1} \approx 30$ meV of confinement in the z-direction, confirming the consistency of the theoretical model.

Longitudinal g-factor g_{h1}

The Zeeman interaction of a bulk (Γ_8) hole with the magnetic field $\boldsymbol{B}$ is described by the 4×4 matrix operator [135], resulting for $\boldsymbol{B} \parallel [111]$ in the following expressions for the effective g-factors: [136]

$$g_{h1} = -6\varkappa - \frac{23}{2}q, \tag{3.3.11a}$$

$$g_{h2} = 2\sqrt{2}q, \tag{3.3.11b}$$

where $\varkappa$ and q are the dimensionless band structure parameters, describing isotropic and cubic contributions to Zeeman effect [137, 138]. In GaAs crystals $\varkappa = 1.2$, $q = 0.02$ [139]. It follows from Eq. (3.3.11b) that non-diagonal g-factor g_{h2} is already present in this model, however, its value $g_{h2} \approx 0.056$ is too small to describe experiment. Moreover, similarly to bulk semiconductors and quantum wells [137, 140, 141, 142], magnetic field induced mixing of heavy and light hole states and quantum confinement strongly renormalizes heavy-hole g-factor in quantum dots from its value in the bulk [143, 144, 145, 146, 147, 148, 149]. In particular, the longitudinal g-factor g_{h1} in the quantum dot is given by, see Appendix A.2.1 for details,

$$g_{h1} = -6\varkappa - (23/2)q + \Delta g_{h1}\,.$$

Here the third term obtained in the second order in L/a has the form

$$\Delta g_{h1} = 24\gamma^2 \frac{m^{1/3}_{hh,z} m^{2/3}_{lh,z}}{m_0} \sum_l \frac{\varkappa_l^2 + \xi_l^2 (L^2/2a^2)}{\mu_l - \mu_1 (m_{lh,z}/m_{hh,z})^{1/3}}\,, \tag{3.3.12}$$

where $a \equiv a_{hh}$, other notations are

$$\begin{aligned}
\varkappa_l &= L \int F_0^{hh}(z) \frac{\partial}{\partial z} F_l^{lh}(z) dz \,, \\
\xi_l^2 &= \rho_l^2 - \frac{4\varkappa_l^2}{\mu_l \sqrt{m_{lh,\|} m_{hh,\|}}/m_{lh,z} - \mu_1 m_{hh,\|}/m_{hh,z}} \,, \\
\rho_l &= \int F_0^{hh}(z) F_l^{lh}(z) dz \,. \qquad (3.3.13)
\end{aligned}$$

Performing summation in Equation (3.3.12) for the set of GaAs parameters γ_1, γ, $\varkappa$, $m_{hh,\|}$ and $m_{lh,\|}$ we obtain a simple expression for the g_{h1}

$$g_{h1} \approx -6\varkappa - (23/2)q + 4.53 + 6.71 \frac{L^2}{a^2} \,, \qquad (3.3.14)$$

where the third and fourth coefficients are calculated numerically. For the g_{h1} calculations an in-plane anisotropy of the dot was neglected, i.e. in the framework of our model we have set $\beta = 0$ and have chosen the angular envelopes ψ_p^n [see Eq. (3.3.5)] as the eigenfunctions of isotropic two-dimensional harmonic oscillator. Note, that trigonal distortion of the in-plane potential described by a small parameter β leads to a correction to g_{h1} quadratic in β. Indeed, as it follows from the symmetry reasons the change of the β sign is equivalent to the rotation of the triangle around z axis by π, in which case g_{h1} remains unchanged. Estimations show that this quadratic correction are negligible.

Mixing of the $\pm 3/2$ states by longitudinal magnetic field

The pyramidal shape of the quantum dot with the three-fold rotation axis z results in the magnetic-field induced mixing of heavy holes with opposite angular momentum projections $\pm 3/2$. The trigonal distortion of the in-plane parabolic confinement described by the term $\propto \beta\rho^3 \cos 3\varphi$ in Equation (3.3.8) mixes states with orbital momentum z components different by ± 3. In particular, the ground heavy-hole state envelope function can be represented in the lowest order in $\beta \ll 1$ as

$$\tilde{\psi}_1^{hh} \propto \exp\left(-\frac{\rho^2}{2a^2}\right)\left(1 + \beta \frac{\rho^3}{a^3} C(\rho) \cos 3\varphi\right) , \qquad (3.3.15)$$

where function $C(\rho)$ is finite at $\rho = 0$ and only terms up to linear order in β are retained. The variational procedure with the space-independent $C(\rho) \equiv C_0$ gives for C_0 a value of $-1/6$.

In the presence of the longitudinal magnetic field the wavevector $\boldsymbol{k}$ in Eq. (3.3.3) is replaced as $\boldsymbol{k} \to \boldsymbol{k} + e\boldsymbol{A}(\boldsymbol{r})/c\hbar$, where $\boldsymbol{A}(\boldsymbol{r})$ is the vector potential of the magnetic field.[1] The vector potential, through the off-diagonal components of the matrix (3.3.3), mixes the ground heavy-hole state with excited light-hole states. By means of the second-order perturbation theory we obtain for the magneto-induced mixing of $3/2$ and $-3/2$ heavy-hole

1 Here we use the hole representation.

states [cf. Eq. (3.3.1)]:

$$\mathscr{H}_{B,3/2,-3/2} \equiv \frac{1}{2}\mu_B g_{h2} B_z = \sum_{lp\pm} \frac{\left\langle \Psi^{hh}_{3/2;11} | \hat{\mathscr{H}}_{\Gamma_8} | \Psi^{lh}_{\pm 1/2;lp} \right\rangle \left\langle \Psi^{lh}_{\pm 1/2;lp} | \hat{\mathscr{H}}_{\Gamma_8} | \Psi^{hh}_{-3/2;11} \right\rangle}{E^{hh}_{z,1} + E^{hh}_{\parallel,1} - E^{lh}_{z,l} - E^{lh}_{\parallel,p}}. \quad (3.3.16)$$

Here only linear in $\boldsymbol{A}$ terms should be retained.

The details of evaluation of the off-diagonal parameter g_{h2} are presented in Appendix A.2.2. Similarly to the calculation of g_{h1}, in the limit $L/a \ll 1$ one can neglect the dependence of hole energy on the in-plane quantum numbers p with the result

$$g_{h2} = \frac{18\hbar^2\gamma^2}{m_0 L} \sum_l \frac{\varkappa_l \rho_l}{E^{lh}_{z,l} - E^{hh}_{z,1}} \times \left\langle \tilde{\psi}^{hh}_1 \middle| (x - \mathrm{i}y) \left(\frac{\partial}{\partial x} - \mathrm{i}\frac{\partial}{\partial y} \right)^2 \middle| \tilde{\psi}^{hh}_1 \right\rangle . \quad (3.3.17)$$

This equation clearly shows that the value of g_{h2} is nonzero provided only that (i) the dot base has a triangular shape, otherwise integration over the in-plane coordinates vanishes, and (ii) the dot is asymmetric in the z direction, otherwise the product $\varkappa_n \rho_n$ vanishes because of the parity.

Using the variational function (3.3.15) we obtain

$$g_{h2} = 36\beta\gamma^2 \frac{\left(m_{hh,z} m^2_{lh,z}\right)^{1/3}}{m_0} \frac{L}{a} \times \sum_l \frac{\varkappa_l \rho_l}{\mu_l - \mu_1 (m_{lh,z}/m_{hh,z})^{1/3}} . \quad (3.3.18)$$

The numerical summation in Equation (3.3.18) yields

$$g_{h2} \approx 10.25\beta \frac{L}{a}. \quad (3.3.19)$$

For reasonable values $\beta = -0.2$, $L/a = 0.3$ we obtain $|g_{h2}| \approx 0.62$, in good agreement with experiment.

3.4 Magneto-optical properties in Voigt geometry

In order to complete our study of the (111) QDs we performed the measurements in Voigt configuration. The applied magnetic field lies in sample plane and is orthogonal to light excitation and detection axis. In this geometry C_{3v} point group indeed does not allow the mixing of the $\pm 3/2$ states by the in-plane magnetic field. In contrary to the longitudinal field $B_{z'}$ the symmetry properties of the transverse magnetic field $B_\perp$ are described by the representation Γ_3. To see whether there exist $\pm 3/2$ heavy-hole coupling the matrix elements need to be calculated: $\langle m' | B_\perp(\Gamma_3) | m \rangle$, where m',$m = \pm 3/2$ is. The direct product $(\Gamma_5^* + \Gamma_6^* \times (\Gamma_3 \times (\Gamma_5 + \Gamma_6))) = 4\Gamma_3$ contains only representation Γ_3 and not Γ_1. Hence all matrix elements are zero resulting in vanishing of in-plane hole g-factor g_h.

Indeed the experiments in Voigt geometry show the vanishing hole g-factor g_h. In the Figure 3.10 we can see two different QDs in Faraday and Voigt configurations. While in longitudinal magnetic field four transitions appear in transverse magnetic field only two transitions were observed overlapping for both polarisations. The Zeeman splitting of trions of one linear polarisation is a sum and of another polarisation is a difference of electron and hole g-factors. Since the transitions for both polarisations overlap the hole g-factor g_h is nearly zero. The g-factor g_h measured in applied transverse magnetic field is negligible small and varying from dot to dot: $\simeq$0.02-0 (see full table in Appendix).

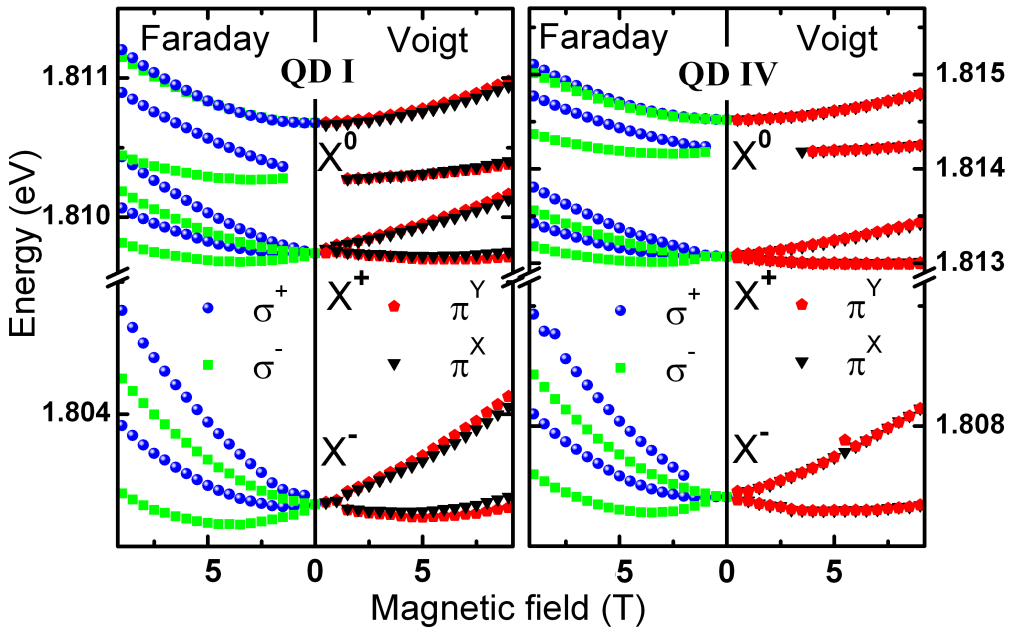

Figure 3.10: The exciton and trion transitions of QD I and QD IV in Faraday and Voigt geometries. Both the bright and the dark transitions of the same polarisation are labeled with the same color for clarity.

In Figure 3.10 the trion transitions of the QD I do not overlap perfectly resulting in hole g-factor $g_h \simeq$0.02 whereas the transitions of QD IV do overlap very well. The small

deviation can take their origin in different quantum dot shape.

Figure 3.11 compares the measured X^0 bright splitting for Faraday and Voigt geometry. Contrary to the Faraday configuration, the Zeeman splitting is not changing its sign in Voigt geometry. In the case of vanishing g-factor g_h and consequently g_{h2} Equation 3.3.2 depends only of the electron g-factor.

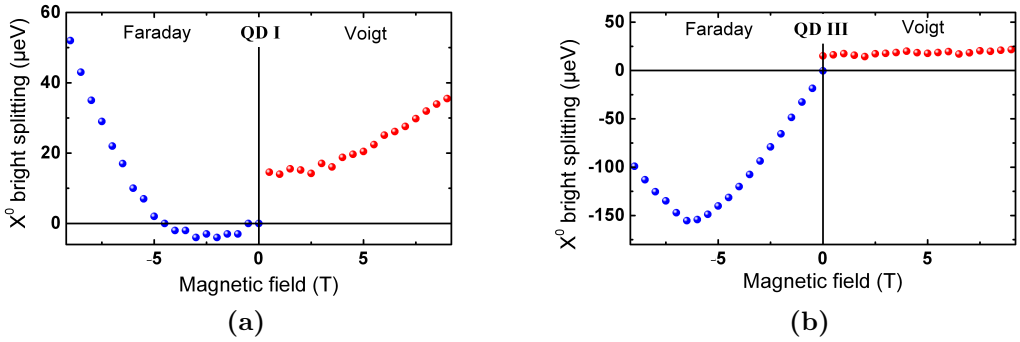

Figure 3.11: (a) and (b) X^0 Zeeman splitting in Faraday and Voigt geometries for QD I and QD III respectively.

3.5 Discussions

The results of g_{h1} and g_{h2} calculations for different values of L/a are presented in Fig. 3.12. $|g_{h2}|$ value varies in the range of 0.3div 0.7 for the reasonable parameters β and L/a which well agrees with the observed data. Note that g_{h1} changes its sign for some critical value of L/a which depends on the calculation parameters, relying on our estimations we believe that the value of g_{h1} for studied dots with the small values of L/a is negative.

It should be emphasized that the developed theory predicts non-zero values of g_{h2} only for the dots of specific trigonal shape. Note that for the isotropic in (x,y)-plane shape as well as for the shape invariant to the $z \to -z$ transformation (i.e. disk or prism) g_{h2} equals to zero. As far as we use Hamiltonian Equation (3.3.3) in spherical approximation, [111] growth-direction is physically equivalent to [001] direction, except for the trigonal shape is naturally obtained in the former case. Our theoretical predictions are in perfect agreement with the recent experimental results of [150] where zero values of g_{h2} were obtained for the disk-shaped [111] quantum dots embedded in nanowires. Two other mechanisms of the $\pm 3/2$ mixing are described in the theoretical part of [136], namely, due to anisotropic corrections to the hole Hamiltonian in magnetic field (proportional to the small parameter q, see Equation (3.3.11)) and the cubic in wavevector terms in the valence band (accounting for the non-centro-symmetricity of the GaAs crystal). However our estimations have shown that those models do not describe experiment quantitatively (the corresponding g_{h2} values are too small).

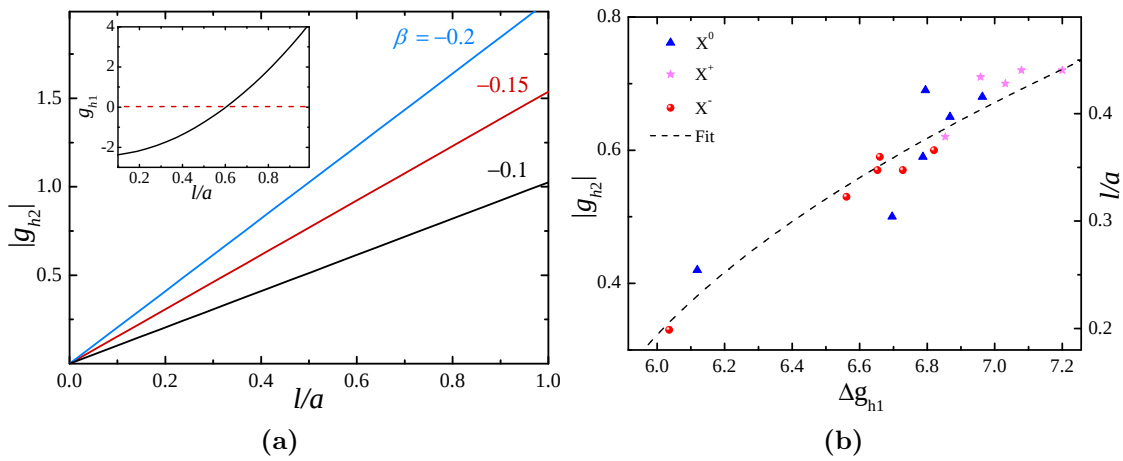

Figure 3.12: (a) Dependence of g_{h2} on the L/a ratio for different trigonality degrees $\beta = -0.1$, $\beta = -0.15$ and $\beta = -0.2$. The inset shows g_{h1} behavior. (b) Correlation of the Δg_{h1} and g_{h2} values. Symbols represent experimental values for different GaAs dots measured in neutral as well as charged complexes, dashed curve stands for theoretical fit with parameters $c_2 = 10.25$, $\beta = -0.16$, $g_{h1,0} = 5.7$, $c_1 = 7.29$. The corresponding values of L/a are presented at the right axis.

Accurate numerical estimations of effective g-factors require the knowledge of spacing between size-quantized levels of heavy and light hole in z-direction. The value of this spacing can be estimated using the anisotropy of the electron g-factor. It is well known that g-factor of the electron confined in quantum dot is strongly anisotropic [151, 152, 129],

and the value of that anisotropy is directly related to the energy spacing between heavy- and light-hole states. For the experimental values of longitudinal ($g_{e,\parallel}$) and transverse ($g_{e,\perp}$) g-factors the anisotropy degree $\delta g_e = (g_{e,\perp} - g_{e,\parallel})/g_{e,\parallel} \approx 40\%$, and using formula of Reference [129] the $E_{lh,0} - E_{hh,0}$ difference can be estimated as 20/30 meV, which is in a good agreement with the values obtained in our simple model of the confinement in z-direction.

As it has been shown above we can use simple formula for g_{h1} and g_{h2} calculation, which using some dimensionless parameters can be written as follows

$$g_{h1} = -6\varkappa + \Delta g_{h1}, \qquad \Delta g_{h1} = \Delta g_{h1,0} + c_1 \frac{L^2}{a^2},$$
$$g_{h2} = c_2 \beta \frac{L}{a}. \tag{3.5.20}$$

Using these relations we can express the g_{h2} value via the g_{h1} renormalization Δg_{h1} using the following relationship

$$g_{h2} = c_2 \beta \sqrt{\frac{\Delta g_{h1} - g_{h1,0}}{c_1}}. \tag{3.5.21}$$

Equation (3.5.21) is very useful for experimental data analysis, because it does not contain any microscopical parameters, such as dot sizes. Figure 3.12 represents experimental results as well as theoretical fit with parameters introduced in caption. The experimental values of g_{h1} were taken with negative signs. One can see that there is indeed a correlation between g_{h2} and g_{h1} which is in good agreement with theoretical predictions.

For an accurate analysis of optical transitions in X^- trion one should take into account modification of the hole wavefunction due to the Coulomb interaction between the hole and two electrons in a complex. As a rough approximation this interaction can be described by an effective in-plane attractive potential, averaged by the electron position in a complex. We have shown (see Appendix A.2.3 for details) that this attraction leads effectively to the isotropization of the hole in-plane motion and to the effective decrease of β. Hence, generally, Coulomb interaction suppresses g_{h2}, the fact that well agrees with experimental data on X^- trions. (see Figure 3.12)

CHAPTER 4

Charge and Fine Structure tuning in GaAs Droplet dots

While in non-intentionally doped samples due to charge fluctuations the neutral X^0 exciton and the positively (negatively) charged exciton $X^+(X^-)$ are observed in the same spectrum (see Figure 1.6) deterministic charging of quantum dots with single electrons in charge tunable structures enables control of charge in the quantum dots and has led to many fascinating discoveries in quantum dot photonics and spin physics [74]. The results presented in this chapter demonstrate the first electrical charge control in novel, strain-free GaAs quantum dots in AlGaAs barriers grown on n+-(100) substrates by molecular droplet epitaxy, described in previous chapter.

Following non-resonant optical excitation in the AlGaAs barrier, the analysis of the QD PL emission as a function of the applied transverse magnetic field B_x = 0-9T was carried out. The hole g-factor changed its sign according to the orientation of the studied QD with respect to applied transverse magnetic field. The evolution of the dark and bright X^0 transitions in an applied transverse magnetic field revealed a surprising interplay of Zeeman and Coulomb interactions [65]:
i) the fine structure splitting δ_1 of the bright transition is tunable and vanishes for certain QDs at applied transverse magnetic field $\approx$ 3T, which makes this structure attractive for entangled photon pairs experiments [115];
ii) the fine structure splitting of the dark transition δ_2 deduced from the model is of the same order of magnitude as δ_1, up to $\approx 100\mu$eV while the reported δ_2 in InGaAs QDs is two order of magnitude smaller than δ_1, with typical value ≈ 1.4 μeV [153].

4.1 Investigated structure: (100)GaAs/AlGaAs droplet quantum dots embedded in Charge Tunable Structure, H10-014-100

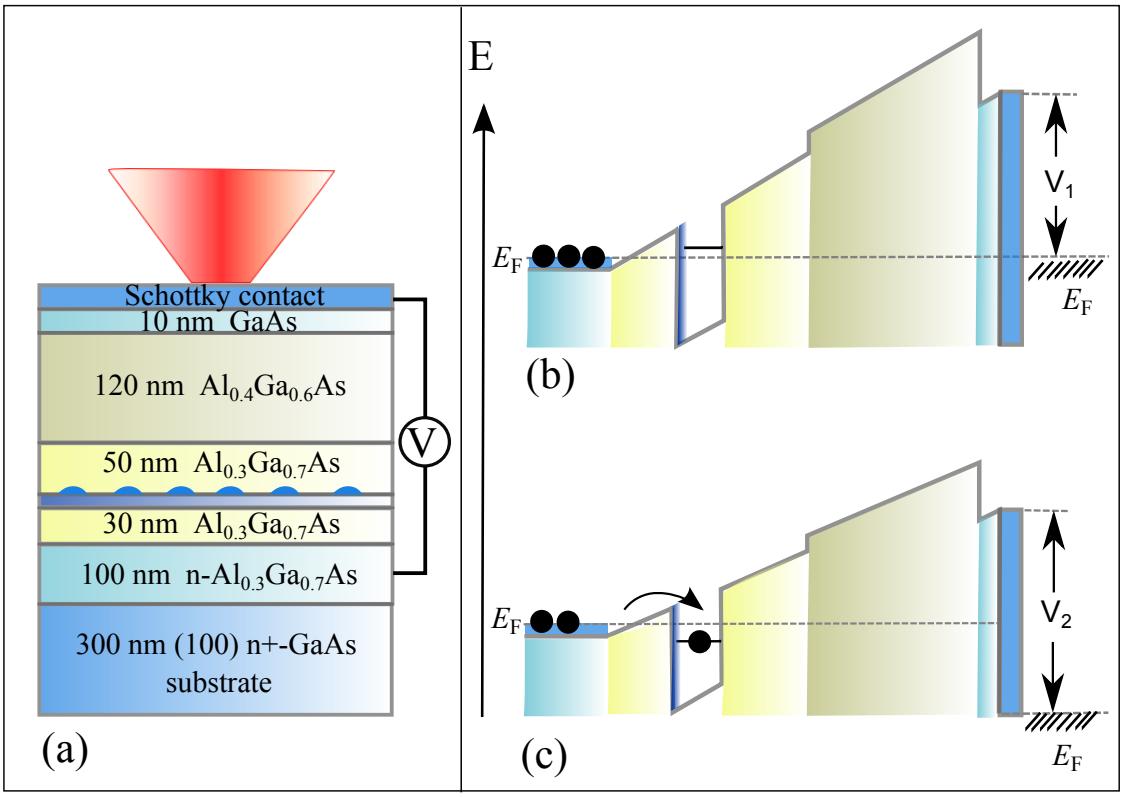

Figure 4.1: (100)GaAs/AlGaAs droplet quantum dots embedded in Charge Tunable Structure: H10-014-100. (a) The schematical drawing of the charge tunable structure. The highly n-doped GaAs substrate followed by n-doped AlGaAs forms an Ohmic back contact and a semitransparent Au/NiCr layer forms the Schottky contact. The excitation and detection is in the growth direction. The energy band potential for different applied biases resulting in an empty QD (b) and a QD filled with one electron (c). The biases are given by: $V_{1(2)}$=-e($V^G_{1(2)}$+V_{Schottky}) with V^G_1=0 and $V^G_1 > 0$.

The sample investigated in this chapter is a charge tunable structure with (100) GaAs/AlGaAs droplet dots [1]. The structure is grown on the highly Si-doped (100) GaAs substrate, see Figure 4.1. The starting 300 nm n^+-GaAs buffer was grown at the growth temperature 580 °C. The doping density is 10^{+18} cm^3. The 100 nm n-$Al_{0.3}Ga_{0.7}As$ layer is grown with a lower doping density $5{\cdot}10^{+18}$ cm^3 followed by 30 nm $Al_{0.3}Ga_{0.7}As$ acting as a tunnel-barrier. Then the formation of 1 nm GaAs wetting layer takes place. The depositing 1.4 monolayers Ga (0.08 ML/s) at 300 °C followed by As-flux ($2.4{\cdot}10^{-4}$ Torr BEP) at 200 °C leads to crystallization of GaAs dots. The structure is then annealed at 425 °C for 10 minutes and capped with 4 nm $Al_{0.3}Ga_{0.7}As$. The annealing was performed

1 The sample structure was grown at the National Institute of Material Science (NIMS, Tsukuba, Japan) in the group of T. Mano, T. Kuroda, and K. Sakoda.

again at a temperature of 640 °C for 5 minutes. The 46 nm $Al_{0.3}Ga_{0.7}As$ and 120 nm $Al_{0.4}Ga_{0.6}As$ barriers are grown at 580 °C followed by 10 nm GaAs.

The charge tunable structure was fabricated by depositing on top on the sample surface a thin semitransparent metallic layer consisting of 4 nm gold and 4.1 nm nickel chromium and another much thicker metallic layer consisting of 120 nm gold and 20 nm titanium for its electrodes, Figure 4.2. The thiner layer is semitransparent allowing excitation and detection of QD-luminescence. The thicker layer is solid enough to enable the bonding the thin wires onto the electrodes. This layer is deposited onto the thin layer leaving holes with ≈ 1 mm radius in order to provide a working area where we can excite the QDs and detect their luminescence.

The contacts were connected by means of ultrasonic welding. The back contact was realized by a indium contact at the bottom of the sample structure.

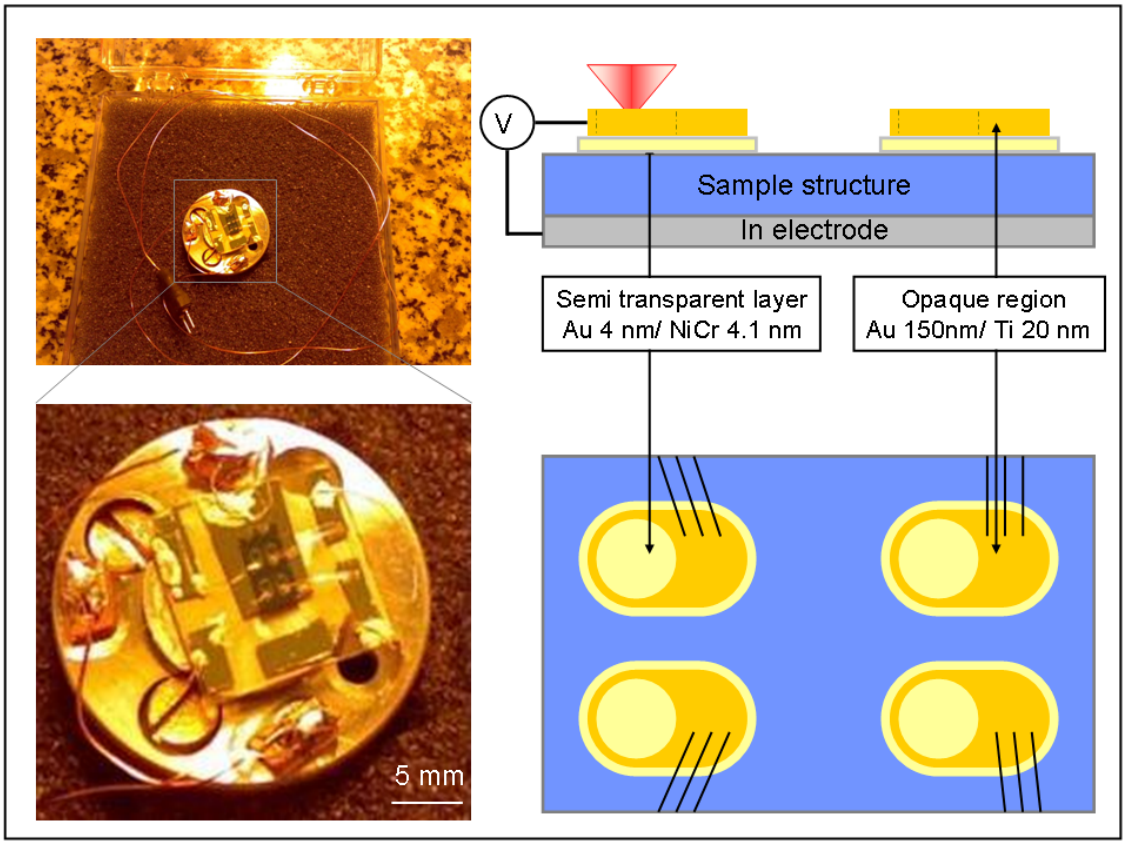

Figure 4.2: The final design of the charge tunable structure adapted to our experimental setup with a microscopic side and top view. The electrodes are connected with thin gold wires. The structure is glued to the 1 x 1 cm sized non-conductive material by means of indium.

4.2 Deterministic control of charge in the droplet quantum dots

The electrical charge tuning in GaAs droplet QDs in AlGaAs barriers, separated from a Fermi sea of electrons by a tunnel barrier, was achieved by applying a bias between the semitransparent Schottky contact and the highly doped back contact. The optical transitions of up to a triply negatively charged exciton X^{3-} were observed for certain dots. All dots show at least the transitions $X^+ \rightarrow X^0 \rightarrow X^-$.

Figure 4.3 shows bias-dependent PL spectra of two different single dots (a) and (c). Under optical non-resonant excitation above a certain bias, typically 1.1 V, the positively charged exciton X^+ appears. Below this bias no emission was detectable. The photo generated carriers tunnel out of the QD before they recombine. A small increase of the bias results in the appearance of the neutral exciton X^0 and both transitions can coexist for certain QDs over a small bias range, see Figure 4.3 (c) and (d). X^+ is here red shifted with respect to X^0, Figure 4.3 (a) and (c). But also QDs with blue shifted X^+ were observed, as mentioned in Chapter 1, and were as well observed.

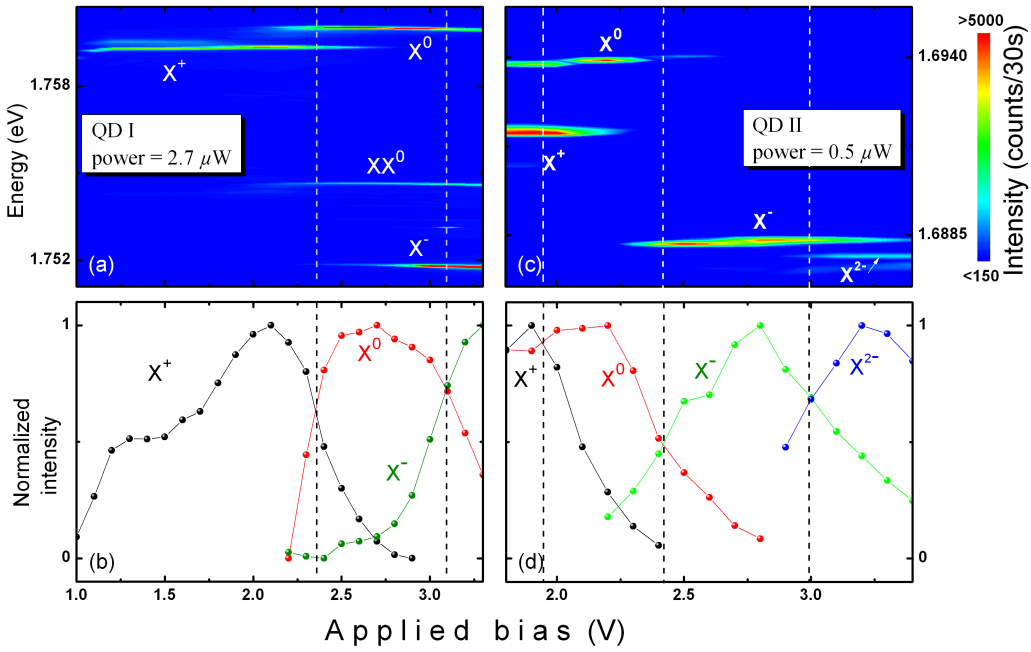

Figure 4.3: Bias-dependent PL intensity map in false color scale (blue <150 counts/30s, red > 5000 counts/30s) of two different QDs. PL contour plot and normalized intensity of a typical QD emitting at high energy (a) and (b), and a QD emitting at lower energy (c) and (d).

Further increasing of the bias leads to charging the QD with an additional electron. The negatively charged exciton X^- is generated and dominates the PL-intensity. The transition line is red shifted with respect to the X^0 by ≈5.6 meV for QDI and ≈8.2 meV for QDII. Depending on the investigated QD an additional electron can be added to the

QD, QDII in Figure 4.3 (c), resulting in generation of doubly negatively charged exciton X^{2-}.

The excitonic transitions could be identified by analyzing the PL polarisation and transition energy in an external transverse magnetic field (Voigt geometry) and the fine structure splitting measurements of exciton and biexciton, Figure 4.4 (a) and (b). According to the selection rules for a trion (X^+ and X^-) in Voigt configuration the quadruplet is observed in the spectrum. If the hole g-factor is zero the two doublets for both linearly polarised detections overlap with each other perfectly. For the QDs with symmetry C_{2v} the hole g-factor does not vanish so the full quadruplet can be measured and used as identification for the trions. In Figure 4.4 (a) the hole g-factor of X^+ is almost equal to the electron g-factor resulting in a vanishing of π^X-polarised doublet whereas the hole g-factor of X^- is significantly smaller than that of the electron resulting in a small splitting of the doublet at higher magnetic field.

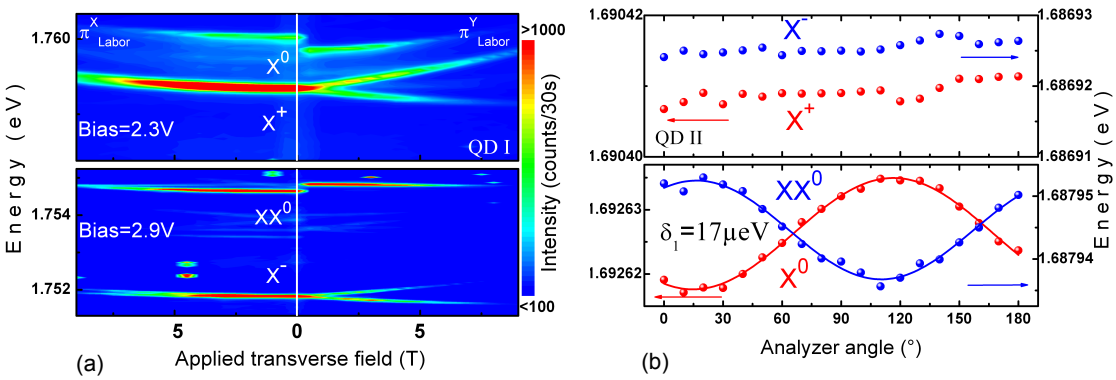

Figure 4.4: Identification of the excitonic states in applied transverse magnetic field (a) and by measuring the fine structure splitting δ_1 (b). The trions X^+ and X^- exhibit four transition for two linear polarised detections. The exciton as well as the biexciton show relatively large δ_1. (b) If the fine structure splitting δ_1 is considerably smaller, like for red shifted QDs, δ_1 evolution of exciton and biexciton is measured whereas the trions do not show any evolution. The scale windows are chosen the same 20 μeV.

In general two types of QD PL spectra were observed: QDs emitting at high and low energy, characterized by their transitions (Figure 4.3 QD I and QD II, respectively). The QDs, which emit usually at $\lambda \approx 700$ nm have very narrow emission lines with Full Width at Half Maximum FWHM ≈ 40 μeV [1] The measured fine structure splitting δ_1 of these QDs lies in range $\approx$ 130-390 μeV. In contrary, the emission lines of red shifted QDs are broader, up to ≈ 200 μeV, but δ_1 is in general much smaller, $\approx$ 15-30 μeV. The red shifted QDs emit at $\lambda \approx 740$ nm. Another difference between two different QD types is their X^- binding energy defined as the energy difference between the trion and exciton emission lines. The X^- binding energy of the red shifted QDs is significantly smaller than the one of the QDs emitting at high energy. While for the red shifted QDs the X^- binding energy

1 The results described below were obtained for the QDs, which emit at high energy that allows, due to the narrow transition line width, a detailed fine structure analysis. These QDs are taken as reference through this chapter.

is ≈5 meV for the QDs emitting at high energy it is ≈8 meV.

While in the QDs emitting at high energy the charged states coexist for certain applied biases the red shifted QDs exhibit sharper transitions from one charge state to another in PL intensity map. Furthermore, the QDs emitting at high energy can be charged only to the negatively charged exciton X^-. In contrary, the transitions of higher charged excitonic states (up to a triply negatively charged exciton X^{3-}, not shown) were observed in the red shifted QDs, see Figure 4.3(c).

All these characteristic differences between two kinds of studied QDs can be explained by their size resulting in varying of confinement. In particular, the QD height seems to be a crucial parameter. In a smaller QD the confinement is better resulting in an energetically higher electron s-state. Hence the spectral transitions of this type are at high energy. On the other hand the better confinement leads to only one possible conduction state. The p-state is not any more quantized. So these QDs can be charged only by two electrons, which occupy the s-state. That is why in the QDs emitting at high energy the doubly and higher negatively charged excitons could not be observed.

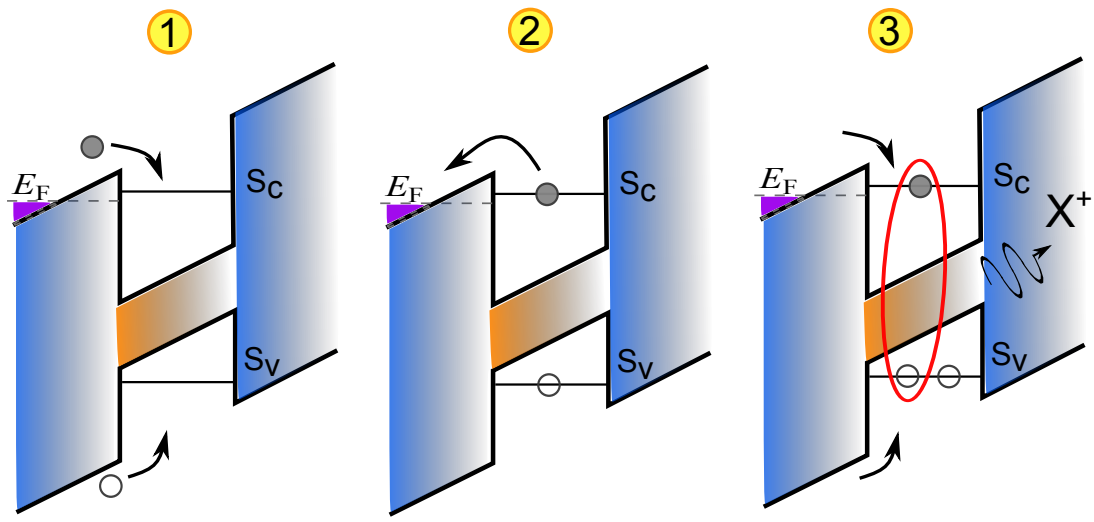

Figure 4.5: Coexisting of excitonic states: X^+ and X^0. Schematical drawing of competition of tunneling out and recombination in a QD resulting in appearance of X^+ and X^0 almost at the same time.

For small bias the positively charged exciton X^+ and neutral exciton X^0 coexist for a certain bias range depending on the dot. The similar coexisting has been observed in [154]. In the Figure 4.5 the schematical explanation is shown. It is based on the competition between tunneling out and the recombination of an exciton in a QD.

In the first step, under non-resonant excitation into the barrier, an optically generated carrier pair is captured in a QD. Due to the low Fermi see the electron tunnels out much more likely than recombine with the hole, step 2 in Figure 4.5. If one introduces τ_t as time before an electron tunnels again out and τ_r as time before an electron-hole pair recombines in step 2 is $\tau_t < \tau_r$. The effective hole mass is nearly one order of magnitude bigger than the electron mass so the hole remains captured in the QD. Since we continually excite the CTS another carrier pair is captured in the QD resulting in the recombination of a

electron-hole pair by emitting X^+, step 3. Indeed, in the step 2 the electron-hole pair can recombine but with lower probability than tunneling process takes place. That results in coexistence of X^+ and X^0. Small increase of the bias results in increasing the tunnel barrier thickness and here $\tau_t > \tau_r$. The tunneling out process becomes less likely. On the other hand the recombination of a captured electron-hole pair becomes more probable and X^0 starts to dominate.

4.3 Neutral exciton fine structure in Voigt configuration and hole-g-factor tuning

The PL-intensity of the excitonic states can be recorded as function of $\lambda/2$-plate position in linear basis. An excitonic polarisation rotated by $\lambda/2$-plate passes analyzer, which is aligned in linear basis and can be analyzed in detail, for more information see Chapter 2.2. Since the linearly polarised eigenstates of an exciton are generally along the crystallographic axes [110] and [1$\bar{1}$0] the QD in-plane orientation can be determined [66, 155]. Figure 4.6 (a) shows schematically the orientation of the applied magnetic field with respect to the sample x,y plane, whose crystallographic axes are well defined. The polar plots as function of analyzer angular position of two different QDs (QD IV and QD V) show that the QDs are orientated orthogonally to each other (QD IV ||[1$\bar{1}$0] Figure 4.6 (b) and QD V ||[110] Figure 4.6 (c)).

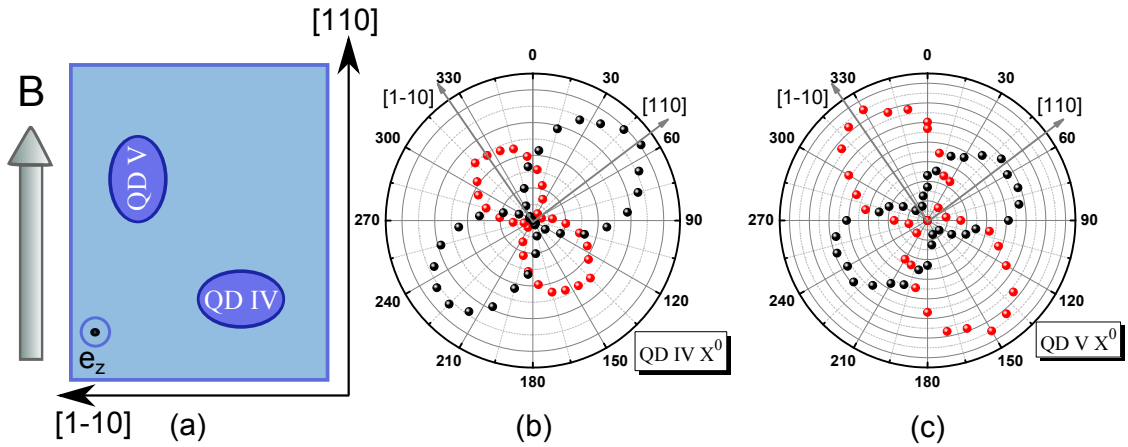

Figure 4.6: The identification of the QD orientation in the structure plane by means of PL contour plot of excitons. (a) The schematical orientation of the applied magnetic field with respect to the crystallographic axes. The detection basis is defined by: [110]$\equiv \pi^X$ and [1$\bar{1}$0]$\equiv \pi^Y$. The dots are oriented in the sample plane according to their polar plots (b) and (c), [66, 155].

It is common to take the crystallographic axis [110] as reference for x-axis with corresponding π^X polarisation and also [1$\bar{1}$0] as reference for y-axis with π^Y polarisation. We will see that these assumptions are coherent with our model approach. It is worth to mention that since these QDs are strain-free, it is possible to identify the QD in-plane orientation by using the exciton fine structure splitting at 0 T. The more intense transition of an exciton detected with polarisation parallel to a certain crystallographic axis yields that the QD is aligned orthogonal to this axis [155].

The study in applied transverse magnetic field revealed interesting magneto-optical properties. The exciton bright spectral positions cross each other at certain magnetic field, Figure 4.7. We will see later more clearly that the same occurs for dark states. The vanishing of the bright X^0 fine structure splitting δ_1 makes this structure potentially attractive for entangled photon pair emission. A similar experimental approach was used in [115], where the exciton splitting of InAs QDs vanished in applied transverse field. Here, this is the first observation of vanishing of the exciton bright splittingin transverse

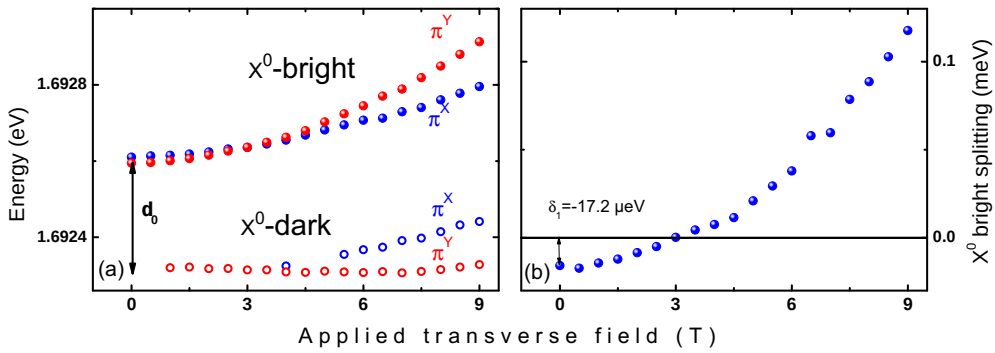

Figure 4.7: Linearly polarised PL spectrum and exciton bright splitting as function of applied transverse magnetic field of QD II. (a) π^X- (blue) and π^Y- (red) polarised PL for a QD II in applied transverse magnetic field .(b) exciton bright splitting as function of transverse magnetic field exhibiting the vanishing of the splitting at 3 T.

magnetic field in GaAs droplet dots. Figure 4.7 (b) shows that the splitting vanishes at a critical magnetic field ≈ 3 T.

4.3.1 Theoretical approach

In order to understand the physical origins behind the observed evolution of the bright and nominally dark X^0 states reported in Figure 4.7, 4.14, 4.15 we present a short theoretical analysis, which allowed us to describe the observed spectra. The fine structure of single dots was studied in Voigt geometry in [65]. We derive the Hamiltonians for our investigated system. For conduction states the Zeeman Hamiltonian is given by:

$$\hat{H}_Z^c = -\mu_\mathrm{B}\left(g_{e,x}^c \hat{S}_x^c B_x + g_{e,y}^c \hat{S}_y^c B_y + g_{e,z}^c \hat{S}_z^c B_z\right), \tag{4.3.1}$$

where $\hat{S}_x^c$ is the conduction electron spin operator and $\mu_\mathrm{B} = \frac{q\hbar}{2m_0}$, with $q = -e$. In C_{2v} geometry the gyromagnetic tensor is diagonal $g_{e,j}^{c(v)} \in \mathrm{Re}$. The g-factors g_e and g_h are transverse g-factors and in order to reduce number of indexes we use only notation $g_{e(h)}$ and keep in mind the meaning of g-factors.
The general form of Zeeman Hamiltonian for valence states is given similarly in valence electron formalism as:

$$\hat{H}_Z^v = |\mu_\mathrm{B}|\left(g_{e,x}^v \hat{S}_x^v B_x + g_{e,y}^v \hat{S}_y^v B_y + g_{e,z}^v \hat{S}_z^v B_z\right). \tag{4.3.2}$$

Here $\hat{S}^v$ is the valence electron pseudo-spin operator.

Since we deal with electron-hole pairs in electron formalism it is useful to write the valence Zeeman Hamiltonian in hole formalism. In order to rewrite the Hamiltonian in the hole formalism we use the Kramers time reversal operator $\hat{K}$ and the hole basis $\mathscr{B}_h = \{|\Uparrow\rangle, |\Downarrow\rangle\}$. First we use this operator to obtain the hole states by using the general equation:

$$\left|\frac{1}{2},m_s\right\rangle^h = \hat{K}\left|\frac{1}{2},m_s\right\rangle^v = (-1)^{1/2-m_s}\left|\frac{1}{2},-m_s\right\rangle^v \tag{4.3.3}$$

We obtain thus:

$$|\Uparrow\rangle = \hat{K}\,|\uparrow\rangle^v = |\downarrow\rangle^v\,; |\Downarrow\rangle = \hat{K}\,|\downarrow\rangle^v = -\,|\uparrow\rangle^v \tag{4.3.4}$$

The Zeeman Hamiltonian is invariant by a global time reversal operation (i.e. including the inversion of the currents producing the external magnetic field). We have:

$$\hat{H}'_Z = \hat{K}\hat{H}_Z\hat{K}^+, \tag{4.3.5}$$

where $\hat{K}$ is the time reversal Kramers operator [156]. For the valence states in C_{2v} geometry we have:

$$\hat{H}^v_Z = \frac{|\mu_\mathrm{B}|}{2}\left(g^v_{e,x}\hat{\sigma}_x + g^v_{e,y}\hat{\sigma}_y + g^v_{e,z}\hat{\sigma}_z\right), \tag{4.3.6}$$

where the Pauli operators are given by $\hat{\sigma}_i = \frac{\hbar}{2}\hat{S}_{v,c}$ and $\hat{S}_{v,c}$ is the pseudo-spin operators for the highest valence states.
So that:

$$\begin{aligned}\hat{H}'^v_Z &= \tfrac{|\mu_\mathrm{B}|}{2}\textstyle\sum_i g_{v,i}\left(\hat{K}\hat{\sigma}_i\hat{K}^{-1}\right)\left(\hat{K}B_i\hat{K}^{-1}\right)\\ &= \tfrac{|\mu_\mathrm{B}|}{2}\textstyle\sum_i g_{v,i}(-\hat{\sigma}_i)(-B_i)\\ &= \tfrac{|\mu_\mathrm{B}|}{2}\textstyle\sum_i g_{v,i}\hat{\sigma}_i B_i = \hat{H}^v_Z,\end{aligned} \tag{4.3.7}$$

with $i = x,y,z$ where wu used $\hat{K}^{-1} = \hat{K}^+$. $\hat{H}'^v_Z$ is also the Zeeman Hamiltonian in hole formalism, hence we have:

$$\hat{H}^h_Z = \frac{|\mu_\mathrm{B}|}{2}\sum_i g_{v,i}\hat{\sigma}^h_i B_i. \tag{4.3.8}$$

It is thus natural to take $g_{v,i} \equiv g_{h,i}$.

Now we turn to matrix representation. Then we have [157].

$$\left[\hat{H}^h_Z\right]_{\mathscr{B}_h} = \left[\hat{H}^e_Z(-\hat{\sigma}_i, -B_i)\right]^*_{\mathscr{B}_v}. \tag{4.3.9}$$

Since in the valence basis $\mathscr{B}_v = \{|\uparrow\rangle^v, |\downarrow\rangle^v\}$ we have

$$\left[\hat{H}^e_Z\right]_{\mathscr{B}_v} = \frac{|\mu_\mathrm{B}|}{2}\sum_i g_{v,i}\sigma_i B_i, \tag{4.3.10}$$

where the Pauli matrices σ_x, σ_y, and σ_z are given by:

$$\sigma_x = \begin{pmatrix} 0 & 1 \\ 1 & 0 \end{pmatrix}, \sigma_y = \begin{pmatrix} 0 & -i \\ i & 0 \end{pmatrix}, \sigma_z = \begin{pmatrix} 1 & 0 \\ 0 & -1 \end{pmatrix}, \tag{4.3.11}$$

then in hole formalism we have:

$$\begin{aligned}\left[\hat{H}^h_Z\right]_{\mathscr{B}_h} &= \tfrac{|\mu_\mathrm{B}|}{2}\textstyle\sum_i g_{v,i}\sigma^*_i B_i\\ &= \tfrac{|\mu_\mathrm{B}|}{2}\textstyle\sum_i g_{h,i}\sigma^*_i B_i\\ &= \tfrac{|\mu_\mathrm{B}|}{2}(g_{h,x}\sigma_x B_x - g_{h,y}\sigma_y B_y + g_{h,z}\sigma_z B_z).\end{aligned} \tag{4.3.12}$$

If we do not reverse the external currents producing the magnetic field we obtain finally:

$$\hat{\mathscr{H}}_Z^h \equiv \left[\hat{H}_Z^h(-\mathbf{B})\right]_{\mathscr{B}_h} = -\frac{|\mu_B|\,\hbar}{2}\left(g_{h,x}\sigma_x B_x - g_{h,y}\sigma_y B_y + g_{h,z}\sigma_z B_z\right). \tag{4.3.13}$$

The whole Hamiltonian is set to $\hat{\mathscr{H}}_{Total} = \hat{\mathscr{H}}_Z^c + \hat{\mathscr{H}}_Z^h + \hat{\mathscr{H}}_{\text{exch}} + \hat{\mathscr{H}}_{\text{Dia}}$, with the well established Coulomb electron hole exchange Hamiltonian [65] using the basis $\{|\Uparrow\downarrow\rangle, |\Downarrow\uparrow\rangle, |\Uparrow\uparrow\rangle$ and $|\Downarrow\downarrow\rangle\}$:

$$\hat{\mathscr{H}}_{\text{exch}} = \frac{1}{2}\begin{array}{c} \begin{array}{cccc} |\Uparrow\downarrow\rangle & |\Downarrow\uparrow\rangle & |\Uparrow\uparrow\rangle & |\Downarrow\downarrow\rangle \end{array} \\ \begin{pmatrix} \delta_0 & \delta_1 & 0 & 0 \\ \delta_1 & \delta_0 & 0 & 0 \\ 0 & 0 & -\delta_0 & \delta_2 \\ 0 & 0 & \delta_2 & -\delta_0 \end{pmatrix} \end{array} \begin{array}{c} \\ |\Uparrow\downarrow\rangle \\ |\Downarrow\uparrow\rangle \\ |\Uparrow\uparrow\rangle \\ |\Downarrow\downarrow\rangle \end{array}. \tag{4.3.14}$$

The diamagnetic Hamiltonian $\hat{\mathscr{H}}_{\text{Dia}}$ represents the diamagnetic effect, which represents the spin independent contribution to the shifts. For investigated QDs it can be taken as:

$$\mathscr{H}_{\text{Dia}} = \gamma_{\text{Dia}} B^2 \mathbb{1}. \tag{4.3.15}$$

We can write the Hamiltonian for the two transverse magnetic field B_x and B_y and they are given by:

$$\mathscr{H}_x = \frac{\mu_{\text{B}} B_x}{2}\begin{pmatrix} \delta_0 & \delta_1 & g_{e,x} & g_{h,x} \\ \delta_1 & \delta_0 & g_{h,x} & g_{e,x} \\ g_{e,x} & g_{h,x} & -\delta_0 & \delta_2 \\ g_{h,x} & g_{e,x} & \delta_2 & -\delta_0 \end{pmatrix}, \tag{4.3.16}$$

and

$$\mathscr{H}_y = i\frac{\mu_{\text{B}} B_y}{2}\begin{pmatrix} \delta_0 & \delta_1 & g_{e,y} & -g_{h,y} \\ \delta_1 & \delta_0 & g_{h,y} & -g_{e,y} \\ -g_{e,y} & -g_{h,y} & -\delta_0 & \delta_2 \\ g_{h,y} & g_{e,y} & \delta_2 & -\delta_0 \end{pmatrix}. \tag{4.3.17}$$

We introduce an entire analytical way to diagonalize these matrices i.e. to find the eigenenergies and eigenvectors. We turn to the basis $\{|X\rangle, |iY\rangle, \left|X^2 - Y^2\right\rangle, |2iXY\rangle\}$, with:

$$\begin{array}{cc} |X\rangle = \frac{|-1\rangle - |+1\rangle}{\sqrt{2}} & |iY\rangle = \frac{-|-1\rangle - |+1\rangle}{\sqrt{2}} \\ \left|X^2 - Y^2\right\rangle = \frac{|+2\rangle + |-2\rangle}{\sqrt{2}} & |2iXY\rangle = \frac{|+2\rangle - |-2\rangle}{\sqrt{2}} \end{array} \tag{4.3.18}$$

The bright states transform like p-orbitals and the dark states like d-orbitals in the transformations letting the QD invariant. For this reason we transform Hamiltonians 4.3.16 and 4.3.17 into $\mathscr{H}_x'$ and $\mathscr{H}_y'$ by using the following operator:

$$P = \begin{array}{c} \begin{array}{cccc} |X\rangle & |iY\rangle & \left|X^2 - Y^2\right\rangle & |2iXY\rangle \end{array} \\ \begin{pmatrix} -\frac{1}{\sqrt{2}} & -\frac{1}{\sqrt{2}} & 0 & 0 \\ \frac{1}{\sqrt{2}} & -\frac{1}{\sqrt{2}} & 0 & 0 \\ 0 & 0 & \frac{1}{\sqrt{2}} & \frac{1}{\sqrt{2}} \\ 0 & 0 & \frac{1}{\sqrt{2}} & -\frac{1}{\sqrt{2}} \end{pmatrix} \end{array} \begin{array}{c} \\ |\Uparrow\downarrow\rangle \\ |\Downarrow\uparrow\rangle \\ |\Uparrow\uparrow\rangle \\ |\Downarrow\downarrow\rangle \end{array} \tag{4.3.19}$$

The Hamiltonian $\mathscr{H}_x'$ is given by $\mathscr{H}_x' = P^{-1}\mathscr{H}_x' P$, with $P^{-1} = P^t$ which is:

$$P^{-1} = \begin{pmatrix} -\frac{1}{\sqrt{2}} & \frac{1}{\sqrt{2}} & 0 & 0 \\ -\frac{1}{\sqrt{2}} & -\frac{1}{\sqrt{2}} & 0 & 0 \\ 0 & 0 & \frac{1}{\sqrt{2}} & \frac{1}{\sqrt{2}} \\ 0 & 0 & \frac{1}{\sqrt{2}} & -\frac{1}{\sqrt{2}}. \end{pmatrix} \tag{4.3.20}$$

It can be easily shown that the identity $P \cdot P^{-1} = \mathbb{1}$ is fulfilled. Now we obtain the Hamiltonian $\mathscr{H}_x'$, which is given by:

$$\mathscr{H}_x' = \frac{\mu_\mathrm{B} B_x}{2} \begin{array}{c} \begin{array}{cccc} |X\rangle & |2iXY\rangle & |iY\rangle & \left|X^2 - Y^2\right\rangle \end{array} \\ \left(\begin{array}{cc|cc} \frac{\delta_0-\delta_1}{2} & \frac{g_{e,x}+g_{h,x}}{2} & 0 & 0 \\ \frac{g_{e,x}+g_{h,x}}{2} & \frac{-\delta_0-\delta_2}{2} & 0 & 0 \\ \hline 0 & 0 & \frac{\delta_0+\delta_1}{2} & \frac{g_{e,x}-g_{h,x}}{2} \\ 0 & 0 & \frac{g_{e,x}-g_{h,x}}{2} & \frac{-\delta_0+\delta_2}{2} \end{array}\right) \end{array} \begin{array}{c} |X\rangle \\ |2iXY\rangle \\ |iY\rangle \\ \left|X^2 - Y^2\right\rangle \end{array} \tag{4.3.21}$$

and similarly for $\mathscr{H}_y'$:

$$\mathscr{H}_y' = \frac{\mu_\mathrm{B} B_y}{2} \begin{array}{c} \begin{array}{cccc} |X\rangle & \left|X^2 - Y^2\right\rangle & |iY\rangle & |2iXY\rangle \end{array} \\ \left(\begin{array}{cc|cc} \frac{\delta_0-\delta_1}{2} & i\frac{g_{e,y}-g_{h,y}}{2} & 0 & 0 \\ -i\frac{g_{e,y}-g_{h,y}}{2} & \frac{-\delta_0+\delta_2}{2} & 0 & 0 \\ \hline 0 & 0 & \frac{\delta_0+\delta_1}{2} & i\frac{g_{e,y}+g_{h,y}}{2} \\ 0 & 0 & i\frac{g_{e,y}+g_{h,y}}{2} & \frac{-\delta_0-\delta_2}{2} \end{array}\right) \end{array} \begin{array}{c} |X\rangle \\ \left|X^2 - Y^2\right\rangle \\ |iY\rangle \\ |2iXY\rangle \end{array} \tag{4.3.22}$$

The Hamiltonians consist of two diagonal blocks. Since every block is a 2×2 matrix it can be easily diagonalized. The eigenenergies of $\mathscr{H}_x'$ are $E_+^{(1)}$ and $E_+^{(2)}$ for bright states ($|X\rangle'$ and $|iY\rangle'$) and $E_-^{(1)}$ and $E_-^{(2)}$ for dark states ($|2iXY\rangle'$ and $\left|X^2 - Y^2\right\rangle'$) with 1,2 standing for matrix block. These eigenenergies are given by:

$$E_\pm^{(1)} = \frac{1}{4}\left(-\delta_1 - \delta_2 \pm \sqrt{(2\delta_0 - \delta_1 + \delta_2)^2 + 4(g_{e,x} + g_{h,x})^2 \mu_\mathrm{B}^2 B_x^2}\right), \tag{4.3.23a}$$

$$E_\pm^{(2)} = \frac{1}{4}\left(\delta_1 + \delta_2 \pm \sqrt{(2\delta_0 + \delta_1 - \delta_2)^2 + 4(g_{e,x} - g_{h,x})^2 \mu_\mathrm{B}^2 B_x^2}\right). \tag{4.3.23b}$$

Similarly we obtain the eigenenergies of $\mathscr{H}_y'$. The eigenenergies are $E_+^{(1)}$, $E_+^{(2)}$ for bright states ($|X\rangle'$ and $|iY\rangle'$) and $E_-^{(1)}$, $E_-^{(2)}$ for dark states ($\left|X^2 - Y^2\right\rangle'$ and $|2iXY\rangle'$). These eigenenergies are given by:

$$E_\pm^{(1)} = \frac{1}{4}\left(\delta_1 - \delta_2 \pm \sqrt{(2\delta_0 + \delta_1 + \delta_2)^2 + 4(g_{e,y} + g_{h,y})^2 \mu_\mathrm{B}^2 B_y^2}\right), \tag{4.3.24a}$$

$$E_\pm^{(2)} = \frac{1}{4}\left(-\delta_1 + \delta_2 \pm \sqrt{(2\delta_0 - \delta_1 - \delta_2)^2 + 4(g_{e,y} - g_{h,y})^2 \mu_\mathrm{B}^2 B_y^2}\right). \tag{4.3.24b}$$

In absence of applied magnetic field only bright exciton eigenstates are optically allowed

and are given by $|X\rangle$ and $|Y\rangle$. The optically inactive dark states at $B_{ext} = 0$ T are given by $|2iXY\rangle$ and $\left|X^2 - Y^2\right\rangle$.
However, in presence of applied transverse magnetic field the eigenstates consist of a mixture of bright and dark states. Due to this mixing, the dark states become optically active. New eigenstates in transverse magnetic field are $|X\rangle'$, $|Y\rangle'$ for bright states and $|2iXY\rangle'$, $\left|X^2 - Y^2\right\rangle'$ for dark states. Since the bright state component determines the polarisation of dark state in presence of transverse magnetic field the blocks of both Hamiltonians are π^X and π^Y polarised. In the case $B_{ext}||e_x$ the state $|X\rangle'$ is a mixture of $|X\rangle$ and $|2iXY\rangle$ whereas for $B_{ext}||e_y$ it as a mixture of $|X\rangle$ and $\left|X^2 - Y^2\right\rangle$ and the same for the eigenstate $|iY\rangle$. This difference is a consequence of rotating magnetic field by $\pi/2$, which is equivalent to the rotating crystal. In this case only $|X\rangle$, and $|Y\rangle$ change their basis according to the transformations $x \to y$, $y \to -x$. The dark states $|2iXY\rangle$ and $\left|X^2 - Y^2\right\rangle$ change only their phase since they transform as $x^2 - y^2 \to -(x^2 - y^2)$ and $2ixy \to -2xy$.

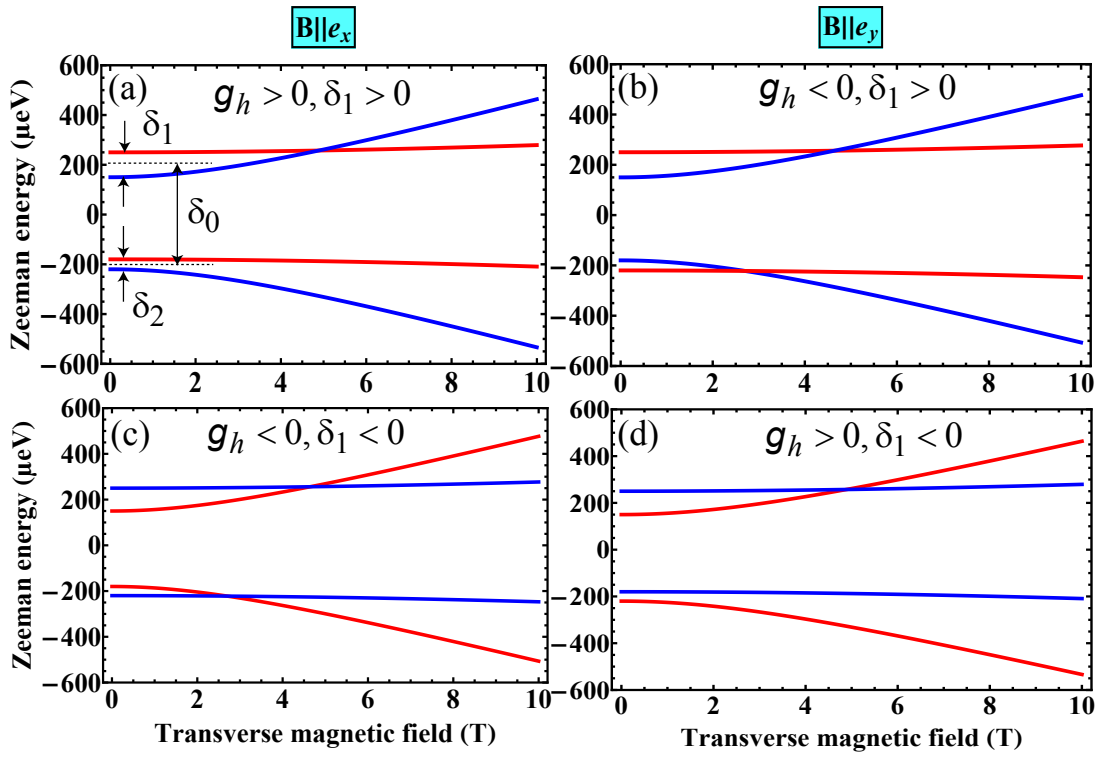

Figure 4.8: Exciton fine structure in Voigt geometry for $\boldsymbol{B}||e_x$ (a), (c) and $\boldsymbol{B}||e_y$ (b), (d). Red and blue lines are π^Y and π^X linearly polarised respectively, according to the eigenvectors obtained from the Hamiltonians. For both magnetic field orientations the eigenenergies are obtained by using the same arbitrary coefficient set and only the sign of hole g-factor g_h and fine structure splitting δ_1 were varied as labeled in figures. Here we assumed $g_e > 0$.

Figure 4.8 shows that, regardless the polarisations, the transition energies obtained from equations for $\boldsymbol{B}||e_x$ and $\boldsymbol{B}||e_y$ are equal provided that both hole g-factor and δ_1 change their sign, see Figure 4.8. Taking into account the polarisation order of excitonic

transitions and comparing with experimental data we noticed that only the equations for the case $\boldsymbol{B}||e_x$ can describe our observations considering the sign of the fine structure splitting δ_1, hole g-factor g_h, and polarisations of the detected emission lines. When both g_e and g_h change their signs no difference occurs because the sum and difference of g_e and g_h a quadratic function is in Equations 4.3.23 and 4.3.24. From here we consider only the case $\boldsymbol{B}||e_x$.

Now we can write the eigenstates of the first block in transverse magnetic field $|X\rangle'$ and $|2iXY\rangle'$. They are given by:

$$|X\rangle' = \frac{\left(E_+^{(1)} + \frac{\delta_0+\delta_2}{2}\right)|X\rangle + \frac{g_{e,x}+g_{h,x}}{2}|2iXY\rangle}{\sqrt{\left(E_+^{(1)} + \frac{\delta_0+\delta_2}{2}\right)^2 + \left(\frac{g_{e,x}+g_{h,x}}{2}\right)^2}}, \tag{4.3.25}$$

and

$$|2iXY\rangle' = \frac{-\frac{g_{e,x}+g_{h,x}}{2}|X\rangle + \left(E_+^{(1)} + \frac{\delta_0+\delta_2}{2}\right)|2iXY\rangle}{\sqrt{\left(E_+^{(1)} + \frac{\delta_0+\delta_2}{2}\right)^2 + \left(\frac{g_{e,x}+g_{h,x}}{2}\right)^2}}. \tag{4.3.26}$$

The eigenstates 4.3.25 and 4.3.26 are orthogonal and π^X polarised. The same way we obtain the eigenenergies of the second block of Hamiltonian 4.3.21.

They are given by:

$$|iY\rangle' = \frac{\left(E_+^{(2)} + \frac{\delta_0-\delta_2}{2}\right)|iY\rangle + \frac{g_{e,x}-g_{h,x}}{2}\left|X^2 - Y^2\right\rangle}{\sqrt{\left(E_+^{(2)} + \frac{\delta_0-\delta_2}{2}\right)^2 + \left(\frac{g_{e,x}-g_{h,x}}{2}\right)^2}}, \tag{4.3.27}$$

and

$$\left|X^2 - Y^2\right\rangle' = \frac{-\frac{g_{e,x}+g_{h,x}}{2}|iY\rangle + \left(E_+^2 + \frac{\delta_0-\delta_2}{2}\right)\left|X^2 - Y^2\right\rangle}{\sqrt{\left(E_+^2 + \frac{\delta_0-\delta_2}{2}\right)^2 + \left(\frac{g_{e,x}-g_{h,x}}{2}\right)^2}}. \tag{4.3.28}$$

These eigenstates are π^Y polarised.

Now we can introduce the relative oscillator strengths $\alpha_{x,y}^2$ and $\beta_{x,y}^2$ (shown in Figure 4.9). They are given by:

$$\alpha_x^2 = \frac{\left(E_+^1 + \frac{\delta_0+\delta_2}{2}\right)^2}{\left(E_+^1 + \frac{\delta_0+\delta_2}{2}\right)^2 + \left(\frac{g_{e,x}+g_{h,x}}{2}\right)^2} \text{ and } \beta_x^2 = 1 - \alpha_x^2, \tag{4.3.29}$$

and

$$\alpha_y^2 = \frac{\left(E_+^2 + \frac{\delta_0-\delta_2}{2}\right)^2}{\left(E_+^2 + \frac{\delta_0-\delta_2}{2}\right)^2 + \left(\frac{g_{e,x}-g_{h,x}}{2}\right)^2} \text{ and } \beta_y^2 = 1 - \alpha_y^2. \tag{4.3.30}$$

These oscillator strengths determine the coupling of bright and dark states in applied transverse magnetic field.

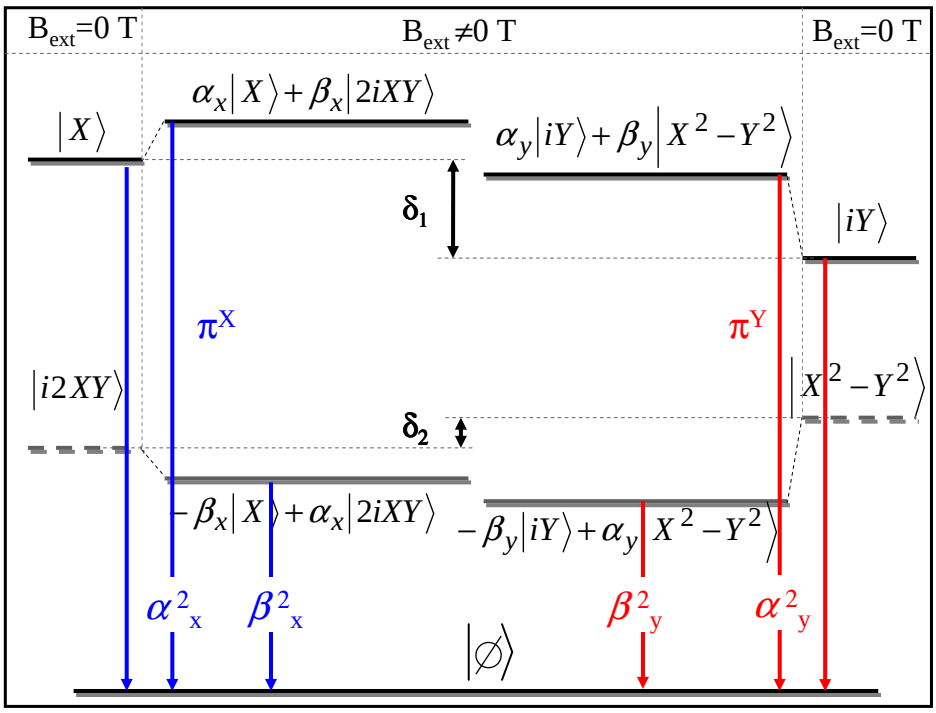

Figure 4.9: Optical recombination of an exciton X^0 in absence and in presence of transverse magnetic field $B_{\text{ext}}||e_x$. The recombination transitions are π^X (blue) and π^Y (red) polarised. The relative oscillator strengths $\alpha^2_{x,y}$ (bright states) and $\beta^2_{x,y}$ (dark states) are given according to the π^X (blue) and π^X (red) polarisations. At $B_{ext} = 0$ the dark states are inactive and are represented by dashed lines thus only two transitions are observed. However, in applied transverse field, due to the bright-dark mixing, the dark states become optically active whose intensities are determined by $\alpha_{x,y}$ and $\beta_{x,y}$. The recombination was adapted to the studied QD IV, see the next subsection.

Now the eigenstates 4.3.25, 4.3.26, 4.3.27, and 4.3.28 are written:

$$|X\rangle' = \alpha_x |X\rangle + \beta_x |2iXY\rangle \text{ and } |2iXY\rangle' = -\beta_x |X\rangle + \alpha_x |2iXY\rangle\,, \tag{4.3.31a}$$

$$|iY\rangle' = \alpha_y |iY\rangle + \beta_y \left|X^2 - Y^2\right\rangle \text{ and } \left|X^2 - Y^2\right\rangle' = -\beta_y |X\rangle + \alpha_y |2iXY\rangle \tag{4.3.31b}$$

Having determined eigenstates and relative oscillator strengths we can present recombination scheme according to the optical selection rules. In Figure 4.9 the excitonic recombination is shown for the case $B_{\text{ext}}||e_x$.
Since we know exactly the relative oscillator strengths $\alpha^2_{x,y}$ and $\beta^2_{x,y}$ (Equations 4.3.29 and 4.3.30, respectively) we can study now the oscillator strengths for both polarisations as function of magnetic field. As we can see electron and hole g-factors determine the bright-dark mixing and also oscillator strengths. Now we can discuss the cases where we consider different extremal hole and electron g-factor ratios $\frac{g_h}{g_e}$.
In Figure 4.10 the oscillator strengths for both π^X and π^y polarisations are given for the

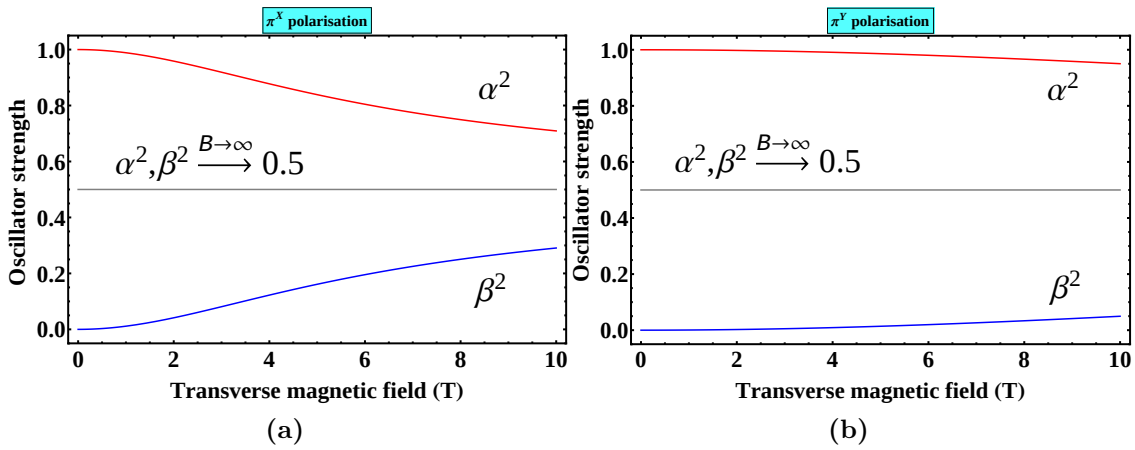

Figure 4.10: Oscillator strengths as function of transverse magnetic field of bright α^2 (red line) and dark states β^2 (blue line) for π^X (a) and π^X (b) polarisations. The gray line represents the oscillator strengths in case of infinite magnetic field. The coefficient set was chosen as for an investigated QD: $\delta_0 = 500\mu$eV, $\delta_1 = 300\mu$eV, $\delta_2 = 100\mu$eV, g_e=1, and g_h=0.5. Note the compensation between g_e and g_h for π_Y polarisation leading to small shift of the bright and dark excitons.

case when hole and electron g-factor ratio is 1/2. In this case the oscillator strength of the dark state for π^X polarisation (a) as function of applied transverse field increases rapidly with magnetic field whereas for the bright state loses its intensity. For π^Y polarisation the bright state oscillator strength is significantly stronger as function of magnetic field than for π^X polarisation and subsequently, the dark state oscillator strength much weaker. We see that in the case $B \to \infty$ the bright and dark state intensities become equal, shown in Figure 4.10 by solid gray line. In Figure 4.11 we see the oscillator strengths for both polarisatios with hole g-factor whose value is 90 % of electron g-factor value (dashed lines) and with the previous ratio 1/2 (solid lines). In this case, for ratio 9/10, the oscillator strength of the dark state for π^X polarisation becomes stronger than for the previous case whereas for π^Y polarisation it becomes very weak so that even at B= 10 T it is very close to zero. Since in this case for π^Y polarisation the intensity of the dark state transition is very weak so this intensity can be too weak to be detected and only one dark state is observed. As we will see, this effect was observed in the QDs where the measured electron and hole g-factors are nearly equal.

Now we discuss the case where hole g-factor is very small, e.g. $\frac{g_h}{g_e} = \frac{1}{10}$, shown in Figure 4.12. In contrary to the case $\frac{g_h}{g_e} = \frac{9}{10}$, the oscillator strength of the bright (dashed red) and dark state (dashed blue) for π^Y polarisation becomes very strong and close to the oscillator strengths for π^Y polarisation (solid dark red) and (solid dark blue). In the case when hole g-factor vanishes, i.e. $g_h = 0$, both π^X and π^Y intensities are equal, shown in Figure 4.12 by dashed gray lines.

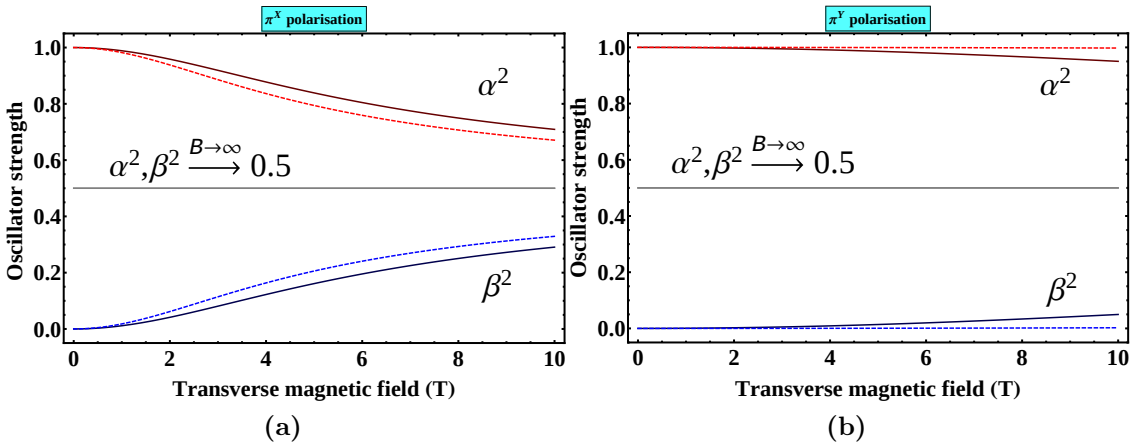

Figure 4.11: Oscillator strengths of bright and dark states for π^X (a) and π^X (b) polarisations as comparison for different hole and electron g-factor ratio. The solid brown and dark blue lines are obtained with the hole and electron g-factor ratio $\frac{g_h}{g_e} = \frac{1}{2}$ as in previous Figure. The dashed red and blue lines are oscillator strengths α^2 and β^2 with the ratio $\frac{g_h}{g_e} = \frac{9}{10}$.

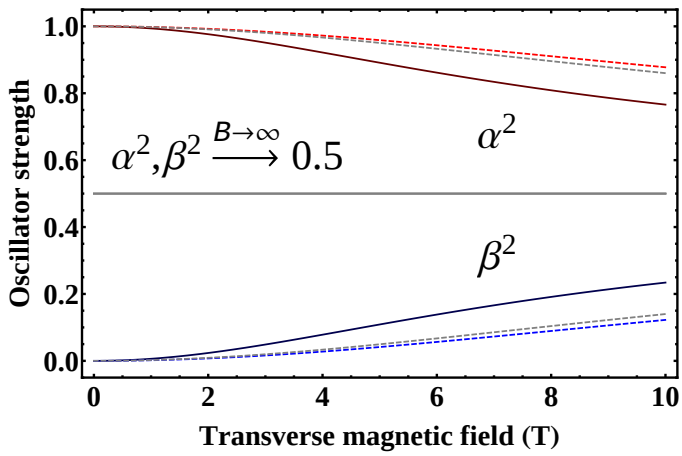

Figure 4.12: Oscillator strengths for the very low ratio $\frac{g_h}{g_e} = \frac{1}{10}$ with the extreme case $g_h = 0$ (dashed gray lines). Solid brown and dark blue lines for π^X and dashed red and blue lines for π^Y polarisation. In the case $g_h = 0$ the intensities of both polarisations are equal.

4.3.2 Experimental observations

Before we start with interpretation of experimental observations we briefly introduce the fit procedure used in our study. The spectral position of excitonic bright and dark transitions is given by: $E=E_0+E_Z+E_{Dia}$. E_Z and E_{Dia} are Zeeman and diamagnetic shifts respectively. The diamagnetic contribution can be experimentally obtained by taking the average of the four spectral transitions at each magnetic field value. We can study the Zeeman splitting fine structure if we subtract the diamagnetic part from the measured spectral position. In order to use all experimental data the diamagnetic shift was extrapolated back to zero

field.

In order to fit all four transitions at the same time the step function fit procedure can be used. This step function enables fitting all transitions with the same coefficient set. The step function is defined as: $f(x) = \frac{1}{2}\left(\frac{x}{|x|} + 1\right)$. The full fit function is then built to: $g(x) = \sum_{i=1}^{4}\{f(x - x_i) - f(x - x_{i+1})\}y_i(x - x_i)$, where $y_i(x)$ is a law fit function and i stands for every step to fit, see Figure 4.13.

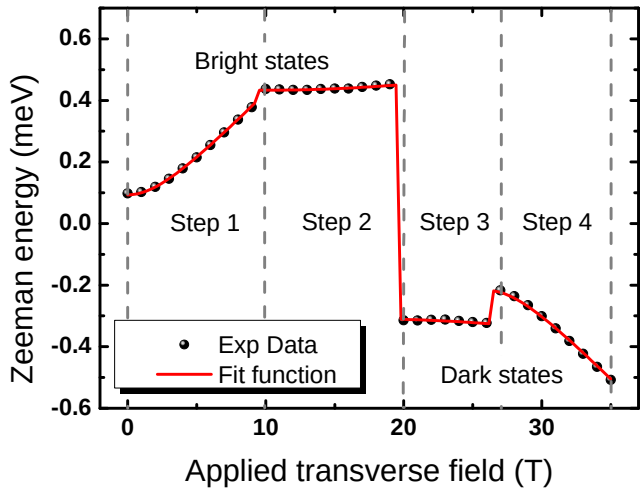

Figure 4.13: The step function fit procedure of an exciton fine structure. Exciton Zeeman shift after subtraction of the diamagnetic part is fitted with fine structure model using the step function fit procedure. All four transitions are fitted simultaneously with the same parameter set.

Considering the fine structure splitting sign we classify the investigated dots with positive and negative sign, which is coherent with QD orientation with respect to the crystallographic axes. These characteristics are given in the Table 4.1.

As mentioned above, in our experiments magnetic field is applied parallel to [110] crystallographic axis and it was not changed with respect to our detection basis. So, using the polar plot measurements we found the proper polarisations of our detection basis. Now, knowing the polarisations of detected emission lines and their corresponding eigenenergies (Equations 4.3.23) the transition energies can be fitted with this model.

In Figure 4.14 three QDs are shown fitted with theoretical approach including the extracted coefficients. It is important to note that we fit all four transitions simultaneously with the same parameters. The main common feature of experimental observations shown in Figure 4.14 is that the absolute value of the bright exciton splitting of all investigated QDs independently from their orientation decreases as function of applied magnetic field. Since QD II has very small fine structure splitting δ_1 we can observe for this QD the zero crossing of the bright splitting at relatively moderate magnetic field ($B_{\text{ext}} = 3$ T). This property is quite useful for polarisation entangled two photon sources and has been used in [115]. The most investigated QDs possessed much bigger fine structure splitting, see Table A.3.2 in Appendix. Nevertheless, we observed that δ_1 vanishes at 10 T for QD IV

and at 9T for QD V due to the relatively high electron g-factors.

Table 4.1: Characteristics of the investigated dots concerning their in-plane orientation with respect to the crystallographic axes and their product of g-factors.

	QD aligned $\|\|[110]$	QD aligned $\|\|[1\bar{1}0]$
	$\delta_1>0$	$\delta_1<0$
$g_e \cdot g_h>0$	QD V, QD VI, QD VIII, QD IX, QD X, QD XI, QD XII, QD XIII, QD XIV, QD XV, QD XVI	—
$g_e \cdot g_h<0$	—	QD I, QD II, QD IV, QD VII

Another interesting observation is shown in Figure 4.14. At 0 T we noticed the fine structure splitting δ_1 of QD II and QD IV is negative whereas for QD V it is positive. If only δ_1 changes its sign for QD V and not the electron and hole g-factor (with respect to QD IV), according to the eigenenergies obtained in the former subsection the energetically highest transition at 0 T of QD V would increase with magnetic field faster than the other bright state. This is definitely not the case. The spectral transition of the highest line shifts more slowly than the one of the other bright state. The only way to explain this effect to change the sign of the electron and hole g-factor product $g_e \cdot g_h$. Since the eigenenergies include the square of the sum and difference of g-factors they are not affected if both electron and hole g-factors change their sign. In contrary, if only either electron or hole g-factor changes its sign it explains this observation. So the g-factor product for QD V is given by $g_e \cdot g_h > 0$.

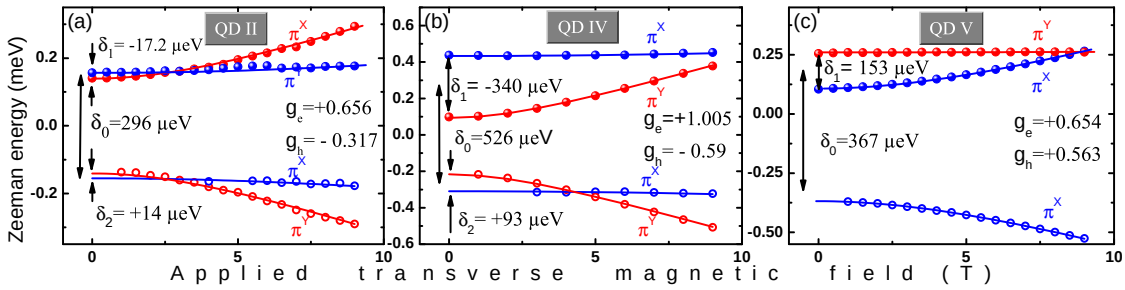

Figure 4.14: Two different types of QDs measured in the same detection basis exhibiting different fine structure splitting sign according to our definition and hole g-factor sign. The solid (red and blue) circles are the exciton bright states ($J = \pm 1$). The hollow (red and blue) circles are the exciton dark states ($J = \pm 2$). The QD II and IV are $\|[1\bar{1}0]\|\mathbf{B}$ and QD $\|[110]\perp\mathbf{B}$. While the fine structure splitting of bright states of the QD II (a) and QD IV (b) is negative in the QD V (c) it is positive. The hole g-factor changes its sign resulting in the reverse excitonic transition order. The g-factor product of QD IV is negative whereas for QD V it is positive.

We notice that the measured electron g-factor, up to $+1$, is very big and is in contradiction with the assumption that the g-factor increases monotonously from the bulk value of the dot compound to the one of the barrier (see e.g. [129]). According to this assumption the electron g-factor g_e is a monotonous function increasing from $g_e(\mathrm{GaAs}) = -0.44$ (in bulk) to $g_e(\mathrm{Al_{0.3}Ga_{0.7}As}) = 0.55$, when confinement increases, due to the increasing of penetration of the electron wave function of the embedded GaAs structure into surrounding

AlGaAs barrier.
However, we measured significantly bigger electron g-factor, which clearly exceeds the electron g-factor of AlGaAs $g_e(\mathrm{Al_{0.3}Ga_{0.7}As}) = 0.55$. The possible explanation for our observation may take its origin in very strong carrier localization. The general form for the electron g-factor is given by:

$$g_e = g_0 - \Delta_g^{(2)}, \tag{4.3.32}$$

where $g_0 = 2.0023$ is the electron g-factor in vacuum [158] and $\Delta_g^{(2)} > 0$ is a correction in terms of second order perturbation involving valence states and higher conduction bands. The strength of the correction term depends directly on the Spin-Orbit gap Δ_{SO} and band gap E_g. The bigger E_g and smaller Δ_{SO} the smaller is the correction term $\Delta_g^{(2)}$. The measured electron g-factors of different semiconductors with different band structure parameters proved this and some of them are listed in Table 4.2: If the carriers are strongly

Table 4.2: Band structure parameters for some different semiconductor including electron g-factor. The band structure parameters were taken from [159] whereas the values for electron g-factor from [160], [161], and [162].

Semiconductor	E_g (eV)[159]	$\Delta_{\mathrm{SO}}(eV)$ [159]	g_e
GaN	3.299	0.017	+1.95 [160]
$\mathrm{Al_{0.3}Ga_{0.7}As}$	1.936	0.323	+0.55 [161]
GaAs	1.519	0.341	-0.44[161]
InAs	0.417	0.39	-15 [162]
InSb	0.235	0.81	-50 [162]

localized the correction term $\Delta_g^{(2)}$ is very small and under certain conditions vanishes. Recent experiments showed that in the very localized electronic states like electronic paramagnetic centers in GaAsN [160] the electron g-factor $g_e \approx 2$, so that the correction term here vanishes $\Delta_g^{(2)} \approx 0$.
In our studied system the carriers are less localized, but still strong enough and the correction term might be of order $\Delta_g^{(2)} \approx 0.8$ - 1 and therefore can explain our observation of high electron g-factor.

The Equations 4.3.23 fit the observed results very well enabling extracting hole g-factor sign. The extracted hole g-factor sign and the sign of fine structure splitting δ_1 are negative for QDs II and IV and positive for QD V. Also the corresponding polarisation order is held as shown in Figure 4.8 (a) and (c).

The values for δ_2 extracted from the fit are surprisingly large compared to bulk values or in InAs/GaAs QDs where $\delta_2 \approx 2\mu$eV [153]. Here values up to 100 μeV were found.
This fact is not explained up to now. One possibility would be that, due to the strong anisotropy and strong confinement, the electron-hole exchange coupling term between $|2\rangle$ and $|-2\rangle$ would be strongly enhanced. When heavy holes and light holes are mixed (due to the QD shape anisotropy) the dark exciton states are mixed with bright states leading to the appearance of a long range contribution in the (e-h) exchange coupling between $|2\rangle$ and $|-2\rangle$ states.

The question is arising whether the QD orientation with respect to the crystallographic

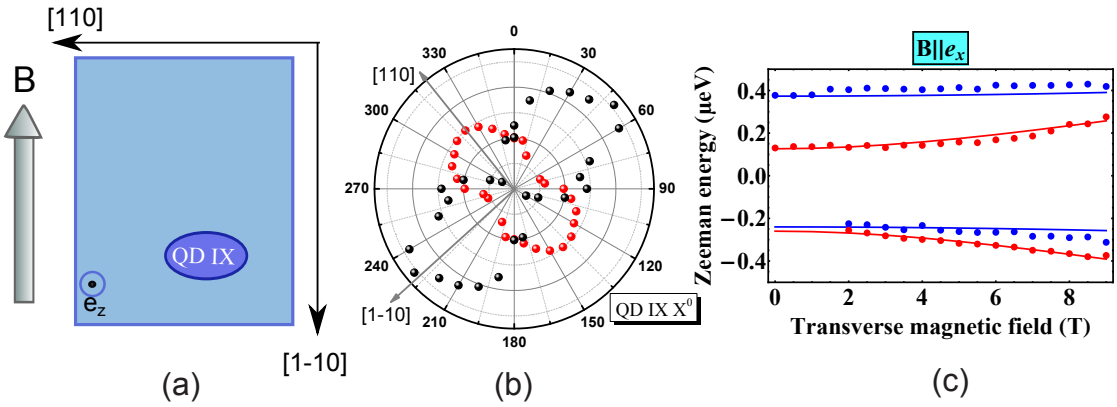

Figure 4.15: In-plane orientation of the QD IX and magnetic field after the sample was rotated but keeping the magnetic field still parallel to π^X polarisation of our detection basis (a) and fine structure of the QD IX (c) (compare with Figure 4.6). Polar diagram reveals the QD orientation |||[110] (b). For theoretical fit electron and hole g-factors of trion X^+ were taken, $g_e = 0.67$ and $g_h = -0.3$. $\delta_1 = -250$ μeV was obtained at 0 T. Other coefficients $\delta_0 = 500$ μeV and $\delta_2 = -20$ μeV were adapted to the best data matching.

axis or to the applied magnetic field is crucial for detemining the hole g-factor sign. To study this detail we rotated the sample and found a QD prolongated |||[110] and since we rotated the sample it is orthogonal to magnetic field orientation, QD $\perp$ **B**. The excitonic fine structure of this QD is shown in Figure 4.15. This QD was found outside the electrodes. Hence we do not control the charge here. As consequence, due to spectral diffusion the spectral positions are less well defined as we integrate over several configurations. To fit these data qualitatively we use electron and hole g-factor extracted from trions, fine structure splitting extracted by using polar plot at 0 T, and we vary δ_0 and δ_2.
When comparing QD IX with QD V (see Figure 4.6 (a)), we notice that despite the same QD orientation || [110] the hole g-factor sign for QD IX is obtained by our theoretical approach to be negative in contrary to the QD V. The difference between these two dots is the QD orientation with respect to the applied magnetic field. This result proves that the QD orientation with respect to the magnetic field is essential to determine the hole g-factor sign. A QD aligned with its longer side parallel or orthogonal to an applied magnetic field changes its hole g-factor sign. Consequently, we predict that for a perfect round QD the hole g-factor vanishes because of high in-plane symmetry. This underlines that the most important factor to determine the transverse hole g-factor is the confinement potential as it was previously in [111] QDs.

Now we study the measured intensities of neutral exciton X^0 by means of our approach developed in the previous section. The relative oscillator strengths of measured bright and dark transitions for both linear polarisations are given experimentally by:

$$\alpha_x^2 = \frac{I^b_{\pi^X}}{I^b_{\pi^X} + I^d_{\pi^X}} \text{ and } \beta_x^2 = \frac{I^d_{\pi^X}}{I^b_{\pi^X} + I^d_{\pi^X}}, \tag{4.3.33}$$

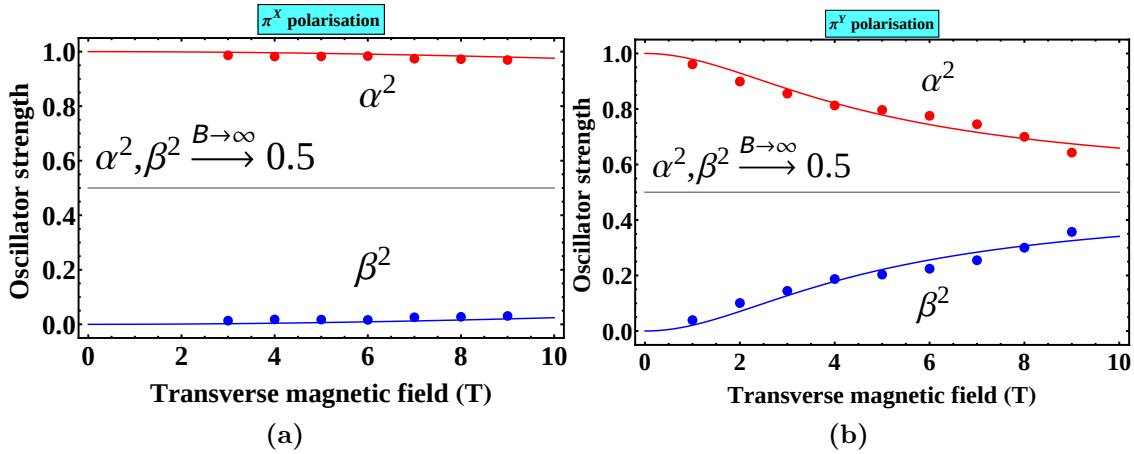

Figure 4.16: QD IV: Oscillator strengths as function of transverse magnetic field of bright α^2 (red line) and dark states β^2 (blue line) for π^X (a) and π^Y (b) polarisations. The gray line represents the oscillator strengths in case of infinite magnetic field where the bright-dark mixing becomes maximal and oscillator strengths of both states become equal. The coefficient set for the investigated QD IV used in theoretical fit is: $\delta_0 = 526\mu$eV, $\delta_1 = -326\mu$eV, $\delta_2 = 93\mu$eV, g_e=1.005, and g_h=0.59.

and

$$\alpha_y^2 = \frac{I^b_{\pi^Y}}{I^b_{\pi^Y} + I^d_{\pi^Y}} \text{ and } \beta_y^2 = \frac{I^d_{\pi^Y}}{I^b_{\pi^Y} + I^d_{\pi^Y}}, \tag{4.3.34}$$

where $I^{b,d}_{\pi^{X,Y}}$ are π^X and π^Y polarised intensities of bright and dark states, respectively. Using the parameter set in theoretical approach extracted from the fitting the excitonic transitions for the QD IV we notice that the measured intensities are very well fitted. Here we could see that if we change the electron or hole g-factor sign as well as the sign of δ_1 or δ_2 the theoretical approach does not fit the experimental data. This supports that our developed approach enables us to study in detail very precisely as well the excitonic fine structure energies as the excitonic transition intensities.
As mentioned before, in the case when $g_h \approx g_e$ the dark state for one polarisation is to weak to be detected resulting in only one observed dark state transition. This was observed for several investigated dots, e.g. QD V shown in Figure 4.14 (c). For this dot the measured electron and hole g-factors are $g_e = 0.65$, $g_h = 0.56$. Here we observed only three transitions: two bright state transitions and one dark state transition π^X polarised. The quality of the fit shows, in addition, that our model explains the observed transfer of oscillator strength from bright to dark states when the transverse magnetic field increases.

4.3.3 Discussions

The fact that the detected intensities reflect directly the oscillator strength of the exciton quadruplet may appear surprising. To explain our good agreement between the experimental data and theoretical approach we introduce here an assumption.

The emission intensity I_i of a given excitonic state X^0 is given by:

$$I_i \propto \frac{N_i}{\tau_i} \propto N_i f_i, \tag{4.3.35}$$

where N_i is the number of excitons of the i-state, τ_i is life time of i-state, f_i is the oscillator strength, and $i = 1,2,3,4$ indexes of two bright and two dark states.
The rate equation is given by:

$$\frac{dN_i}{dt} = -\frac{N_i}{\tau_i} - \frac{N_i}{\tau} + g = -N\left(\frac{\tau + \tau_i}{\tau_i \tau}\right) + g, \tag{4.3.36}$$

where τ corresponds to non radiative processes, g is generation rate with assumption that under non resonant excitation generation of all i-states is equal $g_i = g_j$.
Since we excite with high power (we observe simultaneously charged excitons and biexciton) it is reasonable to assume that non radiative processes τ mainly corresponds to the recapture of second electron-hole pair or individual carriers by the QD leading to the creation of biexciton or charged excitons, respectively. According to this assumption and taking τ identical for all i-states by simplicity, we obtain by solving 4.3.36:

$$N_i = \frac{g\tau}{\tau + \tau_i}. \tag{4.3.37}$$

Now we consider two cases.
(a) the case if $\tau << \tau_i$ (low excitation power): $N_i \cong g$. In this case no information for oscillator strength can be deduced from observed intensities.
(b) the case if $\tau >> \tau_i$ (high excitation power): $N_i \cong \frac{g\tau}{\tau_i}$. Since $I_i \propto \frac{N_i}{\tau_i}$ we obtain:

$$I_i \propto \frac{1}{\tau_i} \propto f_i \propto \alpha_i^2 |\langle S|p_x|X\rangle|^2, \tag{4.3.38}$$

where α_i^2 is relative oscillator strength, $|\langle S|p_x|X\rangle|^2 = |\langle S|p_y|Y\rangle|^2$ are the Kane matrix element. The good agreement between the observed intensities and $\alpha_i^2(B)$ supports this interpretation.

Since the observed Zeeman shifts at high magnetic field are of comparable order of magnitude with electron-hole exchange δ_0 one may expect that a second order perturbation theory should give more accurate determination of electron and hole g-factor.
One can show that in this case δ_0, δ_1, and δ_2 at 0 T can be replaced by magnetic field dependent parameters $\tilde{\delta}_i(B)$:

$$\tilde{\delta_0}(B)_{x,y} = \delta_0(+\left(\left(g_e^{x/y}\right)^2 + \left(g_h^{x/y}\right)^2\right)\mu_B^2 \frac{B^2}{2\delta_0} \tag{4.3.39a}$$

$$\tilde{\delta_1}(B)_{x,y} = \delta_1 \pm g_e^{x/y} g_h^{x/y} \mu_B^2 \frac{B^2}{\delta_0} \tag{4.3.39b}$$

$$\tilde{\delta_2}(B)_{x,y} = \delta_1 \pm g_e^{x/y} g_h^{x/y} \mu_B^2 \frac{B^2}{\delta_0}. \tag{4.3.39c}$$

Figure 4.17 shows theoretical plots of first and second order of perturbation theory

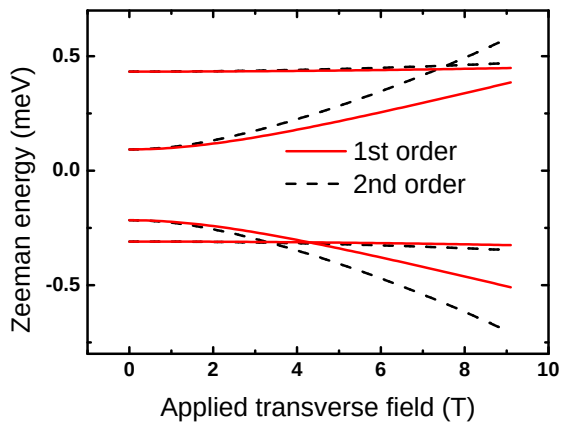

Figure 4.17: Comparison of first and second order of perturbation of the exciton fine structure using the same coefficient set. The case $\boldsymbol{B}||e_y$ is chosen.

using for second order of perturbation the above introduced modifications. Using the same coefficient set for both first and second order we see significant discrepancy in Zeeman energy at higher magnetic field. It means that electron and hole g-factors extracted by means of the second order of perturbation may be lower compared to the ones extracted by using the first order.

Now we can apply the second order of perturbation in order to fit the experimental data. Both the first and second order of perturbation can fit very well the experimental data. Using the second order of perturbation for the QD II one extracts g-factors 33 % lower with respect to the first order of perturbation, both electron and hole g-factor. For the QD IV the second order of perturbation modify the electron g-factor by 30 % and hole g-factor by 21 %. The modified electron g-factor of QD II is lower than the electron g-factor of AlGaAs barrier g_e^{AlGaAs}=0.55. However, the modified electron g-factor of QD IV is still much higher than the g-factor of AlGaAs barrier. It is worth to mention that the second order perturbation model does not change other parameters, especially dark state splitting δ_2.

Another striking fact is that the g-factors extracted for trions X^+ and X^- are very close to the g-factors of excitons extracted by using the first order of perturbation theory, see Table A.2 in Appendix. Finally, we shall keep the values obtained by fitting the exciton spectral positions with first order perturbation theory because they are consistent with the g-factors extracted from trions X^+ and X^-.

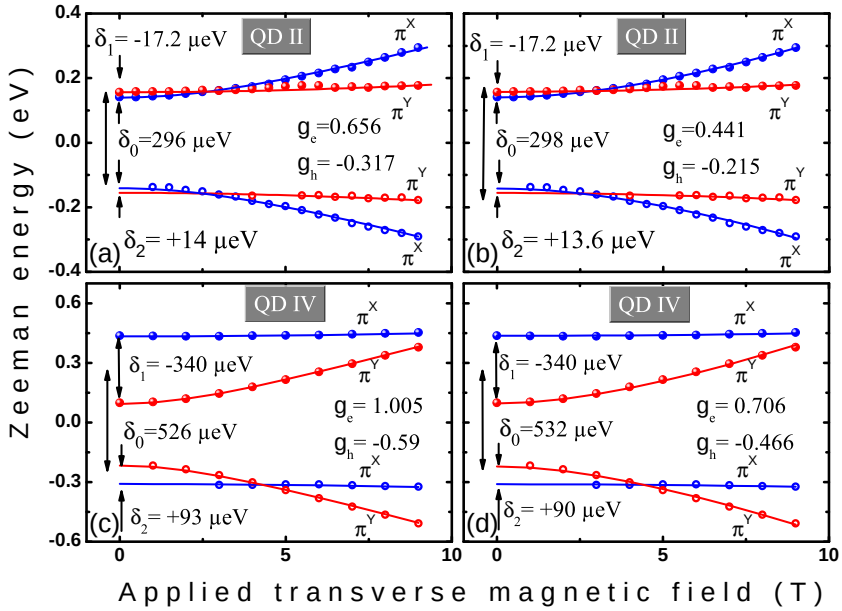

Figure 4.18: Two different QDs QD II ((a) and (b)) and QD IV ((c) and (d)) fitted with the first and second order of perturbation theory resulting in different g-factors. In (a) and (c) the fit equations 4.3.23 obtained using the first order of perturbation theory whereas in (b) and (d) the second order of perturbation was used.

4.4 Charged excitons in transverse magnetic fields: Voigt configuration

The magneto-optical study of trions X^+ and X^- in Voigt configuration helps to identify the charged excitons, as mentioned above. Furthermore, it enables to extract very precisely transverse or in-plane electron and hole g-factors $g_e^\perp$ and $g_h^\perp$. As reminder, we use only notation $g_{e/h}$ and keep in mind the true meaning of g-factors and as notation for applied transverse field we use instead $B_\perp$ only B.

According to the optical selection rules of trions in Voigt configuration four transitions for two linearly polarised detections are allowed. Figure 4.19 (a) shows schematically the allowed optical transition of X^+. The outer and inner doublets are π^Y and π^X polarised, respectively. As it can be easily derived from recombination scheme the Zeeman splitting of the inner doublet is given by $(g_e - g_h)\mu_\mathrm{B}B$ and of the outer by $(g_e + g_h)\mu_\mathrm{B}$, Figure 4.19 (b). In general, from trions it is only possible to extract the absolute values $||g_e| - |g_h||$ for inner and $(|g_e| + |g_h|)$ for outer doublet and not the sign unless using additional information. Since our study of fine structure system in previous subsection could determine electron and hole g-factor sign we use here electron and hole g-factors with their right signs.
So the Zeeman splitting is a linear function and the slopes obtained from linear fits of outer and inner doublet and divided by Bohr magneton μ_B are the sum or difference of electron and hole g-factors. Since we have two unknown coefficients and two equations we

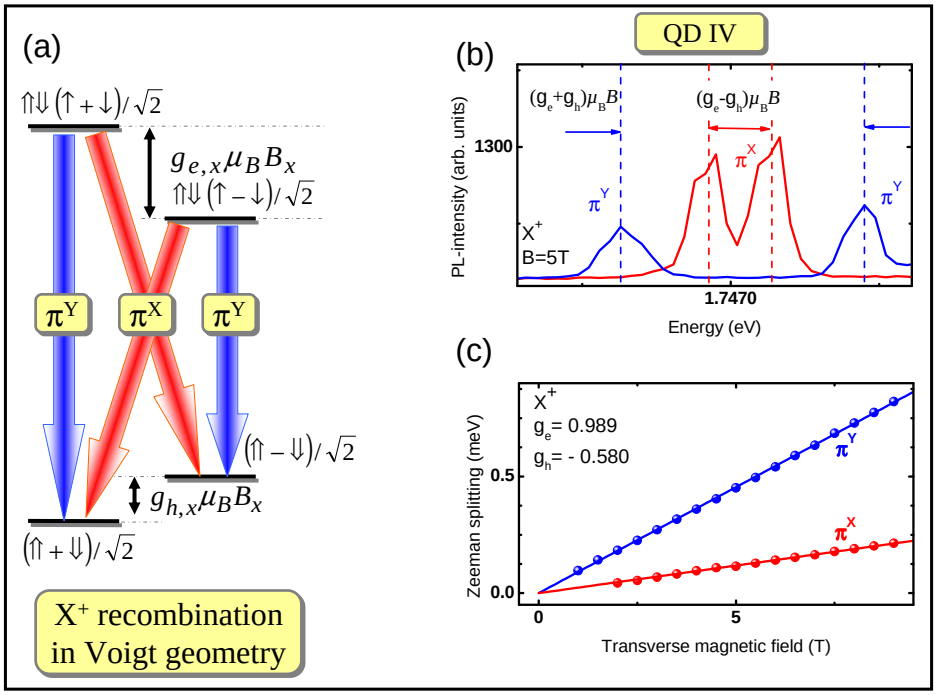

Figure 4.19: QD IV: X^+ optical selection rules in Voigt geometry and transverse electron and hole g-factors extraction. (a) A schematical draw of a typical X^+ recombination according to the optical selection rules in Voigt geometry. (b) The four transitions of X^+ at applied transverse magnetic field 5 T with corresponding Zeeman splittings for outer and inner doublet, which are π^Y and π^X polarised, respectively. (c) The accurate g-factors extraction from the Zeeman splitting for both polarisations.

are able to extract g-factors very precisely, Figure 4.19 (c).

The study of trions in applied transverse magnetic field confirmed the change in sign of the hole g-factor g_h, as described in detail for X^0 in the previous subsection. Depending on the quantum dot in-plane orientation with respect to applied magnetic field the measured hole g-factor was found to be positive or negative. Figure 4.20 shows two different QDs QD V (a) and QD IV (b). The two QDs were measured in the same detection basis and under same conditions, i.e. the magnetic field is applied in the same direction. Considering the positively charged trion X^+, one can see that for QD V the inner doublet is detected in π^Y and the outer doublet in π^X polarisation, Figure 4.20 (a). In contrast to the QD V, the QD IV exhibits the opposite behavior for inner and outer doublets. Now, the smaller splitting (inner doublet) is detected in π^X and the bigger splitting (outer doublet) in π^Y polarisation, Figure 4.20 (b).

This behavior can be qualitatively explained by analyzing the recombination scheme of X^+. Figure 4.20 (c) and (d) shows the recombinations for QD V and QD IV, respectively. According to the optical selection rules for the positively charged exciton X^+ in Voigt geometry the recombination scheme enables to extract inner and outer doublet. Taking

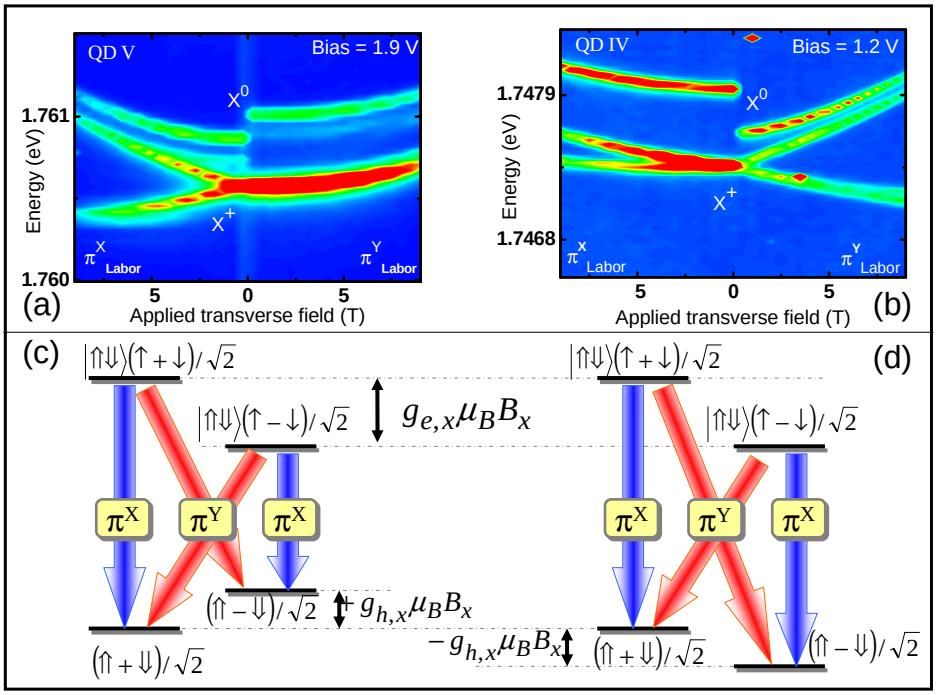

Figure 4.20: Hole g-factor sign changing resulting in modification of optical selection rules in Voigt geometry. (a) and (b) PL intensity map in false color scale (blue <100 counts/30s, red > 1500 counts/30s) of QD V and QD IV exhibiting inner and outer doublets detected with different polarisation. (c) and (d) Optical selection rules of each investigated QD taking into account that hole g-factor changed its sign.

into account that electron and hole g-factor are positive the inner doublet is π^Y and the outer doublet π^X polarised. If now the hole g-factor changes its sign the energy levels of the final state change their order due to the negative hole g-factor. The change of hole g-factor sign results in the reverse spectral order of recombinations. In the new dot IV the inner doublet is π^X and the outer one is π^Y polarised.

4.5 In-plane g-factor anisotropy in single quantum dots

The effective g-factor is isotropic in bulk semiconductors with symmetry T_d. In QWs with lower symmetry it becomes anisotropic and have been studied in detail in past [163, 164, 165] for electron g-factor and for hole g-factor [166]. However, until now no g-factor anisotropy in single dots has been reported to the best of our knowledge.

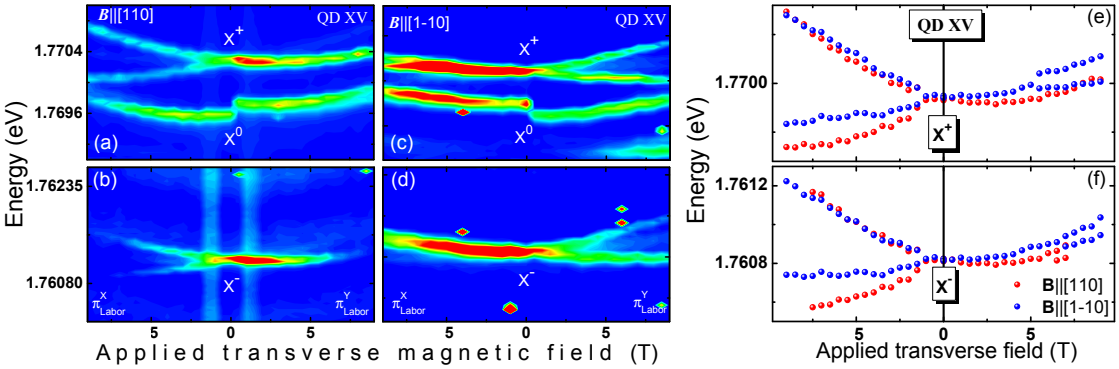

Figure 4.21: Spectra of the QD XV for applied magnetic field ||[110] ((a),(b)) and ||[1$\bar{1}$0] ((c),(d)) showing the in-plane anisotropy of g-factors. In (e) and (f) the mirrored spectral positions for both magnetic field orientations of X^+ and X^- are plotted to clarify the different Zeeman splittings.

We succeeded in electron and hole g-factor anisotropy measurements in single QDs. We found QDs outside the electrode with clear markings on the sample surface enabling us to find the same dots again for experiments in two different magnetic field orientations. Since the surface is very rough there exist a great number of impurities on the surface, which can be clearly seen by our visualization system. They were used as spatial references. Once a QD with good characteristics has been found near good references we studied the magneto-optical properties of this QD in Voigt geometry. Then we rotated the sample by 90° in the x,y plane and found again the QD of interest by using the impurities on the sample surface as spatial references and spectra at 0 T including the fine structure splitting as spectral references.

The change in the hole g-factor sign was discussed earlier, here we focus on the absolute values of g_e and g_h. In Figure 4.21 (e) and (f) we clearly see that the Zeeman splitting of X^+ and X^- is different when comparing different magnetic field orientations. For applied field ||[110] the Zeeman splitting of the outer doublet for both X^+ and X^- is bigger than for the field orientation ||[1$\bar{1}$0]. For the field orientation ||[110] the X^+ splitting of inner doublet is too small to resolve it with our spectral resolution whereas in case of applied field ||[1$\bar{1}$0] we can resolve significantly bigger splitting of the inner doublet. Since the Zeeman splitting directly depends on the g-factors the different Zeeman splittings for two different applied field orientations is a direct proof of the in-plane g-factor anisotropy.

The extracted electron and hole g-factors of negatively charged trion X^- are listed in Table 4.3. Both the electron and hole g-factor are anisotropic. We extracted the g-factors very precisely with very small fit error bars given in Table 4.3. Since we could not resolve the small splitting of X^+ for B ||[110] (Figure 4.21 (a) and (e)) only the g-factors of X^-

are given in Table 4.3. The electron g-factor exhibits strong anisotropy for both QDs whereas the hole g-factor g_h exhibits strong anisotropy only for QD XVI.

Table 4.3: Anisotropic electron and hole g-factors according to the applied field orientation ||[110] and ||[1$\bar{1}$0].

		B ||[110]	B ||[1$\bar{1}$0]
QD XV: X^-	g_e	0.738 ± 0.002	0.543 ± 0.001
	g_h	0.588 ± 0.002	-0.375 ± 0.001
QD XVI: X^-	g_e	0.95 ± 0.003	0.603 ± 0.002
	g_h	0.57 ± 0.003	-0.518 ± 0.002

4.6 Conclusions and discussions

The first electrical control of charge in single QDs grown by Droplet Epitaxy was achieved. The deterministic control of the charge enables studying interesting physical effects in strain free droplet dots. We developed an entire analytical way to solve the eigensystem, which enables us to study the excitonic fine structure in applied transverse magnetic field. By means of the developed method we could study in depth both excitonic spectral positions and their intensities.

The magneto-optical properties of the QDs, which are aligned along the principal crystallographic axes [110] and [1$\bar{1}$0] revealed following interesting physical effects:
i. in fixed detection basis and applied magnetic field the fine structure splitting δ_1 and hole g-factor g_h change their sign when comparing two QDs aligned || [110] and [1$\bar{1}$0] respectively.
ii. The in-depth study proved that the orientation of a QD with respect to the applied magnetic field is essential for changing of the hole g-factor sign and not with respect to the crystallographic axis. The hole g-factor sign of the QDs with their elongated shape parallel to the magnetic field is opposite to the hole g-factor sign of the QDs whose elongated shape is orthogonal to the magnetic field.
iii. For a given bright-dark exchange splitting δ_0 the bright-dark mixing in applied transverse field for a given linear polarisation is determined by electron and hole g-factor ratio $\frac{g_h}{g_e}$. The bigger the ratio the smaller the coupling for one polarisation and the bigger for another polarisation. This effect results in the appearance of dark state only for one polarisation when electron and hole g-factor are close to each other. The excitonic intensities are also consistent with the observations when the hole g-factor changed its sign.

The observation of high electron g-factor and our possible explanation in Chapter 4.3.2 by means of a weak correction term for very strongly localized carriers can be a motivation for further study of electron g-factor whose origin might lie in coupling to higher band elements in framework of $\mathbf{k} \cdot \mathbf{p}$ - theory.

Another remarkable result presented in this chapter concerns the in-plane g-factor anisotropy in Voigt geometry. The anisotropy was observed for both electron and hole g-factors g_e and g_h. We found that the most important factor to determine the transverse hole g-factor and its sign is orientation of the dot with respect to the crystallographic axis being of minor importance. This observation can be an attractive perspective for further in-depth study of electron and hole g-factor anisotropy in droplet dots.

CHAPTER 5

Low field electron-nuclear spin coupling in GaAs QDs under optical pumping conditions

In GaAs 100% of the lattice nuclei have spin 3/2. In bulk GaAs each nucleus is interacting with the surrounding nuclei via the nuclear dipole-dipole interaction. The strength of this interaction represents an effective local magnetic field $B_L \approx 0.15$ mT [6]. In bulk samples the application of an external magnetic field $B_{ext} > B_L$ is necessary to screen the nuclear dipole-dipole interaction to allow build-up of Dynamic Nuclear Polarisation (DNP) due to optical electron spin pumping via the Overhauser effect. One of the outstanding features of quantum dots is the possibility to achieve DNP in zero external magnetic fields [27, 28, 167, 168, 169].

In this chapter the observation of the DNP at zero magnetic field in strain free QDs is reported. A maximal Overhauser shift of 16 μeV corresponding to 12 % of nuclear spin polarisation was observed. In absence of nuclear quadrupolar effects the origin of the screening of the nuclear depolarisation is the Knight field experienced by nuclei. This effective magnetic field experienced by the nuclei in the presence of a spin oriented electron was tuned in both amplitude and direction.

The structures investigated in this chapter are (111)A GaAs/AlGaAs QDs described in Chapter 3. The experiments were performed in Faraday and Voigt geometries under circularly polarised excitation.

5.1 Dynamic Nuclear Polarisation at $B_{ext} = 0$ T

Here we provide first experimental evidence for DNP in strain free dots at zero applied field, where nuclear quadrupole effects are orders of magnitude weaker than in strained dots. Figure 5.1 shows circular polarisation of excitonic states (a) and excitonic spin

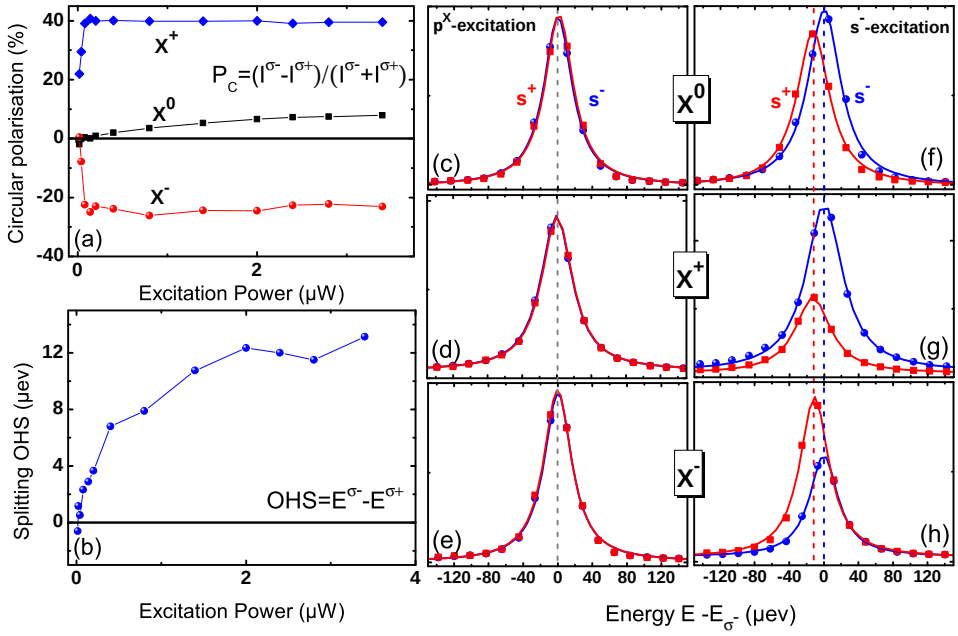

Figure 5.1: QD I: Dynamic Nuclear Polarisation at $B_{ext} = 0$ T. Circular polarisation of X^0, X^+, and X^- (a) measured as function of laser excitation power. (b) The stable nuclear polarisation resulting in Overhauser shift, here $\mathrm{OHS}_{max} = 12$ μeV, detected for all lines as shown in (f), (g), and (h), where the excitation power is 3.5 μW. Under linearly polarised excitation none of the excitonic states exhibit Overhauser shift, (c), (d), and (e). The transition lines are fitted with Lorentzian function. A central energy of σ^- polarised transition of each state is subtracted from the data for every state.

splitting (f), (g), and (h). Under non-resonant circular polarised laser excitation in the AlGaAs barrier the X^+ is highly polarised, 40 % at higher excitation power. The neutral exciton X^0 at very high excitation power is also circularly polarised, ≈ 10 %, due to the linear-to-circular basis transition [28]. X^- polarisation is negative (-20 % see Figure 5.1 (a) and (h)), i.e. cross-polarised with respect to the excitation laser [22, 71]. The resident conduction electron left behind after X^- recombination has therefore the same orientation as the conduction electron which exists during the radiative lifetime of the X^+.

We measure an Overhauser shift of 12-16 μeV Figure 5.1(b), which corresponds to a nuclear polarisation degree of 12%, taking into account that the Overhauser shift for 100% nuclear polarisation in GaAs is 135 μeV. Our sample is subject to charge fluctuations, i.e. during the 1s PL integration time we observe charged (X^+ and X^-) and neutral (X^0)

exciton emission. The X^+ with a well orientated electron spin for resident electron left after $X-$ recombination can polarise the nuclei via the Overhauser effect, the X^0 and the X^- will feel the created nuclear field [28].

In highly strained dots, to explain the observations of DNP at $B_{ext} = 0$ T obtained three effects have been proposed to screen the depolarisation of the nuclei due to the arbitrarily orientated B_L (see chapter 11 in [88]):

(i) The nuclei are effected by the average electron spin polarisation acting like an effective magnetic field B_K (**Knight field**). The time averaged Knight field of an electron in a state $\psi(\boldsymbol{r}_j)$ acting on one specific nucleus j is given by:

$$\boldsymbol{B}_{K_j} = f_e \frac{\nu_0 A^j}{g_N \mu_N} |\psi(\boldsymbol{r}_j)|^2 \langle \hat{\boldsymbol{S}}^e \rangle \tag{5.1.1}$$

where ν_0 is the two atom cell volume, $\boldsymbol{r}_j$ is the position of the nucleus, A^j is the hyperfine interaction constant, g_N and μ_N are the nuclear g-factor and magneton, respectively. f_e is the filling factor $\in$ [0,1] characterizing the average occupation of the dot by electrons, underlining that the Knight field is zero in the absence of electrons. In [27, 167] for InGaAs quantum dots, measurements show B_K in the mT-range, which is sufficient to screen the nuclear dipolar interaction.

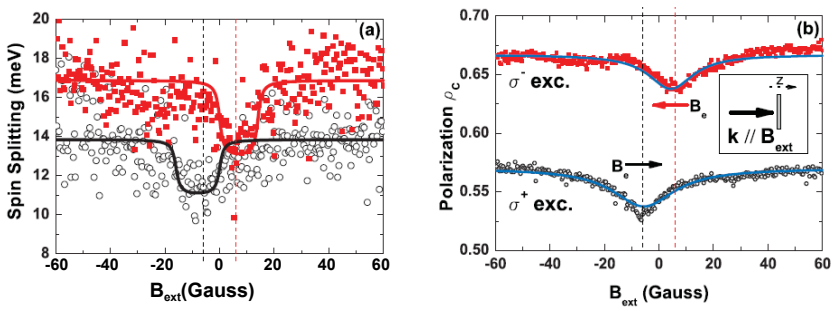

Figure 5.2: Direct measurement of Knight field in strained InAs/GaAs QDs [27]. The observed Knight field in this structure is very low $\approx$ 7 Gauss and is sufficient to screen the nuclear depolarisation.

(ii) In [37] DNP was first constructed in the presence of a well defined electron spin in a charge tunable InGaAs quantum dot. Subsequently the electron was removed from the dot and the nuclear spin polarisation remained stable for several seconds in the absence of any electron spin. In this case the Knight field is also absent and nuclear quadrupole effects [168] have been proposed as a source for this stabilization. Nuclear quadrupole splittings corresponding to effects of internal magnetic fields of tens to hundreds of mT [170] are capable of screening nuclear dipole relaxation in strained structures.

(iii) In principle also the formation of a nuclear polaron can stabilize the nuclear spin system in the absence of external fields [169]. But this requires a very high nuclear polarisation degree which is very difficult to achieve at zero applied field.

In the investigated strain free QDs the Knight field can be considered as the main source of screening of the nuclear depolarisation and hence was studied in detail.

5.2 Knight field tuning

In an applied longitudinal magnetic field we excite with $\sigma^{\pm}$ polarised light and detect $\sigma^{\pm}$ polarised PL. The total Zeeman splitting $E_{\sigma^+} - E_{\sigma^-}$ under circularly polarised excitation includes nuclear field contributions, (Overhauser shift, OHS) in addition to the Zeeman splitting due to the external field. OHS can be obtained by subtraction Zeeman splitting under linearly polarised excitation from the splitting under circularly polarised excitation, Figure 5.3 (a). In the absence of strain (i.e. no nuclear quadrupole effects), DNP at zero

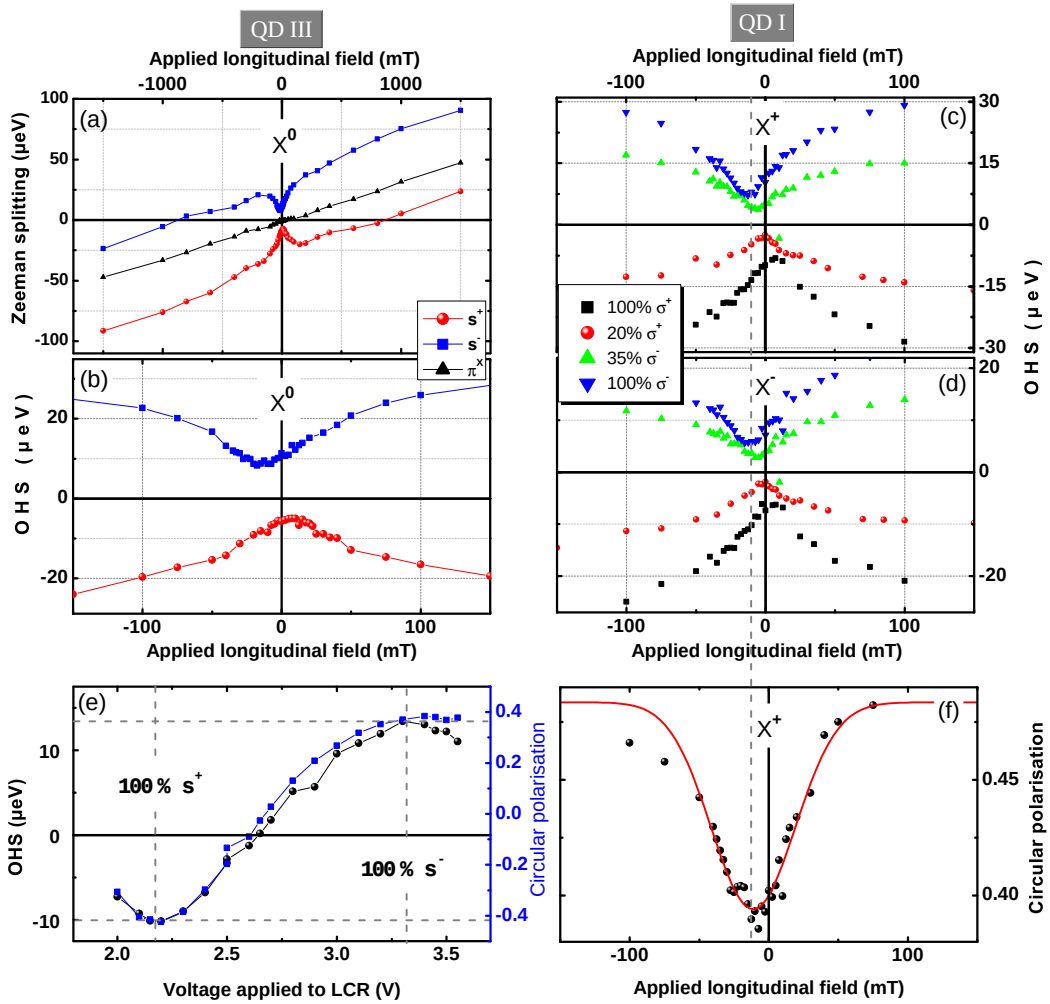

Figure 5.3: Longitudinal magnetic field - Faraday geometry measurement of Knight field in two different QDs. A dip in Overhauser shift observed for all excitonic states X^0 (QD 6) (b), X^+ , and X^- (QD 5), (c) and (d) respectively, for $\sigma^{\pm}$ laser polarisation. The magnetic field, for which this dip occurs is a measure of the Knight field amplitude. Green triangles and red circles for elliptically polarised laser excitation exhibit lower Knight field amplitudes (c) and (d). PL circular polarisation exhibiting also a dip at the same applied magnetic field for σ^+ laser polarisation (f). The dip is fitted with Gaussian function as a guide to the eye.

magnetic field could be enabled by a strong Knight field. In order to evaluate this Knight field we try to compensate it by an external magnetic field. In an applied longitudinal magnetic field in the mT range we compensate the Knight field [27, 167]. In this case, ideally, the nuclei experience a total field that is zero and get depolarised. The nuclear depolarisation results in a dip in Overhauser shift observed for all excitonic states X^0, X^+, and X^-, Figure 5.3 (b), (c), and (d) respectively.

However, the nuclear polarisation i.e. the Overhauser shift does not drop abruptly to zero as the Knight field experienced by each nucleus depends on its exact position r_j in the dot, see Equation 5.1.1. This explains the broadening in Figure 5.3. We find in Figure 5.3 (c), (d), and (f) that both the circular polarisation degree of the emitted light and the Overhauser field pass through a local minimum at $B_{ext,z} \approx -15$ mT. Varying the LCR bias enables us tuning the helicity of the light polarisation from σ^+ to σ^- Figure 5.3 (e) (for more information see Chapter 2). Using this tuning curve we can extract any intermediate elliptical polarisations.
When changing the helicity of the light polarisation, the minimum is observed at $B_{ext,z} \approx +15$ mT, with intermediate values for elliptical polarisation (green triangles and red circles), see Figure 5.3 (b), (c), and (d).

The Knight field is proportional to the average electron spin $\langle \hat{\boldsymbol{S}}^e \rangle$ Equation 5.1.1. The amplitude and direction of the mean electron spin in the X^+ are controlled by the polarisation of the excitation laser. This allows for Knight field tuning [171]. We extracted Knight field amplitudes for every circular and intermediate elliptical excitation polarisation. We observe this as well for all excitonic states X^0, X^+, and X^- Figure 5.4 (a) as for different dots (b) the Knight field exhibits linear dependence on the excitation polarisation. The linear dependence of the field, at which the dip is observed as a function of injected mean electron spin (i.e. laser polarisation) is a strong indication that the Knight field compensation is indeed at the origin of this dip. It is important to note the decrease in nuclear polarisation at $B_{ext,z} = -B_K$ is much more pronounced here than for InGaAs dots reproduced in Figure 5.2 [27], which underlines that the Knight field plays a vital

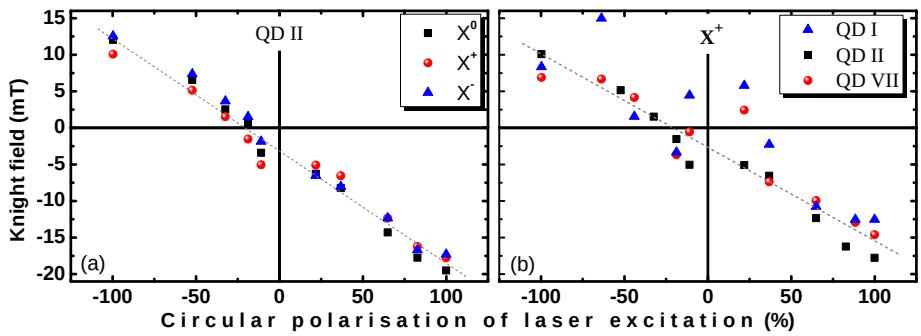

Figure 5.4: Longitudinal magnetic field - Faraday geometry: Knight field tuning in applied longitudinal field as function of laser polarisation. (a) Knight field amplitudes extracted from all excitonic states X^0, X^+, and X^- of QD B and (b) summary of the measurements as in (a) but extracted from X^+ for 3 different dots, demonstrating Knight field tuning, dashed line is a guide to the eye. The data show a roughly linear dependence as $B_K \propto (\langle S_e \rangle = -P_c^{Laser}/2)$.

role in strain free dots for the stabilization of nuclear spins.

5.3 Hanle effect

5.3.1 Phenomenological results

Having established a strong Knight field that under the current optical pumping conditions can be as high as $B_K = 15$ mT, we now test its robustness against the application of a transverse magnetic field $B_{ext,x}$ in the quantum dot plane [1]. In an applied transverse magnetic field electrons polarised along z-direction precess about the applied field. The resulting precession results in depolarisation of the electrons as it can be observed by measuring the circular polarisation of the emitted PL as a function of the applied transverse magnetic field.

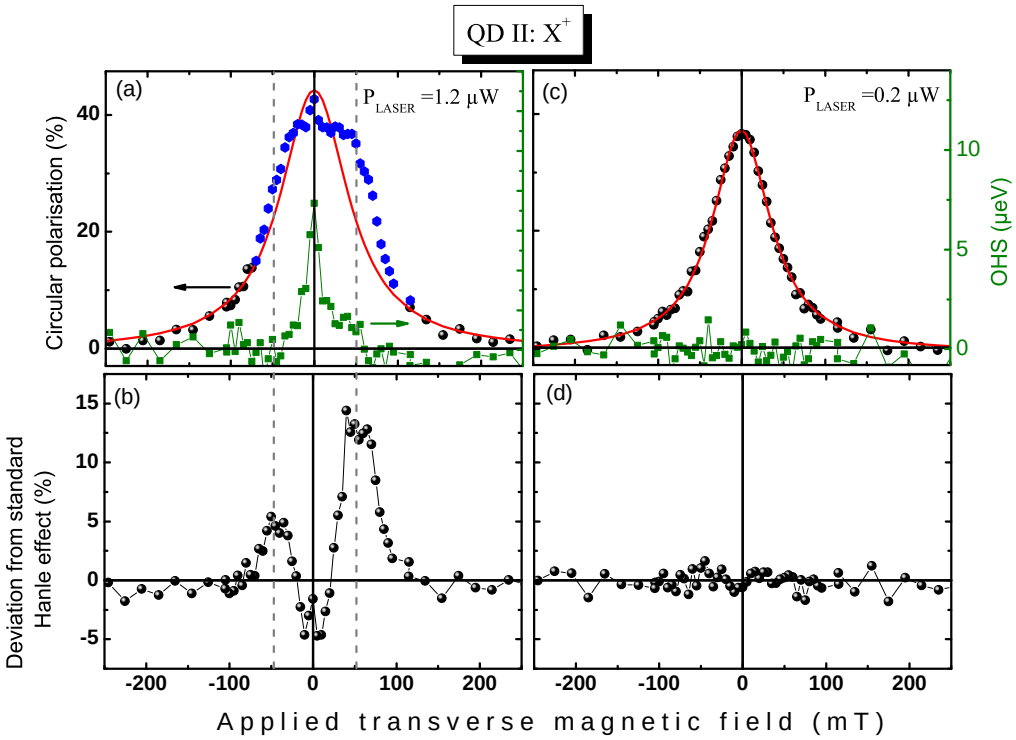

Figure 5.5: Transverse magnetic field - Voigt geometry (a) Hanle effect: Circular polarisation degree of the X^+ emission and OHS as a function of the applied transverse magnetic field. This measurement (black circles and blue hexagons) is done at high laser power creating the Dynamic Nuclear Polarisation. For the blue data points the Overhauser shift is non-zero, for the range with the black data points the Overhauser shift is zero i.e. DNP is absent. These black data points have been used to obtain the standard fit with a Lorentz curve red line. (c) Same measurement as (a) but using very low laser excitation power. Measurements of the Overhauser shift confirm that DNP is absent for low laser power (b) and (d) Here the difference between the data and Lorentz curve is plotted for different laser powers i.e. different Dynamic Nuclear Polarisation.

1 For structures grown along [111] all in plane directions in the x,y plane are of equal symmetry.

We measure PL polarisation in the absence of DNP. This is achieved by lowering the laser power to such an extend that the Overhauser shift completely disappears (see green dots in Figure 5.5 (c)).With a CCD camera as detector the usual technique circular polarisation modulation by using an electro-optical modulator was not possible. In Figure 5.5 (a) we plot the circular polarisation degree of the X^+ as a function of the applied transverse magnetic field $B_{ext,x}$. Having determined the $g_{e,\perp}$ factor beforehand, fitting the Hanle curve with a Lorentzian allows to extract the electron spin lifetime τ_s^* as $B_{1/2} = \hbar/(|g_{e,\perp}|\mu_B\tau_s^*) = 43$ mT. The obtained value of $\tau_s^* = 350$ ps[1] corresponds roughly to the radiative lifetime of the X^+ in these structures, which means that the electron spin is stable during the radiative lifetime [22].

In Figure 5.5 (a) we repeat the same measurement, but with almost one order of magnitude high laser power P_{Laser}=1.2 μW. This results in a strong Knight field (as we have increased the filling factor f_e in Equation 5.1.1) and strong DNP as confirmed by a substantial Overhauser shift in Figure 5.5 (b).
We do observe a clear departure from the simple Hanle depolarisation, as has been reported for InGaAs dots [172], but here in absence of strain and in presence of a very strong Knight field. Several striking changes as compared to the standard Hanle effect of Figure 5.5 (c) emerge:
(i) the Hanle curve is broadened. An increase of $B_{1/2}$ is expected if τ_s^* decreases. This is plausible as the higher laser excitation power makes trapping of additional charges more likely, so the effective time the X^+ complex exists might be shortened as biexcitons or other exciton complexes are formed.
(ii) Around zero-field we observed a pronounced W-shape and a clear departure from the simple Lorentzian dependence of the emitted polarisation on the applied field. Similar feature was observed in Hanle experiment on electrons localized by shallow donors in GaAs [6]. This can be verified in Figure 5.5 (b), where we have subtracted the Lorentz fit from the experimental data. The peaks of the W-shape in the difference (Data- Fit) correspond exactly to the peak and shoulder in Overhauser field Figure 5.5 (a) and (b). For the external magnetic field on where the nuclear polarisation does not exist any more the X^+ circular polarisation is depolarised by external field as in usual Hanle effect.
(iii) The polarisation is not symmetrical when changing sign of $B_{ext,x}$, which is even clearer in Figure 5.7 (b).

Considering the W-shape in polarisation we define a critical magnetic fieed of a peak in W-shape B_C, above which the OHS vanishes entirely and its amplitude $A(B_C)$ Figure 5.6 (a). If we plot the critical field and its amplitude as function of excitation power we notice that both B_C and $A(B_C)$ are saturated Figure 5.6 (b). This observation is coherent with saturation of OHS as function of excitation power, see Figure 5.1 in section 5.1.

These substantial changes of the electron polarisation in applied magnetic fields of only a few mT are at first sight surprising. The situation is very complex and should be viewed both from the electron and nuclear spin point of view. An electron will experience two fields: the transverse external field $B_{ext,x}$ and the Overhauser field B_n, which is for $B_{ext,x} = 0$ purely longitudinal and can be quantified by measuring the Overhauser shift.

1 The electron spin life time τ_s^* in strain free droplet dots has been measured at NIMS, in Japan by our colleagues

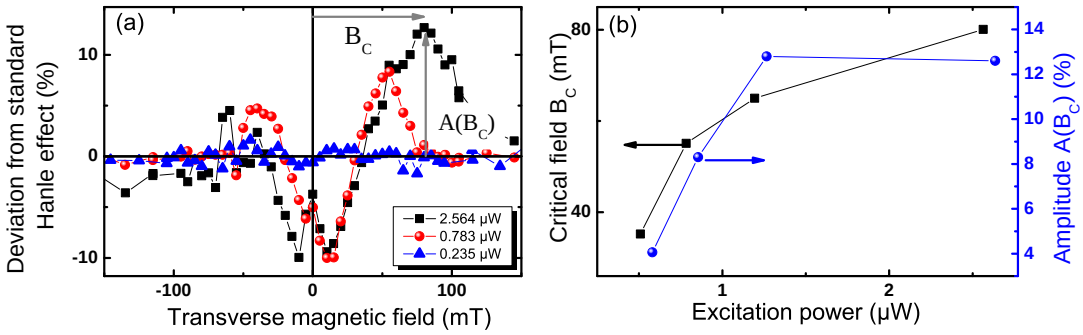

Figure 5.6: QD II: Evolution of W-shape as function of laser excitation power. (a) W-shape of polarisation difference obtained by subtraction the Lorentz fit from the experimental data for different excitation power showing clear evolution. (b) Saturation of B_C and A_{B_C} (as defined in (a))

.

For an Overhauser shift of 10 μeV using $g_{e,\|} \approx 0.8$ we obtain $B_n \approx 220$mT.
As $B_{ext,x}$ increases, B_n will slowly acquire a transverse component. The nuclei in turn will experience in addition to the external field the Knight field B_K due to the presence of the electron spin. So the orientation of the substantial field B_n is governed by B_K and $B_{ext,x}$, as in the absence of quadrupolar fields a rapid establishment of an internal equilibrium among the nuclear spins characterized by a spin temperature is possible [6]. It is the inclination of the strong field B_n (i.e. the generation of a transverse component $B_{n,x}$) that induces the pronounced changes in the electron polarisation when $B_{ext,x}$ is in the mT range and amplify the effect of the external field.

The Lorentz curves describes the depolarisation of the electron spin in applied transverse field without nuclear spin effects. The total field B_{tot} experienced by the electron is the sum of B_{ext} and B_n [173] and as long as the longitudinal component $B_{n,z}$ that we measure via the Overhauser effect is non-zero, the electron will see a tilted field. In Figure 5.5 (a) for $B_{ext,x} = 10$ mT we observe an electron polarisation clearly below the Lorentz curve. For $B_{ext,x} = 50$ mT the opposite is observed: the measured polarisation is above the Lorentzian. As we will see later in theoretical description of experimental results this observation determines the electron g-factor sign. In the case if the measured polarisation is above the Lorentzian corresponding to the standard Hanle effect the electron g-factor is positive.
The exact dependence of the electron polarisation in a total field is given by B_{ext} and the nuclear field B_n which in turn is strongly influenced by the Knight field B_K which is directly proportional to the electron spin. This system with feedback deserves further modeling, see 5.3.2.

Figure 5.7 (b) highlights the pronounced asymmetry when changing sign of the applied field. When changing excitation polarisation from σ^+ to σ^- we obtain again a asymmetric result, but with the reversed sign. This underlines that the nuclei experience a tilted magnetic field, given by the vector sum of B_K and $B_{ext,x}$ as in the oblique Hanle effect used to determine the sign of the electron g-factor [161]. In general, there could be an asymmetry when changing sign of $B_{ext,x}$ if there is an additional longitudinal component

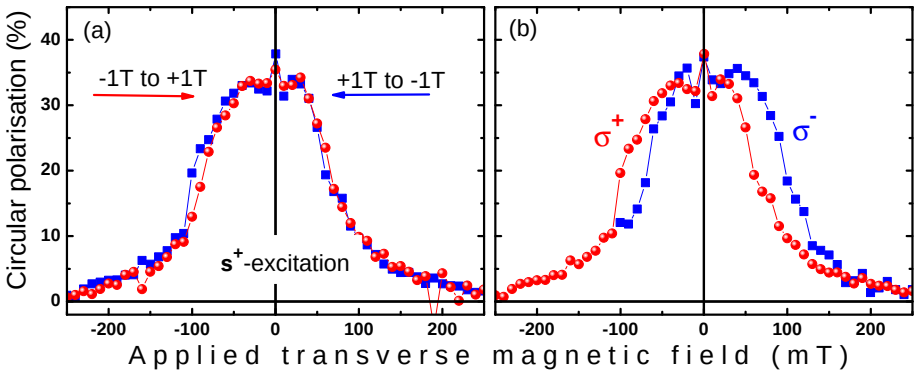

Figure 5.7: QD II: X^+ circular polarisation for sweeping the magnetic field up, from -1 T to 1 T, and down, from +1 T to -1 T (a), and for different circular polarisations of excitation (b). Whereas neither asymmetry nor bistability was observed by sweeping field up and down the asymmetrical behavior depending on excitation helicity was observed.

$B_{ext,z} \neq 0$. We cannot exclude that there is a slight tilt in the sample holder and as a result $B_{ext,z} \neq 0$ but this longitudinal component should not play an important role here for the following reasons: The asymmetry is especially pronounced for this dot. As there is a dot to dot variation, the reason for this the asymmetry cannot be simply attributed to a tilt in the external field.

The behavior discussed for quantum dot QD II is qualitatively reproduced for other dots, as shown in Figure 5.8. Whereas in the dots QD IV and QD V the observed effects are less pronounced other dots QD I and QD VII exhibit almost perfect depolarisation fitted with the usual Lorentzian.

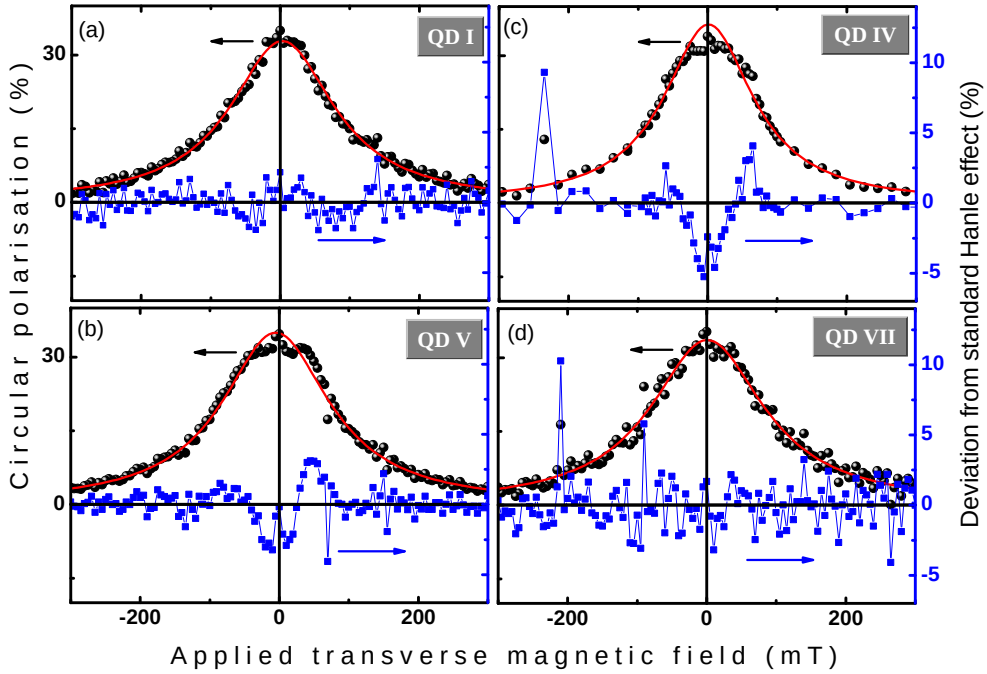

Figure 5.8: X^+ circular polarisation for other investigated QDs including the difference between the experimental data and Lorentzian fit.

5.3.2 Theoretical approach

The following model is based on the approach by D. Paget *etal*. that we have adapted to the GaAs QD case. The nuclear polarisation of each species of nuclei can be written as following [6]:

$$\left\langle \vec{I}_\alpha \right\rangle = \hbar\gamma_\alpha \frac{I_\alpha(I_\alpha+1)}{3} \frac{1}{k_\mathrm{B}\Theta} \vec{B}_\mathrm{T}^\alpha, \tag{5.3.2}$$

with gyromagnetic factor γ_α, α stands for Ga and As nuclei, I_α is nuclear spin, k_B the Boltzmann constant and Θ is the "*nuclear temperature* ". The total magnetic field experienced by nuclei is given by:

$$\vec{B}_\mathrm{T}^\alpha = \vec{B} + \Gamma b_e^\alpha(0) \left\langle \vec{S} \right\rangle, \tag{5.3.3}$$

where $\vec{B}$ is external magnetic field, $\left\langle \vec{S} \right\rangle$ is electron spin polarisation, and $\Gamma = \Gamma_s\Gamma_t$. Γ_s is a factor corresponding to the Knight field averaged on the QD ($\Gamma_s < 1$). Γ_t corresponds to the average fraction of the time a dot is occupied by a trion X^+ ($\Gamma_t < 1$).

Now the nuclear polarisation can be written as:

$$\left\langle \vec{I}_\alpha \right\rangle = \hbar\gamma_\alpha \frac{I_\alpha(I_\alpha+1)}{3}\frac{1}{k_\mathrm{B}\Theta}\vec{B} + \underbrace{\hbar\gamma_\alpha \frac{I_\alpha(I_\alpha+1)}{3}\frac{1}{k_\mathrm{B}\Theta}\Gamma b_e^\alpha(0)\left\langle \vec{S}\right\rangle}_{\equiv A\left\langle \vec{S}\right\rangle}, \tag{5.3.4}$$

We are interested in nuclear field, which is for electron spin precession relevant. The total nuclear field averaged on the dot is given by [6]:

$$\vec{B}_{n,\mathrm{T}} = \vec{B}'_n + A\left\langle \vec{S}\right\rangle, \tag{5.3.5}$$

where $\vec{B}'_n$ is an effective nuclear field. We now write each term $A\left\langle \vec{S}\right\rangle$ and $\vec{B}'_n$ explicitly.

$$A\left\langle \vec{S}\right\rangle = f b_n \frac{\left\langle \vec{S}\right\rangle \cdot \left(\vec{B}+\Gamma b_e\left\langle \vec{S}\right\rangle\right)}{\left(\vec{B}+\Gamma b_e\left\langle \vec{S}\right\rangle\right)^2 + \xi B_\mathrm{L}^2}\Gamma b_e\left\langle \vec{S}\right\rangle, \tag{5.3.6}$$

and

$$\vec{B}'_n = f b_n \frac{\left\langle \vec{S}\right\rangle \cdot \left(\vec{B}+\Gamma b_e\left\langle \vec{S}\right\rangle\right)}{\left(\vec{B}+\Gamma b_e\left\langle \vec{S}\right\rangle\right)^2 + \xi B_\mathrm{L}^2}\vec{B} \equiv K\vec{B}. \tag{5.3.7}$$

where f is the leakage factor [1]. Only the component $\vec{B}'_n$ of the nuclear field is efficient for spin precession.
Indeed, the spin precession equation is given by:

$$\frac{d\vec{S}}{dt} = -\frac{\left\langle \vec{S}\right\rangle - \left\langle \vec{S}_0\right\rangle}{\tau_s^*} - \frac{g_e\mu_\mathrm{B}}{\hbar}\left\langle \vec{S}\right\rangle \times \left(\vec{B}+\vec{B}'_n\right). \tag{5.3.8}$$

In cw-regime $\frac{d}{dt} = 0$ thus we obtain the equation:

$$\frac{g_e}{|g_e|}B_{1/2}\left(\left\langle \vec{S}\right\rangle - \left\langle \vec{S}_0\right\rangle\right) + \left\langle \vec{S}\right\rangle \times \left(\vec{B}+\vec{B}'_n\right) = 0, \tag{5.3.9}$$

where $\langle S_0\rangle$ is the average spin obtained without external magnetic field and in absence of nuclear spin polarisation.

By postulating $\vec{S}_0 = S_0\mathbf{e}_z$ we obtain from Equation 5.3.9 identities:

$$\left\langle \vec{S}\right\rangle \cdot \vec{B} = \langle S_0\rangle B_z, \tag{5.3.10a}$$

$$\left\langle \vec{S}\right\rangle^2 = \langle S_0\rangle \langle S_z\rangle \tag{5.3.10b}$$

and thus

$$\left\langle \vec{S}\right\rangle \cdot \left(\vec{B}+\Gamma b_e\left\langle \vec{S}\right\rangle\right) = \langle S_0\rangle \left(B_z + \Gamma b_e \langle S_z\rangle\right), \tag{5.3.10c}$$

1 Contrary to the work in [6], the averaging is performed here in the case where the Knight field dominates the local field $B_K >> \xi B_\mathrm{L}$

We can thus rewrite K in following form:

$$K \approx f b_n \frac{\langle S_0 \rangle \left(B_z + \Gamma b_e \langle S_z \rangle \right)}{B_z^2 + B_x^2 + 2\Gamma b_e \langle S_0 \rangle B_z + (\Gamma b_e)^2 \langle S_0 \rangle \langle S_z \rangle + \xi B_{\mathrm{L}}^2}. \tag{5.3.11}$$

In order to simplify this expression we introduce the reduced parameters: the circular polarisation of emitted PL ρ, effective Knight field κ, and nuclear field ν, which are given by:

$$\rho \equiv \frac{\langle S_z \rangle}{\langle S_0 \rangle}, \ \kappa \equiv \Gamma b_e \langle S_0 \rangle, \ \nu \equiv f b_n \langle S_0 \rangle .$$

We see that the nuclear field ν depends on the electron g-factor sign. Since for the electron $\mu_{\mathrm{B}}<0$ the nuclear field ν possesses the opposite sign. The Knight field is parallel to the electron spin. The term ξB_{L}^2 corresponds to the local field whose typical values are a few Gauss. With respect to the Knight field measured in our investigated system, up to 150-180 Gauss, the local field term ξB_{L}^2 can be neglected.

Now we obtain a simplified form of K:

$$K_\rho \approx \frac{\nu(B_z + \kappa\rho)}{B_z^2 + B_x^2 + 2\kappa B_z + \kappa^2 \rho}. \tag{5.3.12}$$

The circular polarisation of PL ρ is given by the implicit equation:

$$\rho = \rho_0 \frac{B_{1/2}^2 + B_z^2 \left(1 + K(\rho)\right)^2}{B_{1/2}^2 + (B_x^2 + B_z^2)\left(1 + K(\rho)\right)^2}. \tag{5.3.13}$$

Here $B_z = \frac{B_x}{\cos\theta}$ where θ is the tilt angle of the external magnetic field with respect to the sample normal.

Equation 5.3.13 can be solved only numerically [1]. The solutions of Equation 5.3.13 describe qualitatively very well the experimental observations for different dots in Figure 5.9. At very low field the theoretical curve is below the Lorentzian. At a slightly higher field it crosses the Lorentzian before it slowly overlaps with Lorentzian at much higher field, above $B_x \approx 100$ mT.

If the Overhauser field disappears according to Equation 5.3.13 we obtain a standard Hanle effect. In this case the depolarisation is a Lorentzian function of applied transverse magnetic field. Under experimental conditions it is the case when we excite with low excitation power so that we can not pump optically the nuclear field, see Figure 5.5 (c) and (d).

When we compare the difference of experimental data and theoretical model we notice a reasonably good fitting 5.9 (b) and (d), which supports the theoretical model. The two minima of data coincide exactly with theory. Whereas for QD V two maxima overlap very well for QD II they are slightly shifted. The amplitude difference of maxima takes its origin in theoretical fit function Equation 5.3.13. Up to now , the relative polarisation ρ_0 has been taken equal to 1 and is assumed to be independent on the external and nuclear field. However, when $|B = B_n|$ is small, the contribution of nuclear field fluctuation δB_n

1 In order to solve this implicit equation we used the software Wolfram Mathematica, see Appendix A.4

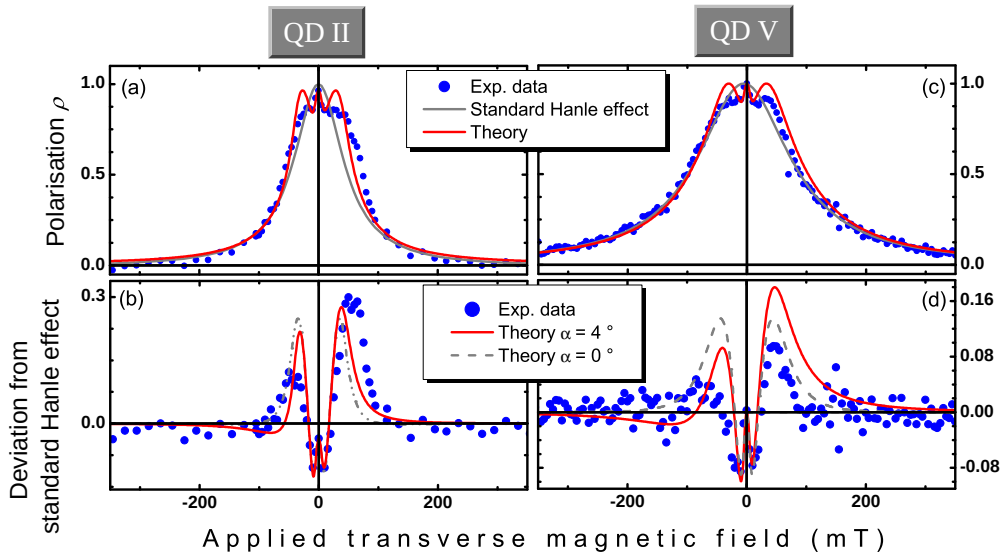

Figure 5.9: Normalized X^+ circular polarisation ρ and the difference between the data and standard Hanle effect (blue symbols) of two different QDs fitted with Equation 5.3.13 (red line). (a) and (b) QD II at P_{LASER}=1.2 μW with $B_{1/2}$ = 100 mT and (c) and (d) QD V excited with P_{LASER}=2.6 μW and with $B_{1/2}$ = 188 mT. In (b) and (d) both $\alpha = 0$ (gray striped line) and $\alpha = 4\,°$ (red solid line) were used to fit the data showing how a small tilt angle affects the depolarisation symmetry.

should be taken into account so that the initial polarisation ρ_0 decreases in very low field and then increases again to unity at high external field.

In some QDs we observed that the measured circular polarisation of emitted PL at B_x=0 lower is than the amplitude of the Lorentzian fit of electron depolarisation, see Figure 5.8 (c), 5.9, and 5.10 (a). This can be explained by the magnetic field dependence of circular polarisation observed in optically modulated spectroscopy measurements avoiding the build up of a nuclear polarization through optical pumping [174]. The circular polarisation ρ at low field is then lower than at high field ρ_0 where it is saturated. The initial circular polarisation ρ_0 is given by:

$$\rho_0 = \frac{B_x^2 + \rho_0(0)\delta B_n^2}{B_x^2 + \delta B_n^2}, \tag{5.3.14}$$

where δB_n is nuclear field fluctuation and $\rho_0(0)$ is polarisation measured at $B_x = 0$ T [16, 174].

Related to our fit function it means that in low field region $\rho_0(0)$ get depolarised and at higher field ρ_0. We obtain now a new approximated implicit equation:

$$\rho = \frac{B_x^2 + \rho_0(0)\delta B_n^2}{B_x^2 + \delta B_n^2} \frac{B_{1/2}^2 + B_z^2\left(1 + K(\rho)\right)^2}{B_{1/2}^2 + \left(B_x^2 + B_z^2\right)\left(1 + K(\rho)\right)^2}. \tag{5.3.15}$$

A better approximation would include the nuclear field in ρ_0 according to:

$$\rho_0 \cong \frac{(B_x^2 + B_{n,x}^2) + \rho_0(0)\delta B_n^2}{(B_x^2 + B_{n,x}^2) + \delta B_n^2}. \tag{5.3.16}$$

Figure 5.10 (a) and (b) shows circular polarisation of a dot whose initial polarisation $\rho_0(0)$ is significantly lower than the Lorentzian amplitude. This behavior varies from dot to dot and is here much more pronounced than in the QD II Figure 5.9 (a) and comparable to QD IV Figure 5.8 (c).
We can see that if we normalize both the experimental data and Lorentzian function with respect their maxima the fit function does not fit very well at higher field, Figure 5.10 (c) and (d). The normalization of data by dividing by their maximum modifies $B_{1/2}$. Subsequently, the Lorentzian does not fit the data very well any more. This results in mismatching between the data, Lorentzian, and subsequently, theoretic fit.
In low field, however, the theoretical function fits also very well. In contrary, if the data are normalized with respect to the Lorentzian amplitude obtained for a dot of interest the theoretical function fits very well every where Figure 5.10 (a) and (b). Hence the fit function of the theoretical model needs to be optimized with respect to initial PL polarisation $\rho_0(0)$ to fit the data in both low and high field range.

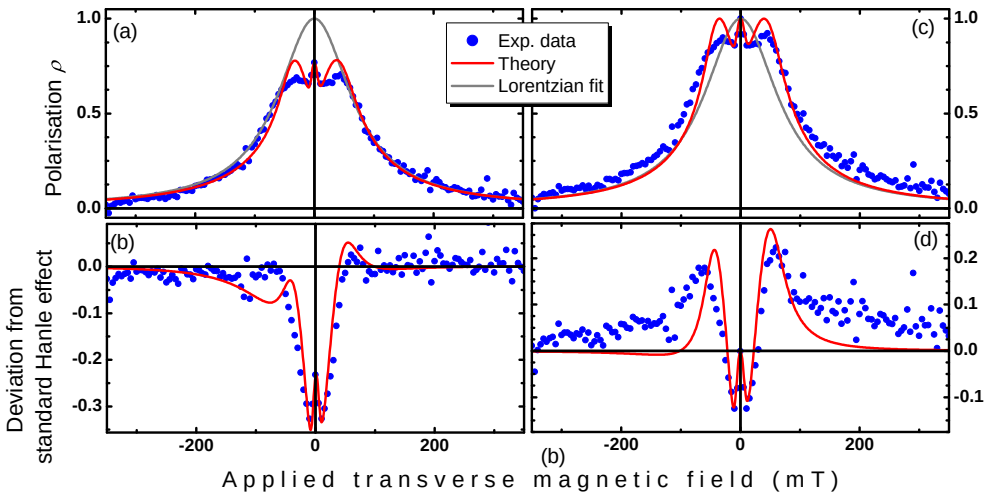

Figure 5.10: X^+ circular polarisation and the difference between the experimental data and Lorentzian fit for two different normalization procedures fitted with Equation 5.3.15 (red line). In (a) and (b) the experimental data are normalized with respect to the Lorentzian fitting these data i.e. divided by the amplitude of Lorentzian whereas in (c) and (d) the data are normalized with respect to maximum of the data themselves. The standard Lorentzian fit is obtained by fitting the high magnetic field domain only.

5.4 Conclusions and discussions

We investigated a strain-free system with focus on the Dynamic Nuclear Polarisation at $B_{ext} = 0$ T. The Overhauser shift up to 15-16 μeV was observed at $B_{ext} = 0$ T corresponding to nuclear spin polarisation ≈ 12 %. Due to the nuclear dipole-dipole interaction i.e. due to the local field B_L nuclear spins can not get polarised unless any screen mechanisms are present protecting the nuclear spin polarisation.
Whereas in strained QDs, e.g. GaAs/InGaAs, strong quadrupole effects play an essential role of screening mechanism in our investigated QDs, in absence of strong quadrupole effects, the Knight field B_K acts as a screening mechanism. We measured the Knight field $B_K^{max} \approx 15 - 18$ mT by applying external longitudinal magnetic field to cancel it, which is one order of magnitude higher than in strained InAs/GaAs QDs in [27].

In absence of additional effects the electron spin polarisation precesses in applied transverse magnetic field and is described by a Lorentzian function. In presence of high Knight field we observed an interplay between external field B_{ext}, Knight field B_K, and nuclear field B_n in an applied transverse magnetic field B_{ext} resulting in a clear departure from standard Hanle depolarisation. The theoretical model based on the nuclear temperature [6] was adapted to the QD case and could describe Hanle effects observed in our QDs qualitatively well.
On the one hand the theoretical model fits the depolarisation very well. On the other hand fitting the Hanle W-shape confirms the Knight field amplitude measured in applied longitudinal magnetic field.

CHAPTER 6

Conclusions and perspectives

The aim of this work was to study the electron and nuclear spin physics in strain free GaAs single dots grown by "droplet" epitaxy along different crystallographic directions.
We studied in detail the effect of a longitudinal magnetic field $\boldsymbol{B} \parallel z' \parallel [111]$ in strain free GaAs quantum dots grown on [111] substrates. In longitudinal magnetic field the optically forbidden dark transitions in addition to optically active bright transitions for both charged and neutral excitons were observed. We observed a strongly non-monotonous, sign changing field dependence of the bright neutral exciton Zeeman splitting. This surprising experimental result was explained and well described[1] by the interplay between exchange and Zeeman effects and the mixing of $\pm 3/2$ heavy-hole states induced by longitudinal magnetic field, an inherent property of systems with C_{3v} point-group symmetry. The theoretical approach can be extended also to the observations in Voigt geometry where the magnetic field is applied orthogonal to the growth and excitation axis.
It should be emphasized that the developed theory predicts non-zero values of g_{h2} only for the dots of specific trigonal shape. Note that for the isotropic in (x,y)-plane shape as well as for the shape invariant to the $z \to -z$ transformation (i.e. disk or prism) g_{h2} equals to zero. Our theoretical predictions are in perfect agreement with the recent experimental results of [150] where zero values of g_{h2} were obtained for the disk-shaped [111] quantum dots embedded in nanowires. This reflects the fact that the confinement potential and its symmetry gives the main contribution to the non-diagonal part of g-tensor.
Two other mechanisms of the $\pm 3/2$ mixing have been first proposed in the theoretical part of [136], namely, due to anisotropic corrections to the hole Hamiltonian in magnetic field (proportional to the small parameter q and the cubic in wavevector terms in the valence band, accounting for the non-centro-symmetricity of the GaAs crystal). However the corresponding contributions do not describe experiment quantitatively (the corresponding g_{h2} values are one order of magnitude too small).

We succeeded the first electrical control of charge in single QDs grown by Droplet Epitaxy, on (100) substrates. A QD could be electrically charged with electrons up to X^{3-} state consisting of an hole and 4 electrons. However, not all investigated dots exhibit

1 The theory was developed in collaboration with E. L. Ivchenko, M. M. Glazov and M. V. Durnev from the Ioffe-Institut, St. Petersburg, Russia.

the same charging characteristics. Nevertheless, in all dots at least $X^+ \rightarrow X^0 \rightarrow X^-$ transitions were observed when increasing the applying bias.
The exciton fine structure was studied in detail by means of an entire analytical method enabling us to solve the eigensystem. By applying transverse magnetic field the magneto-optical properties of the QDs, which are aligned along the principal crystallographic axes [110] and [1$\bar{1}$0] revealed following interesting physical effects:
i. in the fixed detection basis and applied magnetic field the bright exciton fine structure splitting δ_1 and hole g-factor g_h change their sign when comparing two QDs aligned parallel to [110] and [1$\bar{1}$0] crystallographic axes, respectively.
ii. The in-depth study proved that the orientation of a QD with respect to the applied magnetic field is essential for changing of the hole g-factor sign and not with respect to the crystallographic axis. The hole g-factor sign of the QDs with their elongated site parallel to the magnetic field is opposite to the hole g-factor sign of the QDs whose elongated site is orthogonal to the magnetic field.
iii. In addition, the developed model allows us to describe accurately the bright-dark mixing induced by applied transverse magnetic field and the corresponding transfer of oscillator strength.

Furthermore we measured significantly higher electron g-factor, up to 1, with respect to the electron g-factor of bulk $Al_{0.3}Ga_{0.7}As$ (0.55) and GaAs (-0.44). It means that the measured electron g-factor can not be explained by a model where the electron g-factor is a monotonous function increasing with confinement from $g_e(\text{GaAs}) = -0.44$ (in bulk) to $g_e(Al_{0.3}Ga_{0.7}As) = 0.55$ (in barrier). In our system the electron g-factor exceeded the one of surrounding barrier roughly by factor 2. This can be a motivation for in-depth theoretical study of g-factors in our investigated system.

We observed in strain-free (111)A QDs Dynamic Nuclear Polarisation at $B_{ext} = 0$ T. We measured Overhauser shifts as high as 15-16 μeV at $B_{ext} = 0$ T. In common Stranski-Krastanov grown strained QDs the depolarisation of nuclear spin polarisation is screened by strong quadrupole effects. The "droplet" QDs investigated in this wirk are strain-free and the nuclear dipole-dipole interaction leading to the depolarisation of nuclear spin polarisation is screened by Knight field B_K.
We measured Knight field $B_K^{max} \approx 15 - 18$ mT by applying external longitudinal magnetic field in order to compensate it, which is one order of magnitude higher than in strained InAs/GaAs QDs in [27]. We were able to tune its amplitude and direction with the electron spin prepared by optical pumping.

In presence of high Knight field we observed an interplay between external field B_{ext}, Knight field B_K, and nuclear field B_n in an applied transverse magnetic field B_{ext} resulting in a clear departure from standard Hanle depolarisation. The theoretical model developed in the of electron bound to donors in GaAs [6] based on the existence of nuclear temperature was adapted to the QD case and could describe qualitatively well the non-monotonous Hanle effects observed in our QDs.
On the one hand the theoretical model fits the depolarisation very well. On the other hand fitting the Hanle W-shape confirms Knight field amplitude measured in applied longitudinal magnetic field and the electron g-factor sign.

Résumé

Introduction

Dans la plupart des semi-conducteurs, le spin électronique est relativement bien découplé des degrés de liberté de charge et de mouvement orbital. Dans les boîtes quantiques, où le mouvement d'un électron est confiné dans les trois directions sur des longueurs de l'ordre de 10 nanomètres, il est de plus relativement bien protégé des fluctuations des charges environnantes. Dans de telles nanostructures, qui ont certaine analogies avec les atomes, l'interaction hyperfine est le mécanisme d'interaction dominant entre le spin d'un porteur confiné et celui des noyaux des atomes constitutifs de la boîte quantique, ce qui en fait un système modèle pour l'étude du problème du spin central.

Le principe de base de la mesure et des manipulations de spin dans les boîtes quantiques que nous décrivons repose sur la forte interaction spin-orbite clivant les états de valence, ce qui permet d'établir une correspondance entre le spin d'un électron excité et la polarisation du laser effectuant le pompage optique. L'initialisation du spin d'un électron ou d'un trou avec une impulsion laser polarisée circulairement correspond au transfert du moment angulaire des photons d'excitation aux électrons, régi par l'interaction spin-orbite. Cette dernière permet en outre d'établir les règles de sélection du pompage optique.

Une fois initialisé, les conditions pour effectuer des manipulations cohérentes contrôlées du spin sont favorables, car les principales sources de relaxations connues pour les matériaux massifs ou les nanostructures présentant un confinement partiel des porteurs ne fonctionnent pas aux porteurs localisés dans les boîtes quantiques [12, 13, 14]. Cependant, il a été fait remarqué très tôt que les interactions avec les fluctuations du champ nucléaire, d'orientations aléatoire, des atomes constituant la boîte quantique peuvent limiter sévèrement limiter le temps de cohérence de spin de l'électron [15, 16, 17, 18]. De fait, cette prédiction a été confirmée indépendamment pour les électrons confinés dans des pièges électrostatiques à partir de mesures de transport en régime quantique, et dans la spectroscopie optique de nano-cristaux insérés dans des matrices [19, 20]. Ainsi, la motivation forte pour accroître le temps de décohérence du spin a conduit les chercheurs à porter un intérêt accru pour la physique du spin dans les boîtes quantiques[21].

Le système de spin nucléaires peut rester stable jusqu'à plusieurs heures sous certaines conditions, ce sui présente un intérêt certain pour le stockage de l'information [26]. L'interaction hyperfine permet aussi d'accorder finement l'énergie exacte des états électroniques et de contrôler la polarisation de la lumière émise. Ceci est vrai en particulier dans les expériences réalisées en l'absence de champ magnétique [27-29] et pourrait s'avérer

important pour les applications en photonique [27, 28, 29]. Par exemple, la connaissance de la base exacte des états de polarisation est crucial pour évaluer de degré d'intrication des sources de paires de photons basées sur les cascades radiatives entre états de conduction et de valence dans des boîtes quantiques individuelles [30, 31, 32]

Nous allons présenter dans cette thèse les propriétés magnéto-optiques de boîtes quantiques individuelles de GaAs insérées dans une matrice de GaAlAs.

Chapitre 1: introduction aux boîtes uniques

Les boîtes quantiques réalisées à partir de matériaux semi-conducteurs sont des objets de tailles nanométriques qui contiennent typiquement plusieurs dizaine de millier d'atomes d'un composé semi-conducteur inséré dans un autre composé présentant une largeur de bande interdite plus importante, l'ensemble constituant un puits de potentiel. Il en résulte un confinement quantique des porteurs dans les trois directions de l'espace. Parmi les combinaisons de matériaux puits/barrière couramment utilisées et bien caractérisées à ce jour, citons GaInAs/GaAs ou CdTe/ZnTe, permettant le réalisation de boîtes quantiques contraintes par épitaxie à jets moléculaires en régime de Stranski-Krastanov, ou GaAs/AlGaAs permettant la réalisation de boîtes non-contraintes par épitaxie à jets moléculaires par la méthode de Volmer-Weber nouvellement utilisée.

Du fait du confinement tridimensionnel des porteurs sur des longueurs plus petites que la longueur d'onde de de Broglie, les énergies des états électroniques localisés sont quantifiées, les boîtes pouvant être alors vues à l'échelle mésoscopique comme des "atomes artificiels". De fait, les expériences de micro-luminescence [9], de corrélation de photons [45] et la diffusion de laser résonante [46] ont établi le caractère atomistique des transitions entre états électroniques. Ceci a été à la base de la motivation dans de nombreuses équipes de sonder et de manipuler les états de charge et de spin de porteurs individuels. Les expériences entreprises ont pour but d'évaluer la possibilité d'utiliser les états quantiques dans une boîte comme digit quantique élémentaire dans un processeur quantique [47].

Les boîtes quantiques sans contraintes etudiées sont obtenues par une méthode originale d'épitaxie dans le mode de croissance de Volmer-Weber, qui repose sur la nucléation à partir de gouttelettes de gallium, dans un bâti d'épitaxie à jets moléculaires du National Institute for Material Science NIMS à Tsukuba au Japon. Contrairement au mode de croissance des boîtes quantiques Stransky-Krastanov gouverné par les contraintes, l'épitaxie à partir de gouttelettes permet une grande latitude dans le choix des paramètres de maille et l'orientation cristalline des matériaux constituant la barrière.

De plus, on peut faire croître ce type de boîte, communément dénommées boîtes "gouttelettes", sur différents substrats : Si, Ge, et composés III-V en général. Ceci les rend compatibles avec les technologies couramment employées en micro-électronique. Leur géométrie et leur taille peut aussi être modulée (Figure 1.3)), ce qui permet d'ajuster leur paramètres physiques ; en particulier leur longueur d'onde d'émission, située autour de 780 nm, peut être ajustée en résonance avec les transitions dans l'atome de rubidium pour le stockage non classique de la lumière dans des systèmes quantiques hybrides. La formation d'une couche de mouillage sous-jacente aux boîtes " gouttelettes " de GaAs peut être supprimée sous certaines conditions (Figure 1.4).

Les échantillons que nous avons explorés durant cette thèse sont originaux par plusieurs aspects: les boîtes quantiques "gouttelettes" de GaAs permettent d'effectuer des investigations sur la physique du spin des porteurs et des noyaux atomiques en l'absence de contraintes i.e. en l'absence d'effets quadrupolaires nucléaires importants. Par ailleurs, l'obtention de boîtes de symétrie d'ordre élevé par croissance épitaxiale selon l'axe [111] et possédant un clivage de structure fine excitonique très faible nous ont permis de révéler une physique du spin nouvelle dans des échantillons ne présentant pas de couche de mouillage.

L'excitation d'une boîte quantique dans son état fondamental avec une énergie appropriée correspond à la transition d'un électron dans un état de valence vers un état de

conduction, et en la formation d'une paire électron-trou en interaction coulombienne que nous appellerons état exciton. Après un temps de l'ordre de la nanoseconde, l'électron de conduction recombine avec un trou de valence, ce qui se traduit par l'émission spontanée d'un photon dont le mode de polarisation est déterminé par l'état de l'exciton. Dans ce travail, nous nous intéressons plus particulièrement aux configurations les plus fréquentes: une paire électron de conduction-trou de valence X^0, deux paires électron-trou XX^0 (biexciton)), l'exciton chargé (ou trion) soit négativement X^- ($\Uparrow\uparrow\downarrow$ ou $\Downarrow\uparrow\downarrow$) ou positivement X^+ ($\Uparrow\Downarrow\uparrow$ or $\Uparrow\Downarrow\downarrow$). Les flèches $\uparrow$ ($\downarrow$) représentent ici l'état de spin des électrons de conduction, $\Uparrow$ ($\Downarrow$) le pseudo-spin des trous, et par exemple $\Downarrow\uparrow\downarrow$ représente $\frac{1}{\sqrt{2}}(\uparrow\downarrow - \downarrow\uparrow)\otimes\Downarrow$, où l'antisymétrie des états de conduction apparaît de façon plus explicite[1], voir Figure 1.6 (c). Du fait de la forte localisation de la fonction d'onde des porteurs, les effets coulombiens directs et d'échange sont particulièrement intenses dans les boîtes quantiques.

Sur la Figure 1.6 (a)), nous avons représenté les quatre états de l'exciton les plus bas en énergie. La raie d'émission spectrale correspondant à l'exciton neutre X^0 est dédoublée, le clivage spectral s'élevant ici à $\delta_1 \approx 300$ μeV. Ceci est la manifestation de la structure fine des états excitoniques induite par la partie anisotrope de l'interaction d'échange électron-trou[2]. Pour les excitons neutres en champ magnétique nul, et en l'absence de polarisation des noyaux, les règles de sélection sont affectées par l'interaction d'échange entre électron et trou. Celle-ci fait intervenir notamment une contribution induite par l'anisotropie de la boîte (AEI) provenant à la fois du défaut de symétrie cylindrique sa forme et/ou de l'anisotropie des interfaces entre la boîte quantique et la matrice dans laquelle elle est insérée [65, 76].

Du fait de l'interaction d'échange anisotrope, la recombinaison d'un exciton neutre se traduit par un doublet de raies polarisées linéairement dans des directions distinctes, et séparées par une énergie δ_1 qui peut varier d'une boîte à l'autre, allant, dans le cas des boîtes de GaAs, de quelques μeV pour les boîtes les plus symétriques à quelques centaines de μeV pour les plus allongées. L'énergie d'émission du biexciton XX^0 est décalée de celle de l'exciton, ici de 4 meV environ vers les faibles énergies, du fait de la compétition entre la partie attractive et la partie répulsive des interactions coulombiennes entre les charges. Comme le biexciton est un état singlet, la structure fine qui apparaît dans sa raie d'émission provient de celle de l'exciton, état final de la transition optique associée. C'est pourquoi on obtient un spectre qui reflète en miroir celui de l'exciton neutre X^0.

Les projections selon l'axe de quantification, choisi selon l'axe de croissance de la structure, pour les électrons sont $S_z = \pm 1/2(\uparrow\downarrow)$ et pour les trous lourds $J_z = \pm 3/2$ ($\Uparrow\Downarrow$). La projection du moment angulaire total est donnée par: $J_z^{total} = S_z + J_z$. De ce fait, les quatre états les plus bas en énergie possibles pour l'exciton ont pour projections: $J_z^{total} = \pm 1$ pour les états optiquements actifs ($\downarrow\Uparrow$ ou $\uparrow\Downarrow$) dits états *brillants*, et $J_z^{total} = \pm 2$ pour les états optiquement inactifs ($\uparrow\Uparrow$ ou $\downarrow\Downarrow$) dits états *noirs* ou *sombres*.

En l'absence d'interaction d'échange, les quatre états sont dégénérés en énergie, Figure 1.7.

1 Cette représentation est valide pour le doublet de Kramers le plus bas en énergie du trion, l'antisymétrisation avec le trou restant n'étant pas explicitée ici car, les électrons de conduction formant un singlet de spin, l'interaction d'échange de Coulomb n'introduit pas de levée de dégénérescence supplémentaire pour ce doublet.

2 Rappelons que l'interaction d'échange électron-trou correspond en fait à l'échange coulombien entre un électron de conduction et les électrons de valence restant.

La contribution isotrope à l'interaction d'échange lève partiellement cette dégénérescence, en clivant les états brillants et les états noirs d'une énergie notée δ_0. Les valeurs prises par δ_0 dépendent du confinement dans la boîte quantique et de sa forme, et sont typiquement de l'ordre de quelques centaines de μeV (pour les boîtes " gouttelettes " de GaAs : 200-550 μeV selon la boîte) à comparer aux 100 μeV dans le matériau massif. Notons qu'au mieux, une boîte de forme sphérique ne pourrait être de symétrie plus élevée que T_d (symétrie tétrahédrale) pour un matériau binaire comme GaAs, du fait de la symétrie de la matrice cristalline sous-jacente. De ce fait, l'interaction d'échange coulombienne clive les états noirs de l'exciton d'une quantité δ_2, très faible dans les matériaux massifs et les puits quantiques (de l'ordre du μeV).

En général, les boîtes quantiques sont des objets de symétrie relativement basse, typiquement C_{3v}, C_{2v} ou C_2. De ce fait, les clivages d'échange δ_0 et δ_2 sont modifiés, et le clivage des états brillants par la contribution anisotrope de l'échange apparaît (sauf en principe dans celles de symétrie C_{3v}). Pour les boîtes de symétrie C_{2v}, l'émission des états d'exciton brillants est polarisée selon les axes cristallographiques [110] et [1$\bar{1}$0], Figure 1.7. Les états brillants sont notés $|X\rangle = \frac{1}{\sqrt{2}}(|-1\rangle - |+1\rangle)$ et $|Y\rangle = -\frac{1}{i\sqrt{2}}(|-1\rangle + |+1\rangle)$ et les états noirs $\left|X^2 - Y^2\right\rangle = \frac{|2,2\rangle + |2,-2\rangle}{\sqrt{2}}$ et $|2XY\rangle = \frac{|2,2\rangle - |2,-2\rangle}{i\sqrt{2}}$ en analogie avec les orbitales " p " et " d " de l'atome d'hydrogène. Nous définirons respectivement par la suite le clivage algébrique des états brillants par $\delta_1 = E(|Y\rangle) - E(|X\rangle)$ et celui des états noirs par $\delta_2 = E(\left|X^2 - Y^2\right\rangle) - E(|2XY\rangle)$.

Si un porteur, électron ou trou, est présent dans la boîte avant que celle-ci ne soit excitée, on photo-génère un exciton négativement ou positivement chargé. Comme trois charges sont alors présentes dans la boîte, on emploie alors le terme générique de trion comme nous l'avons vu ci-dessus. La raie d'émission de l'exciton chargé, ou trion positif, X^+ a une raie d'émission qui peut être décalée vers les hautes ou faibles énergies par rapport à celle de l'exciton neutre X^0, selon la taille de la boîte [77, 78]. Sur la Figure 1.6 (a), X^+ est décalée vers le bleu d'environ 1 meV. L'exciton chargé négativement X^- est toujours décalé vers le rouge par rapport à X^0 (dans la Figure 1.6 (a), le décalage est d'environ 7 meV).

Ces caractéristiques sont le résultat de la différence de confinement entre les électrons de conduction et les trous lourds, plus localisés par le potentiel de confinement. Dans le cas des trions, l'interaction de Coulomb directe et d'échange conduit bien à une renormalisation des énergies de transitions, mais pas à une levée de dégénérescence conduisant à l'apparition d'une structure fine pour le doublet fondamental[1], conséquence du théorème de Kramers [46, 65, 59].

1 En l'absence de champ magnétique ou nucléaire.

Chapitre 2: dispositif expérimental

Les mesures de spectroscopie de boîtes individuelles ont été réalisées sous excitation non résonante dans la barrière de $Al_{0.3}Ga_{0.7}As$ à basse température (4 K) dans un microscope confocal.

On emploie la microscopie optique confocale en spectroscopie dans le but de sélectionner une source d'émission unique dans le plan sur lequel se répartissent les boîtes quantiques d'un échantillon donné, (cf. plan 2 dans la Figure 2.1 (a)).La source d'excitation utilisée est un laser dont le faisceau peut être focalisé dans le plan de boîtes. De plus, un sélecteur de mode spatial[1] situé avant le système de détection (spectromètre imageur et caméra CCD) est placé sur l'axe de détection dans le plan conjugué optique du plan focal. Du fait de la faible profondeur de champ du microscope[2], seule la luminescence émise depuis le plan focal peut être détectée en pratique (la luminescence des plans 1 et 3 n'est pas focalisée dans le plan). Le sélecteur de mode permet d'éliminer de plus les signaux émis autour du point focal en dehors d'une zone dont le diamètre est de l'ordre de la longueur d'onde de détection.
Un point pratique important est la coïncidence entre les faisceaux d'excitations et de détection. Si cette condition n'est pas réalisée avec précision, le signal émis ne peut être détecté, cf. Figure 2.1 (b).

De façon à caractériser la résolution spatiale du microscope confocal que nous avons construit durant cette thèse, et ce y compris aux températures cryogéniques, nous avons procédé comme suit. Nous avons utilisé deux réseaux métalliques fonctionnant en transmission ou en réflexion. Le premier a été utilisé pour la configuration Faraday, et le second pour la configuration Voigt. Le réseau en transmission est constitué de rubans métalliques d'aluminium déposés sur un substrat de verre, de largueur 5 μm et distants de 5 μm également. Le réseau est monté sur les nano-positionneurs piézoélectriques de façon à pouvoir le translater perpendiculairement à l'orientation des bandes d'aluminium, par rapport au point focal d'un faisceau laser dont la longueur d'onde simule celle de l'émission. Le positionneur piézoélectrique selon l'axe z permet d'ajuster la position verticale du réseau afin de le placer dans le plan focal du microscope à la longueur d'onde utilisée, afin d'obtenir une tache laser focalisée. Les positionneurs piézoélectriques selon les directions transverse x (ou y) servent à translater le réseau sous la tache du laser. On mesure alors les oscillations du signal transmis en fonction du déplacement horizontal. Le diamètre de la tache d'excitation mesurée est de 633 nm à 690 nm, longueur d'onde d'émission d'une diode laser proche de la longueur d'onde caractéristique de la luminescence des boîtes de GaAs étudiées (voir Table 2.1). On procède de façon similaire pour le réseau en réflexion.

Afin de pouvoir contrôler et mesurer la polarisation de la lumière à l'excitation et à la détection, nous avons utilisé des composants optiques biréfringents (cf. Figure 2.2). Nous avons caractérisé une lame à cristaux liquides programmable agissant comme un élément à retard variable fonctionnant dans les gammes de longueur d'ondes utilisées (cf. figures 2.7 et 2.8).

1 Une fibre optique monomode dont le cur a un diamètre de 5 μm, couramment utilisée pour acheminer le signal optique du microscope au système de détection, remplit aussi cette fonction.

2 L'ouverture de la lentille frontale est de NA=0.68

Enfin pour effectuer des mesures sur boîtes uniques en configuration de Voigt, i.e. avec un champ magnétique appliqué perpendiculairement à l'axe de croissance et à l'axe de propagation de la lumière près de l'échantillon, nous avons conçu et construit durant cette thèse un adaptateur associé à un système de compensation de déphasage à la réflexion utilisant lui aussi les lames retard à cristaux liquides.

Chapitre 3: mélange des états de trous lourds ± 3/2 dans les boîtes " gouttelettes " de GaAs sur substrat (111)A

La recherche de méthodes pour générer et manipuler des états quantiques intriqués est l'une des motivations majeures de la physique expérimentale dans le domaine des nanosciences. La proposition initiale d'utiliser la cascade exciton-biexciton dans les boîtes quantiques pour générer des paires de photons intriqués en polarisation [113] est conditionné à l'emploi de boîtes de haute symétrie où les états brillants de l'exciton neutre X^0 sont dégénérés, i.e. ont un paramètre de clivage de structure fine δ_1 nul. Cependant en pratique la plupart des boîtes présentent une asymétrie naturelle induisant une contribution à l'échange coulombien électron-trou $\delta_1 \neq 0$ dans la majorité des systèmes de boîtes étudiés [48, 50, 114]. Ainsi une recherche très inventive s'est développée afin de tenter de réduire ou d'ajuster le clivage de structure fine à zéro, reposant sur des techniques originales [30, 115, 116, 117] plus ou moins simples à mettre en uvre.

Une approche alternative récente a été proposée, consistant à utiliser des échantillons élaborés sur des substrats présentant une surface orientée selon la direction (111)A. La croissance s'y effectue donc selon la direction cristallographique [111], correspondant également à l'orientation de la plupart des nano-fils [118]. L'avantage des structures élaborées selon cette direction de croissance est qu'elles présentent, tant pour les puits que pour les boîtes quantiques, des interfaces de symétrie appartenant au groupe ponctuel C_{3v} . De ce fait, des clivages de structure fine natifs très faibles pour les boîtes quantiques insérées dans les nanostructures (111) ont été prédits [119, 120] puis observés [121, 122, 123].

Dans le chapitre 3 de cette thèse, nous montrons la première investigation en spectroscopie réalisée sur les boîtes quantiques symétriques obtenues par croissance sur substrat (111)A. Le faible clivage de structure fine inhérent à ce type de boîtes en fait un système prometteur pour la réalisation de sources de photons intriqués en polarisation à partir de la cascade radiative biexciton-exciton. En ce qui concerne leur élaboration, différentes températures de recuit conduisent à des formes de symétries diverses, allant de formes hexagonales irrégulières à des formes triangulaires. Pour une température de recuit de 500 °C, les boîtes présentent une forme clairement triangulaire, tandis qu'à une température de recuite de 200 °C les boîtes sont plutôt cylindriques (cf. Figure 3.2).

Dans les spectres de photoluminescence sous champ magnétique longitudinal appliqué le long de l'axe de croissance, nous observons en plus des états brillants attendus des transitions habituellement interdites pour les boîtes sur substrat (001), à la fois pour les excitons neutres et chargés (cf. Figure 3.4).

Sous champ magnétique longitudinal $B_{z'} \neq 0$ appliqué selon la direction z'=[111], on observe *quatre* raies d'émission pour l'exciton neutre X^0 dans toutes les boîtes observées. Les deux raies sombres ($J_{z'}^{total} = \pm 2$), optiquement inactives pour les boîtes (001) deviennent partiellement brillantes et se joignent au doublet Zeeman des états brillants ($J_{z'}^{total} = \pm 1$) pour former un quadruplet radiatif.

Les observations expérimentales pratiquées montrent que les états de trou lourd dont la projection du moment angulaire selon l'axe de croissance z' est $+3/2$ et $-3/2$ sont couplées par le champ longitudinal dès que $B_{z'}$ est non nul. Cependant le couplage ne se manifeste clairement que lorsqu'il devient comparable au clivage d'échange δ_0. Dans le cas des excitons chargés, les transitions interdites par les règles de sélectrion dipolaires

électriques dans l'orientation [001] deviennent permises dans l'orientation [111], et l'on observe un quadruplet radiatif même à faible champs $B_{z'}$. Ceci provient du fait qu'ici, l'échange coulombien électron-trou ne produit pas de structure fine pour les trions. Ces caractéristiques sont donc inhérentes aux boîtes quantiques sur substrat (111), et n'est pas corrélé à un abaissement de symétrie fortuit du potentiel de confinement, comme c'est le cas pour les boîtes (001), ou à la présence d'une asymétrie de contrainte, comme dans les boîtes d'InAs [50, 114].

Dans le cas des excitons neutres X^0, nous avons découvert de plus une dépendance fortement non monotone du clivage Zeeman des excitons "brillants" ($J_{z'}^{total} = \pm 1$) en fonction du champ magnétique appliqué (cf. Equation 3.3.2), résultant de l'effet conjugué de l'interaction d'échange et de l'effet Zeeman (Figure 3.5(a)-(c)). Lorsque le champ appliqué $B_{z'}$ augmente, le clivage Zeeman décroît d'abord pour atteindre des valeurs négatives, atteignant un minimum, puis croît avec le champ magnétique, s'annulant autour de $B_{z'}^0 \simeq 4.5$ T pour prendre des valeurs positives à fort champ.

Pour les boîtes présentant ce changement de signe du clivage Zeeman, la valeur exacte de $B_{z'}^0$ fluctue d'une boîte à l'autre. Le clivage entre états "brillants" induit par le champ peut être extrait directement du spectre de X^0 même en présence de l'interaction d'échange électron-trou anisotrope 1 en suivant la procédure décrite dans le supplément de la publication [28]. Les résultats sont reportés sur la Figure 3.5(d) et démontrent clairement le changement de signe du clivage Zeeman. Le clivage entre états brillants et leur dépendance au champ magnétique est très variable d'une boîte à l'autre. Ainsi la boîte II dont les caractéristiques spectrales d'émission sont très voisines de la boîte I (énergies de transition, quadruplet radiatif excitonique, valeurs des facteurs de Landé effectifs et énergies d'échanges), nous observons un clivage d'échange positif, fonction monotone croissante, mais non-linéaire, du champ magnétique (Figure 3.5(h)).

L'énergie du clivage Zeeman est en valeur absolue trois fois plus grand dans la boîte II que dans la boîte I. Les deux boîtes présentent une émission prononcée de leur états sombres, ceux-ci pésentant également un clivage Zeeman fonction monotone croissante du champ magnétique.

Nous présentons dans un deuxième temps une théorie microscopique, développée en collaboration étroite avec nos collègues de l'Institut A. F. Ioffe (St. Pétersbourg, Russie), du mélange entre états de trous lourds de composante moment angulaire $\pm$ 3/2 dans les boîtes " gouttelettes " de GaAs sur substrat (111)A. Les états mélangés sous champ magnétique $B_{z'} \neq 0$ s'écrivent: $|h,+\rangle = C_1 \,|+3/2\rangle' + C_2 \,|-3/2\rangle'$ et $|h,-\rangle = -C_2 \,|+3/2\rangle' + C_1 \,|-3/2\rangle'$ où les coefficients $C_{1(2)}$ sont déterminés uniquement par le rapport du termes non-diagonal au terme diagonal du tenseur de Landé g effectif pour les trous lourds g_{h2}/g_{h1}. La présence du coefficient C_2 ouvre deux canaux de recombinaison radiative supplémentaires associés aux transitions impliquant des transitions habituellement interdites ou des états nois pour les boîte (001).

Le modèle théorique proposé prend en compte la symétrie trigonale C_{3v} de ces boîtes résultant de leur forme typique révélée par microscopie à force atomique (Figure 3.2). Les calculs pour déterminer les états de trous ont été menés dans le formalisme de l'hamiltonien de Luttinger, en tenant compte du caractère trigonal spécifique du potentiel de confinement (Figure 3.9).

Le modèle présente un bon accord quantitatif avec les règles de sélection des transitions optiques observées expérimentalement, les intensités des transitions radiatives et les clivages

en énergie à la fois en champ magnétique longitudinal et transverse, pour les excitons neutres et chargés dans toutes les boîtes individuelles étudiées. Le tenseur gyromagnétique des trous, ainsi que le facteur de Landé des électrons ont pu être déterminés pour ce nouveau système.

La distorsion trigonale du potentiel de confinement parabolique dans le plan décrit par le terme proportionnel à $\propto \beta\rho^3 \cos 3\varphi$ de l'équation 3.3.8 mélange les états dont la composante de moment orbital selon z' diffère de ± 3. Nous insistons sur le fait que la théorie développée prédit des valeurs non nulles pour g_{h2} seulement pour des boîtes spécifiquement de symétrie trigonale. On remarque que pour les boîtes isotropes dans le plan (x,y) ou les boîtes possédant un plan de symétrie selon ce plan (de formes respectives en prisme cylindrique ou à base triangulaire), g_{h2} est strictement nul. L'opérateur hamiltonien de Luttinger utilisé au départ du calcul dans l'équation 3.3.3 est formulé dans l'approximation sphérique. De ce fait, sa formulation opératorielle est identique dans les directions [111] et [001] où il possède une expression simple. Le potentiel de confinement trigonal est ajouté ensuite pour les boîtes (111), et diffère bien sûr de celui des boîtes (001). Nos prédictions théoriques sont en parfait accord avec les résultats expérimentaux récents de la référence [150] ou des valeurs nulles de g_{h2} ont été obtenues pour des boîtes [111] en forme de disque insérées dans des nano-fils.

Deux autres mécanismes contribuant au mélange entre états $\pm 3/2$ sont décrits dans la partie théorique de la référence [136]: l'un repose sur des termes correctifs d'anisotropie portant sur l'hamiltonien de trou sous champ magnétique proportionnels au paramètre de Luttinger q, (voir Equation 3.3.11), et l'autre sur les termes cubiques par rapport au vecteur d'onde dans la bande de valence, prenant en compte le caractère non centro-symétrique du cristal de GaAs. Cependant nos estimations montrent que ces contributions ne peuvent à elles seules décrire les expériences de façon quantitative (les valeurs obtenues pour g_{h2} sont alors bien trop petites). Nos calculs du tenseur de Landé effectif pour les trous sont en très bon accord avec les estimations théoriques actuelles et nos résultats expérimentaux. Une relation simple entre composantes g_{h2} et g_{h1} a pu être établie, en très bon accord avec les valeurs expérimentales pour un grand nombre de boites.

Chapitre 4: Manipulation de charge et structure fine dans les boîtes quantigues de GaAs

Ce chapitre est centré sur l'étude des structures à charge ajustable dont la croissance a été effectuée[1] sur des substrats de GaAs orientés selon (001) et dopés n^+.

Les structures à charge ajustables ont été obtenues en déposant à la surface de l'échantillon une fine couche métallique constituée de 4 nm d'or et 4.1 nm d'alliage Nickel-Chrome, et une couche plus épaisse, non contine, comportant de 120 nm d'or et de 20 nm de titane, le tout constituant l'électrode de surface et réalisant ainsi une barrière de Schottky (cf. Figure 4.2). La couche fine est semi-transparente, permettant ainsi l'excitation et la détection de la photoluminescence des boîtes. La couche épaisse est suffisamment robuste pour permettre d'y souder des fils conducteurs fins. Elle présente de plus des ouvertures circulaires d'un rayon typique de 1 mm de façon à créer des zones où il est possible d'exciter et de détecter la photoluminescence. Une couche d'indium est déposée sur le substrat n^+ de l'échantillon, réalisant ainsi un contact ohmique. La tension de polarisation est appliquée entre l'électrode de surface et l'électrode arrière (cf. Figures 4.1 et 4.2).

Dans les échantillons non dopés intentionnellement l'exciton neutre X^0 et les excitons chargés $X^+(X^-)$ son observés simultanément sur les spectres intégrés temporellement, du fait des fluctuations de charges. Dans les structures à charge ajustable, les boîtes quantiques peuvent être chargées en appliquant une tension aux électrodes. Il en résulte la possibilité de contrôler de façon déterministe la charge électrique des boîtes insérées dans la partie intrinsèque de la structure. Grâce au blocage de Coulomb, il est ainsi possible de préparer des boîtes avec un, deux, ... électrons.

Dans toutes les boîtes étudiées, il est possible au moins d'observer sur l'émission les passages successifs de $X^+ \rightarrow X^0 \rightarrow X^-$ quand on augmente la tension (Figure 4.3). Les sauts en énergie correspondant au changement de la charge sont caractéristiques de ce type de structure [74], ainsi que l'effet Stark confiné sur les différentes excitations.

Cependant, des études détaillées menées sous champ magnétique transverse sont nécessaires pour identifier sans ambigüité les états de charge grâce aux structures fines des excitons et de leur complexes et leur caractéristiques d'émission. Nous avons ainsi développé une méthode entièrement analytique pour résoudre le problème des énergies et états propres pour les excitons neutres et chargés, y compris en champ transverse. Le modèle obtenu est ajusté simultanément sur les quatres raies des quadruplets émis avec un seul jeu de paramètres ; les facteurs g obtenus varient peu avec le degré de charge de l'exciton. Nous avons montré que l'on peut annuler le clivage de structure fine de l'exciton pour des champs magnétiques transverses modérés, ce qui représente une possibilité très intéressante pour la réalisation de sources efficaces de paires de photons intriqués en polarisation, tout comme dans les boîtes d'InAs [115].

Les propriétés magnéto-optiques des boîtes quantiques, qui dans ces échantillons sont de symétrie C_{2v} et sont orientées selon les axes cristallographiques [110] et $[1\bar{1}0]$, ont révélé les caractéristiques physiques intéressantes suivantes:

1 L'échantillon a été élaboré à l'Institut National de Science des Matériaux (NIMS) à Tsukuba au Japon dans le groupe de T. Mano, T. Kuroda et K. Sakoda.

i. Pour une base de polarisation en détection donnée et sous champ magnétique transverse donné (configuration de Voigt), les signes du paramètre de structure fine δ_1 et celui du facteur de Landé des trous lourds g_h changent lorsque l'on compare des boîtes dont l'axe principal d'élongation est orienté parallèlement à [110] et [1$\bar{1}$0], (Figure 4.14).
ii. Une étude approfondie montre que l'orientation de la boîte par rapport au champ magnétique est en fait essentielle pour déterminer le signe du facteur de Landé g_h indépendamment de l'orientation cristallographique. Les boîtes dont l'axe principal d'élongation est parallèle au champ magnétique présentent un facteur de Landé g_h opposé à celui des boîtes dont l'axe est orthogonal au champ (cf. Figure 4.15). Il est clair qu'ainsi on constate que g_h est bien anisotrope dans le plan, comme présumé à partir de l'étude des symétries.
iii. Une propriété remarquable présentée dans ce chapitre concerne l'anisotropie du facteur de Landé en champ magnétique transverse pour les électrons et les trous lourds (Figure 4.21 et Table 4.3). Ceci ouvre des perspectives intéressantes pour des études approfondies des facteurs gyromagnétiques dans les boîtes quantiques non-contraintes.
iv. Les raies des quadruplets émis par les excitons neutres et chargés se répartissent en deux doublets polarisées linéairement selon les directions [110] ou à [1$\bar{1}$0].]. Dans le cas des excitons neutres, le mélange entre états "brillants" ($J_z^{total} = \pm 1$) et "noirs" ($J_z^{total} = \pm 2$) est déterminé par les rapports entre les facteurs de Landé effectifs d'électron et de trou lourd au paramètre de clivage d'échange δ_0 entre les états brillants et noirs g_e/δ_0 et g_h/δ_0. La polarisation des raies "sombres" est déterminée par celle de leur composante "brillante". Ce mélange est de plus déterminé par la somme et la différence des facteurs g, conditionnant ainsi la force d'oscillateur des transitions optiques. Ainsi, lorsque les deux facteurs g s'équilibrent pour un état sombre de polarisation donnée, la transition associée peut devenir indétectable, alors que l'intensité de la raie sombre orthogonale reste élevée (Figure 4.16). Toutes ces observations restent valables lorsque le signe de g_h change.

Nous avons enfin montré expérimentalement, et confirmé par la modélisation, que l'on peut annuler le clivage de structure fine du doublet brillant de X^0 pour des champs magnétiques transverses modérés, ce qui représente une possibilité très intéressante pour la réalisation de sources efficaces de paires de photons intriqués en polarisation, tout comme dans les boîtes d'InAs [115].

L'observation de valeurs très élevées, proches de l'unité, pour le facteur de Landé de l'électron est discutée dans la section 4.3.2 où nous en proposons une explication qualitative, reposant sur la localisation très forte de celui-ci dans la boîte quantique. La correction par rapport au facteur de Landé dans le vide $g_0 \approx 2$, que l'on peut estimer par un calcul de perturbation au deuxième ordre dans le cadre de la théorie $\mathbf{k} \cdot \mathbf{p}$, est ici réduite. Cette situation est analogue à celle rencontrée dans certains centre paramagnétiques [160] (Figure 4.14).

L'ensemble de ce chapitre ouvre des perspectives intéressantes pour des études approfondies sur le facteur gyromagnétique des électrons et des trous dans les boîtes quantiques non contraintes.

Chapitre 5: Effets nucléaires dans les boîtes quantiques de GaAs élaborées sur substrat [111]

Les noyaux atomiques du gallium et de l'arsenic ont tous ont un spin nucléaire $I=3/2$. Dans le GaAs massif, chaque noyau interagit donc avec ses voisins par interaction dipolaire. La force de cette interaction peut être caractérisée par un champ magnétique effectif local B_L de l'ordre de $B_L \approx 0.15$ mT [6], dont l'orientation est aléatoire et fluctue lentement dans le temps. Ainsi, l'application d'un champ externe $B_{ext} > B_L$ est-ellle nécessaire pour masquer l'interaction dipolaire entre noyaux et permettre ainsi la construction d'une polarisation nucléaire en régime dynamique (DNP) par pompage optique orienté des électrons via l'effet Overhauser. Une des caractéristiques étonnantes des boîtes quantiques est de permettre d'obtenir une polarisation nucléaire dynamique en l'absence de champ magnétique externe [27, 167, 168, 28, 169].Dans le cas de boîtes obtenues par méthode Stranski-Krastanov, certains auteurs ont invoqué la présence d'effets quadrupolaires forts induits par les contraintes [168] pour expliquer l'immunité de la polarisation nucléaire vis-à-vis du champ local. Nous présentons ici les premières observations de DNP sur des boîtes quantiques non contraintes, i.e. en l'absence d'effets quadrupolaires appréciables.

Ainsi, on a pu mesurer un décalage Overhauser de 16 μeV sur l'énergie des électrons de conduction, correspondant à une polarisation nucléaire de 12 % dans les boîtes de GaAs en champ magnétique externe nul (Figure 5.1). En l'absence d'effet quadrupolaire, c'est le champ Knight moyen de l'électron photo-généré qui masque ici le champ local. Nous avons exploré en détail le rôle du fort champ magnétique effectif perçu par les noyaux induit par la présence d'un électron possédant une orientation de spin bien déterminée, appelé champ Knight. Celui-ci est d'après nos mesures, de l'ordre de 15 mT pour la plupart des boîtes (cf. Figure 5.3). Il est donc de fait bien plus important que le champ local. Par ailleurs les champs Knight obtenu dans les boîtes GaAs sont plus d'un ordre de grandeur plus forts que ceux observés typiquement dans les boîtes d'InAs/GaAs contraintes [27] (figure 5.2).

Nous avons montré que le champ Knight est proportionnel au spin moyen des électrons $\langle \hat{\boldsymbol{S}}^e \rangle$ (Equation 5.1.1). L'amplitude et le sens du spin moyen électronique dans le trion X^+ est contrôlée par la polarisation du faisceau laser d'excitation. Cette dernière est ajustée au moyen d'une lame retard programmable. Le champ Knight est estimé en lui opposant un champ magnétique externe en configuration Faraday, ce qui diminue la polarisation de l'électron et la valeur du champ Overhauser. Nous avons ainsi vérifié que le champ magnétique effectif perçu par les noyaux (champ Knight) est bien une fonction linéaire du spin moyen de l'électron généré dans la boîte (cf. Figure 5.4).

Les rôles conjoints du champ Knight et du champ nucléaire induit par effet Overhauser ont été étudiés en champ magnétique transverse (configuration de Voigt). Le spin moyen des électrons photo-générés orienté initialement le long de l'axe de croissance z' effectue un mouvement de précession autour du champ magnétique pendant leur temps de vie, ce qui a pour effet de les dépolariser partiellement ou totalement selon l'intensité du champ magnétique. Ce phénomène s'observe directement sur le taux de polarisation de la lumière émise par la boîte, qui décroît lorsque le champ magnétique augmente. Nous mesurons le taux de polarisation de la photoluminescence d'une boîte individuelle en fonction de la puissance d'excitation, afin d'évaluer l'impact de la DNP sur la loi de dépolarisation en fonction du champ magnétique appliqué (Figure 5.5 (a,b)). A très faible puissance, la DNP est pratiquement absente, et nous retrouvons les profils Hanle lorentziens habituels

(Figure 5.5 (c,d) tracés en points verts). A plus forte puissance, les profils se déforment considérablement aux faibles champs magnétiques, et ne rejoingnent la forme classique qu'aux très forts champs magnétiques, Figure 5.5 (a,b).

Nous avons attribué la distorsion des profils de dépolarisation Hanle en faible champ et sous forte puissance à la présence d'un champ Knight appréciable. En effet, le spin moyen électronique croît comme la fraction temporelle relative f_e (cf. Equation 5.1.1)où la boîte est occupée par un électron de conduction (i.e. par un trion X) . Ces expériences sont à rapprocher de celles pratiqués sur des boîtes quantiques d'InGaAs dans GaAs où un effet Hanle anormal a pu être observé [172], présentant de plus un comportement bistable avec le champ magnétique. Dans ces échantillons contraints, les effets quadrupolaires ont été invoqués comme la cause de l'apparition de ces effets. Ici en revanche, les boîtes de GaAs sont non contraintes, et les effets quadrupolaires sont négligeables. Cependant, l'écart observé par rapport aux profils Hanle classique reste présent, sans toutefois présenter d'effets de bistabilité, et repose entièrement sur la présence d'un champ Knight plus important à faible champ. Résumons les caractéristiques de l'effet Hanle sur les boîtes de GaAs:

(i) Les courbes de dépolarisation Hanle sont élargies à forte puissance, le paramètre d'élargissement lorentzien $B_{1/2}$ augmente. Ceci traduit une diminution du temps de vie de spin τ_s^* par rapport à sa valeur initiale. Notons que cette dernière s'identifie au temps de vie radiatif du trion à faible puissance, le spin de l'électron étant relativement stable dans la boîte. Nous attribuons cette diminution essentiellement à un phénomène de recapture d'un électron pour former un biexciton, ou tout autre processus conduisant à la formations de complexes excitoniques autres que X^+.

(ii) A faible champ magnétique, les courbes de dépolarisation prennent, à forte puissance, une forme caractéristique en "W" très différente des profils Hanle lorentziens habituels, réminiscence des expériences de dépolarisation Hanle pratiquées sur les électrons localisés dans les donneurs de GaAs massif [6]. Ceci peut être observé plus clairement encore sur la Figure 5.5 (b)), où nous avons représenté l'écart par rapport au profil Hanle lorentzien déduit des régions correspondant aux forts champs magnétiques ($B \gg B_{1/2}$). Les maxima de la courbe des écarts en fonction du champ magnétique transverse, elle aussi en "W", coïncident exactement avec le maximum et les épaulements de la courbe expérimentale représentant le décalage Overhauser mesuré (i.e. le champ nucléaire longitudinal) en fonction du champ.

Nous avons décrit le phénomène de dépolarisation Hanle en présence d'effets nucléaires par un modèle basée sur l'approche faite dans la référence [6]qui postule l'existence d'une température de spin, mais ici dans le cas où le champ local est supplanté par un fort champ Knight dans le domaine des faibles champs externes. Le modèle théorique reproduit raisonnablement bien les caractéristiques courbes expérimentales, confirmant la forte contribution du champ Knight au champ magnétique effectif total perçu par les noyaux. De plus l'amplitude du champ Knight déduit des ajustements du modèle en champ transverse est très voisine de celle déterminée en configuration Faraday.

En corollaire, les mesures d'effet Hanle permettent de déterminer sans ambigüité le signe du facteur de Landé effectif des électrons de conduction.

Chapitre 6: conclusions et perspectives

Nous avons étudié effectué dans ce mémoire des études de magnéto-luminescence sur des boîtes quantiques individuelles de GaAs insérées dans une matrice de GaAlAs, boîtes qui se distinguent de la plupart des systèmes étudiés par l'absence des contraintes. Nous avons pu mesurer l'impact de l'orientation cristalline du substrat sur lequel s'effectue la croissance de ces boîtes sur les propriétés magnéto-optiques. Dans les boîtes élaborées sur substrat (111)A, sous champ magnétique longitudinal en configuration Faraday, les transitions interdites pour l'orientation (001) deviennent ici permises, à la fois pour les excitons neutres et chargés. Pour l'exciton neutre, un comportement non monotone de l'éclatement des états "brillants" a pu être observé et modélisé, celui-ci s'annulant et changeant de signe pour un champ magnétique non nul. Cet effet a pu être interprété comme du a l'action conjuguée entre l'échange électron-trou et l'effet Zeeman, et le mélange des états $|\pm 3/2\rangle$ induit par le champ longitudinal, une propriété inhérente au groupe ponctuel C_{3v} caractérisant la symétrie de la boîte. Par contre, en champ transverse en configuration de Voigt, on observe que seul subsiste l'effet Zeeman sur l'électron de conduction, comme on le prévoit par la théorie des groupes. Enfin, un modèle théorique est proposé[1] permettant de donner une loi générale simple liant les deux terme du tenseur gyromagnétique des trous lourds.

Nous avons pu présenter les premières expériences pratiquées sur des structures à boîtes quantique GaAs "gouttelettes" à charge ajustable, élaborées sur substrat orienté (001). Nous avons pu ainsi démontrer la charge progressive des boîtes électron par électron d'une boîte vide jusqu'à trois électrons dans certaines boîtes, ce qui se traduit par l'apparition de raies d'émissions associées au complexe X^{3-}. Cependant, toute les boîtes ne présentent pas les mêmes caractéristiques vis-à-vis de la charge. Cependant, nous avons pu observer dans toutes les boîtes le passage abrupt entre les régimes d'émission $X^+ \rightarrow X^0 \rightarrow X^-$ en augmentant la tension.

La structure fine des excitons a été étudiée en détail et analysée au moyen d'un modèle analytique y compris en champ transverse permettant d'établir les états et énergies propres. Pour ces boîtes quantiques qui sont de symétrie C_{2v} et alignées selon des directions cristallographiques [110] et [1$\bar{1}$0], nous avons mis au jour des propriétés magnéto-optiques intéressantes en champ magnétique transverse:

i.les signes du paramètre de structure fine δ_1 ainsi que celui des facteurs de Landé transverse du trou g_h change lorsque l'axe principal de la boîte passe de l'orientation [110] à [1$\bar{1}$0].

ii. Le signe du facteur g des trous est déterminé par l'orientation de l'axe principal de la boîte par rapport au champ magnétique, indépendamment de son orientation cristallographique.

iii. Le modèle développé permet de prévoir le mélange les états excitoniques "brillants" et "noirs" par le champ magnétique et le transfert correspondant de force d'oscillateur. La polarisation des raies "sombres" est déterninée par celle de leur composante brillante.

Nous avons observé la polarisation dynamique des noyaux à champ nul dans les boîtes

1 Celui-ci a été développé en collaboration avec E. L. Ivchenko, M. M. Glazov and M. V. Durnev de l'Institut A.F. Ioffe de St. Pétersbourg en Russie

quantiques sans contraintes élaborées sur substrat (111)A. Les décalages Overhauser mesurés s'élèvent à 15-16 μeV, correspondant à un champ nucléaire de 0.25 T environ. Dans les boîtes contraintes épitaxiées en régime Stranski-Krastanov, la dépolarisation du champ nucléaire par effet dipolaire est masquée par les effets quadrupolaires importants dont elles sont le siège. Ceux-ci réduisent cependant la polarisation nucléaire obtenue à champ externe nul. Les boîtes "gouttelettes" étudiées dans ce travail sont elles non contraintes, et les interactions dipolaires sont masquées par le fort champ Knight des électrons. Les valeurs mesurées pour ce dernier s'élèvent à $B_K^{max} \approx 15 - 18$ mT à champ nul, c'est-à-dire un ordre de grandeur plus élevées que dans les boîtes contraintes d'InGaAs dans GaAs. Nous avons établi expérimentalement sa dépendance linéaire par rapport au spin moyen des électrons photo-générés.

En champ magnétique transverse, nous avons observé des déviations significatives par rapport à l'effet Hanle normal dans le domaine des faibles champs. Celles-ci sont dues à l'action conjointe du champ Knight et du champ externe pour les noyaux, et à celle du champ Overhauser et du champ externe pour les électrons. Sur l'hypothèse de l'existence d'une température de spin nucléaire, Nous avons développé un modèle auto-cohérent dans le régime où le champ Knight supplante le champ local, et avons pu décrire les principales caractéristiques physiques des courbes de dépolarisation du spin électronique sous champ transverse. Les valeurs trouvées pour le champ Knight sont en bon accord avec celles mesurées en champ longitudinal. Enfin, ce modèle permet de déterminer sans ambigüité le signe du facteur de Landé effectif de l'électron dans la boîte quantique.

L'ensemble de ces travaux montre que les boîtes quantiques de GaAs élaborées par épitaxie "gouttelette" sont des objets prometteurs pour la réalisation de sources de photons intriqués en polarisation. Par ailleurs, l'absence de transitions interdites pour les boîtes élaborées sur substrat (111) permet d'envisager des mesures précises de l'effet Overhauser à la fois sur les électrons et les trous lourds [175].

APPENDIX A

Appendix

A.1 The heavy-hole Zeeman Hamiltonian in the basis $|3/2\rangle', |-3/2\rangle'$

The effective Hamiltonian in longitudinal magnetic field can be described in terms of method of the invariants:

$$\hat{H} = B_{z'}\hat{S}_{z'}^{eff} \in \Gamma_2 \otimes \Gamma_2 = \Gamma_1. \tag{A.1.1}$$

Hereafter the Hamiltonian $\hat{H}$ is a scalar. The two conditions are:

- the presentations are of dimension 2
- the condition $\Gamma_{\mathrm{j}} \otimes \Gamma_2 \supset \Gamma_1$ has only one solution in this group: $\Gamma_{\mathrm{j}} = \Gamma_2$.

Consequently the effective Hamiltonian can be now written:

$$\hat{H} = B_{z'}\hat{O}(\Gamma_2), \tag{A.1.2}$$

with $\hat{S}_{z'}^{eff} = \hat{O}(\Gamma_2)$.

The heavy-hole states can be written as:

$$\phi\left(\frac{3}{2},m\right) \equiv \left|\frac{3}{2},m\right\rangle \equiv |m\rangle\,, m = \pm\frac{3}{2}.$$

The following relations can be helpful by writing the bra and ket elements as combination of heavy-hole states:

$$\langle\Psi\left(\Gamma_5\right)| \in \Gamma_5^* = \Gamma_6 \text{ and } \langle\Psi\left(\Gamma_6\right)| \in \Gamma_6^* = \Gamma_5.$$

So the bra and ket elements are given by:

$$|\Psi\left(\Gamma_5\right)\rangle \equiv -i\left|\frac{3}{2}\right\rangle + \left|-\frac{3}{2}\right\rangle,\ |\Psi\left(\Gamma_6\right)\rangle \equiv -\left|\frac{3}{2}\right\rangle + i\left|-\frac{3}{2}\right\rangle, \tag{A.1.3}$$

and

$$\langle \Psi\left(\Gamma_5\right)| \equiv i\left\langle \frac{3}{2}\right| + \left\langle -\frac{3}{2}\right|,\ \langle \Psi\left(\Gamma_6\right)| \equiv -\left\langle \frac{3}{2}\right| - i\left\langle -\frac{3}{2}\right|. \tag{A.1.4}$$

The spin operator acts on the valence states like[Koster]:

$$\hat{S}_{z'}^{eff}\left|\Psi\left(\Gamma_5\right)\right\rangle = -c_1\left|\Psi\left(\Gamma_6\right)\right\rangle,\ \hat{S}_{z'}^{eff}\left|\Psi\left(\Gamma_6\right)\right\rangle = -c_1\left|\Psi\left(\Gamma_5\right)\right\rangle. \tag{A.1.5}$$

Further $|\Psi(\Gamma_5)\rangle$ will be abbreviated to $|\Psi_5\rangle$ and $|\Psi(\Gamma_6)\rangle$ to $|\Psi_6\rangle$.

Now it can be checked which matrix elements vanish and which do not vanish.

$$\begin{aligned}\langle\Psi_5|\,\hat{S}_{z'}^{eff}\,|\Psi_5\rangle &\in \Gamma_5^* \otimes (\Gamma_2 \otimes \Gamma_5)\\ &= \Gamma_6 \otimes (\Gamma_2 \otimes \Gamma_5)\\ &= \Gamma_6 \otimes \Gamma_6\\ &= \Gamma_2 \neq \Gamma_1\\ &\Rightarrow \langle\Gamma_5|\,\hat{S}_{z'}^{eff}\,|\Gamma_5\rangle = 0.\end{aligned} \tag{A.1.6}$$

Similar for another diagonal matrix element:

$$\begin{aligned}\langle\Psi_6|\,\hat{S}_{z'}^{eff}\,|\Psi_6\rangle &\in \Gamma_6^* \otimes (\Gamma_2 \otimes \Gamma_6)\\ &= \Gamma_5 \otimes (\Gamma_2 \otimes \Gamma_6)\\ &= \Gamma_5 \otimes \Gamma_5\\ &= \Gamma_2 \neq \Gamma_1\\ &\Rightarrow \langle\Gamma_6|\,\hat{S}_{z'}^{eff}\,|\Gamma_6\rangle = 0.\end{aligned} \tag{A.1.7}$$

We see that both diagonal matrix elements are zero. In contrary the non-diagonal matrix elements do not vanish:

$$\begin{aligned}\langle\Psi_5|\,\hat{S}_{z'}^{eff}\,|\Psi_6\rangle &\in \Gamma_5^* \otimes (\Gamma_2 \otimes \Gamma_6)\\ &= \Gamma_6 \otimes \Gamma_5 = \Gamma_1\\ &\Rightarrow \langle\Gamma_5|\,\hat{S}_{z'}^{eff}\,|\Gamma_6\rangle \neq 0.\end{aligned} \tag{A.1.8}$$

and

$$\begin{aligned}\langle\Psi_6|\,\hat{S}_{z'}^{eff}\,|\Psi_5\rangle &\in \Gamma_6^* \otimes (\Gamma_2 \otimes \Gamma_5)\\ &= \Gamma_5 \otimes \Gamma_6 = \Gamma_1\\ &\Rightarrow \langle\Gamma_6|\,\hat{S}_{z'}^{eff}\,|\Gamma_5\rangle \neq 0.\end{aligned} \tag{A.1.9}$$

The matrix of the spin operator in the basis $\{|\Psi_5\rangle, |\Psi_6\rangle\}$ is given by:

$$\begin{array}{c|cc} \hat{S}_{z'}^{eff} & |\Psi_5\rangle & |\Psi_6\rangle \\ \hline |\Psi_5\rangle & 0 & c \\ |\Psi_6\rangle & c^* & 0. \end{array} \tag{A.1.10}$$

Indeed we need a matrix in the basis $\left\{\left|\frac{3}{2}\right\rangle', \left|-\frac{3}{2}\right\rangle'\right\}$. So now the states $\left|\frac{3}{2}\right\rangle'$ and $\left|-\frac{3}{2}\right\rangle'$ must be expressed as combination of $|\Psi_5\rangle$ and $|\Psi_6\rangle$. After a few calculations the desired states are given by:

$$\begin{aligned} \left|\frac{3}{2}\right\rangle' &= \frac{1}{2}\left[i\,|\Psi_5\rangle - |\Psi_6\rangle\right] \\ \left|-\frac{3}{2}\right\rangle' &= \frac{1}{2}\left[|\Psi_5\rangle - i\,|\Psi_6\rangle\right]. \end{aligned} \tag{A.1.11}$$

Now all matrix elements in the basis $\left\{\left|\frac{3}{2}\right\rangle', \left|-\frac{3}{2}\right\rangle'\right\}$ can be easily calculated.

$$\begin{aligned} \left\langle \frac{3}{2},\frac{3}{2}\right| \hat{S}_{z'}^{eff} \left|\frac{3}{2},\frac{3}{2}\right\rangle' &= \frac{1}{4}\left[\left(-i\,\langle\Psi_5| - \langle\Psi_6|\right)\hat{S}_{z'}^{eff}\left(i\,|\Psi_5\rangle - |\Psi_6\rangle\right)\right] \\ &= \frac{1}{4}\left[ic - ic^*\right] = \frac{i}{4}\left[c - c^*\right], \end{aligned} \tag{A.1.12}$$

$$\begin{aligned} \left\langle \frac{3}{2},-\frac{3}{2}\right| \hat{S}_{z'}^{eff} \left|\frac{3}{2},-\frac{3}{2}\right\rangle' &= \frac{1}{4}\left[\left(\langle\Psi_5| + i\,\langle\Psi_6|\right)\hat{S}_{z'}^{eff}\left(|\Psi_5\rangle - i\,|\Psi_6\rangle\right)\right] \\ &= \frac{1}{4}\left[-ic + ic^*\right] = -\frac{i}{4}\left[c - c^*\right], \end{aligned} \tag{A.1.13}$$

$$\begin{aligned} \left\langle \frac{3}{2},-\frac{3}{2}\right| \hat{S}_{z'}^{eff} \left|\frac{3}{2},\frac{3}{2}\right\rangle' &= \frac{1}{4}\left[\left(\langle\Psi_5| + i\,\langle\Psi_6|\right)\hat{S}_{z'}^{eff}\left(i\,|\Psi_5\rangle - |\Psi_6\rangle\right)\right] \\ &= \frac{1}{4}\left[-c - c^*\right] = -\frac{i}{4}\left[c + c^*\right], \end{aligned} \tag{A.1.14}$$

$$\begin{aligned} \left\langle \frac{3}{2},\frac{3}{2}\right| \hat{S}_{z'}^{eff} \left|\frac{3}{2},-\frac{3}{2}\right\rangle' &= \frac{1}{4}\left[\left(-i\,\langle\Psi_5| - \langle\Psi_6|\right)\hat{S}_{z'}^{eff}\left(|\Psi_5\rangle - i\,|\Psi_6\rangle\right)\right] \\ &= \frac{1}{4}\left[-c - c^*\right] = -\frac{i}{4}\left[c + c^*\right]. \end{aligned} \tag{A.1.15}$$

So we obtained all matrix elements and the matrix in the basis $\left\{\left|\frac{3}{2}\right\rangle', \left|-\frac{3}{2}\right\rangle'\right\}$ is then given:

$$\begin{array}{c|cc} \hat{S}^{eff}_{z'} & \left|\frac{3}{2}\right\rangle' & \left|-\frac{3}{2}\right\rangle' \\ \hline \left|\frac{3}{2}\right\rangle' & i\left(\frac{c-c^*}{4}\right) & -\left(\frac{c+c^*}{4}\right) \\ \left|-\frac{3}{2}\right\rangle' & -\left(\frac{c+c^*}{4}\right) & -i\left(\frac{c-c^*}{4}\right). \end{array} \tag{A.1.16}$$

We introduce following relations:

$$g_{h1} \equiv i\left(\frac{c-c^*}{2}\right) = \mathrm{Im}(c) \tag{A.1.17a}$$

$$g_{h2} \equiv -\left(\frac{c+c^*}{2}\right) = -\mathrm{Re}(c). \tag{A.1.17b}$$

With the introduced hole-g-factors the matrix is given by:

$$\begin{array}{c|cc} \hat{S}^{eff}_{z'} & \left|\frac{3}{2}\right\rangle' & \left|-\frac{3}{2}\right\rangle' \\ \hline \left|\frac{3}{2}\right\rangle' & \frac{g_{h1}}{2} & g_{h2} \\ \left|-\frac{3}{2}\right\rangle' & g_{h2} & -i\frac{g_h 1}{2} \end{array} \tag{A.1.18}$$

and the spin operator can be rewritten as:

$$\hat{S}^{eff}_{z'} = g_{h1}\frac{\hat{\sigma}_{z'}}{2} + g_{h2}\frac{\hat{\sigma}_{x'}}{2}, \tag{A.1.19}$$

with Pauli matrices $\hat{\sigma}_{z'}$ and $\hat{\sigma}_{x'}$. The heavy-hole Zeeman Hamiltonian in the basis $\left\{\left|\frac{3}{2}\right\rangle', \left|-\frac{3}{2}\right\rangle'\right\}$ is given by:

$$\mathscr{H}_{\boldsymbol{B}} = \frac{1}{2}\mu_B B_{z'} \begin{bmatrix} g_{h1} & g_{h2} \\ g_{h2} & -g_{h1} \end{bmatrix} \tag{A.1.20}$$

A.2 g-factor calculation and Coulomb interaction used in chapter 3

A.2.1 Calculation of g_{h1}

The corresponding contribution to the ground state of the 3/2 heavy hole can be found in the second order of the perturbation theory from the following relation

$$\Delta E_{B,3/2} \equiv \frac{1}{2}\Delta g_{h1}\mu_B B_z = \tag{A.2.21}$$

$$\sum_{lp\pm} \frac{\left\langle \Psi^{hh}_{3/2;11} | \hat{\mathscr{H}}_{\Gamma_8} | \Psi^{lh}_{\pm 1/2;lp} \right\rangle \left\langle \Psi^{lh}_{\pm 1/2;lp} | \hat{\mathscr{H}}_{\Gamma_8} | \Psi^{hh}_{-3/2;11} \right\rangle}{E^{hh}_{z,1} + E^{hh}_{\|,1} - E^{lh}_{z,l} - E^{lh}_{\|,p}},$$

where summation includes all states of the light hole, described by the two indices l and p. Using the hole envelopes one can rewrite (A.2.21) in the form

$$\begin{aligned}\Delta E_{B,3/2} &= \sum_{lp}(E^{hh}_{z,1}+E^{hh}_{\parallel,1}-E^{lh}_{z,l}-E^{lh}_{\parallel,p})^{-1} \\ &\times\left(\left\langle F^{hh}_1\psi^{hh}_1|\tilde{H}|F^{lh}_l\psi^{lh}_p\right\rangle\left\langle F^{lh}_l\psi^{lh}_p|\tilde{H}^*|F^{hh}_1\psi^{hh}_1\right\rangle+\left\langle F^{hh}_1\psi^{hh}_1|\tilde{I}|F^{lh}_l\psi^{lh}_p\right\rangle\left\langle F^{lh}_l\psi^{lh}_p|\tilde{I}^*|F^{hh}_1\psi^{hh}_1\right\rangle\right) .\end{aligned} \tag{A.2.22}$$

Here operators $\tilde{H}$ and $\tilde{I}$ are the components of the Hamiltonian (3.3.3) modified in the presence of magnetic field:

$$\tilde{H} = -\sqrt{3}Bk_z\left[k_x - \mathrm{i}k_y + \frac{e}{c\hbar}(A_x - \mathrm{i}A_y)\right] ,$$

$$\tilde{I} = -\frac{\sqrt{3}}{2}B\left[(k_x-\mathrm{i}k_y)^2 + \frac{2e}{c\hbar}\left\{(k_x-\mathrm{i}k_y)(A_x-\mathrm{i}A_y)\right\}\right] ,$$

$k_\alpha = -\mathrm{i}\partial/\partial x_\alpha$, the curly brackets denote a symmetrized product of the corresponding operators. In the calculation of the energy shift by means of Equation (A.2.22) one has to take only linear in the magnetic field contributions. In the limit $L/a \ll 1$ the energy denominator in Equation (A.2.22) can be expanded in powers of this ratio. Performing summation over the index p we directly arrive at equation (3.3.12) from the main text.

A.2.2 Calculation of g_{h2}

Starting from Equation (3.3.16) and using the components of the Luttinger Hamiltonian $\tilde{H}, \tilde{I}$ in the magnetic field we arrive at

$$\begin{aligned}g_{h2} = \frac{12\hbar^2\gamma^2}{m_0L}\sum_{lp}\frac{\varkappa_l\rho_l}{E^{hh}_{z,1}+E^{hh}_{\parallel,1}-E^{lh}_{z,l}-E^{lh}_{\parallel,p}} \\ \times\left(\frac{1}{2}\left\langle\tilde{\psi}^{hh}_1\left|\nabla^2_-\right|\psi^{lh}_p\right\rangle\left\langle\psi^{lh}_p\,|r_-|\,\tilde{\psi}^{hh}_1\right\rangle\right. \\ \left.+\left\langle\tilde{\psi}^{hh}_1\,|\nabla_-|\,\psi^{lh}_p\right\rangle\left\langle\psi^{lh}_p\,|\{\nabla_- r_-\}|\,\tilde{\psi}^{hh}_1\right\rangle\right) ,\end{aligned} \tag{A.2.23}$$

where $r_- = x - \mathrm{i}y \propto \mathrm{e}^{-\mathrm{i}\varphi}$, $\nabla_- = \partial/\partial x - \mathrm{i}\partial/\partial y \propto \mathrm{e}^{-\mathrm{i}\varphi}$. Note that at $\beta = 0$ the mixing described by Equation (A.2.23) vanishes because in this case the matrix elements of operators proportional to $\mathrm{e}^{-\mathrm{i}\varphi}$ and $\mathrm{e}^{-2\mathrm{i}\varphi}$ cannot be nonzero simultaneously.

If $L/a \ll 1$, we can neglect the in-plane energies $E^h_{\parallel,p}$ in the denominator of Equation (A.2.23). Then the summation in Equation (A.2.23) over the index p can be performed analytically, and in the first order in $L/a \ll 1$ we obtain formula (3.3.17).

A.2.3 Coulomb interaction

The systematic differences between off-diagonal g-factors g_{h2} for X^+ and X^- trions seen in Table A.1 indicate a nonnegligible role of the Coulomb interaction. Indeed, the value of g_{h2} found from the spectrum of X^+ trion radiative recombination corresponds to the off-diagonal g-factor of resident hole, while the value g_{h2} extracted from the X^- spectrum

gives the g-factor of the hole in a trion.

To analyze the Coulomb effect in an X^- trion we use the adiabatic approximation, separate electron and hole motions and introduce an effective in-plane potential induced by two electrons and acting on a hole of the negatively charged trion [134]

$$V_C^{\text{eff}}(\rho_h) = -2\frac{e^2}{\epsilon_b}\int \frac{|\psi^e(\rho_e)|^2}{|\rho_e - \rho_h|}d\rho_e \,, \tag{A.2.24}$$

where ϵ_b is the static dielectric constant of the dot material, $\psi^e(\rho_e)$ is the wavefunction of the in-plane electronic ground state, $\rho_{e,h}$ are the electron and hole in-plane coordinates. If the trigonal distortion of the electronic state is disregarded, its wavefunction can approximately be described by a Gaussian as

$$\Psi_e(\rho_e) = \frac{1}{\sqrt{\pi}a_e}\exp\left(-\frac{\rho_e^2}{2a_e^2}\right), \tag{A.2.25}$$

where a_e is the localization radius of an electron. In this case the integral in (A.2.24) can be calculated analytically and the effective Coloumb potential reduces to

$$V_C^{\text{eff}}(\rho_h) = -2\frac{e^2\sqrt{\pi}}{\epsilon_b a_e}\exp\left(-\frac{\rho_h^2}{2a_e^2}\right) I_0\left(\frac{\rho_h^2}{2a_e^2}\right) \,, \tag{A.2.26}$$

where $I_0(x)$ is the modified Bessel function of the first kind. This potential is axially symmetric and, hence, leads to a reduction of the triangularity of the quantum dot and decrease in g_{h2}. If the confining potential for the electron is much stronger than that for the hole, $a_e \ll a_h$, the effective potential (A.2.26) reduces to that of the point charge $V_C^{\text{eff}} = -2e^2/(\epsilon_b\rho_h)$. An estimation shows that the Coulomb-induced correction δg_{h2} to the g_{h2} absolute value is negative and equals to $\delta g_{h2} \approx ?$.

A.3 Tables of the extracted parameters of all investigated QDs in Faraday and Voigt geometries

A.3.1 Table of the extracted parameters of all investigated (111)A QDs in Faraday and Voigt geometries

Table A.1: The extracted coefficients and parameters of all investigated (111)A QDs for Faraday $B||\vec{e}_z$ and Voigt $B\perp\vec{e}_z$ configurations.

		QD I		QD II		QD III		QD IV		QD V	
		$B\|\|\vec{e}_z$	$B\perp\vec{e}_z$	$B\|\|\vec{e}_z$	$B\perp\vec{e}_z$	$B\|\|\vec{e}_z$	$B\perp\vec{e}_z$	$B\|\|\vec{e}_z$	$B\perp\vec{e}_z$	$B\|\|\vec{e}_z$	$B\perp\vec{e}_z$
X^0	E_0 (eV)	1.81032		1.79581		1.81968		1.8142		1.82081	
	$\delta_0(\mu\text{eV})$	362		347.8		422.7		325.3		317.2	
	g_e	0.47	0.769	0.44	0.755	0.49	0.757	0.47	0.796	0.5	0.785
	g_h	0.71	0.072	0.72	0.008	1.16	0.025	0.72	0.006	0.73	0.058
	$\|g_{h2}\|$	0.50	–	0.68	–	0.42	–	0.59	–	0.65	–
X^+	E_0 (eV)	1.80974		1.79388		–		1.81307		1.81929	
	g_e	0.47	0.792	0.44	0.782	–	–	0.47	0.841	0.50	0.814
	g_h	0.71	0.071	0.72	0.006	–	–	0.72	0.029	0.73	0.057
	$\|g_{h2}\|$	0.62	–	0.72	–	–	–	0.70	–	0.72	–
X^-	E_0 (eV)	1.80366		1.78963		1.8127		1.8077		1.81446	
	g_e	0.49	0.73	0.46	0.742	0.51	0.729	0.48	0.798	0.5	–
	g_h	0.83	0.074	0.71	0.021	1.21	0.018	0.79	0.006	0.74	–
	$\|g_{h2}\|$	0.53	–	0.60	–	0.33	–	0.57	–	0.57	–
		QD VI		QD VII		QD VIII		QD IX			
		$B\|\|\vec{e}_z$	$B\perp\vec{e}_z$	$B\|\|\vec{e}_z$	$B\perp\vec{e}_z$	$B\|\|\vec{e}_z$	$B\perp\vec{e}_z$	$B\|\|\vec{e}_z$	$B\perp\vec{e}_z$		
X^0	E_0 (eV)	1.79513		1.81651		1.7727		1.7716			
	$\delta_0(\mu\text{eV})$	380.7		302		385		395			
	g_e	0.44	–	0.48	–	0.3757	–	0.3811	–		
	g_h	0.72	–	0.80	–	0.6583	–	0.6836	–		
	$\|g_{h2}\|$	0.56	–	0.69	–	0.45	–	0.6472	–		
X^+	E_0 (eV)	1.79349		1.81517		1.77049		1.76897			
	g_e	0.44	–	0.47	0.813	0.3757	–	0.3811	–		
	g_h	0.72	–	0.75	0.001	0.6583	–	0.6836	–		
	$\|g_{h2}\|$	0.68	–	0.71	–	0.61	–	0.6789	–		
X^-	E_0 (eV)	1.78686		1.81025		1.77049		1.76897			
	g_e	0.47	–	0.49	0.764	0.4178	–	0.4069	–		
	g_h	0.81	–	0.80	0	0.672	–	0.765	–		
	$\|g_{h2}\|$	0.53	–	0.50	–	0.2357	–	0.487	–		

A.3.2 Table of the extracted parameters of all investigated (100) QDs

Table A.2: The extracted coefficients and parameters of all investigated (100) QDs for Voigt $B \perp \vec{e}_z$ configuration.

		QD I	QD II	QD IV	QD V	QD VII	QD IX	QD X	QD XI
X^0	$\delta_0(\mu\text{eV})$	362	296	526	367	387	507	–	–
	$\delta_1(\mu\text{eV})$	-180	-17.2	-340	153	-287	-250	-266	-207
	$\delta_2(\mu\text{eV})$	–	-14	-93	–	–	–	–	–
	g_e	0.804	0.656	1.005	0.654	0.827	–	–	–
	g_h	-0.501	-0.317	-0.590	0.563	-0.611	–	–	–
X^+	g_e	0.736	0.561	0.989	0.635	0.726	0.670	0.659	–
	g_h	-0.605	-0.345	-0.580	0.526	-0.639	-0.326	-0.322	–
X^-	g_e	0.752	0.674	1.028	0.646	–	–	–	–
	g_h	-0.562	-0.33	-0.562	0.558	–	–	–	–

A.4 Hanle effect: fitting with model from Chapter 5 by using Mathematica

The Mathematica code used within this thesis are introduced in this subsection.

θ =+0.000; (* tilt angle of sample with respect to the quantization axis in °*)
ΔB=75;(* half of FWHM in mT measured in experiment*)
ρmax=1.0;
listpolar1 = {};

$$\text{f[Bx\_]}=\frac{1+\left(\frac{(i-400)Tan\left[\frac{\theta}{180}\pi\right]}{\Delta B}\right)^2}{1+\left(\frac{(i-400)}{\Delta B}\right)^2\left(1+Tan\left[\frac{\theta}{180}\pi\right]^2\right)}\text{; (*Lorentzian with tilt angle*)}$$

Do[{ρ_0 = f[Bx_]; point1 = {i - 400,ρ_0};
listpolar1 = Append[listpolar1, point1]}, {i, 0, 800}] ps = {GrayLevel[0.6],};
ListPlot[{listpolar1}, AxesOrigin -> {0, 0}, PlotRange -> All, PlotStyle -> ps](*plot of a Lorentzian*)
listpolar3 = Import["File path", "table"] (* Load the experimental data *)
κ = +14;(* Knight field in mT, with sign of <S0>*)
ν = -85;(* Overhauser field in mT, with sign of -ge_effectif*<S0>*)
Bn = 150; (* fluctuations nuclear field in mT*)
(* fit function *)

$$\text{g[}\rho\text{\_, Bx\_]} =\frac{\text{Bx}^2+1\text{Bn}^2}{\text{Bx}^2+\text{Bn}^2}\frac{\left(1+\left(\frac{\text{BxTan}\left[\frac{\theta}{180}\pi\right]}{\Delta B}\right)^2\left(1+\frac{\nu\left(\text{BxTan}\left[\frac{\theta}{180}\pi\right]+\kappa\rho\right)}{\text{Bx}^2+\left(\text{BxTan}\left[\frac{\theta}{180}\pi\right]\right)^2+2\kappa\text{BxTan}\left[\frac{\theta}{180}\pi\right]+\kappa^2\rho}\right)^2\right)}{\left(1+\left(\frac{\text{Bx}}{\Delta B}\right)^2\left(1+\text{Tan}\left[\frac{\theta}{180}\pi\right]^2\right)\left(1+\frac{\nu\left(\text{BxTan}\left[\frac{\theta}{180}\pi\right]+\kappa\rho\right)}{\text{Bx}^2+\left(\text{BxTan}\left[\frac{\theta}{180}\pi\right]\right)^2+2\kappa\text{BxTan}\left[\frac{\theta}{180}\pi\right]+\kappa^2\rho}\right)^2\right)}\text{-}$$

ρ;
listpolar5 = {}; Do[{root1 = NSolve[g[ρ, i - 400] == 0, ρ, Reals];
parm = Flatten[root1];
valist1 = ρ} /. parm[[1]];
point1 = Prepend[valist1, i - 400];
listpolar5 = Append[listpolar5, point1]}, {i, 0, 800}];
ps1 = {GrayLevel[0.6], Black, Directive[Green, PointSize[Large]]};
ListPlot[{listpolar1, listpolar5, ρmax listpolar3},
AxesOrigin -> {0, 0}, PlotRange -> All, PlotStyle -> ps1]
(* Solve numerically the equation and plot the result *)

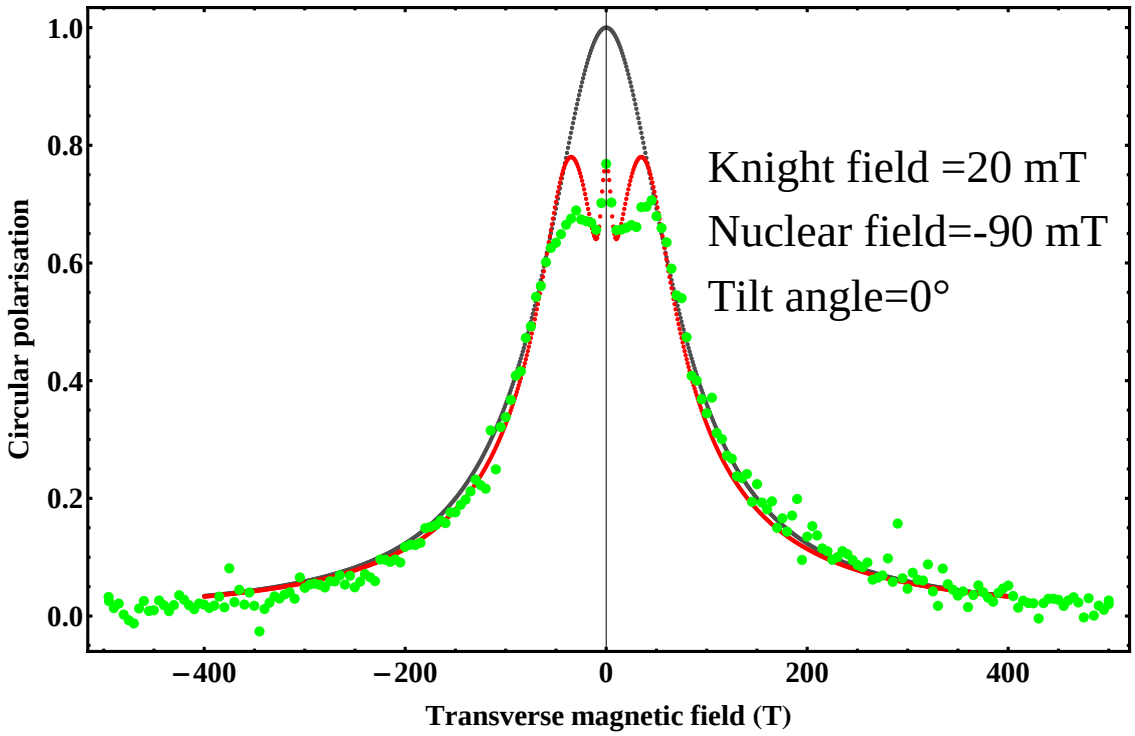
Knight field =20 mT
Nuclear field=-90 mT
Tilt angle=0°
Circular polarisation
Transverse magnetic field (T)
1.0
0.8
0.6
0.4
0.2
0.0
−400
−200
0
200
400

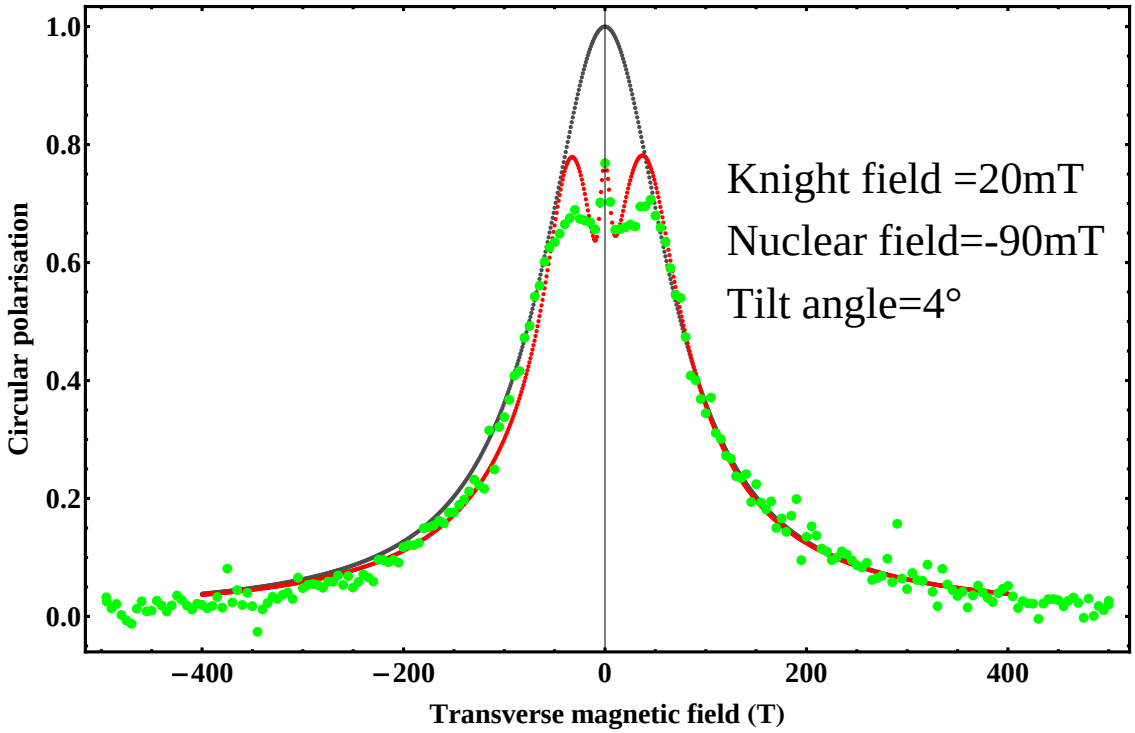
Knight field =20mT
Nuclear field=-90mT
Tilt angle=4°
Circular polarisation
Transverse magnetic field (T)
1.0
0.8
0.6
0.4
0.2
0.0
−400
−200
0
200
400

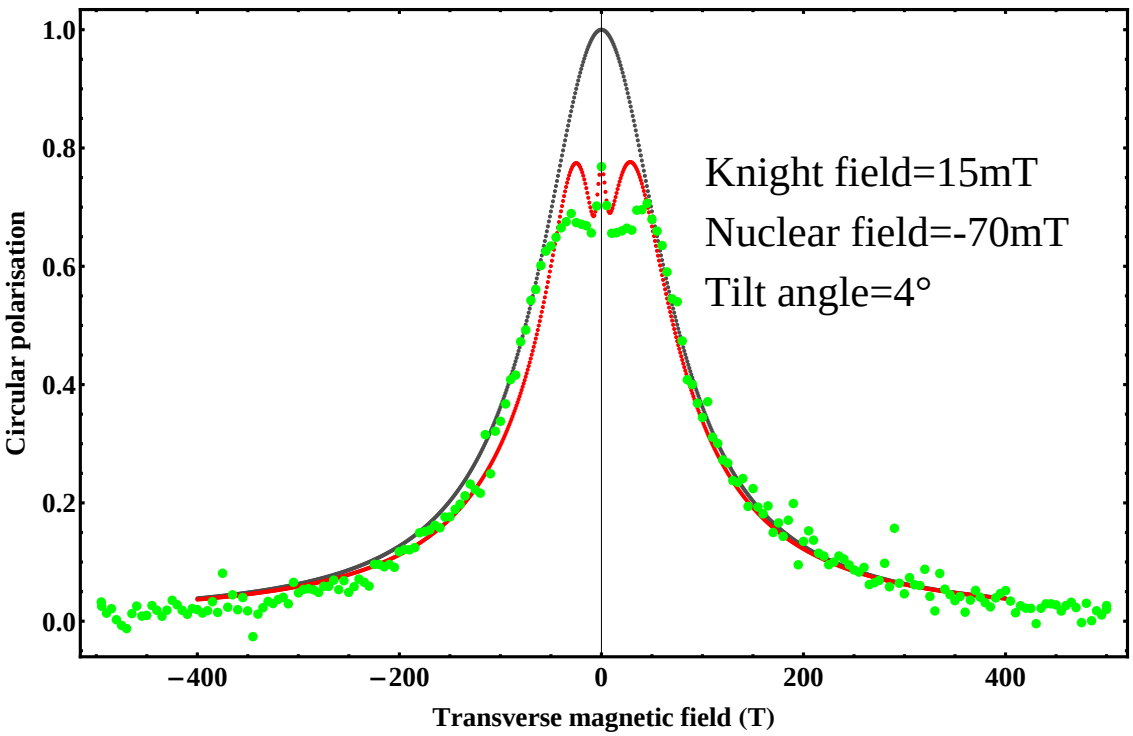
Knight field=15mT
Nuclear field=-70mT
Tilt angle=4°
Circular polarisation
Transverse magnetic field (T)
1.0
0.8
0.6
0.4
0.2
0.0
−400
−200
0
200
400

List of Figures

List of Tables

Bibliography

[1] J. Brossel, A. Kastler, and J. Winter. *J. de Physique et le Radium*, 13:668, 1952.

[2] W. D. Knight. Nuclear magnetic resonance shift in metals. *Phys. Rev.*, 76(8): 1259–1260, Oct 1949. doi: 10.1103/PhysRev.76.1259.2.

[3] Albert W. Overhauser. Polarization of nuclei in metals. *Phys. Rev.*, 92:411–415, 1953.

[4] Georges Lampel. Nuclear dynamic polarization by optical electronic saturation and optical pumping in semiconductors. *Phys. Rev. Lett.*, 20(10):491–493, Mar 1968. doi: 10.1103/PhysRevLett.20.491.

[5] F. Meier and B. Zakharchenya. Optical orientation. *Modern Problems in Condensed Matter Sciences (North-Holland, Amsterdam).*, 8, 1984.

[6] D. Paget, G. Lampel, B. Sapoval, and V. I. Safarov. Low field electron-nuclear spin coupling in gallium arsenide under optical pumping conditions. *Phys. Rev. B*, 15: 5780–5796, Jun 1977. doi: 10.1103/PhysRevB.15.5780.

[7] V. L. Berkovitz, A. I. Ekimov, and V. I. Safarov. Optical orientation in a system of electrons and lattice nuclei in semiconductors. experiment. *Sov. Phys. JETP*, 38, 1974.

[8] R. I. Dzhioev, V. L. Korenev, I. A. Merkulov, B. P. Zakharchenya, D. Gammon, Al. L. Efros, and D. S. Katzer. Manipulation of the spin memory of electrons in n-GaAs. *Phys. Rev. Lett.*, 88(25):256801, Jun 2002. doi: 10.1103/PhysRevLett.88.256801.

[9] J. Y. Marzin, J. M. Gérard, A. Izraël, D. Barrier, and G. Bastard. Photoluminescence of single InAs quantum dots obtained by self-organized growth on GaAs. *Phys. Rev. Lett.*, 73(5):716–719, Aug 1994. doi: 10.1103/PhysRevLett.73.716.

[10] D. Gammon, S.W. Brown, E.S. Snow, T.A. Kennedy, D.S. Katzer, and D. Park. Nuclear spectroscopy in single quantum dots: Nanoscopic raman scattering and nuclear magnetic resonance. *Science*, 277:85–88, 1997.

[11] S. W. Brown, T. A. Kennedy, and D. Gammon. Optical NMR from single quantum dots. *Solid State Nuclear Magnetic Resonance*, 11(1-2):49 – 58, 1998.

[12] Alexander V. Khaetskii and Yuli V. Nazarov. Spin relaxation in semiconductor quantum dots. *Phys. Rev. B*, 61(19):12639–12642, May 2000. doi: 10.1103/PhysRevB.61.12639.

[13] M. Paillard, X. Marie, P. Renucci, T. Amand, A. Jbeli, and J. M. Gérard. Spin relaxation quenching in semiconductor quantum dots. *Phys. Rev. Lett.*, 86(8): 1634–1637, Feb 2001. doi: 10.1103/PhysRevLett.86.1634.

[14] Miro Kroutvar, Yann Ducommun, Dominik Heiss, Max Bichler, Dieter Schuh, Gerhard Abstreiter, and Jonathan J. Finley. *Nature*, 432:81, 2004.

[15] Guido Burkard, Daniel Loss, and David P. DiVincenzo. Coupled quantum dots as quantum gates. *Phys. Rev. B*, 59(3):2070–2078, Jan 1999. doi: 10.1103/PhysRevB.59.2070.

[16] I. A. Merkulov, Al. L. Efros, and M. Rosen. Electron spin relaxation by nuclei in semiconductor quantum dots. *Phys. Rev. B*, 65(20):205309, Apr 2002. doi: 10.1103/PhysRevB.65.205309.

[17] M.I. Dyakonov and V.I. Perel. *Zh.E ksp. Teor. Fiz.*, 65(362), 1973.

[18] M.I. Dyakonov and V.I. Perel. *Sov. Phys. JETP*, 38(177), 1974.

[19] J. R. Petta, A. C. Johnson, J. M. Taylor, E. A. Laird, A. Yacoby, M. D. Lukin, C. M. Marcus, M. P. Hanson, and A. C. Gossard. Coherent manipulation of coupled electron spins in semiconductor quantum dots. *Science*, 309(5744):2180–2184, 2005. doi: 10.1126/science.1116955.

[20] P.-F. Braun, X. Marie, L. Lombez, B. Urbaszek, T. Amand, P. Renucci, V. K. Kalevich, K. V. Kavokin, O. Krebs, P. Voisin, and Y. Masumoto. Direct observation of the electron spin relaxation induced by nuclei in quantum dots. *Phys. Rev. Lett.*, 94(11):116601, Mar 2005. doi: 10.1103/PhysRevLett.94.116601.

[21] Hendrik Bluhm, Sandra Foletti, Izhar Neder, Mark Rudner, Diana Mahalu, Vladimir Umansky, and Amir Yacoby. Dephasing time of GaAs electron-spin qubits coupled to a nuclear bath exceeding 200 μs. *Nature Physics*, 7:109, Dec 2010.

[22] A. S. Bracker, E. A. Stinaff, D. Gammon, M. E. Ware, J. G. Tischler, A. Shabaev, Al. L. Efros, D. Park, D. Gershoni, V. L. Korenev, and I. A. Merkulov. Optical pumping of the electronic and nuclear spin of single charge-tunable quantum dots. *Phys. Rev. Lett.*, 94(4):047402, Feb 2005. doi: 10.1103/PhysRevLett.94.047402.

[23] B. Eble, O. Krebs, A. Lemaître, K. Kowalik, A. Kudelski, P. Voisin, B. Urbaszek, X. Marie, and T. Amand. Dynamic nuclear polarization of a single charge-tunable InAs/GaAs quantum dot. *Phys. Rev. B*, 74(8):081306, Aug 2006. doi: 10.1103/PhysRevB.74.081306.

[24] A. I. Tartakovskii, T. Wright, A. Russell, V. I. Fal'ko, A. B. Van'kov, J. Skiba-Szymanska, I. Drouzas, R. S. Kolodka, M. S. Skolnick, P. W. Fry, A. Tahraoui, H.-Y. Liu, and M. Hopkinson. Nuclear spin switch in semiconductor quantum dots. *Phys. Rev. Lett.*, 98(2):026806, Jan 2007. doi: 10.1103/PhysRevLett.98.026806.

[25] P. Maletinsky, M Kroner, and A. Imamoglu. Breakdown of the nuclear-spin-temperature approach in quantum-dot demagnetization experiments. *Nature Phys.*, 5(6):407, 2009.

[26] J. M. Taylor, C. M. Marcus, and M. D. Lukin. Long-lived memory for mesoscopic quantum bits. *Phys. Rev. Lett.*, 90(20):206803, May 2003. doi: 10.1103/PhysRevLett.90.206803.

[27] C. W. Lai, P. Maletinsky, A. Badolato, and A. Imamoglu. Knight-field-enabled nuclear spin polarization in single quantum dots. *Phys. Rev. Lett.*, 96(16):167403, Apr 2006. doi: 10.1103/PhysRevLett.96.167403.

[28] Thomas Belhadj, Claire-Marie Simon, Thierry Amand, Pierre Renucci, Beatrice Chatel, Olivier Krebs, Aristide Lemaître, Paul Voisin, Xavier Marie, and Bernhard Urbaszek. Controlling the polarization eigenstate of a quantum dot exciton with light. *Phys. Rev. Lett.*, 103(8):086601–, August 2009.

[29] L. A. Larsson, E. S. Moskalenko, and P. O. Holtz. Manipulating the spin polarization of excitons in a single quantum dot by optical means. *Applied Physics Letters*, 98 (7):071906, 2011.

[30] N. Akopian, N. H. Lindner, E. Poem, Y. Berlatzky, J. Avron, D. Gershoni, B. D. Gerardot, and P. M. Petroff. Entangled photon pairs from semiconductor quantum dots. *Phys. Rev. Lett.*, 96(13):130501, Apr 2006. doi: 10.1103/PhysRevLett.96.130501.

[31] A. Dousse, J. Suffczynski, A. Beveratos, O. Krebs, A. Lemaitre, I. Sagnes, J. Bloch, P. Voisin, and P. Senellart. Ultrabright source of entangled photon pairs. *Nature*, 466:217–220, 2010.

[32] R. M. Stevenson, C. L. Salter, A. Boyer de la Giroday, I. A. Farrer, C. A. Nicoll, D. A. Ritchie, and A. J. Shields. Coherent entangled light generated by quantum dots in the presence of nuclear magnetic fields. *ArXiv e-prints*, 2011.

[33] C. Latta, A. Hogele, Y. Zhao, A. N. Vamivakas, P. Maletinsky, M. Kroner, J. Dreiser, I. Carusotto, A. Badolato, D. Schuh, W. Wegscheider, M. Atature, and A. Imamoglu. Confluence of resonant laser excitation and bidirectional quantum-dot nuclear-spin polarization. *Nature Phys.*, 5(8):758, 2009.

[34] Xiaodong Xu, Wang Yao, Bo Sun, Duncan G. Steel, Allan S. Bracker, Daniel Gammon, and L. J. Sham. Optically controlled locking of the nuclear field via coherent dark-state spectroscopy. *Nature (London)*, 459:1105, 2009.

[35] E. A. Chekhovich, M. N. Makhonin, J. Skiba-Szymanska, A. B. Krysa, V. D. Kulakovskii, M. S. Skolnick, and A. I. Tartakovskii. Dynamics of optically induced nuclear spin polarization in individual InP/$Ga_xIn_{1-x}P$ quantum dots. *Phys. Rev. B*, 81(24):245308, Jun 2010. doi: 10.1103/PhysRevB.81.245308.

[36] P.-F. Braun, B. Urbaszek, T. Amand, X. Marie, O. Krebs, B. Eble, A. Lemaitre, and P. Voisin. Bistability of the nuclear polarization created through optical pumping in

$In_{1-x}Ga_xAs$ quantum dots. *Phys. Rev. B*, 74(24):245306, Dec 2006. doi: 10.1103/PhysRevB.74.245306.

[37] P. Maletinsky, C. W. Lai, A. Badolato, and A. Imamoglu. Nonlinear dynamics of quantum dot nuclear spins. *Phys. Rev. B*, 75(3):035409, Jan 2007. doi: 10.1103/PhysRevB.75.035409.

[38] R. Kaji, S. Adachi, H. Sasakura, and S. Muto. Hysteretic response of the electron-nuclear spin system in single $In_{0.75}Al_{0.25}As$ quantum dots: Dependences on excitation power and polarization. *Phys. Rev. B*, 77(11):115345, Mar 2008. doi: 10.1103/PhysRevB.77.115345.

[39] M. Issler, E. M. Kessler, G. Giedke, S. Yelin, I. Cirac, M. D. Lukin, and A. Imamoglu. Nuclear spin cooling using overhauser-field selective coherent population trapping. *Phys. Rev. Lett.*, 105(26):267202, Dec 2010. doi: 10.1103/PhysRevLett.105.267202.

[40] M. S. Rudner, L. M. K. Vandersypen, V. Vuletic, and L. S. Levitov. Generating entanglement and squeezed states of nuclear spins in quantum dots. *Phys. Rev. Lett.*, 107(20):206806–, November 2011.

[41] E. M. Kessler, S. Yelin, M. D. Lukin, J. I. Cirac, and G. Giedke. Optical superradiance from nuclear spin environment of single-photon emitters. *Phys. Rev. Lett.*, 104(14): 143601, Apr 2010. doi: 10.1103/PhysRevLett.104.143601.

[42] E. M. Kessler, G. Giedke, A. Imamoglu, S. F. Yelin, M. D. Lukin, and J. I. Cirac. Dissipative phase transition in central spin systems. *ArXiv e-prints*, 2012.

[43] L. Childress, M. V. Gurudev Dutt, J. M. Taylor, A. S. Zibrov, F. Jelezko, J. Wrachtrup, P. R. Hemmer, and M. D. Lukin. Coherent dynamics of coupled electron and nuclear spin qubits in diamond. *Science*, 314(5797):281–285, 2006. doi: 10.1126/science.1131871.

[44] G. Balasubramanian, P. Neumann, D. Twitchen, R. Markham, M. Kolesov, N. Mizuochi, J. Isoya, J. Achard, J. Beck, J. Tissler, V. Jacques, P. R. Hemmer, F. Jelezko, and J. Wrachtrup. Measurement of the knight field and local nuclear dipole-dipole field in an InGaAs/GaAs quantum dot ensemble. *Nature Materials*, 8: 383, 2009.

[45] P. Michler, A. Kiraz, C. Becher, W. V. Schoenfeld, P. M. Petroff, Lidong Zhang, E. Hu, and A. Imamoglu. A quantum dot single-photon turnstile device. *Science*, 290(5500):2282–2285, 2000.

[46] Alexander Högele, Stefan Seidl, Martin Kroner, Khaled Karrai, Richard J. Warburton, Brian D. Gerardot, and Pierre M. Petroff. Voltage-controlled optics of a quantum dot. *Phys. Rev. Lett.*, 93(21):217401, Nov 2004. doi: 10.1103/PhysRevLett.93.217401.

[47] F. Henneberger and O. Benson. Semiconductor quantum bits. *Pan Stanford Publishing*, 2008.

[48] D. Gammon, E. S. Snow, B. V. Shanabrook, D. S. Katzer, and D. Park. Fine structure splitting in the optical spectra of single GaAs quantum dots. *Phys. Rev. Lett.*, 76(16):3005–3008, Apr 1996. doi: 10.1103/PhysRevLett.76.3005.

[49] J. Hours, P. Senellart, E. Peter, A. Cavanna, and J. Bloch. Exciton radiative lifetime controlled by the lateral confinement energy in a single quantum dot. *Phys. Rev. B*, 71(16):161306, Apr 2005. doi: 10.1103/PhysRevB.71.161306.

[50] L. Besombes et al. Exciton and biexciton fine structure in single elongated islands grown on a vicinal surface. *Phys. Rev. Lett.*, 85(2):425–428, Jul 2000. doi: 10.1103/PhysRevLett.85.425.

[51] L. Goldstein, F. Glas, J. Y. Marzin, M. N. Charasse, and G. Le Roux. Growth by molecular beam epitaxy and characterization of InAs/GaAs strained-layer superlattices. *Applied Physics Letters*, 47(10):1099–1101, 1985.

[52] D. Leonard, K. Pond, and P. M. Petroff. Critical layer thickness for self-assembled InAs islands on GaAs. *Phys. Rev. B*, 50(16):11687–11692, Oct 1994. doi: 10.1103/PhysRevB.50.11687.

[53] P. Offermans, P.M. Koenraad, J.H. Wolter, K. Pierz, M. Roy, and P.A. Maksym. Formation of InAs quantum dots and wetting layers in GaAs and AlAs analyzed by cross-sectional scanning tunneling microscopy. *Physica E*, 26(1-4):236 – 240, 2005. doi: DOI:10.1016/j.physe.2004.08.104.

[54] R. Hanson, L. P. Kouwenhoven, J. R. Petta, S. Tarucha, and L. M. K. Vandersypen. Spins in few-electron quantum dots. *Rev. Mod. Phys.*, 79(4):1217–1265, Oct 2007. doi: 10.1103/RevModPhys.79.1217.

[55] R. Takahashi, K. Kono, S. Tarucha, and K. Ono. Voltage-selective bidirectional polarization and coherent rotation of nuclear spins in quantum dots. *Phys. Rev. Lett.*, 107(2):026602, Jul 2011. doi: 10.1103/PhysRevLett.107.026602.

[56] J. C. Girard, A. Lemaître, A. Miard, C. David, and Z. Z. Wang. Low temperature scanning tunneling microscopy wave-function imaging of InAs/GaAs cleaved quantum dots with similar height. *J. Vac. Sci. Technol.*, B27:891, 2009.

[57] N. Koguchi, S. Takahashi, and T. Chikyow. *J. Cryst. Growth*, 111:688, 1991.

[58] J. G. Keizer, J. Bocquel, P. M. Koenraad, T. Mano, T. Noda, and K. Sakoda. Atomic scale analysis of self assembled GaAs/AlGaAs quantum dots grown by droplet epitaxy. *Applied Physics Letters*, 96(6):062101, 2010. doi: 10.1063/1.3303979.

[59] Thomas Belhadj, Takashi Kuroda, Claire-Marie Simon, Thierry Amand, Takaaki Mano, Kazuaki Sakoda, Nobuyuki Koguchi, Xavier Marie, and Bernhard Urbaszek. Optically monitored nuclear spin dynamics in individual GaAs quantum dots grown by droplet epitaxy. *Phys. Rev. B*, 78(20):205325, Nov 2008. doi: 10.1103/PhysRevB.78.205325.

[60] T. Mano, privat communication.

[61] URL `http://www.ioffe.ru/SVA/NSM/Semicond/GaAs/index.html`.

[62] M. Grundmann, O. Stier, and D. Bimberg. InAs/GaAs pyramidal quantum dots: Strain distribution, optical phonons, and electronic structure. *Phys. Rev. B*, 52: 11969–11981, Oct 1995. doi: 10.1103/PhysRevB.52.11969.

[63] Gabriel Bester and Alex Zunger. Cylindrically shaped zinc-blende semiconductor quantum dots do not have cylindrical symmetry: atomistic symmetry, atomic relaxation, and piezoelectric effects. *Phys. Rev. B*, 71:045318, Jan 2005. doi: 10.1103/PhysRevB.71.045318.

[64] Olivier Krebs and Paul Voisin. Giant optical anisotropy of semiconductor heterostructures with no common atom and the quantum-confined pockels effect. *Phys. Rev. Lett.*, 77:1829–1832, Aug 1996. doi: 10.1103/PhysRevLett.77.1829.

[65] M. Bayer et al. Fine structure of neutral and charged excitons in self-assembled InGaAs/AlGaAs quantum dots. *Phys. Rev. B*, 65(19):195315, May 2002.

[66] T. Belhadj, T. Amand, A. Kunold, C.-M. Simon, T. Kuroda, M. Abbarchi, T. Mano, K. Sakoda, S. Kunz, X. Marie, and B. Urbaszek. Impact of heavy hole-light hole coupling on optical selection rules in GaAs quantum dots. *Applied Physics Letters*, 97(5):051111, 2010.

[67] A. V. Koudinov, I. A. Akimov, Yu. G. Kusrayev, and F. Henneberger. Optical and magnetic anisotropies of the hole states in stranski-krastanov quantum dots. *Phys. Rev. B*, 70(24):241305, Dec 2004. doi: 10.1103/PhysRevB.70.241305.

[68] Y. Léger, L. Besombes, L. Maingault, and H. Mariette. Valence-band mixing in neutral, charged, and Mn-doped self-assembled quantum dots. *Phys. Rev. B*, 76: 045331, 2007.

[69] I. A. Akimov, A. Hundt, T. Flissikowski, and F. Henneberger. Fine structure of the trion triplet state in a single self-assembled semiconductor quantum dot. *Applied Physics Letters*, 81(25):4730–4732, 2002. doi: 10.1063/1.1527694.

[70] S. Cortez, O. Krebs, S. Laurent, M. Senes, X. Marie, P. Voisin, R. Ferreira, G. Bastard, J-M. Gérard, and T. Amand. Optically driven spin memory in n-doped InAs-GaAs quantum dots. *Phys. Rev. Lett.*, 89(20):207401, Oct 2002. doi: 10.1103/PhysRevLett.89.207401.

[71] S. Laurent, M. Senes, O. Krebs, V. K. Kalevich, B. Urbaszek, X. Marie, T. Amand, and P. Voisin. Negative circular polarization as a general property of n-doped self-assembled InAs/GaAs quantum dots under nonresonant optical excitation. *Phys. Rev. B*, 73(23):235302, Jun 2006. doi: 10.1103/PhysRevB.73.235302.

[72] A. Greilich, D. R. Yakovlev, A. Shabaev, Al. L. Efros, I. A. Yugova, R. Oulton, V. Stavarache, D. Reuter, A. Wieck, and M. Bayer. Mode locking of electron spin coherences in singly charged quantum dots. *Science*, 313(5785):341–345, 2006.

[73] H. Drexler, D. Leonard, W. Hansen, J. P. Kotthaus, and P. M. Petroff. Spectroscopy of quantum levels in charge-tunable InGaAs quantum dots. *Phys. Rev. Lett.*, 73(16): 2252–2255, Oct 1994. doi: 10.1103/PhysRevLett.73.2252.

[74] R. J. Warburton, C. Schäflein, D. Haft, F. Bickel, A. Lorke, K.Karrai, J.M. Garcia, W. Schoenfeld, and P. M. Petroff. Optical emission from a charge-tunable quantum ring. *Nature (London)*, 405:926, 2000.

[75] R. J. Warburton, B. T. Miller, C. S. Dürr, C. Bödefeld, K. Karrai, J. P. Kotthaus, G. Medeiros-Ribeiro, P. M. Petroff, and S. Huant. Coulomb interactions in small charge-tunable quantum dots: A simple model. *Phys. Rev. B*, 58:16221, 1998. doi: 10.1103/PhysRevB.58.16221.

[76] H. Tong and M. W. Wu. Theory of excitons in cubic III-V semiconductor GaAs, InAs and GaN quantum dots: Fine structure and spin relaxation. *Phys. Rev. B*, 83: 235323, Jun 2011.

[77] M. Abbarchi et al. Exciton fine structure in strain-free GaAs/$Al_{0.3}Ga_{0.7}As$ quantum dots: Extrinsic effects. *Phys. Rev. B*, 78(12):125321, Sep 2008. doi: 10.1103/PhysRevB.78.125321.

[78] M. Abbarchi et al. Magneto-optical properties of excitonic complexes in GaAs self-assembled quantum dots. *Phys. Rev. B*, 81(3):035334, Jan 2010. doi: 10.1103/PhysRevB.81.035334.

[79] William K. Liu, Kelly M. Whitaker, Alyssa L. Smith, Kevin R. Kittilstved, Bruce H. Robinson, and Daniel R. Gamelin. Room-temperature electron spin dynamics in free-standing ZnO quantum dots. *Phys. Rev. Lett.*, 98(18):186804, May 2007. doi: 10.1103/PhysRevLett.98.186804.

[80] D. H. Feng, I. A. Akimov, and F. Henneberger. Nonequilibrium nuclear-electron spin dynamics in semiconductor quantum dots. *Phys. Rev. Lett.*, 99(3):036604, Jul 2007. doi: 10.1103/PhysRevLett.99.036604.

[81] A. Abragam. Principles of nuclear magnetism. *Oxford University Press*, 1961.

[82] Jan Fischer, W. A. Coish, D. V. Bulaev, and Daniel Loss. Spin decoherence of a heavy hole coupled to nuclear spins in a quantum dot. *Phys. Rev. B*, 78(15):155329, Oct 2008. doi: 10.1103/PhysRevB.78.155329.

[83] B. Eble, C. Testelin, P. Desfonds, F. Bernardot, A. Balocchi, T. Amand, A. Miard, A. Lemaître, X. Marie, and M. Chamarro. Hole–nuclear spin interaction in quantum dots. *Phys. Rev. Lett.*, 102(14):146601, Apr 2009. doi: 10.1103/PhysRevLett.102.146601.

[84] E. A. Chekhovich, A. B. Krysa, M. S. Skolnick, and A. I. Tartakovskii. Light-polarization-independent nuclear spin alignment in a quantum dot. *Phys. Rev. B*, 83(12):125318, Mar 2011. doi: 10.1103/PhysRevB.83.125318.

[85] P. Fallahi, S. T. Y ılmaz, and A. Imamoğlu. Measurement of a heavy-hole hyperfine interaction in InGaAs quantum dots using resonance fluorescence. *Phys. Rev. Lett.*, 105(25):257402, Dec 2010. doi: 10.1103/PhysRevLett.105.257402.

[86] P. Desfonds, B. Eble, F. Fras, C. Testelin, F. Bernardot, M. Chamarro, B. Urbaszek, T. Amand, X. Marie, J. M. Gerard, V. Thierry-Mieg, A. Miard, and A. Lemaitre. Electron and hole spin cooling efficiency in InAs quantum dots: The role of nuclear field. *Appl. Phys. Lett.*, 96(17), 2010.

[87] C. Testelin, F. Bernardot, B. Eble, and M. Chamarro. Hole–spin dephasing time associated with hyperfine interaction in quantum dots. *Phys. Rev. B*, 79(19):195440, May 2009. doi: 10.1103/PhysRevB.79.195440.

[88] M. Dyakonov. Spin physics in semiconductor nanostructures. *Springer Series in Solid-State Science, Springer-Verlag Berlin*, 157, 2008.

[89] D. Gammon, Al. L. Efros, T. A. Kennedy, M. Rosen, D. S. Katzer, D. Park, S. W. Brown, V. L. Korenev, and I. A. Merkulov. Electron and nuclear spin interactions in the optical spectra of single GaAs quantum dots. *Phys. Rev. Lett.*, 86(22):5176–5179, May 2001. doi: 10.1103/PhysRevLett.86.5176.

[90] B. Urbaszek, P.-F. Braun, T. Amand, O. Krebs, T. Belhadj, A. Lemaître, P. Voisin, and X. Marie. Efficient dynamical nuclear polarization in quantum dots: Temperature dependence. *Phys. Rev. B*, 76(20):201301, Nov 2007. doi: 10.1103/PhysRevB.76.201301.

[91] Alexander V. Khaetskii, Daniel Loss, and Leonid Glazman. Electron spin decoherence in quantum dots due to interaction with nuclei. *Phys. Rev. Lett.*, 88(18):186802, Apr 2002. doi: 10.1103/PhysRevLett.88.186802.

[92] Y. G. Semenov and K. W. Kim. Effect of an external magnetic field on electron-spin dephasing induced by hyperfine interaction in quantum dots. *Phys. Rev. B*, 67(7):073301, Feb 2003. doi: 10.1103/PhysRevB.67.073301.

[93] D. Paget. Optical-detection of nmr in high-purity GaAs - direct study of the relaxation of nuclei close to shallow donors. *Phys. Rev. B*, 25:4444, 1982. doi: 10.1103/PhysRevB.25.4444.

[94] M. Paillard, X. Marie, E. Vanelle, T. Amand, V. K. Kalevich, A. R. Kovsh, A. E. Zhukov, and V. M. Ustinov. Time-resolved photoluminescence in self-assembled InAs/GaAs quantum dots under strictly resonant excitation. *Applied Physics Letters*, 76(1):76–78, 2000.

[95] C.-Y. Lu, Y. Zhao, A. N. Vamivakas, C. Matthiesen, S. Fält, A. Badolato, and M. Atatüre. Direct measurement of spin dynamics in InAs/GaAs quantum dots using time-resolved resonance fluorescence. *Phys. Rev. B*, 81(3):035332, Jan 2010. doi: 10.1103/PhysRevB.81.035332.

[96] A. Muller, E. B. Flagg, P. Bianucci, X. Y. Wang, D. G. Deppe, W. Ma, J. Zhang, G. J. Salamo, M. Xiao, and C. K. Shih. Resonance fluorescence from a coherently

driven semiconductor quantum dot in a cavity. *Phys. Rev. Lett.*, 99(18):187402, Nov 2007. doi: 10.1103/PhysRevLett.99.187402.

[97] Nick A. Vamivakas, Yong Zhao, Chao-Yang Lu, and Mete Atatüre. Spin-resolved quantum dot resonance fluorescence. *Nature Phys.*, 5:198–202, 2009.

[98] Benito Alen, Alexander Högele, Martin Kroner, Stefan Seidl, Khaled Karrai, Richard J. Warburton, Antonio Badolato, Gilberto Medeiros-Ribeiro, and Pierre M. Petroff. Absorptive and dispersive optical responses of excitons in a single quantum dot. *Applied Physics Letters*, 89(12):123124, 2006. doi: 10.1063/1.2354431.

[99] S. A. Crooker, J. Brandt, C. Sandfort, A. Greilich, D. R. Yakovlev, D. Reuter, A. D. Wieck, and M. Bayer. Spin noise of electrons and holes in self-assembled quantum dots. *Phys. Rev. Lett.*, 104:036601, Jan 2010.

[100] Yan Li, N. Sinitsyn, D. L. Smith, D. Reuter, A. D. Wieck, D. R. Yakovlev, M. Bayer, and S. A. Crooker. Intrinsic spin fluctuations reveal the dynamical response function of holes coupled to nuclear spin baths in (In,Ga)As quantum dots. *Phys. Rev. Lett.*, 108:186603, 2012.

[101] R. Dahbashi, J. Hübner, F. Berski, J. Wiegand, X. Marie, K. Pierz, H. W. Schumacher, and M. Oestreich. Measurement of heavy-hole spin dephasing in (InGa)As quantum dots. *Applied Physics Letters*, 100(3):031906, 2012.

[102] M. Minsky. *Scanning*, 10, 1988.

[103] M. Minsky. *U.S. Patent 3013467.*

[104] P. Brackenhoff, G. J. Blom and P. Barends. Confocal scanning light microscopy with high apertureimmersion lenses. *Journal of Microscopy*, 117:219, 1979.

[105] T Wilson and C. J. R. Sheppard. *Theory and practice of scanning optical microscopy.* Acad. Press, 1984.

[106] S. Wilhelm, B. Gröbler, M. Gluch, and H. Heinz. Principles - confocal laser scanning microscopy. *Carl Zeiss Advanced Imaging Microscopy, Jena*, 2003.

[107] L. D. Dickson. *Appl. Opt.*, 9:1854, 1970.

[108] A. A. Self. *Appl. Opt.*, 22:658, 1983.

[109] A. E. Siegman. *Lasers.* University Science Books, 1986.

[110] Introduction to Gaussian Beam Optics Melles Griot, www.mellesgriot.com.

[111] URL `www.wikipedia.org`.

[112] URL `http:/www.roperscientific.de/speccams.html`.

[113] Oliver Benson et al. Regulated and entangled photons from a single quantum dot. *Phys. Rev. Lett.*, 84(11):2513–2516, Mar 2000. doi: 10.1103/PhysRevLett.84.2513.

[114] M. Bayer et al. Electron and hole g factors and exchange interaction from studies of the exciton fine structure in $In_{0.60}Ga_{0.40}As$ quantum dots. *Phys. Rev. Lett.*, 82(8): 1748–1751, Feb 1999. doi: 10.1103/PhysRevLett.82.1748.

[115] R. M. Stevenson et al. A semiconductor source of triggered entangled photon pairs. *Nature (London)*, 439:179, 2006.

[116] J. D. Plumhof et al. Strain-induced anticrossing of bright exciton levels in single self-assembled GaAs/$Al_xGa_{1-x}As$ and $In_xGa_{1-x}As$/GaAs quantum dots. *Phys. Rev. B*, 83(12):121302, Mar 2011. doi: 10.1103/PhysRevB.83.121302.

[117] W. Langbein et al. Control of fine-structure splitting and biexciton binding in $In_xGa_{1-x}As$ quantum dots by annealing. *Phys. Rev. B*, 69(16):161301, Apr 2004. doi: 10.1103/PhysRevB.69.161301.

[118] J. Lu, M. J. R. Hoch, P. L. Kuhns, W. G. Moulton, Z. Gan, and A. P. Reyes. Nuclear spin-lattice relaxation in n -type insulating and metallic GaAs single crystals. *Phys. Rev. B*, 74(12):125208, Sep 2006. doi: 10.1103/PhysRevB.74.125208.

[119] Andrei Schliwa et al. In(Ga)As/GaAs quantum dots grown on a (111) surface as ideal sources of entangled photon pairs. *Phys. Rev. B*, 80(16):161307, Oct 2009. doi: 10.1103/PhysRevB.80.161307.

[120] Ranber Singh and Gabriel Bester. Nanowire quantum dots as an ideal source of entangled photon pairs. *Phys. Rev. Lett.*, 103(6):063601, Aug 2009. doi: 10.1103/PhysRevLett.103.063601.

[121] T. Mano et al. Self-assembly of symmetric gaas quantum dots on (111)A substrates: Suppression of fine-structure splitting. *Appl. Phys. Express*, 3:065203, 2010.

[122] K. F. Karlsson et al. Fine structure of exciton complexes in high-symmetry quantum dots: Effects of symmetry breaking and symmetry elevation. *Phys. Rev. B*, 81(16): 161307, Apr 2010. doi: 10.1103/PhysRevB.81.161307.

[123] Erik Stock et al. Single-photon emission from ingaas quantum dots grown on (111) GaAs. *Appl. Phys. Lett.*, 96(9):093112, 2010.

[124] Masafumi Jo, Takaaki Mano, Marco Abbarchi, Takashi Kuroda, Yoshiki Sakuma, and Kazuaki Sakoda. Self-limiting growth of hexagonal and triangular quantum dots on(111)A. *Crystal growth design*, 12:1411?1415, 2012.

[125] J. Puls et al. Magneto-optical study of the exciton fine structure in self-assembled CdSe quantum dots. *Phys. Rev. B*, 60(24):R16303–R16306, Dec 1999. doi: 10.1103/PhysRevB.60.R16303.

[126] N. S. Averkiev et al. *Sov. Phys. Solid State*, 23:1851, 1981.

[127] David Press et al. Complete quantum control of a single quantum dot spin using ultrafast optical pulses. *Nature*, 456:218–211, 2008.

[128] *Superlattices and Other Heterostructures*, E.L. Ivchenko and G. Pikus, Springer Series in Solid-State Sciences, Berlin 1995.

[129] E. L. Ivchenko. *Optical spectroscopy of semiconductor nanostructures.* Alpha Science, 2005.

[130] M. Semina and R Suris. Effect of localization in quantum wells and quatum wires on heavy-light hole mixing and acceptor binding energy. *Semoconductors*, 45:917, 2011.

[131] A. Wojs, P. Hawrylak, S. Fafard, and L. Jacak. Electronic structure and magneto-optics of self-assembled quantum dots. *Phys. Lett. B*, 54:5604, 1996.

[132] Weiming Que. Excitons in quantum dots with parabolic confinement. *Phys. Rev. B*, 45(19):11036–11041, May 1992.

[133] Pawel Hawrylak. Excitonic artificial atoms: Engineering optical properties of quantum dots. *Phys. Rev. B*, 60(8):5597–5608, August 1999.

[134] M. Semina, R. Sergeev, and R. Suris. Localization of electron-hole complexes at fluctuations of interfaces of quantum dots. *Semiconductors*, 40:1338–1345, 2006.

[135] G. L. Bir and G. E. Pikus. *Symmetry and deformation effects in semiconductors.* Nauka, 1972.

[136] G. Sallen, B. Urbaszek, M. M. Glazov, E. L. Ivchenko, T. Kuroda, T. Mano, S. Kunz, M. Abbarchi, K. Sakoda, D. Lagarde, A. Balocchi, X. Marie, and T. Amand. Dark-bright mixing of interband transitions in symmetric semiconductor quantum dots. *Phys. Rev. Lett.*, 107:166604, Oct 2011. doi: 10.1103/PhysRevLett.107.166604.

[137] J. M. Luttinger. *Phys. Rev.*, 102:1030, 1956.

[138] Laura M. Roth. Theory of the faraday effect in solids. *Phys. Rev.*, 133(2A): A542–A553, January 1964. URL `http://link.aps.org/doi/10.1103/PhysRev.133.A542`.

[139] X. Marie et al. Hole spin quantum beats in quantum-well structures. *Phys. Rev. B*, 60(8):5811–5817, Aug 1999. doi: 10.1103/PhysRevB.60.5811.

[140] L. R. Ram-Mohan, K. H. Yoo, and R. L. Aggarwal. Transfer-matrix algorithm for the calculation of the band structure of semiconductor superlattices. *Phys. Rev. B*, 38(9):6151–6159, September 1988. URL `http://link.aps.org/doi/10.1103/PhysRevB.38.6151`.

[141] Th. Wimbauer, K. Oettinger, Al. L. Efros, B. K. Meyer, and H. Brugger. Zeeman splitting of the excitonic recombination in $In_xGa_{1-x}As/GaAs$ single quantum wells. *Phys. Rev. B*, 50(12):8889–8892, September 1994. URL `http://link.aps.org/doi/10.1103/PhysRevB.50.8889`.

[142] A. A. Kiselev and L. V. Moiseev. Zeeman splitting of heavy-hole states in III-V and II-VI heterostructures. *Phys. Solid. State*, 38:866–871, 1996.

[143] A. V. Nenashev, A. V. Dvurechenskii, and A. F. Zinovieva. Wave functions and g-factor of holes in Ge/Si quantum dots. *Phys. Rev. B*, 67(20):205301–, May 2003.

[144] T. Nakaoka, T. Saito, J. Tatebayashi, and Y. Arakawa. Size, shape, and strain dependence of the $g-$factor in self-assembled In(Ga)As quantum dots. *Phys. Rev. B*, 70(23):235337–, December 2004.

[145] T. Nakaoka, T. Saito, J. Tatebayashi, S. Hirose, T. Usuki, N. Yokoyama, and Y. Arakawa. Tuning of g-factor in self-assembled In(Ga)As quantum dots through strain engineering. *Phys. Rev. B*, 71(20):205301–, May 2005.

[146] Craig E. Pryor and Michael E. Flatté. Landé $g-$factors and orbital momentum quenching in semiconductor quantum dots. *Phys. Rev. Lett.*, 96(2):026804–, January 2006.

[147] Till Andlauer and Peter Vogl. Electrically controllable $g-$tensors in quantum dot molecules. *Phys. Rev. B*, 79(4):045307–, January 2009.

[148] Weidong Sheng. Electrical tuning of exciton $g-$factors in quantum dot molecules: Effect of hole localization. *Applied Physics Letters*, 95:113105, 2009.

[149] S. J. Prado, C. Trallero-Giner, A. M. Alcalde, V. Lopez-Richard, and G. E. Marques. Influence of quantum dot shape on the Landé-$g-$factor determination. *Phys. Rev. B*, 69(20):201310–, May 2004.

[150] B. J. Witek, R. W. Heeres, U. Perinetti, E. P. A. M. Bakkers, L. P. Kouwenhoven, and V. Zwiller. Measurement of the $g-$factor tensor in a quantum dot and disentanglement of exciton spins. *Phys. Rev. B*, 84(19):195305–, November 2011.

[151] I. A. Yugova, A. Greilich, E. A. Zhukov, D. R. Yakovlev, M. Bayer, D. Reuter, and A. D. Wieck. Exciton fine structure in InGaAs/GaAs quantum dots revisited by pump-probe faraday rotation. *Phys. Rev. B*, 75(19):195325, May 2007. doi: 10.1103/PhysRevB.75.195325.

[152] A. A. Kiselev, E. L. Ivchenko, and U. Rössler. Electron $g-$factor in one- and zero-dimensional semiconductor nanostructures. *Phys. Rev. B*, 58(24):16353–16359, December 1998.

[153] E. Poem, Y. Kodriano, C. Tradonsky, N. H. Lindner, B. D. Gerardot, P. M. Petroff, and D. Gershoni. Accessing the dark exciton with light. *Nat. Phys.*, 6:993, 2010.

[154] M. Baier, F. Findeis, A. Zrenner, M. Bichler, and G. Abstreiter. Optical spectroscopy of charged excitons in single quantum dot photodiodes. *Phys. Rev. B*, 64:195326, 2001.

[155] M. Abbarchi, T. Kuroda, C. Mastrandrea, A. Vinattieri, S. Sanguinetti, T. Mano, K. Sakoda, and M. Gurioli. Fine structure splitting of quantum dot excitons: Role of geometry and environment. *Physica E*, 42:881883, 2010.

[156] Albert Messiah. *Quantum Mechanis.* New York, Interscience und Amsterdam, 1961/62.

[157] E. Ivchenko and G. Pikus. *Supperlattices and Other Heterestructures: Symmetry and Optical Phenomena*. Springer Berlin Heidelberg, 1997.

[158] URL `http://physics.nist.gov/cgi-bin/cuu/Category?view=html&All+values.x=80&All+values.y=11`.

[159] I. Vurgaftman, J. R. Meyer, and L. R. Ram-Mohan. Band parameters for III-V compound semiconductors and their alloys. *J. Appl. Phys.*, 89:5815–5875., 2001.

[160] X. J. Wang, I. A. Buyanova, F. Zhao, D. Lagarde, A. Balocchi, X. Marie, C.W. Tu, J. C. Harmand, and W. M. Chen. Room-temperature defect-engineered spin filter based on a non-magnetic semiconductor. *Nature materials*, 8:198–, 2009.

[161] Claude Weisbuch and Claudine Hermann. Optical detection of conduction-electron spin resonance in GaAs, $Ga_{1-x}In_xAs$, and $Ga_{1-x}Al_xAs$. *Phys. Rev. B*, 15:816–., 1977.

[162] Landolt-Börnstein. *Physics of Group IV Elements and III-V Compounds*. Springer-Verlag, Berlin, 1982.

[163] M. Oestreich, A. P. Heberle, W. W. Rühle, R. Nötzel, and K. Ploog. Extreme anisotropy of the $g-$factor in quantum wires. *Europhys. Lett.*, 31:399, 1995.

[164] J. Huebner, S. Kunz, S. Oertel, D. Schuh, M. Pochwala, H. T. Duc, J. Färstner, T. Meier, and M. Oestreich. Electron $g-$factor anisotropy in symmetric (110)-oriented GaAs quantum wells. *Phys. Rev. B*, 84(4):041301–, July 2011.

[165] P. S. Eldridge, J. Hübner, S. Oertel, R. T. Harley, M. Henini, and M. Oestreich. Spin-orbit fields in asymmetric (001)-oriented $GaAs/Al_xGa_{1-x}As$ quantum wells. *Phys. Rev. B*, 83(4):041301–, January 2011.

[166] Yu. G. Kusrayev, A. V. Koudinov, I. G. Aksyanov, B. P. Zakharchenya, T. Wojtowicz, G. Karczewski, and J. Kossut. Extreme in-plane anisotropy of the heavy-hole $g-$factor in (001)-CdTe/CdMnTe quantum wells. *Phys. Rev. Lett.*, 82(15):3176–3179, April 1999.

[167] E. S. Moskalenko, L. A. Larsson, and P. O. Holtz. Spin polarization of the neutral exciton in a single InAs quantum dot at zero magnetic field. *Phys. Rev. B*, 80(19): 193413, Nov 2009. doi: 10.1103/PhysRevB.80.193413.

[168] R. I. Dzhioev and V. L. Korenev. Stabilization of the electron-nuclear spin orientation in quantum dots by the nuclear quadrupole interaction. *Phys. Rev. Lett.*, 99:037401, 2007. doi: 10.1103/PhysRevLett.99.037401.

[169] R. Oulton, A. Greilich, S. Yu. Verbin, R. V. Cherbunin, T. Auer, D. R. Yakovlev, M. Bayer, I. A. Merkulov, V. Stavarache, D. Reuter, and A. D. Wieck. Subsecond spin relaxation times in quantum dots at zero applied magnetic field due to a strong electron-nuclear interaction. *Phys. Rev. Lett.*, 98(10):107401, Mar 2007. doi: 10.1103/PhysRevLett.98.107401.

[170] Ceyhun Bulutay. Quadrupolar spectra of nuclear spins in strained $In_xGa_{1-x}As$ quantum dots. *Phys. Rev. B*, 85:115313, 2012.

[171] M. N. Makhonin, E. A. Chekhovich, P. Senellart, A. Lemaître, M. S. Skolnick, and A. I. Tartakovskii. Optically tunable nuclear magnetic resonance in a single quantum dot. *Phys. Rev. B*, 82(16):161309, Oct 2010. doi: 10.1103/PhysRevB.82.161309.

[172] O. Krebs, P. Maletinsky, T. Amand, B. Urbaszek, A. Lemaître, P. Voisin, X. Marie, and A. Imamoglu. Anomalous hanle effect due to optically created transverse overhauser field in single InAs/GaAs quantum dots. *Phys. Rev. Lett.*, 104(5):056603, Feb 2010. doi: 10.1103/PhysRevLett.104.056603.

[173] T. Auer, R. Oulton, A. Bauschulte, D. R. Yakovlev, M. Bayer, S. Yu. Verbin, R. V. Cherbunin, D. Reuter, and A. D. Wieck. Measurement of the knight field and local nuclear dipole-dipole field in an InGaAs/GaAs quantum dot ensemble. *Phys. Rev. B*, 80(20):205303, Nov 2009. doi: 10.1103/PhysRevB.80.205303.

[174] P.-F. Braun, , B. Eble, L Lombez, B. Urbaszek, T. Amand, X. Marie, P. Renucci, O. Krebs, A. Lemaître, P. Voisin, V. K. Kalevich, and K. V. Kavokin. Spin relaxation of positive trions in InAs/GaAs quantum dots: the role of hyperfine interaction. *phys. stat. sol. (b)*, 243(15):3917, 2006.

[175] E. A. Chekhovich, M. M. Glazov, M Senellart P. Krysa, A. B. Hopkinson, A. Lemaître, M. S. Skolnick, and A. I. Tartakovskii. Element-sensitive measurement of the hole-nuclear spin interaction in quantum dots. *Nature Physics*, page 1038, 2012.

Acknowledgements

After three years of my Ph.D. in Toulouse it is time to conclude that the success of this thesis can not be associated to an individual person. I am very grateful for any support in word and deed of everybody who contributed to my thesis directly and indirectly.
The work of this thesis was funded by the European Union in the framework of the Initial Training Network Spinoptronics and it was an honour to have contributed to the project.

First of all, I wish to acknowledge my supervisor Thierry AMAND and Xavier MARIE who let me accomplish my Ph.D. in their group. I am very grateful for Thierry‘s support in both research concerning my Ph.D. and usual life. He helped me a lot at the beginning as I just arrived in Toulouse by resolving of number of administrative tasks.
Thierry had always good ideas to explain, sometimes entirely new, physical effects. He showed me once again, that one has understood well any physics only when one can explain it the easiest way. I am grateful for a great number of his inputs on results interpretation, in general, and this thesis, in particular.

I thank Bernhard URBASZEK, my co-supervisor, for his engagement and ambitious experimental ideas pushing me forward. With his comprehensive experimental knowledge he guided me to the successful accomplishment of my thesis. Even in such cases where the difficult problems appeared to be impossible to be solved his advices always helped and motivated to keep trying.

I wish to thank Grégory SALLEN for two successful years spent together in the lab and for his support. We spent together as well hard time including non-stop experiments lasting several weeks as more relaxing time, during which he was a great French teacher. In particular, for conversations in French I am very grateful to him.

I gratefully acknowledge Eugenius IVCHENKO, Misha GLAZOV and Misha DURNEV from the Ioffe Institute, St. Petersburg, Russia for the collaboration. I thank Mark STEVENSON and Andrew SHIELDS from Toshiba Research Ltd. Cambridge, UK, for they let me accomplish my secondment in their lab and Jonas NILSSON for his secondment in our lab performing together excellent experiments.

Furthermore, I would like to thank Louis BOUET a new Ph.D. student stepping in my path for his inputs. He integrated fast and actively in our group and gathered during his master thesis a solid basis for his Ph.D. thesis. I hope I could transfer all knowledge concerning the experimental setup he will need.

I thank Daniel PAGET and Christophe TESTELIN for their willingness to be reporting referees and to co-examine my Ph.D. defense. Also I would like to thank Guillaume CASSABOIS and Michel GOIRAN for being a part of my thesis commission and for

co-examining my Ph.D. defense.

I thank our Japanese team from the NIMS in Tsukuba for their high quality samples enabling me to obtain such good and interesting results.

I would like also to acknowledge all members of the group "Optoélectronique Quantique" for a lovely working atmosphere: Tiantian ZHANG, Quang Ha DUONG, Cong Tu NGUYEN, Philippe BARATE, Simone MAZZUCATO, Delphine LAGARDE, Hélène Carrère, Pierre RENUCCI, and Andrea BALOCCHI.

All my colleagues from the IT network I would like to thank for very interesting and exciting time spending together at our project meetings and conferences. I did really enjoy our meetings, which became by and by as family reunions. For such a lovely atmosphere I am very grateful.

Finally, my special thanks go to all members of my family for their support in word and deed. It was a difficult and hard time at the beginning but we managed it together!!!